Electrical properties of various single-wall carbon nanotube networks

JOMBERT, Alice,Stécy

Electrical properties of various single-wall carbon nanotube networks

Alice Stécy Jombert

A thesis submitted in conformity with the requirements for the degree of Doctor of Philosophy

Chemistry department
and
School of Engineering

Electrical properties of various single-wall carbon nanotube networks

A. S. Jombert

Abstract

This thesis investigates conduction mechanisms of covalently and non covalently functionalised single wall carbon nanotube (SWCNT) networks. Unlike previous strategies where diamines were used, a novel route to covalently bridge SWCNTs by organic molecular linkers is proposed. The bridging relies on using modified Sonogashira and Ullmann couplings, which have the advantage of using spectroscopic evidence to ascertain the success of the bridging. Platinum-enriched SWCNTs were produced by coordinating Pt to pyridine ligands grafted on SWCNTs. Networks of covalently bridged SWCNTs, Pt-enriched SWCNTs and their SWCNT precursors were fabricated by vacuum filtration. In addition to these networks, networks of non covalently functionalised SWCNTs were built up using layer-by-layer (LbL) deposition. This second approach required the wrapping up of SWCNTs by ionic surfactants to exploit their electrostatic interactions.

Electrical properties, such as current-voltage and the current dependence on temperature and electrode separation are discussed for both filtered SWCNT and SWCNT LbL networks. Combined analyses of these characteristics were carried out to identify dominant conduction mechanisms. In this study, a modified quantum tunnelling model was proposed to best describe the in-plane electrical behaviour of the filtered SWCNT networks. As for SWCNT LbL networks, the in-plane conduction was shown to be governed by the Poole-Frenkel mechanisms while direct tunnelling dominates the out-of-plane conduction. Furthermore, the charge storage capacity of cut-SWCNT LbL networks integrated into metal-insulator-semiconductor devices are discussed in view of organic memory device applications.

Key words

Carbon nanotube; network; thin film; functionalisation; surfactant; diazonium radical addition; homo-coupling; cross-coupling; platinum; coordination; molecular linker; molecular bridge; electrical characteristics; conduction mechanism; charge transport

Declaration and Statement of copyright

I declare that no part of the material offered has previously been submitted by myself for a degree in this or another university.

A. S. Jombert

February 2010

In memory of

Mr F. Jombert and *Mr G. Houblon*

Acknowledgements

First and foremost, all glory belongs to God to whom I am ever grateful for His blessings.

This thesis would not have been possible unless a One North East (Grant No. SP 082) and EPSRC-GB (DTA studentship) had provided tuition fees and living expenses for the first year and the subsequent two years and three months, respectively.

My grateful thanks go to my family and friends for their encouragement. I particularly thank Dr L. Sabin who monitored my "PhD time", and Prof. G. R. Foulger and Dr G. Heinrich for their advice and support.

I express my gratitude to all those who supported me through their prayers. I am indebted to Dr M. K. Bayazit, Dr M. Mabrook and Dr C. 'Big Boss' Pearson, and I would like to show my gratitude to Dr P. M. Ushasree, Dr A. Chakraborty, Dr (to be) C. Herron, Dr A. Suri, and of course Dr E. Gümüs Bayazit. I would like to particularly thank Dr (to be) M. Beyene and Miss U. Woy.

I thank my supervisors Dr K. S. Coleman and Dr D. A. Zeze for their advice and guidance.

It is my pleasure to thank those who made this thesis possible by allowing me access to their facilities and sharing their knowledge, in particular Prof. M.C. Petty, Prof. T. Marder and Prof. K. Durose and his team. I also thank Prof. D. Wood and his team for authorising me to use their cleanroom and equipment.

I thank Mr J. E. Gibson, Mr W. D. Carswell, Ms J. Magee, Mr L. Bowen, Dr B. Mendis, and Dr. Graham Beamson of the National Centre for Electron Spectroscopy and Surface Analysis.

Table of contents

List of figures

List of tables

List of abbreviations/symbols

A_l	Absorption at wavelength l
Φ	Barrier height
$\vec{C}_h$	Chiral vector
e_r	Dielectric constants
m_{eff}	Effective mass
m_{eff}	Effective mobility
m	Electron mass
e_l	Extinction coefficient at wavelength l
e_0	Free space permittivity
l	Path length
$\hbar$	Planck constant divided by 2π
b_{PF}	Poole-Frenkel coefficient
b_{RS}	Richardson-Schottky coefficient
l	Wavelength
σ	Conductivity
$\vec{a}_1$, $\vec{a}_2$	unit vectors
AFM	Atomic force microscope
BE	Binding energy
CMC	Critical micellar concentration
CNT	Carbon nanotube
Conc.	Concentration
CVD	Chemical vapour deposition
DTAB	Dodecyltrimethylammonium bromide
E, F	Electric field
e, q	Electron charge
E_g	potential energy barrier
eV	Electron Volt
G	Conductance
h	Planck constant
HiPCO	High pressure carbon monoxide
I	Current
I-d	Current-electrode separation
I-T	Current-temperature
I-V	Current-voltage
J	Current density
k_B, k	Boltzmann constant
LbL	Layer-by-layer
MWCNT	Multi wall carbon nanotube
PAA	Polyacrylic acid
PEI	Polyethylene imine
PMMA	Polymethylmethacrylate
PSS	Polystyrene sulphonate
PTFE	Polytetrafluoroethylene
SDS	Sodium dodecylsulfate
SEM	Scanning electron microscope
SWCNT	Single wall carbon nanotube
TGA-MS	Thermogravimetry analysis coupled with mass spectrometry
TMSA	Trimethylsilyl acetylene
V	Voltage
VRH	Variable Range Hopping
XPS	X-ray electron spectroscopy

Introduction

Carbon nanotubes have generated a lot of interest since their discovery[1], and a great deal of effort has been focused on exploring their physical properties[2]. The electrical performance displayed by carbon nanotubes, encourage their integration into electronic devices[3]. Thus, strategies for scaling up devices based on individual nanotubes have been developed[4]. However, these are still limited by the inability to produce nanotubes exhibiting repeatable properties. Properties of SWCNT networks, which differ from those of individual SWCNTs, are reviewed elsewhere[5]. The difficulty in manipulating nanometric objects also hinders the integration of SWCNTs into electronic devices. However, working with SWCNT networks reduces the discrepancy in their properties and facilitate their integration.

Two-dimensional SWCNT networks are of particular interest for transparent[6] and flexible[7] electronics. Applications in which randomly oriented SWCNT networks can be included extend from transparent electrodes in solar cells[8] and light emitting devices[9] to gas sensors[10]. Consequently, it is important to understand the transport mechanisms in SWCNT networks to achieve a successful integration of SWCNTs, with a view to producing tangible devices. This is particularly relevant in the case of SWCNTs, which can be metallic or semiconducting, adding a further level of complexity to the networks. Furthermore, the structure of SWCNTs is known to be affected by chemical functionalisation[11]. Thus, SWCNT networks can display different properties upon modifications undergone by nanotubes. This makes the study of the properties of the SWCNT networks compelling in each case. Identifying conduction mechanisms, is of high relevance for electronic devices as it allows for an improved understanding of the material, as well as optimising the parameters involved in the conduction to improve performance.

The work presented in this thesis contributes to improving the understanding of the electrical properties of functionalised SWCNT networks. With this intent, chemical modifications such as Ullmann and Sonogashira couplings were performed to bridge the SWCNTs. Networks of bridged SWCNTs and their SWCNT precursors were

fabricated by filtration, while non covalently functionalised SWCNT networks were built up by layer-by layer deposition. Conduction models governing charge transport mechanisms across all SWCNT networks were identified.

This thesis details the fabrication of two-dimensional, randomly orientated SWCNT networks, and the study of their electrical properties. The SWCNTs contributing to the networks underwent covalent or non covalent functionalisations. Distinct modifications such as surfactant wrapping, radical additions, molecular bridging of SWCNTs and platinum coordination, were performed on the SWCNTs. Spectroscopic analyses such as Raman, UV-visible-near IR and XPS spectroscopy were used to characterise the SWCNTs, and determine the success of the different reactions. Dominant conduction mechanisms across networks produced from these modified SWCNTs were determined, using combined analyses of the current-voltage characteristics and their temperature dependence.

The work presented in this thesis is divided into four result chapters. The first deals with the construction and study of SWCNT networks built up using the layer-by-layer (LbL) deposition method. The dominant conduction mechanism across SWCNT LbL networks is identified, and the integration of SWCNT LbL networks into organic memory devices is provided as an example of its application. The last three result chapters deal with the fabrication of SWCNT precursors, bridged SWCNTs and Pt-SWCNTs, and the fabrication of their networks by vacuum filtration. Conduction mechanisms in these SWCNT networks are also identified.

Chapter	Content	Objective
Introduction	General introduction	Context and purpose of this thesis
1	Description of the nature, structure, properties and particularities of individual SWCNT and SWCNT networks	Establishment of a fundamental knowledge on carbon nanotubes
2	Fabrication and characterization of SWCNT LbL networks followed by their electrical study. Demonstration of charge storage capability of cut-SWCNT LbL networks.	Fabrication and study of SWCNT networks where the nanotubes' junctions are mainly made of insulating material
3	Functionalisation of SWCNTs by radical addition, fabrication of SWCNT networks and their electrical characterization with an emphasss on their electronic transport	Evidence of addition to SWCNTs and identification of conduction mechanisms in SWCNT precursors to be used as references
4	Formulation of organic molecular bridges between SWCNTs using coupling reactions and the electrical study of networks subsequently produced from the bridged nanotubes	Methodology for bridging SWCNTs with conductive organic molecules and influence of the bridging species on the electrical properties of SWCNT networks
5	Coordination of SWCNTs to create Pt-enriched SWCNT networks and discussion over the possibility of Pt-bridges between nanotubes	Determination of the conduction model for the platinum enriched SWCNT networks
Conclusion	Discussion on the processes, obstacles encountered and results achieved.	Highlights of this research and propositions for future directions

Table 1 Thesis overview/organisation

Chapter 1
Background information on carbon nanotubes

Carbon nanotubes (CNTs) are part of the fullerene family, the third known allotropic form of carbon after graphite and diamond. Contrary to graphite and diamond, CNTs are carbon nanostructures. They are shaped like hollow tubes closed at their extremities. These tubes have diameters in the nanometre range in comparison to their lengths, which can reach hundreds of microns. Therefore, they are considered to be 1-dimensional nanostructures.

1.1 Carbon nanotubes' structure

Despite indications of an earlier discovery of CNTs by different groups[12,13], it is widely accepted that CNTs were discovered by *Sumio Iijima* in 1991[1]. Driven by research into the study of fullerenes, he discovered nanotubes in the soot of carbon as a result of arc-discharge evaporation[1]. *Figure 1-1* shows the representation of a C_{60} fullerene molecule alongside the first electron micrographs of multi-wall carbon nanotubes (MWCNT) and single-wall nanotubes (SWCNT).

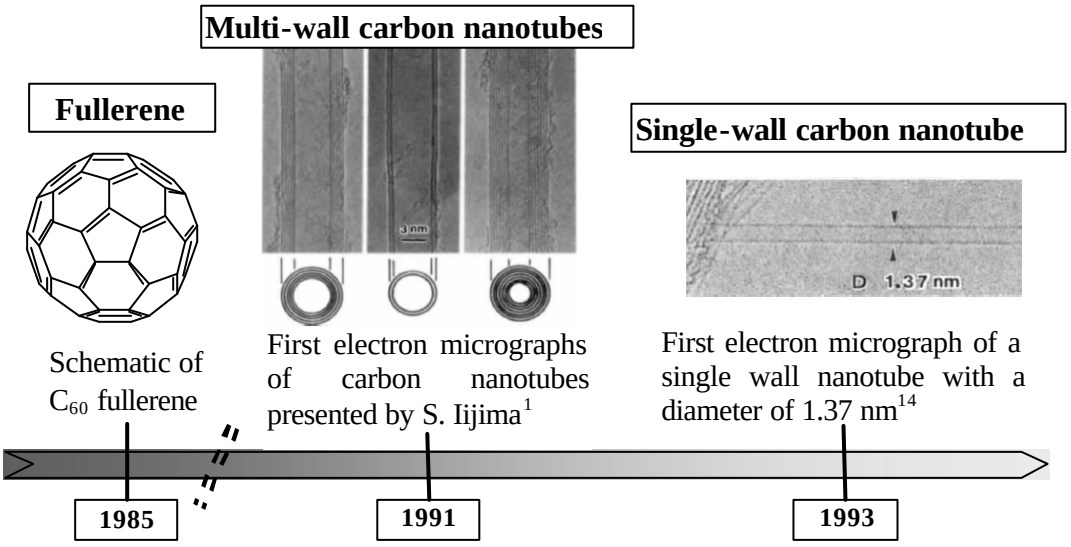

Figure 1-1 Schematic of a fullerene (C_{60}), first electron micrographs of carbon nanotubes[1] Reprinted by permission from Macmillan Publishers Ltd: Nature 354, 6348 p.56, copyright 1991 *and first electron micrograph of a single-wall carbon nanotube*[14] Reprinted by permission from Macmillan Publishers Ltd: Nature 363, 6430 p.603, copyright 1993

Figure 1-1 illustrates the main structural differences between carbon nanotubes. MWCNTs contain two or more carbon shells while SWCNTs have only one shell. The fact that carbon nanotubes are MWCNTs or SWCNTs affects their properties (e.g. electronic transport). However, other major structural parameters such as the diameter must be considered. The SWCNTs structure has a direct influence on their electronic nature, which can be metallic or semiconducting based on their geometry (length and diameter) and helicity. Different aspects of CNTs have been extensively investigated such as their growth[15], their structure[16], their electronic transport[17] and their electrical properties[18].

The atomic arrangement of CNTs was first presented in 1991[1]. The extremities are fullerene-like structures whose configuration allows the closure of nanotubes given the alternation between the hexagonal and pentagonal primitive cells. Along the nanotubes, each carbon atom is bonded with 3 others by a trigonal arrangement with sp^2 hybridization. Thus, the carbon atoms are laid out on a honeycomb crystalline lattice which is is analogous to that of graphene. The similarity between CNTs and graphene led to the representation of a nanotube as one sheet of graphene rolled-up on itself. Thus, SWCNT can theoretically be referred to as a single rolled-up graphene sheet. For MWCNTs, several graphene sheets are rolled-up around a common axis. Although a graphene sheet can be rolled-up in innumerable ways, each SWCNT can be identified by one chiral vector. The SWCNT is characterised by its structure which is defined by this chiral vector which contains information on its nature. For a lattice with unit vectors $\vec{a}_1$ and $\vec{a}_2$, a chiral vector $\vec{C}_h$ can be defined by *equation 1-1*:

$$\vec{C}_h = n \times \vec{a}_1 + m \times \vec{a}_2 . \qquad (1\text{-}1)$$

$\vec{C}_h$ is the vector representing the circumference of the SWCNT and the integers (*n*, *m*) define the helicity of a SWCNT. Thus, $\vec{C}_h$ gives access to their diameter and their structure is defined by their helicity. A representation of the helicity and the type of nanotube is shown in *Figure 1-2*. This is valid for the SWCNTs as the MWCNTs are composed of several SWCNTs with different helicities.

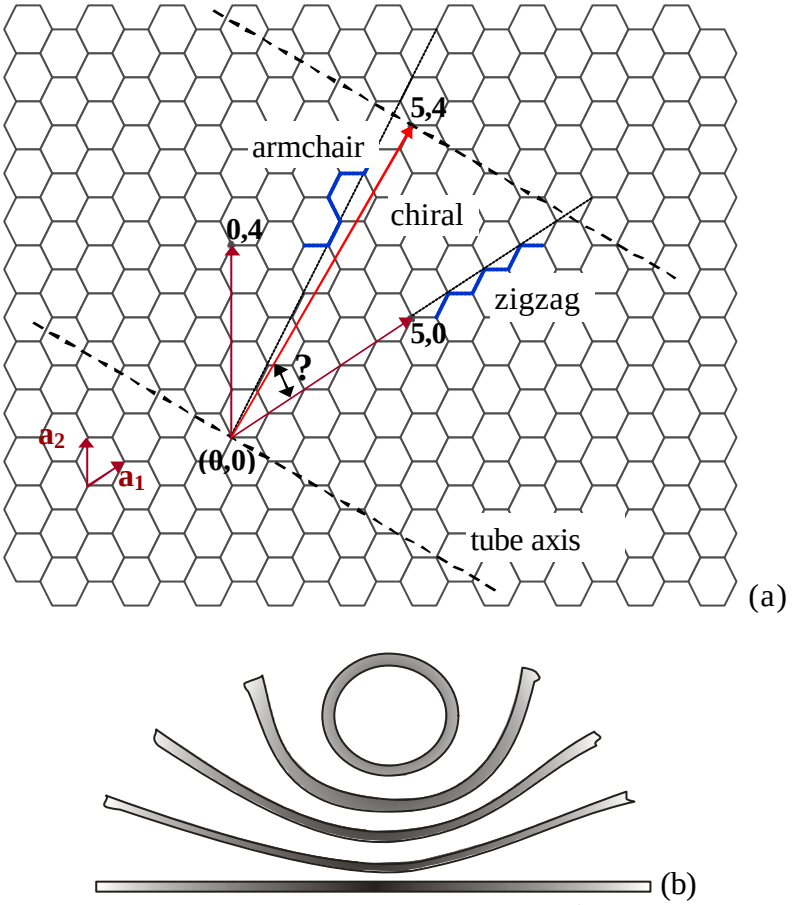

Figure 1-2 (a) SWCNT rolled up directions on a sheet of graphene. The axis used as the rolling up direction is the vector $\vec{C}_h$ and the dashed lines are parallel of the nanotube axis. The chiral angle ? is defined by $\vec{a}_1$ and $\vec{C}_h$. For zigzag CNTs ? = 0°, for armchair CNTs ? = 30° and for chiral CNTs 0 < ? < 30°. (b) Schematic of the rolling-up of a graphene sheet to form a SWCNT.

For $n = m$, the nanotube has an armchair structure while for m or $n=0$, the nanotube has a zigzag structure while for all other values of m and n, the nanotube has a chiral structure. Thus, CNTs are classified according to their number of walls and their chirality. Although there are an infinite number of axes, which allows the formation of a nanotube from a sheet of graphene, the symmetric nature of the graphene lattice leads to only 3 families of carbon nanotubes: zigzag, armchair and chiral.

The SWCNTs structure is fundamental to determine their properties. *Hamada and co-workers*[17] showed that SWCNTs could be metallic or semiconducting, which has been confirmed in other studies[19]. The metallic or semiconducting nature is dependent on its helicity and diameter. SWCNTs are metallic for $n-m=3\ell$ and are semiconducting for $n-m\neq 3\ell$ (ℓ integer) [17,20]. This double nature is reflected

in their electronic densities of states found by *Saito and co-workers*[21]. The van Hove singularities, present in their density of state, are a sign of their one-dimensional character[22].

Further, calculations revealed that provided there is a uniform distribution of chiral vectors, growths of SWCNTs will lead to a ratio of 1/3 metallic and 2/3 semiconducting[21]. The Kataura plots of SWCNTs (energy gap versus diameter) helped to determine whether the SWCNTs are semiconducting or metallic by using their structural properties[23].

1.2 Properties of the CNTs

The significant interest and research effort currently invested in SWCNTs are essentially due to their potential to yield excellent physical properties. Furthermore, in addition to their ability to be semiconducting or metallic, SWCNTs exhibit interesting mechanical, electrical, thermal and optical properties which are linked to their geometry and chirality. For instance, the thermal conductivity of SWCNTs is dependent on the diameter, temperature and chirality of the SWCNTs[24].

1.2.1 Electrical properties

As mentioned before, the electronic properties of carbon nanotubes result from their helicity. Due to their geometry, they are considered a one-dimensional material and they are the unique structure which exhibits a ballistic transport[25,26,27,28] (or quasi ballistic transport in double-wall nanotube[29]) along their axis. The impact of the carbon nanotube's geometry on their electrical properties was well demonstrated, for instance a study showed the diversity of 4-point probes resistances for individual nanotubes. Thus, resistances from 2.0×10^{2} Ω for a 9.1-nm-radius CNT to a 2.4×10^{8} Ω for a 6.3-nm-radius CNT and resistances per micron from 2.0×10^{2} $\Omega.\mu m^{-1}$ to 4.8×10^{8} $\Omega.\mu m^{-1}$ were obtained[30]. Two-probe measurements carried out on individual MWCNTs resulted in an average resistance and conductivity of 7.2 $k\Omega.\mu m^{-1}$ and 1.85×10^{3} $S.cm^{-1}$, respectively[31]. Resistances in the range of 160-500 kΩ at room temperature were later reported for individual semiconducting SWCNTs with

diameters greater than 2 nm while reaching megaohms for diameters less than 1.5 nm[32]. The dependence of the electrical properties of the nanotubes over their diameter and helicity has already been established[20]. Current densities greater than 10^9 A/cm² has also been reported for individual SWCNTs using low-resistance contacts (Ti/Au electrodes)[33]. This level of current density was also observed for MWCNTs[34].

1.2.2 Mechanical properties

Carbon nanotubes are seen as the ultimate carbon structure to replace carbon fibres due to the similarities in their structures. For instance, tensile strengths for CNT ropes and carbon fibres were found at 3.6 GPa and 3.0 GPa, respectively[35]. Greater tensile strengths were calculated from this data giving 7.5 GPa for the SWCNT bundles and 22.2 GPa for an individual SWCNT[35]. The structural differences between nanotubes and carbon fibres also impact on the thermoelastic properties of composites. Improvements in the thermoelastic properties of CNT loaded polymers compared to carbon fibre loaded epoxy were also predicted[36]. Thus, the superior mechanical properties (such as the stiffness) of the CNT over the carbon fibres, makes it possible to achieve performances similar to that of carbon fibres-load composites with a lesser loading of CNTs. In addition, their low density implies that the overall weight of the composite is not notably affected, although its properties are significantly enhanced. Thus, extensive research efforts have been vested in studying the mechanical properties of CNTs as a result of their potential, which has led to some remarkable results. For instance, their Young's modulus was theoretically estimated as high as 1.8 TPa[37] and 1.25 TPa[38] for individual MWCNTs and individual SWCNTs, respectively. Micro-Raman analyses further confirmed the magnitude of the estimations of the Young's modulus at 3005 GPa and 2437 GPa for SWCNT and MWCNT, respectively[39].

1.2.3 Thermal properties

In microelectronics, as the number of transistors in a chip increases (Moore's law) more heat is generated, thus thermal management becomes a challenge[40]. This is due

to less space available as the consequence of the cluttering of the devices which causes the dissipation of heat by convection to be less effective. Theoretical thermal conductivities of CNTs have been predicted to reach 3000-6600 $W.m^{-1}.K^{-1}$ [41,42] therefore, CNTs are part of the novel technologies whose performances can meet the cooling need[43]. However, calculations showed that the thermal conductance of SWCNTs is lower than previously thought, despite a longer length where the ballistic transport can occur[44]. This was later validated by experimental data[45]. Nonetheless, high thermal conductances are predicted to be reached for nanotubes with lengths greater than tens of microns[44]. Experimental data obtained for a 2.76-µm-long individual SWCNT were found to be in agreement with the prediction[46]. A series of experiment analyses confirmed the high thermal conductivities of nanotubes. For instance, thermal conductivities of about 3500 $W.m^{-1}.K^{-1}$ at room temperature for a 2.6 µm individual SWCNT with a diameter of 1.7 nm were found within 20% of the predictions[47]. Other measurements on individual MWCNTs also showed a thermal conductivity at room temperature to be greater than 3000 W/K[32] and a thermoelectric power of 80 µV/K [45,48]. Measurements carried out at room temperature on individual ropes of SWCNTs led to a range of thermal conductivities from 1750 $W.m^{-1}.K^{-1}$ to 5800 $W.m^{-1}.K^{-1}$ [48]. Aligned bundles of SWCNTs exhibit thermal conductivity as high as 200 $W.m^{1}.K^{1}$ at room temperature[49,50].

1.2.4 Chemical properties

The difficulty of solubilisation of carbon nanotubes, the poor interface quality between CNTs and matrixes for nanocomposites are foremost issues which hinder their integration in different applications. These issues can be addressed by functionalising the nanotubes[51].

The structure of carbon nanotubes allows them to offer a wide range of chemical properties, from the insertion of small molecules like hydrogen and fullerenes into their cavities, to the addition of functionalised groups selectively located at their tip ends. *Figure 1-5* illustrates chemical modifications that carbon nanotubes can undergo[52].

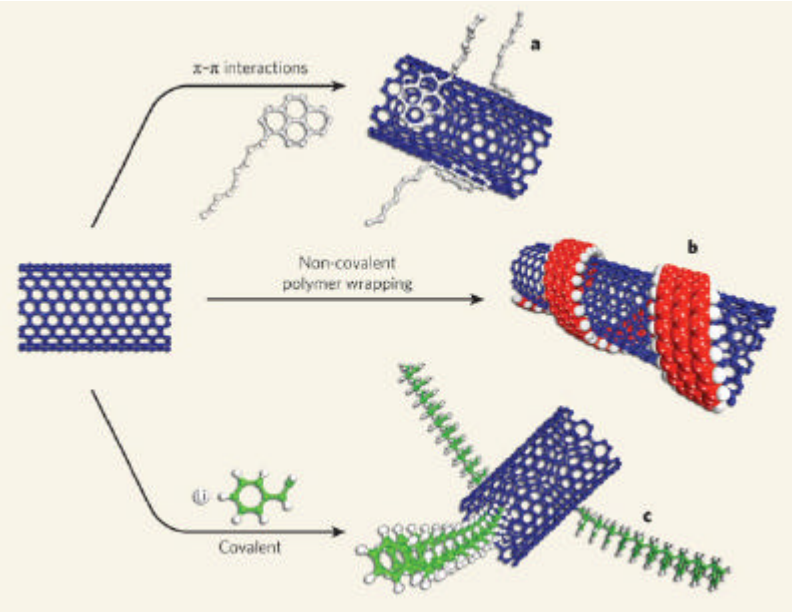

Figure 1-3: Chemical modification of carbon nanotubes. a, Aromatic molecules can be appended to nanotubes using certain non-covalent interactions (known as p–p interactions). b, Non-covalent interactions (including p–p interactions, van der Waals forces and charge-transfer interactions) can be used to wrap polymers around nanotubes. c, Chemical groups can be covalently attached to nanotubes. [52]. Reprinted by permission from Macmillan Publishers Ltd: Nature 447, 7148 p.1066, copyright 2007

Carbon nanotubes inherit their chemical properties from both graphene and fullerenes. Thus, the chemical stability of CNTs, mainly from their honeycomb lattice (like the graphene) is diminished by the curvature of the nanotubes, which explains a higher reactivity at their end.

The pyramidalization angle[i] formalism[53], also used for the fullerenes[54,55], demonstrates the existence of different levels of reactivity for CNTs depending on its localised curvature. This leads to the basic principle: the bigger the curvature, the higher the reactivity. This explains the low reactivity inside the nanotube compared to the outside. This formalism, quantifying localised curvatures, also explains why the defect sites on the sidewalls of the CNTs are favoured locations for covalent bindings, showing that covalent reactions occur preferentially on and around the defect sites[56-58].

In the covalent functionalisation of the CNTs, a distinction can be drawn between the covalent bonds taking place on and/or around the defects (as well as tip ends) and the

[i] Pyramidalization angle: deviation between real position of coordinate atom and position of the same atom if it was in a planar molecule

covalent bonds generated on 'flat' sidewalls. Covalent functionalisations by oxidation/carboxylation and radical additions are presented below.

1.2.4.1 Oxidation/carboxylation

The reactions for covalent functionalisation need to be aggressive in order to disrupt the stability of the CNTs. Thus, harsh conditions are needed to oxidise/carboxylate CNTs but prolonging the oxidation/carboxylation can cut them. Oxidation is done by heating the CNTs in presence of an oxidizing agent. This agent could be a gas, e.g. air[59,60] or ozone[61-63], or an oxidizing liquid usually nitric and/or sulphuric acids[64-68].
Gas phase oxidations tend to form hydroxyl and carbonyl groups whereas liquid phase oxidations lead to carboxylic acid groups[69]. Carboxylated CNTs have the advantage of being more soluble in water however, their electronic properties are disrupted and the semiconducting nanotubes are doped with holes[70].

1.2.4.2 Radical addition

Radical additions on CNTs surfaces are mainly carried out using diazonium salts following a process developed by *Tour and co-workers*[71,72] but a few radical additions carried out without diazonium salts have been recently reported[73,74].
The radical addition is self limited by the radicals reacting to each other, with the solvent and the bi-products created as much as reacting with the CNTs. Radical additions have also been shown to occur preferentially on metallic CNTs[75].

By nature, the covalent functionalisation of CNTs inserts defects into their structure. As a result, their performances decline as the perfection of their structure deteriorates. For instance their thermal conductivity drops (e.g. decrease of about 100 W/mK for 180 H atom attached) as nanotubes are covalently functionalized[76,77]. Covalent functionalisations also worsen the electrical properties of the CNTs. Contrary to an ionic functionalisation which can, depending on the dopant used, increase or decrease the electrical conductivity as it does not disturb the electronic structure of the nanotube, the covalent functionalisation interrupts the delocalization of the π-system by creating sp^3 bonds[78].

As stated above, covalent bonding disrupts the nanotubes' structure, which significantly reduces their performance while non covalent functionalisations provide an alternative to this. The molecules (surfactants[ii], polymers or aromatic molecules) are adsorbed on the surface of the CNTs instead of being grafted onto them.

1.2.4.3 Polymer (or surfactant) wrapped SWCNTs

This type of non covalent functionalisation of nanotubes, deals with polymers and surfactants. These are able to wrap SWCNTs due to adsorptions based on van der Waals and hydrophobic interactions. For instance, helical wrappings of SWCNTs by poly(phenylacetylenes) has been observed[79].

Studies show the ability[80] and the diversity of surfactants[81,82] used to disperse SWCNTs in aqueous solutions. The surfactants are adsorbed on the SWCNTs with different possible organizations[83] due to hydrophobic and van der Waals interactions between their hydrophobic backbones and the nanotubes.

The mechanisms, which allow some polymer wrapping around CNTs, are considered to be led by van der Waals interactions[84,85] or thermodynamically driven[86,87]. The forces holding them together are believed to be CH-π interactions[88], or van der Waals forces[89,90].

1.2.4.4 p-stacking

When there is an overlapping of π orbitals of juxtaposed aromatic molecules, the π-π interactions create stacks of these molecules. It is believed that, at different degrees, both van der Waals, hydrophobic and electrostatic forces contribute to these π-π interactions[91]. Being a network of aromatic rings it is possible to functionalise the sidewalls of the CNTs with molecules having aromatic rings[92].

The properties of CNTs are related to their fabrication processes and techniques via their structures (number of shells, geometry[iii] and perfection[iv] of the structure), which are determined during their growth. Initially fabricated by the arc-discharge method[1],

[ii] Surfactant: **sur**face **act**ive age**nt**
[iii] The geometry of the nanotube stands for their length and diameter
[iv] The perfection of the structure of the nanotube stands for to the presence and amount of defects

the carbon nanotubes can now also be synthesized by laser ablation, chemical vapour deposition (CVD) and high pressure carbon monoxide (HiPCO).

1.3 Growth of SWCNTs

A self-assembly process is at the origin of the carbon nanotube's growth regardless of the production technique used. In the case of SWCNTs, the presence of catalytic nanoparticles is required to initiate the growth mechanisms. These nanoparticles, usually made of transition metals: iron, cobalt or nickel, act as nucleation sites and their sizes determine whether or not nanotube growth can take place[93]. While the lengthening step of the formation found a consensus, the nucleation mechanisms are still not understood and several models have been presented.

Different growth mechanisms are reported for all production techniques such as arc discharge[1], laser ablation, chemical vapour deposition (CVD)[94], high pressure carbon monoxide (HiPCO) process[95]. The yarmulke[v] model proposed by *Dai and co-workers*[96] is the dominant hypothesis for the CVD growth. This model, valid when the carbon source is a gas, suggests that the carbon atoms are forming a graphene cap around the catalytic nanoparticle. This occurs to minimize its surface energy and the presence of this cap has to be maintained for the duration of the nanotube formation. Thus, the newly arrived carbon atoms are inserted preferentially between the nanotube edge and the nanoparticle[96]. Details of SWCNT growth models are available in a review by *Harris*[97].

1.4 SWCNT networks and their electrical properties

Two strategies are usually followed for the study of nanotubes. The first approach involves the use of individual nanotubes, while the second consists of either using a nanotubes assemblage (bundle, mat or network) or a nanotubes-integrated matrix (film or composite). This second approach is often chosen to avoid the challenge of the nanomanipulation and the difficulty with implementing large scale fabrications of

[v] Yarmulke (Yiddish for skullcap) is the term chosen by *Dai et al.* to name their growth model

devices. The interest also lies in the optical, mechanical and electrical properties of carbon nanotube networks which make them good candidates for applications such as transparent electrodes[98]. Thus, the work presented here was performed using this second strategy, where networks of nanotubes were fabricated and studied.

The multiplicity of phenomena happening is explained by the diversity of nanotubes composing the network (diversity of CNTs mentioned in *sections 1.1* and *1.2*). For instance, the junctions between two SWCNTs exhibit linear conductance responses as high as 0.28 e^2/h [1.08×10^{-5} S] between two metallic SWCNTs while it may be greater than 0.02 e^2/h [7.7×10^{-7} S] between two semiconducting nanotubes[99]. Complexity is also the result of parameters such as the length of the nanotubes constituting the network which influence the network conductivity[100] and parameters such as the network's thickness can also influence the conduction type within it[101]. Therefore the diversity of properties displayed by nanotube networks makes it impossible to establish any standards for one type of network. This section provides a selection of results obtained for pristine SWCNT networks for reference.

In SWCNT networks, where metallic and semiconducting nanotubes are mixed together, the ratio 1/3 metallic and 2/3 semiconducting is assumed to be preserved[21]. To have a metallic behaviour, the amount of metallic nanotubes has to be sufficient to overcome the percolation threshold and create a metallic path across the network. Percolation threshold in 2-D nanotube networks is achieved when an important increase of the conductance is observed for the threshold concentration[102]. Using SWCNT in sodium dodecyl sulphate solution, a metallic percolation threshold was reported, when the fraction of SWCNT in the film was about 5.5×10^{-3}.[103] Provided the percolation of metallic nanotubes is not attained (or that the metallic nanotubes have been burnt off), SWCNT networks are likely to exhibit p-type semiconductor behaviour[104,105]. The p-doped characteristic of nanotubes was shown to be non intrinsic to their nature. It is rather explained by the high energy barrier contact between the CNTs and the metal contacts. These energy barriers being influenced by the doping of the nanotubes, n-type CNTs are therefore possible providing an adequate functionalisation[106].

At room temperature, the resistivities in the parallel direction to aligned SWCNTs is close to that of individual SWCNT ropes at 0.72 or 0.825 mΩ.cm for the annealed sample[107]. Measurements in the parallel direction to SWCNT ropes displayed lower electrical resistivities, ranging from 0.34×10^{-4} to 1.0×10^{-4} Ω.cm (equivalent to electrical conductivities from 10000 to 30000 S/cm)[108]. In the case of randomly oriented SWCNTs films, electrical conductivities are several orders of magnitude less than those of SWCNT ropes[109-111]. *Table 1-1* compares conductivities of SWCNT ropes and those of randomly oriented pristine SWCNT networks.

	Conductivity (S/cm)	Growth	Purification	Reference
SWCNT ropes	10000-30000	Laser ablation	No	Thess[108]
Randomly disposed SWCNT	250	Arc discharge	none	Bekyarova[109]
	230		Yes	
	400		Yes (hydroxyl groups)	
	50	Laser ablation	Yes	Saran[110]
	1.3×10^{5}	HiPCO	Yes	Sreekumar[111]
	0.9×10^{5}		Yes (followed by heat treatment)	

Table 1-1 Electrical conductivities of SWCNTs networks depending on SWCNTs orientation, growth methods and, presence or absence of a purification step

Another parameter, which also declines in nanotube networks, is the mobility; low mobilities were obtained in random SWCNT networks (from ~10 cm²/Vs for low density networks to ~100 cm²/Vs for higher density ones[104]). This contrasts with the 100000 cm^2/Vs at room temperature[112] estimated for individual semiconducting SWCNT. The electrical properties displayed by networks of nanotubes tend to be worse than individual nanotubes or ropes. However, the current density of SWCNT bundles exhibit 10^9 A/cm^2, which is similar to that of individual SWCNTs (or MWCNT), although several nanotubes contribute to the conduction. The self-heating of the nanotubes provokes current breakdowns, observed beyond a current saturation step[113].

The SWCNT networks exhibit a metallic behaviour at high temperatures, which is overtaken by a non-metallic one as the temperature passes a crossover temperature[114].

Current-voltage measurements carried out on SWCNT mats are also in accordance with the idea of having metallic and non-metallic types of conduction depending on the temperature region[115]. These results are not standard as a non-metallic behaviour at higher temperatures and a metallic one at lower ones was expected and not vice versa.

Variable range hopping (VRH) conduction was found to be the conduction model which governs the electrical transport in both ropes[116,117] and mats of CNT[115,118]. Recent electrical measurements, carried out on SWCNT networks of various thicknesses further confirmed this VRH conduction[119]. However, for small systems, the conduction can be dominated by the tunnelling phenomena. It is the case at low temperatures, when the current-voltage characteristics of SWCNT networks were well fitted to the fluctuation-induced tunnelling model[114]. Thus, such SWCNT systems led to conduction mechanisms based on the hopping mechanism or the tunnelling phenomenon. A recent conduction model was proposed by Kaiser and co-workers to explain the conduction in SWCNT networks. They proposed a metallic conduction model, where the transport is interrupted by thin tunnelling barriers, backscattering by zone boundary phonons and VRH, to explain the electronic conduction in SWCNT networks[245]. Thermoelectric power at ~60 µV/K and ~40 µV/K at 300 K was also discovered from transport type analysis[104,105]. For SWCNT mats exhibiting a thermoelectric power of ~40 µV/K, a relation between the thermoelectric power and the alignment or misalignment of the CNTs in the system was also established[120]. External factors, such as the presence of gas in the sample environment, were also seen to impact the thermoelectric power of SWCNT ropes[121].

Electrical properties of SWCNT networks lack consistency and using identical nanotubes would induce more uniformity. Researches showed that nanotubes can be produced by using short CNTs as seeds to initiate the growth. The same nanotube was cut, and the short CNTs produced were used as templates and amplified during the growth[122]. Therefore, this process makes possible the fabrication of networks where the presence of particular types of nanotube is enhanced. Therefore, these networks are expected to help setting standards in the properties of such CNT systems.

SWCNTs networks can be incorporated in devices such as light emitting devices, solar cells and transistors, and chemical functionalisations, often required for their

integration into devices, impact on the SWCNTs properties. Thus, it is important to identify the electrical behaviour of functionalised SWCNT networks. This thesis contributes to these research efforts in characterising the electrical properties of networks made of covalently and non covalently modified SWCNTs. The aim is to establish the dominant conduction mechanisms across such SWCNT networks.

Chapter 2
SWCNT layer-by-layer films

2.1 Introduction

Layer-by-layer (LbL) deposition technique is a process used to build-up multilayered films by exploiting the interactions between reagents. The multilayered films subsequently produced can offer special characteristics depending on the reagents used[123]. The interest in this deposition technique lies in its simplicity to implement and the sub-nanometre[vi] level of thickness control that it provides. LbL method competes and even exceeds techniques such as Langmuir-Blodgett and self-assembly[124] because of the wide range of reagents available for this process. Applications for the LbL technique range from biotechnology[125] to microelectronics[126].

Building up carbon nanotube multilayered films using layer-by-layer deposition was shown to be possible in 2002[127] and studies of their structural, mechanical, electrical, and thermal properties were carried out[128].

This chapter reports on the fabrication of SWCNT LbL films and the identification of the transport mechanisms governing the conduction based on the combined study of their electrical characteristics (current-voltage, current electrode separation and current-temperature). Furthermore, the charge storage capability of cut-SWCNT LbL films integrated in metal-insulator-semiconductor devices is demonstrated.

2.2 Principle of the LbL deposition

The principle of the LbL has been known since 1966 when *R. Iler*[129] discovered that anionic particles create a monolayer as they bonded to cationic surfactants adsorbed

[vi] Typical thicknesses of a monolayer vary between 0.5 nm and 5 nm

on surfaces. In 1991, *G. Decher and J. Hong*[130] applied this principle to organic polyelectrolytes. Then, the technique has been used in several disciplines for numerous applications from encapsulation[131] to sensors[132,133] and coatings[134].

The electrostatic attractions are the driving factor on which the LbL depositions are commonly based. However, short ranging interactions like hydrophobic interactions should still be considered as an important factor for multilayer fabrication[135]. LbL films can also be built up without employing electrostatic charges; in fact donor-acceptor interactions[136] and specific recognition[137] are amongst the interactions used to stack layers.

In the case of LbL depositions driven by electrostatic interactions (forces used to build up the multilayered films presented in this work), the deposition process requires complementarities of the electrostatic charges of its reagents. Therefore, from small molecules to polymers, all types of reagents are allowed provided they carry electrostatic charges.

To allow the formation of a multilayered film the same polyelectrolyte complex formation occurring in the solution has to take place on the surface. A polyelectrolyte complex is formed when two aqueous solutions of polyelectrolytes carrying opposite charges are mixed together. An insoluble complex is formed as the polyelectrolytes precipitate provided the charge density of the polyelectrolytes is high enough for attractive electrostatic interactions to overcome the backbone repulsions.

In solution, for a charge density high enough, the charges of the monomers are repulsing each other, therefore all polyelectrotytes are stretched. The range (short or long) of the electrostatic interactions between monomers can also depend on the levels of salts contained. As the ions from the salt in the solution join up the opposite charges of the polyelectrolyte, fewer charges are left available and the electrostatic interactions have a short range. This causes the polyelectrolytes to be compact. For low ionic strength solutions, the polyelectrolytes are expected to be stretched due to long range interactions of the monomers repelling each other[138]. In

this work, no salt was added to the solutions to maximise the length of the polyelectrolytes (so their surface coverage) and minimise the thickness of their layers.

When a charged surface is interacting with an oppositely charged solution (e.g. dipping, spraying or spin coating) an electric field is created at the interface between the surface and the solution. This electric field attracts counterions from the solution, which are confined at the interface. These counterions create a screening effect, which causes the electric field to decrease as the distance to the surface increases. The confined counterions are adsorbed on the surface due to the ionic interactions, which neutralize the charges of the surface. The electrostatic charges of ions carrying the same charge as the surface are repelled by the electrostatic field. Therefore, these ions, required for the neutrality of the polyelectrolyte solution, do not approach the surface and only the desired polyelectrolytes are deposited.

The polyelectrolytes are not flat on the surface, instead they form loops. Thus, the charges located on the loops of the polyelectrolytes allow the overcompensation of the surface charges. An inversion of charge of the surface takes place as it now carries the charge of the adsorbed polyelectrolytes.

As the adsorption carries on, the density of opposite charges increases, then stabilises. This stabilisation occurs when new polyelectrolytes cannot access the surface as they are repelled by the adsorbed polyelectrolytes, which carry the same electrostatic charges. This typically happens after 20-30 minutes of deposition[138].

The attractive and repulsive principle of electrostatic charges is exploited to build up LbL films, as opposite charges are subdued to an electrostatic attraction. Therefore, alternating layers of cationic and anionic molecules layers allows the building up of multi-layers films. Thus, in principle, LbL deposition can occur with any cationic and anionic molecules since it is the reversal of electrostatic charges that is responsible for the building process.

2.3 Carbon nanotube multilayered films

As stated previously, the LbL method requires the alternated reversal of electrostatic forces (charges) to build-up multilayered films. As such, to build-up LbL films of carbon nanotubes, electrostatic charges have to be adjoined to the CNTs. This is achieved by functionalising the nanotubes. In *Chapter 1*, two functionalisation approaches were introduced: the covalent and non-covalent functionalisations. Both methods can supply charges to the nanotubes depending on the functional groups added on. Nonetheless, the integrity of the structure of the nanotubes is preserved with the non-covalent functionalisation. Therefore, the nanotubes were functionalised with ionic surfactants to obtain the electrostatic charges needed.

The surfactant functionalisation of the carbon nanotubes results from their adsorption onto the nanotube's surface via hydrophobic and van der Waals forces (see *section 1.2.4.3*). For the LbL process applied here, the non-covalent functionalisation of the nanotubes consisted of wrapping the nanotubes with anionic and cationic surfactants. A description of the process, used to build-up carbon nanotube multilayered films with the layer-by-layer method, is presented below.

2.3.1 Substrate preparation

Substrate cleaning

The substrates were left in a piranha solution (H_2SO_4:H_2O_2 at 1:1) for 20 minutes, in order to eliminate impurities. After washing in two successive deionised water baths, the substrates were sonicated in deionised water. This was followed by a rinse in propan-2-ol. This procedure was sufficient to obtain contamination-free substrates.

"Seed" polyelectrolyte multilayer

Prior to depositing the nanotubes loaded LbL film, each substrate was coated by 2-3 "seed" bi-layers of polyelectrolytes to charge the surface and increase the amount of nanotubes deposited from their first layer. These seed multilayers were always started by the adsorption of polyethyleneimine (PEI), a branched polyelectrolyte whose adsorption structure was shown to be patch-like flat in the dried state[139]. Desorptions of PEI from the layer were observed between pH 9.7 and pH 5.8[140]. Thus, pH of the

PEI solution used was set at pH 6.2 with tris(hydroxymethyl)aminomethane (Tris) buffer. Tris buffer was also used for the other polyelectrolytes to avoid charge transfer between layers, which could end up reaching the pKa of the acid and base polyelectrolytes. Reaching their pKa would result in protonated polyelectrolytes, which would not have charges available to carry on the deposition. The first polyelectrolyte adsorption is attributed to bridging attraction between the non charged surface and the PEI, which provides a high adhesion[141]. This first PEI layer provides a positively charged surface onto which a negatively charged polyelectrolyte is subsequently deposited. Another layer of PEI is deposited and as stated in the *section 2.2*, the alternated reversal deposition process is repeated until the desired number of layers is achieved. The polyelectrolytes used as seed layers include PEI for the positive charge and polystyrenesulphonate (PSS) or polyacrylicacid (PAA) for the negative charge. Their chemical structure is given in *Table 2-1*.

PEI	PSS	PAA
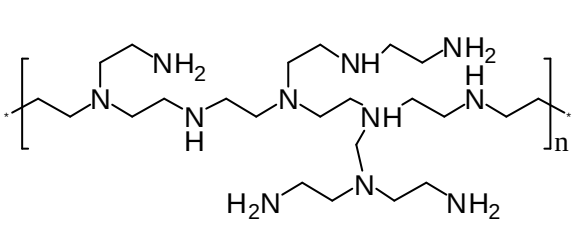	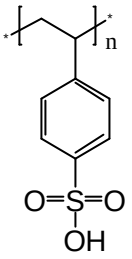	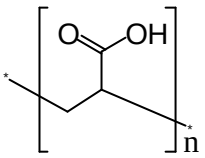

Table 2-1 Monomer structures of the polyelectrolytes used in this work

The seed layer deposition is influenced by parameters such as the pH of the solutions, salt concentration, deposition time and rinsing and drying steps. To minimize the thickness of these seed multilayers, rinsing and drying steps were performed after each polyelectrolyte solution dip[124] and no salt was added to the polyelectrolyte solutions leading to stretched polyelectrolytes. As the surface adsorption rates decrease after 20 min, the deposition time was kept to 30 min to minimise discrepancy in the films thickness[124].

2.3.2 Carbon nanotube wrapping

As mentioned in *Chapter 1*, surfactants interact with SWCNTs by van der Waals interactions and hydrophobic bounding. These interactions take place between the

non-polar termination (hydrophobic) of the surfactant and the nanotube's surface so the hydrophilic termination (polar head) of the surfactant is directed towards the aqueous solution. The surfactants, located at the interface between the nanotube and the solvent, reduce the interface energy between the water and the SWCNTs. Thus, the dispersion of surfactant wrapped SWCNTs is facilitated and the solubility of the SWCNT/surfactant assembly in an aqueous solution increases.

For the wrapping to occur, the concentration of surfactants in the solution has to be higher than their critical micellar concentration (CMC), as the amphiphilic molecules have the ability to self-organize in micelles[vii], providing that their CMC is reached. Amphiphilic molecules are spontaneously self-assembled in micelles when their CMC is reached as they act to minimize the contact between their hydrophobic termination and the aqueous solvent. Micelles formations are entropy driven as both hydrophobic effect and entropy of transfer of hydrocarbon from water are the major factors contributing to the micellisation[142]. In a non polar solvent, reverse micelles are formed under the same principle. Thus, in aqueous solutions, the hydrophobic terminations of the surfactants are directed towards the interior of the micelle and their polar heads towards the solution. In oil, their polar heads are directed toward the interior of the reverse micelle. An amphiphilic monomer and its micellar self-organisations are illustrated in *Figure 2-1*.

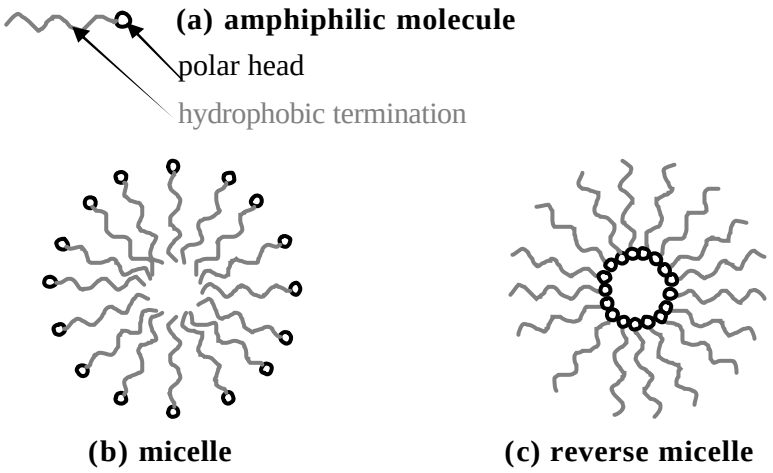

Figure 2-1 (a) monomer of an amphiphilic molecule, (b) micelle self-organisation of monomer in aqueous solvent provided monomer concentration > CMC and (c) reverse micelle self-assembly of monomer in oil based solvent for monomer concentration > CMC

[vii] Micelle: molecular structure resulting of the self assembly of amphiphilic molecules

Once the surfactants solutions are prepared, the same self-organisation process takes place when micelles are in the presence of poorly soluble compounds. This phenomenon is exploited in detergents to remove non soluble matter as well as in lubricants[143]. The wrapping of surfactants around SWCNTs occurs according to the process of micellar self-organisation seen in *Figure 2-1 (b).* Thereby, the surfactant wrapping of the nanotubes is basically the formation of micelles around the SWCNTs and in order for this wrapping to occur and be stable, the CMC of the surfactant solutions has to be reached[144].

Micelles are dynamic structures given that intermicellar exchanges occur in solution. Thus, to have stable solutions the surfactant concentrations have to be higher than their CMC. The ultrasonication of SWCNTs in surfactant solutions has therefore two aims: firstly, breaking down the bundles of SWCNTs in smaller bundles and individual nanotubes and secondly, disturbing the micellar structures in order for the micellisation to be reassembled around the SWCNTs. After sonication the SWCNTs are dispersed in the surfactant and these solutions will be used for the layer-by-layer process. The ionic surfactants used in this work are sodium dodecyl sulfate (SDS) and dodecyltrimethylammoniumbromide (DTAB), which provide negative and positive charges respectively. *Figure 2-2* displays the chemical representations of these surfactants.

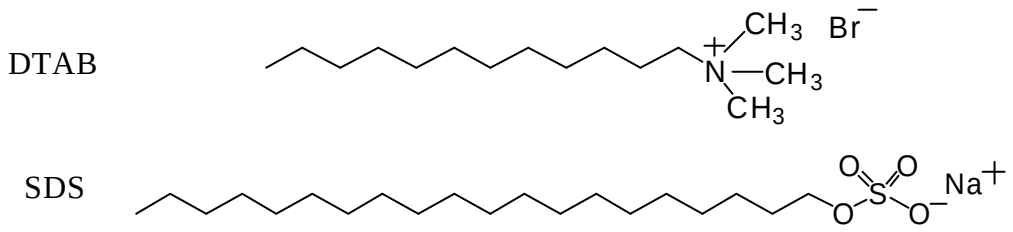

Figure 2-2 Chemical representation of DTAB and SDS surfactants

2.3.3 SWCNT LbL film building process

Dipping a substrate in a charged solution is the first deposition method used to build up LbL films[124]. Following this dipping process, spraying[145], spin-coating[146] and continuous flow[147] methods have been reported as LbL methods. The advantages of the spraying over the dipping lies principally in its convenience, as it can easily be employed for large areas. Yet, with this technique, the intermediate rinse steps are

essential to the film quality[145]. The spin coating technique used for LbL depositions provided faster deposition process and higher ordered multilayers films than the dipping process[146]. The LbL films built-up by dipping appeared more uniformed than the film built-up using a cell flow[147].

The LbL multilayered films built up in this work were made by solution dipping. This was preferred to the spin coating as the dipping method does not restrict the size of the samples. The dipping process was also chosen over the spraying technique to avoid creating aerosols containing carbon nanotubes.

The deposition process exploited in this work consists of dipping the pre-charged substrate into solutions of surfactant-wrapped nanotubes. The excess of surfactant is eliminated by rinsing the substrate with deionised water and drying it with a N_2 flow after each dip. The next layer is then deposited onto the previously adsorbed layer. One sequence of the building up of the SWCNT LbL film is illustrated in *Figure 2-3 (a)*.

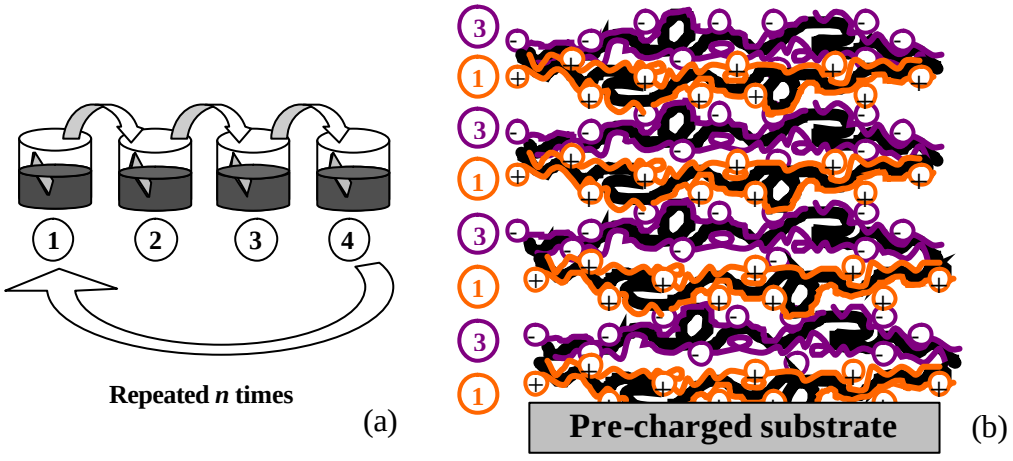

Figure 2-3 (a) build up process: ① cationic surfactant bath for the deposition of the positively charged monolayer, ③ anionic surfactant bath for the deposition of the negatively charged monolayer and ② & ④ water baths to remove the excess of surfactant. (b) multilayer LBL film of SWCNT

Based on the charge reversal principle described in *section 2.2*, phase 1 corresponds to the dipping of the negatively charged substrate into positively charged nanotube solution (DTAB wrapped SWCNTs) and phase 3 relates to the dipping of the positively charged substrate into negatively charged nanotube solution (SDS wrapped SWCNTs). The multilayered film is then built-up by repeating this

sequence *n* times. *Figure 2-3* (*b*) shows the building up after the sequence was repeated *n* times.

2.4 SWCNTs and SWCNT LbL film characterisations

The quality of the structure of the SWCNTs integrated in the LbL films was assessed by Raman and UV-visible-near IR spectroscopies. Raman spectroscopy also provided confirmation that the transfer of nanotubes from the solution to the substrate had occurred. The morphology of the SWCNT LbL films was revealed in AFM scans. The analysis was completed by conductive AFM scans, which provided scans of the current distribution across the SWCNT LbL films subjected to an electric field.

2.4.1 Raman spectroscopy

The presence of SWCNTs in the LbL films has been assessed by Raman spectroscopy. The lattice vibrations along the nanotube axis are equivalent to the vibrations by elongation, which are occurring between the carbon atoms in the graphene (CNTs represented as graphene sheets rolled-up on themselves, see *Chapter 1*). Because SWCNTs are composed of sp^2 carbon atoms (see *Chapter 1*), their Raman signal is around 1590 cm^{-1} whereas the peak positioned at about 1320 cm^{-1} represents the response of sp^3 carbon atoms. *Figure 2-4* compares the Raman spectra of pristine TS-SWCNTs[viii] ("as received" in the form of powder) with that of TS-SWCNTs integrated in an LbL film.

[viii] TS-SWCNT for SWCNTs from Thomas Swan which were shown to be a mixture of SWCNTs, DWCNTs and few walls-MWCNTs with a high proportion of DWCNTs.

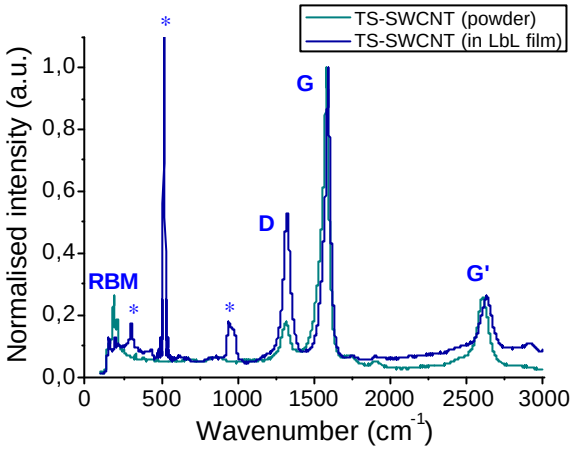

*Figure 2-4 Raman spectra of as received TS-SWCNTs (powder) and TS-SWCNT LbL film. The three peaks marked by * are known to be from the Si/SiO$_2$ substrate used for the LbL deposition*[148]

Figure 2-4 shows the expected Raman spectra for the SWCNTs[149]. The G-band of the sp^2 vibrations in longitudinal and transversal directions and the D-band of the sp^3 vibrations are positioned at around 1590.9 cm^{-1} and 1322.6 cm^{-1}, respectively. Bands of the radial breathing modes (RBM) for the vibration in the perpendicular direction of the nanotube's axes are located at 154.9 and 198.7 cm^{-1}. The G'-band, overtone of the D-band, is positioned at 2604.5 cm^{-1} and 2628.5 cm^{-1} for TS-SWCNTs as powder and for TS-SWCNTs in LbL film, respectively. This upshift to higher wave numbers of the G'-band of TS-SWCNTs in LbL film is explained by the stress from the LbL film[150].
Note: Transmission electron microscope pictures of SWCNTs from Thomas Swan supplier (TS-SWCNTs) showed that there was a mixture of SWCNT, double-wall CNTs (DWCNTs) and few wall-MWCNTs with a high proportion of DWCNTs.

The ratio between the intensities of the sp^2 and sp^3 peaks (I_{sp2}/I_{sp3}) is much higher in the case of the TS-SWCNTs powder (I_{sp2}/I_{sp3}=8.5) than the TS-SWCNTs in the LbL film (I_{sp2}/I_{sp3}=2.1). This difference is explained by the presence of surfactant in the film whose hydrophobic parts are chains of sp^3 carbon atoms. These sp^3 carbon atoms are therefore enhancing the intensity of this D-band. The presence of DWCNTs and MWCNT in the sample also explains the broadening of the base of the G-band. This broadening, the result of the interactions with phonons, makes the transversal peak indistinguishable from the longitudinal peak. It is important to note that three peaks from the Si/SiO$_2$ substrate appear on the second spectrum.

2.4.2 UV-visible-near IR spectroscopy

The UV-visible-near IR spectroscopic analyses inform on the electronic structure of SWCNTs. The observation of van Hove singularities in SWCNT spectra is typical to the 1-dimensional nature of their density of states[20]. Thus, the UV-visible-near IR analyses provide an insight into the disruption of the electronic structure of the SWCNTs. The van Hove singularities represent energy transitions of metallic and semiconducting nanotubes. Dispersions of SWCNTs in DTAB and in SDS, at 1:4 mg/ml of SWCNT in solutions, were prepared by ultrasonication and were left to stand for a couple of days so that the non dispersed SWCNTs would settle at the bottom. The UV-visible-nIR analyses were performed on stabilised dispersions of cationic-SWCNTs and anionic-SWCNTs in DTAB and SDS solutions, respectively. The spectra were recorded for wavelengths within the range 480-1300 nm to avoid the noise signal resulting from the presence of water in the solutions. Normalised absorption spectra for both SWCNT solutions are presented in *Figure 2-5*.

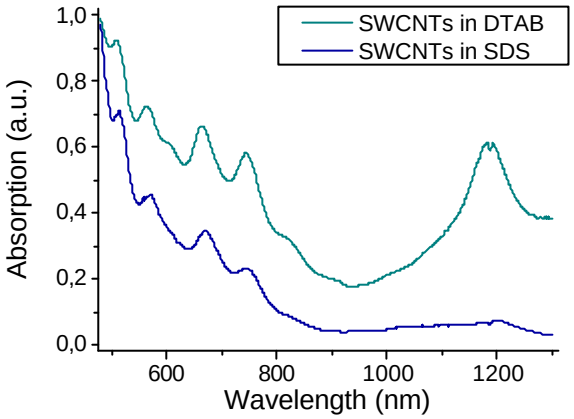

Figure 2-5 Absorption spectra normalised at 480 nm of SWCNT in DTAB and SDS solutions at 0,65%wt and 1%wt in water, respectively.

The UV-visible-near IR spectra of both SWCNT dispersions (*Figure 2-5*) show van Hove singularities, which are indicative of the uni-dimensional nature of the SWCNTs[20]. The positions of the singularities displayed in *Figure 2-5* are in agreement with interband transitions whose positions for HiPCO SWCNTs are[151]:

- *400-650 nm for the first interband transition of metallic nanotubes,*
- *900-1600 nm for the first interband transition of semiconducting nanotubes and*
- *550-900 nm for the second interband transition of semiconducting nanotubes.*

Thus, the singularities, observed in *Figure 2-5* from 480 to 650 nm, correspond to the first interband transition of the metallic SWCNTs, and the second interband transition of the semiconducting SWCNTs. The fact that the singularities for the first interband transitions of semiconducting SWCNTs are not visible is explained by the broadness of the singularities. All singularities displayed in *Figure 2-5* are broad because of interactions between bundled SWCNTs[152]. This indicates the presence of bundles of SWCNTs in the dispersions used to build up the multilayered films.

The empirical Beer-Lambert law (*equation 2-1*) expresses the relationship between the absorption and the concentration of substances as:

$$A_l = e_l \, l \, C \qquad (2\text{-}1)$$

Where A_l, e_l, l and C are the absorption at the wavelength l, the extinction coefficient 25.5 $(mg/L)^{-1}$ cm^{-1} at 500 nm[153], the path length and the concentration, respectively.
Figure 2-5 indicates that the concentrations at 500 nm are $C_{SWCNT/DTAB} = 310$ mg/L and $C_{SWCNT/SDS} = 6944$ mg/L, respectively. These proportional coefficients and the absence of crossover in the plots of the absorption spectra of *Figure 2-5* indicate that the SWCNT are more soluble in SDS than in DTAB.

2.4.3 SWCNT LbL film morphology

The arrangement of the SWCNTs on the surface of the LbL film was investigated with an atomic force microscope (AFM). This investigation was completed with a study of the current distribution across the LbL film using a conductive AFM tip.

Topography

Figure 2-6 shows the presence of SWCNTs in the LbL films and their local arrangement on the surface.

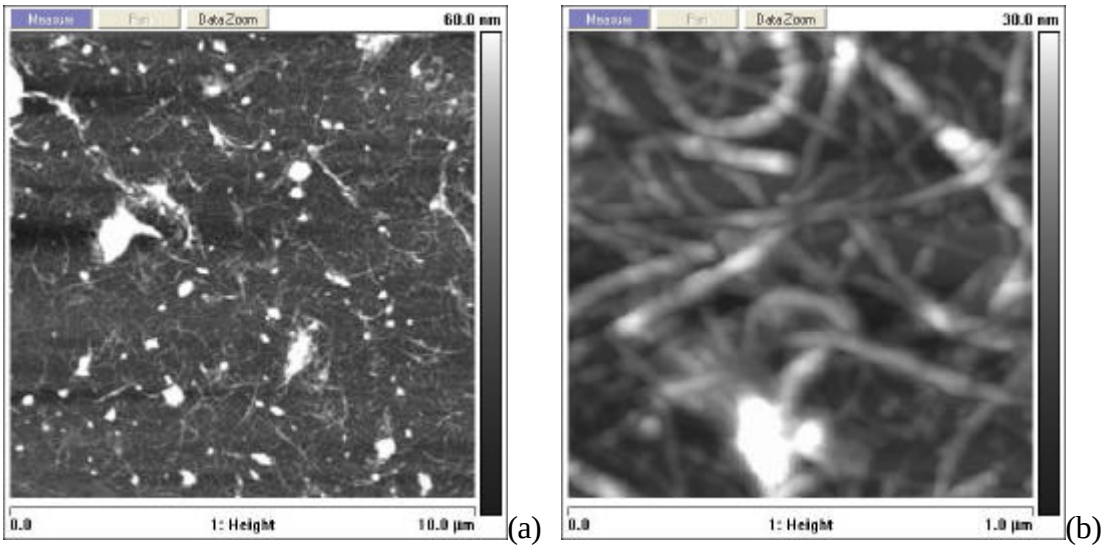

Figure 2-6 AFM image of a 20 bi-layers SWCNT LbL film (a) 10mm scale and (b) 1mm scale. SWCNT bundles are randomly deposited at the surface.

Figure 2-6 (a) and *(b)* shows the topographic picture of SWCNT LbL films. SWCNTs and SWCNT bundles are randomly distributed onto the surface with their axes mostly parallel to the surface plane. This picture confirms the data from the UV-visible-near IR spectra, indicating the presence of bundles, which are transferred in the multilayered films. This 2-dimensional arrangement of the surface can be explained by the different layers stacking on top of each others. A small amount of interpenetration is expected between the SWCNT layers as their size would prevent them from being displaced[154]. Overall, a network of randomly oriented SWCNTs is created as the nanotubes are interconnected to each other. *Figure 2-6 (a)* also displays lumps of what is expected to be micelles aggregates. Thickness of 8.8, 10.8 and 10.5 nm for 10, 20 and 30 bi-layers SWCNT LbL films, respectively, were measured with the AFM. This contrasts with the estimate of 70 nm for 10 bi-layers SWCNT LbL films obtained using a quartz crystal microbalance (QCM)[155]. The discrepancy cannot only be explained by the fact that the AFM provided local analyses (micron scale), where the area scanned was thinner, while the QCM analysed areas at the centimetre scale. Though the same deposition technique was employed for both LbL processes, the rinsing techniques were different. In this case, the substrates were dipped into a beaker of deionised water instead of being rinsed with flow of deionised water. Thus, this difference of thickness is explained by desorptions of SWCNTs, which occurred during the rinsing step[156-157].

Electric mapping

LbL thin films were built-up on metal coated glass slides, in order to be analysed with a conductive AFM. This technique, valid for resistive films, consists of applying a potential between the metallic substrate and the metal coated AFM tip. The current tunnels through the out-of plane direction of the LbL films, and is sensed as the tip scans the surface. The resulting image is the current distribution (electrical mapping) across the film. Its intensity varies, depending on the conductivity of the material that it passes through. These images provide an insight on whether or not conductive paths are created by the SWCNT networks and their distribution. The electrical mapping, shown in *Figure 2-7*, displays the current intensity in a 5 bi-layers LbL film where no nanotubes were loaded. *Figure 2-8* shows the current mapping of a 10 bi-layers SWCNT LbL film.

Figure 2-7 Electrical AFM picture of a 5 bi-layers LbL thin film without SWCNTs, 10 V applied

In *Figure 2-7*, the white dots in the picture are the currents detected by scanning the insulating 5 bi-layers of LbL film[ix] with a 10 V bias. The film appears to be insulating despite the sparks of current. The current intensity scale shows that the level of current registered (10^{-10}-10^{-9} A) is small for the 10 V bias applied.

[ix] Insulating 5 bi-layers LbL film: (PEI/PSS)2 (DTAB/SDS)5

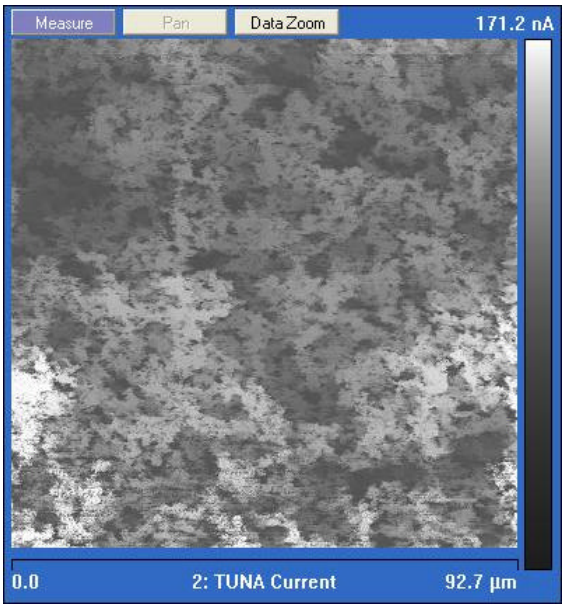

Figure 2-8 Electrical AFM picture of SWCNT LbL film with 10 bi-layers of SWCNTs; applied voltage ~1 V

Figure 2-8 shows the current mapping on almost 100µm scale of a 10 bi-layers SWCNT LbL film. A current level of around 10^{-7} A is obtained when a voltage of 1 V is applied across the film. This picture revealed the existence and distribution of conductive materials across the LbL film. The arrangement of the conductive region provides further evidence of the islands-like structure, which is characteristic of multilayered films built-up using the LbL method[158]. *Figure 2-8* also shows the presence of a long range network of nanotubes created by the stacking of SWCNT patches allowing conduction paths across the LbL film. Therefore, any electrical conduction in the SWCNT LbL film is the result of the presence of nanotubes in the LbL films. The current level displayed in *Figure 2-8* is consistent with the one in current maps recently reported[159].

2.5 SWCNT LbL films: electrical characterization

Electrical characteristics (voltage and temperature dependence of the current) of SWCNT LbL multilayered films were obtained by current-voltage (I-V) and current-temperature (I-T) measurements. These characteristics will be the basis of the electrical study carried out to identify the conduction mechanism across such films.

2.5.1 Electrical contact

Nanotube-metal coupling

Access to the intrinsic electrical properties of the film requires minimising the contact resistance between the electrodes and the SWCNT film. As the nanotubes were wrapped with surfactants (insulating materials), the choice of metal for the contacts was made considering the work function of the SWCNTs. Rhodium and palladium have been shown to provide the best electrical contacts and exhibit quasi ohmic contacts with CNTs[160]. For instance, an ab initio study found Pd as the best metal to establish contact with the nanotubes[161]. Calculations based on quantum mechanics showed that titanium forms ohmic contacts with both metallic and semiconducting SWCNTs[162]. Therefore, in absence of Pd, titanium was used for the metal contacts.

Electrode deposition

In-plane and out-of-plane configurations were used to study the SWCNT LbL films. The electrodes, for the in-plane configuration, were made of chromium/gold (Cr/Au) or titanium/gold (Ti/Au) electrodes. The choice of gold was dictated by its work function (greater than that of nanotubes) and noble metal quality (non-reactive with the surfactant solutions). The sub-layer of Cr (or Ti) was deposited to increase its adhesion to the substrate. A schematic of the device is shown in *Figure 2-9*.

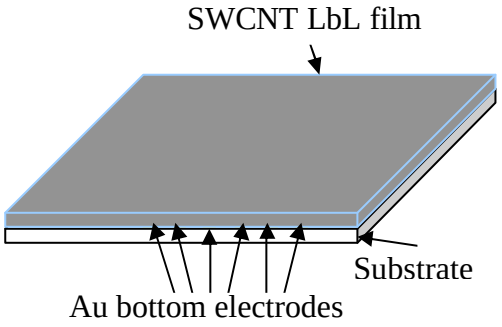

Figure 2-9 Schematic of the arrangement of electrodes in the in-plane configuration

In the out-of-plane configuration, the bottom electrodes are made of Cr/Au or Ti/Au for the same reasons. The top electrodes were made of aluminium to minimize (if any) metal migration during the out-of-plane measurements. *Figure 2-10* illustrates the architecture of the device for the out-of-plane measurements.

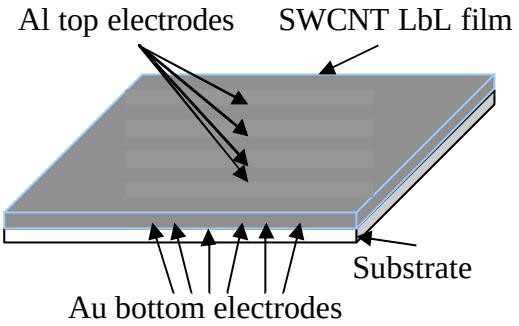

Figure 2-10 Schematic of the arrangement of electrodes in the out-of-plane configuration

Metal contacts were deposited by electron beam or thermal evaporation on the substrates before the film deposition. The shape and separation of the electrodes were determined by the designs of the shadow masks. Compared to the photolithography process where micron size resolutions are reached, this method allows faster electrode depositions. It also avoids contamination of the sample by chemicals (photoresist and developer) whose use is inherent to the photolithography process. Shadow masks are plates where holes of different geometries are drilled. The evaporated metals are deposited on the sample through these holes. Therefore, the electrodes adopt the design of the holes. In this case, the holes have a millimetre size as they were made by drilling into metallic plates.

2.5.2 SWCNT LbL films: current-voltage measurements

I-V characteristics were measured at room temperature in a dark rig using a 2400 Keithley source meter.

2.5.2.1 In-plane configuration

In-plane I-V characteristics of LbL networks were measured at room temperature for different electrode separations and for voltages from -200 to 200 V. *Figure 2-11* displays the I-V characteristics for an LbL film without SWCNTs with electrode separations of 6 and 10 mm. The measurements were carried out at room temperature on LbL films having the architecture illustrated in *Figure 2-9*.

Similarly, current responses for LbL networks made with 5, 10 and 20 bi-layers of SWCNTs were measured, with I-V characteristics for 5 bi-layers shown overleaf in *Figure 2-12*.

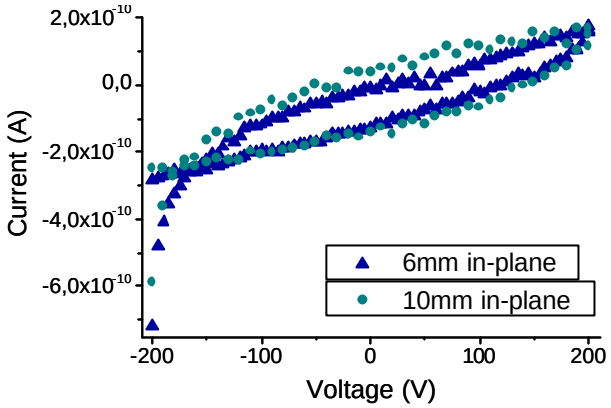

Figure 2-11 I-V plots of 5 bi-layers LbL thin film built-up without SWCNTs

Figure 2-11 shows that LbL thin films which do not contain nanotubes display a current in the order of 10^{-10} A in these conditions. Therefore, any trend observed in the SWCNT LbL films will be the result of the presence of SWCNTs. This supports the conclusions made from the conductive AFM pictures.

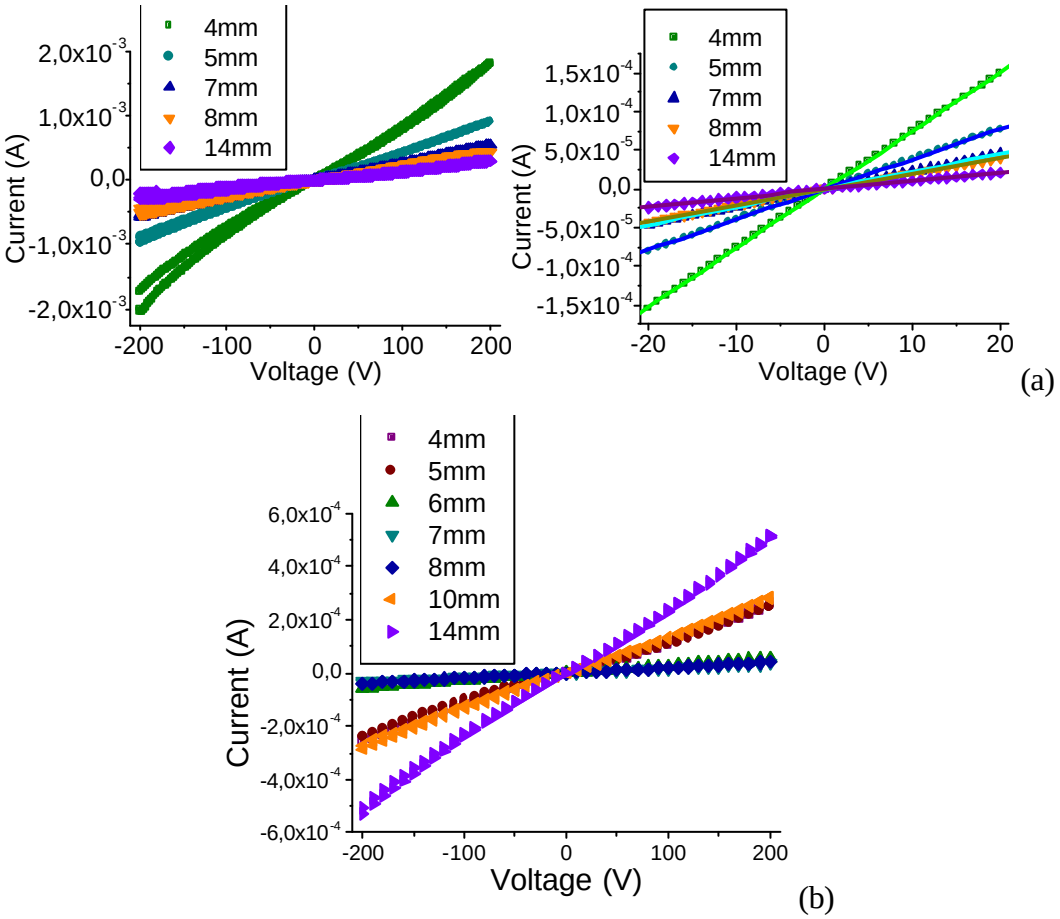

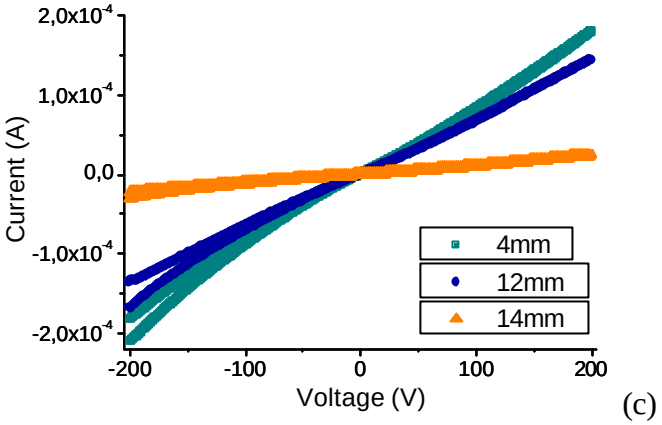

Figure 2-12 In-plane I-V characteristics for (a) 5 bi-layers LbL network with electrode separations of 4, 5, 7, 8 and 14 mm. (top) Bias from -200 to +200 V (bottom) bias from -20 to +20 V (b) 10 bi-layers LbL network with electrode separations of 4, 5, 6, 7, 8, 10 and 14 mm (c) 20 bi-layers LbL film with electrode separations of 4, 12 and 14 mm

Table 2-2 indicates the currents at 200 V found from these characteristics, for the 4 and 14 mm electrode separations.

Number of bi-layers	Current (A)	
	4 mm	14 mm
5	1.8×10^{-3}	3×10^{-4}
10	2.67×10^{-4}	5.16×10^{-4}
20	1.8×10^{-4}	2.48×10^{-5}

Table 2-2 Current at 200 V with 4 and 14 mm electrode spacing

The I-V plots displayed in *Figure 2-12* suggest the following

* The current is likely to be higher as the electrode separations are shorter. It is due to the electrical field which increases as the electrode separation decreases. Yet, it is not always observed in the 10 bi-layers SWCNT LbL film.

* The I-V curves of the SWCNT LbL thin films obtained during this study are characterised by the linearity of the current at low voltage as shown in *Figure 2-12 (b)*. The transition, between the linear and non linear regions, occurred around 25 V, regardless of the film thickness.

* Increasing the SWCNT LbL film thickness does not always lead to an increase of current as it is shown in *Table 2-2*. This can be explained by the concentration of nanotubes in the solution, which gradually drops as they are transferred on the substrate. This results in a less concentrated solution for the following dipping.

Moreover, the fact that surfactants are also transferred affects the stability of the dispersion.

The increase of current with the decrease of the electrode separation is in accordance with data already reported, though the transition from a linear to a non linear region occurs at much lower voltages than the ones shown in *Figure 2-12*[155]. Similar to the data in *Table 2-3*, the study of the impact of the number of layers on the current magnitude for MWCNT/glucose oxidase LbL film revealed the presence of an optimum film thickness for which the current is maximal[163].

The study of the in-plane electrical characteristics of SWCNT LbL films revealed that a 10 bi-layers-thick film was an optimum. LbL films built up with TS-SWCNTs and SWCNTs displayed the same electrical behaviour: a linear region at low voltages (up to ~25 V) and a non linear region at high voltages.

2.5.2.2 Out-of-plane configuration

Twenty bi-layers of SWCNT LbL films were built up to measure the out-of-plane I-V characteristics at room temperature, using the configuration shown in *Figure 2-10*. The voltage was limited to 5 V to avoid current breakdowns. *Figure 2-13* shows an average of 3 typical I-V characteristics obtained for such measurements.

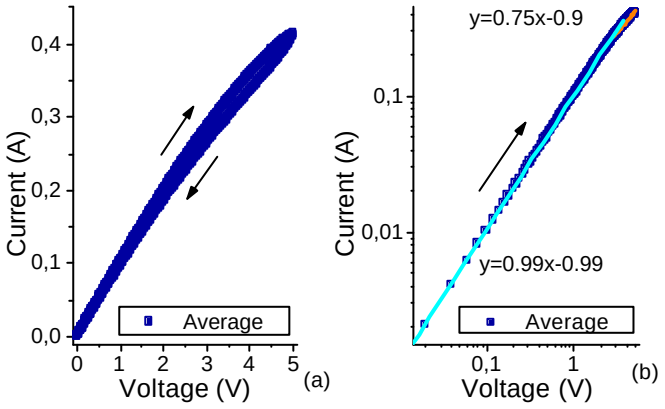

Figure 2-13 (a) Out-of-plane I-V characteristics for a 20 bi-layers SWCNT LbL film; (b) Log-log scale

The out-of-plane I-V characteristic displayed in *Figure 2-13 (a)* is linear at low voltages (up to around 2.2 V), afterwards, the trend slightly curves. *Figure 2-13 (b)* shows the 0.75 slope found between 3 and 5 V while a slope of 1 was found at low voltages. Then the current deviates from its ohmic-like behaviour at high voltages. The deviation from the linear behaviour is attributed to the beginning of a current

saturation, which is followed by a current breakdown (see *Appendix A, Figure A-9*). The ohmic behaviour and current intensity (~0.4 A at 5 V) of the I-V characteristic displayed in *Figure 2-13 (a)* contrast with results (non linear behaviour and current at ~0.1 mA at 5 V) reported in such films[155].

2.5.3 SWCNT LbL films: current-temperature measurements

Current-temperature (I-T) characteristics were plotted to find out the current dependence with the temperature. For that, I-V measurements carried out at different temperatures were used to extract the I-T characteristics. The measurements were carried out using a Janis Research/CTI cryogenics' cryostat rig at about 2×10^{-4} mbar with a 331 temperature controller from LakeShore. The voltage was applied using a Keithley 2400 source metre. All measurements were carried out in the dark.

2.5.3.1 In-plane configuration

I-V characteristics were measured on 20 bi-layers of SWCNT LbL films, with the in-plane configuration, set at different temperatures. The current dependence with the temperature was extracted from these measurements. *Figures 2-14* and *2-15* display typical I-T characteristics between 150 and 350 K obtained for such a film at 1, 5, 10 and 20 V with 1 and 4 mm as electrode separations.

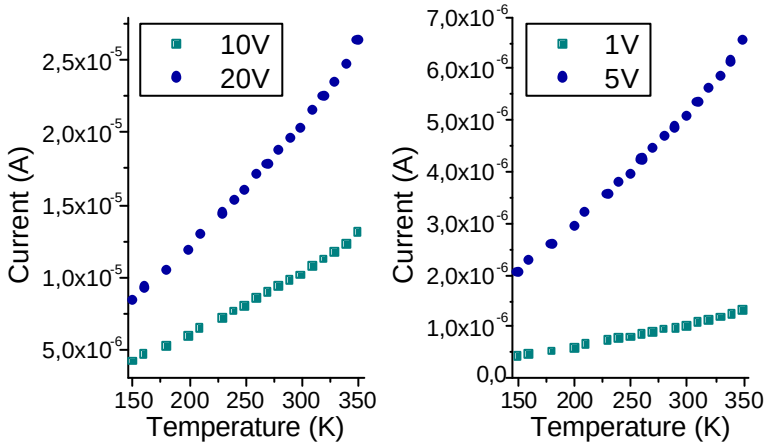

Figure 2-14 I-T characteristics at 0.4, 1, 5, 10 and 20 V for a 20 bi-layers SWCNT LbL film with 1 mm of electrode separation

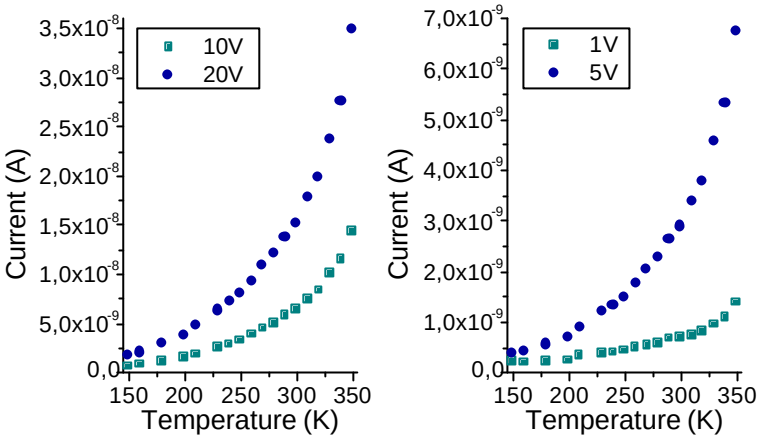

Figure 2-15 I-T characteristics at 0.4, 1, 5, 10 and 20 V for a 20 bi-layers SWCNT LbL film with 4 mm of electrode separation

Figures 2-14 and *2-15* show the I-T characteristics obtained for a 20 bi-layer-SWCNT LbL film with 1 and 4 mm of electrode separations, respectively. Although both figures display a consistent decrease of the current intensity as the temperature is reduced from 350 K to 150 K, their I-T characteristics are completely different. Indeed, for small electrode separations (1 mm) the I-T plots in *Figure 2-14* appear fairly straight but non linear. For wider electrode separations the current increases exponentially with the temperature. This exponential trend is well pronounced for temperatures above 300 K (*Figure 2-15*).

2.5.3.2 Out-of-plane configuration

I-V measurements carried out with the out-of-plane configuration showed the presence of short-circuits for 5 and 10 bi-layers of SWCNT LbL films. So, the out-of-plane measurements were only performed on 20 bi-layers of SWCNT LbL films. Short-circuits are suggested to be caused by the non homogeneous distribution of material in the film, which leads to a direct contact between the bottom and the top electrodes. The presence of pinholes can also explained these short-circuits as pinholes can act as growth centres where evaporated metal can penetrate and create metal filament across the layers[164]. The voltage applied was limited at ±1 V for the temperature dependence study. I-T characteristics from 50 to 350 K are displayed in *Figure 2-16* for 0.5 and 1 V.

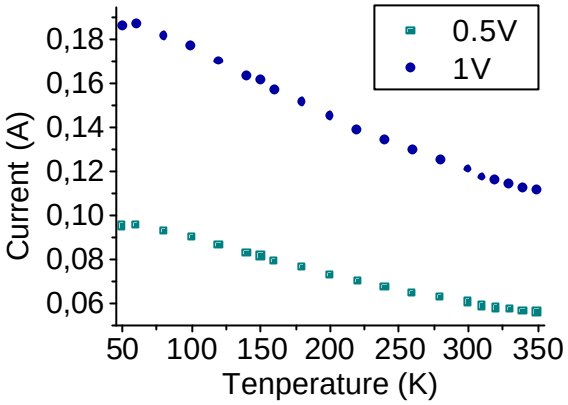

Figure 2-16 Out-of-plane I-T plots for a 20 bi-layers SWCNT LbL film at V=0.5 V and V=1 V

Figure 2-16 shows that over the whole temperature range the current constantly increases as the temperature reduces. This influence of the temperature on the conductivity rules out any conduction model displaying an increase of current with temperature. In addition, the variation of the current intensity over the whole range of temperature is small. Thus, *Figure 2-16* suggests that the conduction in the out-of-plane direction of the SWCNT LbL films can be governed by tunnelling mechanisms. Tunnelling phenomena tend to have a temperature dependence via the dielectric constant of the material[165].

2.6 SWCNT LbL films: conduction models

In this section, the electrical characteristics presented in *section 2.5* are analysed according to possible conduction models occurring in insulating films. The aim of this study is to identify the dominant transport mechanism across the SWCNT LbL films.

The fabrication method used to build up the SWCNT LbL film relies on the wrapping up of the SWCNTs by the surfactants, and on the electrostatic charges balancing each others. The wrapping of the SWCNTs does not need to be total to allow the dispersion. The carboxylic groups, present on the SWCNTs' surface, bear a negative charge in aqueous solvent and can balance a previous positive charge. Then the nanotubes can be in contact with each other, forming different junctions: SWCNT-surfactant-SWCNT; SWCNT-surfactant-surfactant-SWCNT and SWCNT-SWCNT. These possibilities show that in addition to one or two coating(s) of surfactant (insulating coating) between the SWCNTs, it is also likely to have

nanotubes in direct contact. This allows different types of charge transport to take place simultaneously. Therefore, it is only the conduction model that dominates the transport across the SWCNT LbL film which can be identified here.

2.6.1 Transport in thin insulating films

The insulating nature of the surfactant interfaces between SWCNTs leads to consider the conduction with a metal-insulator-metal configuration. Though the electrode separation in the in-plane direction is measured in millimetres, effects occurring in insulating thin films were considered. In this section, the analysis of the electronic transport across the SWCNT LbL films was carried out according to: hopping, tunnelling, Richardson-Schottky, Poole-Frenkel and space charge limited conductions.

The I-V and I-T characteristics of SWCNT LbL films revealed different behaviours the in-plane and out-of-plane configurations. This suggests that the dominant transport mechanisms are different for these configurations. Though the configurations are studied separately, the same method of plotting the I-V and I-T data according to the analytical expressions is used in both configurations. For this, the I-V and I-T characteristics were plotted following the analytical expressions of each conduction model. To simplify the viewing, the analytic equations are manipulated in order to have a proportional relationship between the current and the voltage for the I-V plot and between the current and the temperature for the I-T plots.

2.6.2 Conduction model: in-plane configuration

The I-V characteristics at room temperature of 5, 10 and 20 bi-layers SWCNT LbL films are presented in *Figure 2-17* with logarithmic scales.

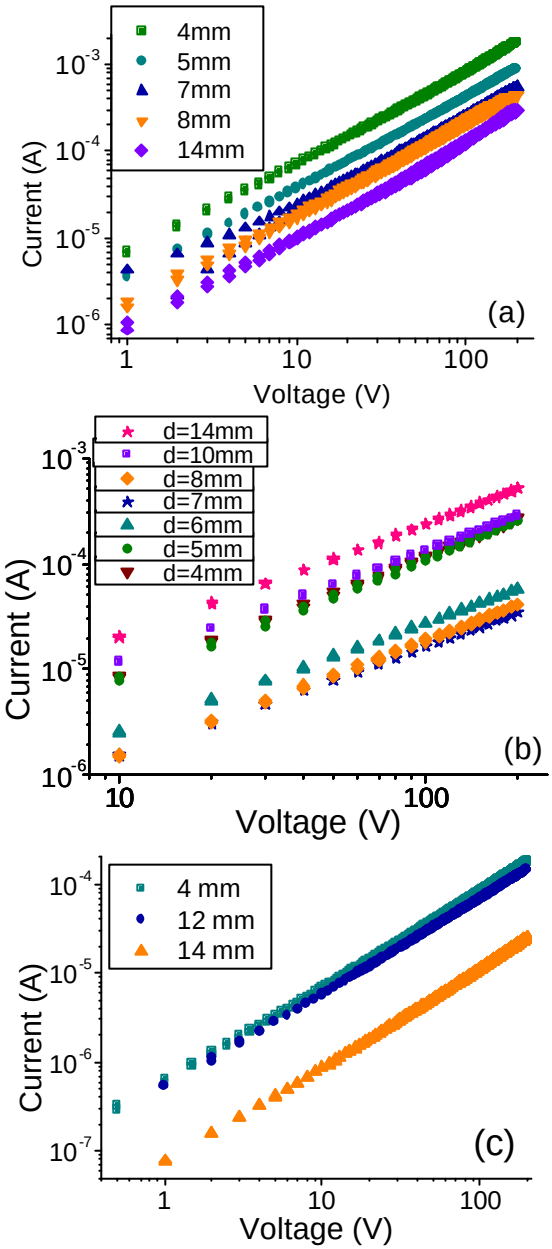

Figure 2-17 Log-log scale plots of in-plane I-V characteristics of SWCNT LbL films built-up with: (a) 5 bi-layers, (b) 10 bi-layers and (c) 20 bi-layers

Figure 2-17 shows I-T characteristics of a typical 20 bi-layers of SWCNT LbL film at 1, 5, 10 and 20 V for 1 and 4 mm electrode separation with logarithmic scales.

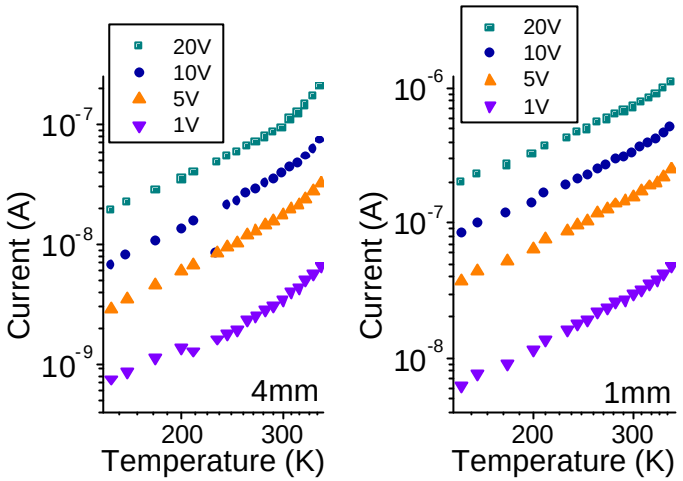

Figure 2-18 Plotting using log-log scale of the I-T characteristics at 1, 5, 10 and 20 V for electrode separations of 1 and 4 mm

The electrical characteristics in both *Figures 2-17* and *2-18* are parallel. This means that the I-V and I-T plots have similar trends whatever the electrode separations. Thus, in the following study, only the I-V characteristics of the 20 bi-layers SWCNT LbL film at 4 and 14 mm will be used. Regarding the I-T characteristics of the 20 bi-layers SWCNT film, only the characteristics at 1 V and 20 V are considered for both 1 and 4 mm electrode separation.

It is important to note that the current and current density are related by $J = I/S$ where S is the section traversed by the current flow and the electric field and the voltage are linked by $E = V/d$ where d is the electrode separation. Here both S and d are constants. Consequently, there is a proportional behaviour between I and J and between E and V that does not affect the electrical field and temperature dependence of the current density. For simplicity I and V are considered rather than J and E.

2.6.2.1 Fowler-Nordheim conduction model

Two tunnelling phenomena are taken into account here; the direct tunnelling and the Fowler-Nordheim tunnelling. Tunnelling transport corresponds to the ability of an electron to move across potential barriers having higher energies. In the direct tunnelling conduction, the carrier passes a rectangular energy barrier without interaction. For high electric fields, a similar phenomenon takes place leading to the Fowler-Nordheim conduction. But in this case, the energy barrier is triangular due to

the high electric field. The current density expression in the Fowler-Nordheim model is given by *equation 2-2*[166].

$$J_{FN} = \frac{q^3}{8\pi h\Phi} E^2 \exp\left(-\frac{4\sqrt{2m\,(q\Phi)^3}}{3\hbar qE}\right) \qquad (2\text{-}2)$$

Where q, m, E, h, $\hbar$, Φ are the electronic charge, the free-electron mass, the electric field, the Planck constant, the planck constant divided by 2π and the barrier height, respectively. Applying the logarithm function to *equation 2-2* leads to *equation 2-3*:

$$\ln\left(\frac{J_{FN}}{E^2}\right) = \ln\left(\frac{q^3}{8\pi h\Phi}\right) - \frac{4\sqrt{2m\,(q\Phi)^3}}{3\hbar qE} \qquad (2\text{-}3)$$

Given that $\ln\left(\frac{q^3}{8\pi h\Phi}\right)$ and $\frac{4\sqrt{2m\,(q\Phi)^3}}{3\hbar q}$ are constant:

$$\ln\left(\frac{J_{FN}}{E^2}\right) \propto \frac{1}{E} \qquad (2\text{-}4)$$

Figure 2-19 displays the data of the I-V characteristics for 1 and 4 mm electrode separations according to *equation 2-4*.

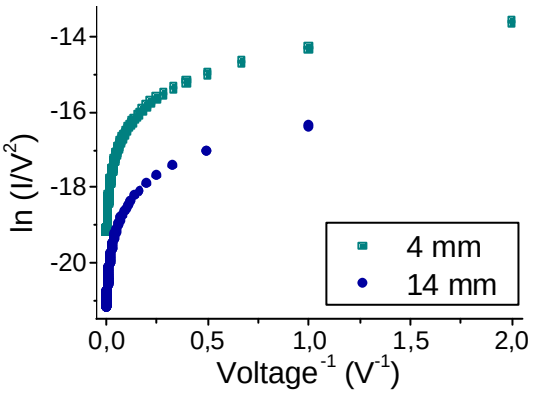

Figure 2-19 $\ln\left(J_{FN}/E^2\right)$ *versus* $1/E$ *plots of the I-V characteristics according to the Fowler-Nordheim model for 1 and 4 mm as electrode separations*

Figure 2-19 shows that the $\ln\left(J_{FN}/E^2\right)$ *versus* $1/E$ plots of the data points of the I-V characteristics display a non linear behaviour with a limited range of voltages showing a possible linear behaviour at high voltages. This means that $\ln\left(J_{FN}/E^2\right)$ is not proportional to $1/E$ and consequently, the Fowler-Nordheim conduction is unlikely to dominate the transport across the SWCNT LbL film.

According to *equation 2-2*, $\ln(I \times d^2) \propto d$ should give a proportional relation between the electrode separation and the current, if the Fowler-Nordheim conduction dominates the transport mechanism. $\ln(I \times d^2)$ *versus* d data points were plotted in *Figure 2-20.*

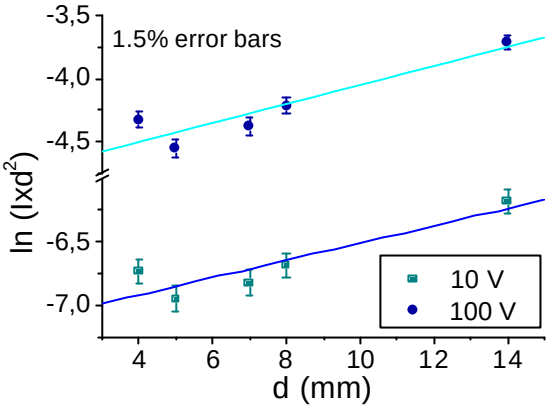

Figure 2-20 $\ln(I \times d^2)$ *versus* d *plots at 10 and 100 V of a 5 bi-layer TS-SWCNT LbL film*

Figure 2-20 displays linear fits for the $\ln(I \times d^2)$ *versus* d plots at 10 and 100 V. No acceptable linear fit could be plotted for the voltage dependence of the current.

The analytic expression of the Fowler-Nordheim current density does not contain a temperature expression. An impact of the temperature through the constants of *equation 2-2* would lead to a small temperature dependence of the current density yet *Figures 2-14* and *2-15* showed a clear temperature dependence of the I-T characteristics.

Although the possibility of tunnelling phenomena across the SWCNT LbL films cannot be dismissed, *Figures 2-19* and 2-20 showed that a conduction mechanism based on the Fowler-Nordheim effect does not dominate the electronic transport across the films despite acceptable fits for the current electrode separation plots.

2.6.2.2 Hopping conduction model

Hopping transport takes place in the energy gap of an insulator or semiconductor in the presence of localized states. This conduction corresponds to the hopping of charge carriers between these states. When the carriers 'hop' from one localised state to its spatially nearest state, the conduction is called the nearest-neighbour hopping[167]. In variable range hopping (VRH), the charge carriers hop between localized states of favourable energy which are not necessarily the spatially closest

ones. The VRH conduction is commonly reported as the mechanism occurring in SWCNT networks (see *section 1.6 Chapter 1*). For a uniform density of states, the equation of the conductance in the VRH model is given by *equation 2-5*[119,168]:

$$G(T) = G_0 \exp\left[-\left(\frac{T_0}{T}\right)^p\right] \qquad (2\text{-}5)$$

where p=1+d, with d the dimension, G_0 and T_0 are characteristics of the sample independent of the temperature, and $k_B T_0 = 3/l^2 N(0) d$ with λ the localization length, N(0) the density of states at the Fermi level and d the sample thickness. Applying the logarithm function to *equation 2-5* gives *equation 2-6*:

$$\ln(G) \propto T^{-1/p} \qquad (2\text{-}6)$$

Then, $\ln(G)$ *versus* $T^{-1/p}$ of the data points from the I-T characteristics were plotted in *Figure 2-21*.

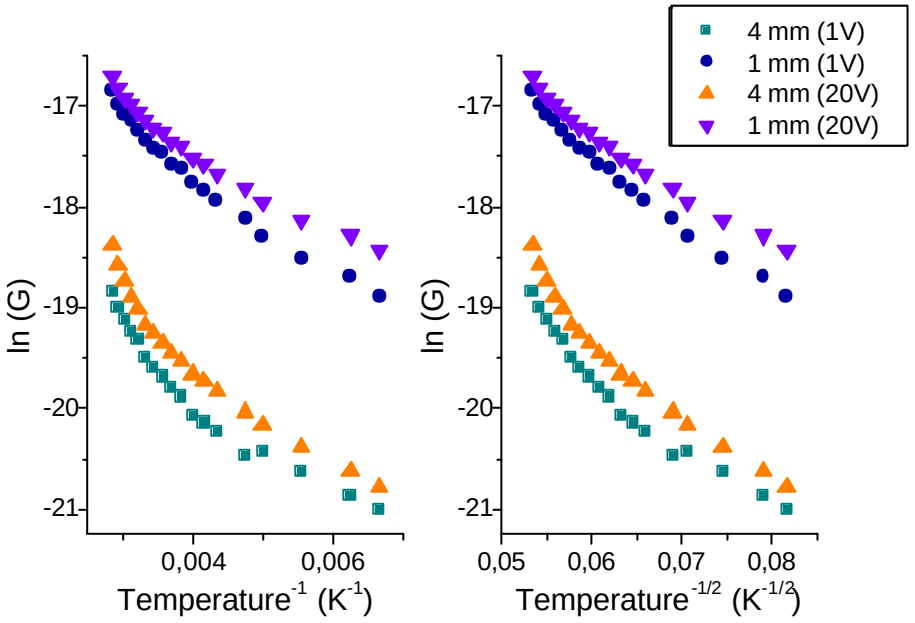

(a)

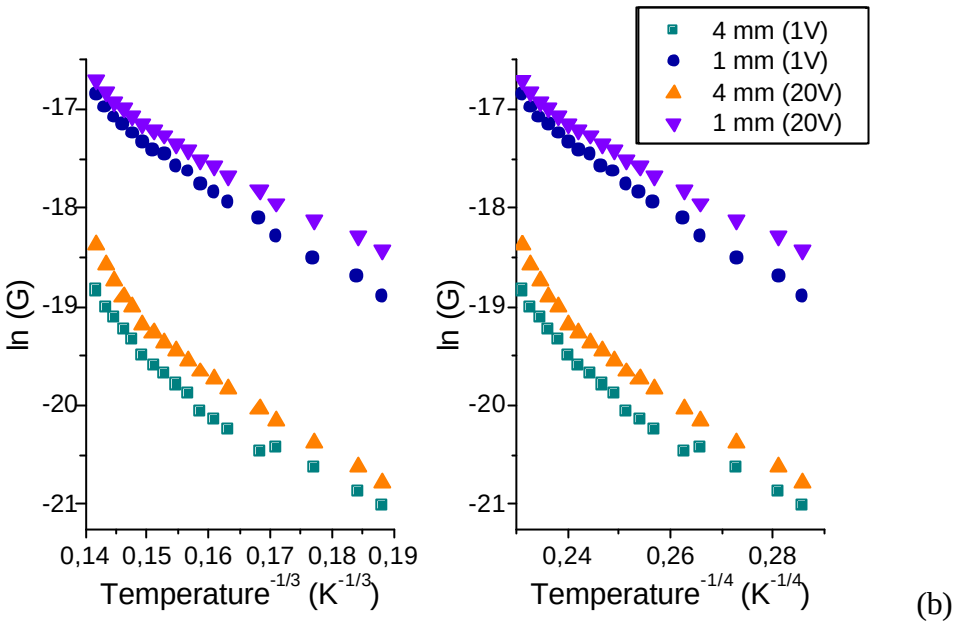

Figure 2-21 $\ln(G)$ *versus* $T^{-1/p}$ *plots of the I-T characteristics at 1 and 20 V and 1 and 4 mm electrode separation for (a) p=1 and p=2 and (b) p=3 and p=4*

None of the I-T characteristics shown in *Figure 2-21* according to the VRH conduction model displayed a linear behaviour. This implies that the VRH mechanism does not dominate the conduction over the full temperature range.

2.6.2.3 Richardson-Schottky conduction model

The cathode becomes positively charged when an electron is extracted from it. This charge image contributes to the potential barrier between the metal and the insulator as it creates an attractive force on the electron. An electric field will interact with the image potential which will lower the potential barrier of $\Delta\phi$. Then, electrons injected into the insulator conduction band will have to overcome a potential barrier of $\phi_0 - \Delta\phi$ (*Figure 2-23*).

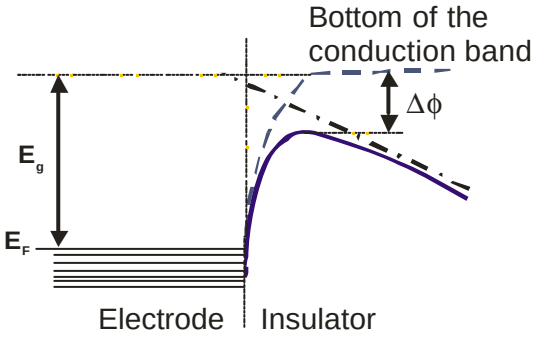

Figure 2-22 Schematic of Schottky effect at neutral contact with E^F*, the Fermi energy level;* E^0*, the vacuum energy level; and* Df*, the barrier height attenuation adapted from Simmons*[169]

Equation 2-7 gives the current density expression in the Richardson-Schottky case[169]

$$J_{RS} = AT^2 \exp\left(\frac{-f_0}{kT}\right) \exp\left(\frac{b_s F^{\frac{1}{2}}}{kT}\right) \qquad (2\text{-}7)$$

Applying the logarithm to *equation 2-7* leads to *equations 2-8* and *2-9* for the dependence of the current in voltage and temperature, respectively.

$$\ln(J_{RS}) \propto F^{\frac{1}{2}} \qquad (2\text{-}8)$$

$$\ln\left(\frac{J_{RS}}{T^2}\right) \propto \frac{1}{T} \qquad (2\text{-}9)$$

The data points of the I-V and I-T characteristics were plotted according to the Richardson-Schottky model in *Figures 2-23* and *2-24*, respectively.

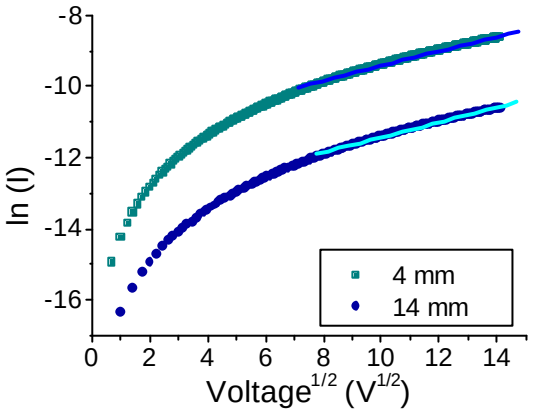

Figure 2-23 $\ln(J_{RS})$ *versus* $V^{1/2}$ *plots of the voltage dependence of the current according to the Richardson-Schottky model for electrode separations of 1 and 4 mm*

Figure 2-23 shows acceptable linear fittings of the $\ln(J_{RS})$ *versus* $V^{1/2}$ plots from 60.5 (7.78 $V^{1/2}$) to 200 V and from 70 (8.37 $V^{1/2}$) to 200 V obtained for 4 and 14 mm electrode separation, respectively. Thus, the I-V characteristics are in agreement with the Schottky-Richardson model at high voltages. According to the Schottky-Richardson theory, the $\ln(J_{RS}/T^2)$ *versus* $1/T$ of the data points from the I-T characteristics were plotted in *Figure 2-24*.

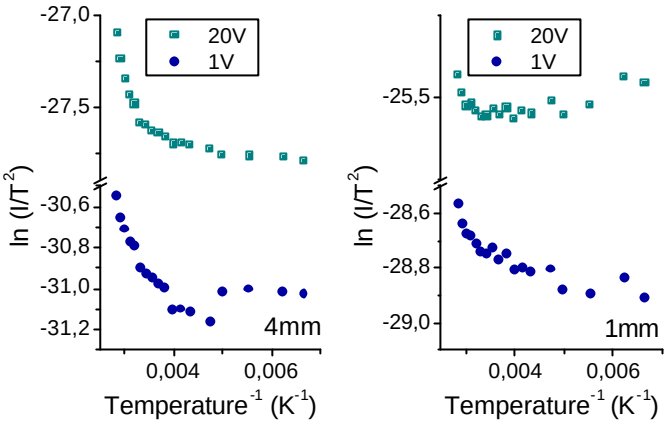

Figure 2-24 $\ln\left(J_{RS}/T^2\right)$ *versus* $1/T$ *plots of the I-T characteristics according to the Richardson-Schottky model at 1 and 20 V for electrode separations of 1 and 4 mm*

Figure 2-24 shows that the $\ln\left(J_{RS}/T^2\right)$ *versus* $1/T$ plots from the I-T characteristics display a non linear behaviour from 100 to 350 K. According to *equation 2-7*, $\ln(I) \propto d^{-1/2}$ gives a proportional relationship between the electrode separation and the current. $\ln(I)$ *versus* $d^{-1/2}$ plots were plotted in *Figure 2-25*.

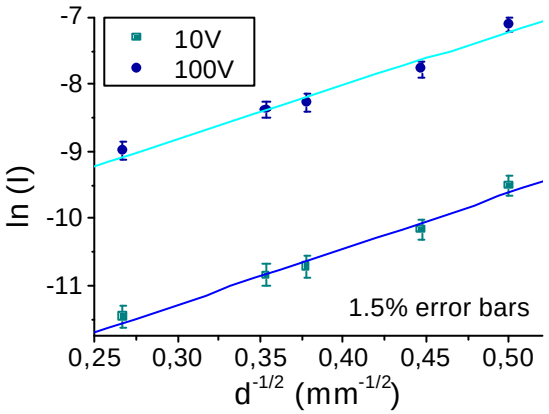

Figure 2-25 $\ln(I)$ *versus* $d^{-1/2}$ *plots at 10 and 100 V of a 5 bi-layers TS-SWCNT LbL film*

Figure 2-25 shows good linear fits of the $\ln(I)$ *versus* $d^{-1/2}$ plots with 1.5% error. The linear behaviour observed at high voltage in *Figure 2-23* is in accordance with the Richardson-Schottky model. But, none of the $\ln\left(J_{RS}/T^2\right)$ *versus* $1/T$ plots (*Figure 2-24*) displayed any linearity. Thus, the Schottky-Richardson effect was discounted as the dominant transport mechanism.

2.6.2.4 Space charge limited conduction model

Space charge limited conduction (SCLC) occurs when the carrier injection is faster than their transport across the film. At low voltages intrinsic carriers circulate across the material following an ohmic conduction. As the voltage increases, the number of carriers injected from the electrode increases and dominates the conduction. There is the creation of a space-charge leading to quadratic I-V characteristics. In presence of potential wells (traps) in the forbidden band, a proportion of the injected carriers fill the traps. This limits the space-charge effect as the carriers are captured. The slope of ln (I) versus ln (V) is 2 when one carrier contributes to the conduction and 3 when there are two carriers. Once all the traps are filled, the slope of ln (I) versus ln (V) is higher than 3, and the conduction operates in a trap-free regime. The analytic expression of the SCLC is given by *equation 2-10*.

$$J = \frac{9\varepsilon_0\varepsilon_r\mu_{eff}\theta}{8d^3}V^n \qquad (2\text{-}10)$$

where $n = 1$ in the linear regime and $n \geq 2$ in the quadratic regime, d is the electrode separation, μ_{eff} is the effective mobility and ε_0 and ε_r are the free space permittivity and the dielectric constants respectively. The expression of θ is dependent on the nature of the traps. In presence of shallow traps:

$$\theta = \frac{2}{N_t}\left(\frac{2\pi m_p^* kT}{h^2}\right)^{\frac{3}{2}}\exp\left(\frac{E_v - E_t}{kT}\right) \qquad (2\text{-}11)$$

The expression of the current in the quadratic regime in presence of deep traps becomes:

$$I = \frac{9}{8}\,\frac{\varepsilon\varepsilon_0\mu_{eff}AN_vV^2}{\gamma d^3 N_t}\,\exp\left(\frac{E_v - E_t}{kT}\right) \qquad (2\text{-}12)$$

Applying the logarithm to *equation 2-10*

$$\ln\left(J_{SCL}\right) = \ln\left(\frac{9\varepsilon_0\varepsilon_r\mu_{eff}\theta}{8d^3}\right) + n\ \ln\left(V\right) \qquad (2\text{-}13)$$

$\ln\left(\frac{9\varepsilon_0\varepsilon_r\mu_{eff}\theta}{8d^3}\right)$ being constant for the voltage dependency

$$\ln\left(J_{SCL}\right) \propto n\ \ln\left(V\right) \qquad (2\text{-}14)$$

According to *equation 2-14*, the slope of $\ln(J_{SCL})$ *versus* $\ln(V)$ will be n which is superior or equal at 2 in the quadratic regime.

Temperature dependence

- Shallow traps

Using the full expression of q, *equation 2-10* can be written in the case of shallow traps as:

$$J_{SCL} = \frac{9\varepsilon_0\varepsilon_r\mu_{eff}V^n}{8d^3} \times \frac{2}{N_t}\left(\frac{2\pi m_p^* kT}{h^2}\right)^{\frac{3}{2}} \exp\left(\frac{E_v - E_t}{kT}\right) \qquad (2\text{-}15)$$

$$\ln\left(\frac{J_{SCL}}{T^{\frac{3}{2}}}\right) = Ln\left[\frac{18\varepsilon_0\varepsilon_r\mu_{eff}V^n}{8d^3N_t}\left(\frac{2k\pi m_p^*}{h^2}\right)^{\frac{3}{2}}\right] + \frac{E_v - E_t}{kT} \qquad (2\text{-}16)$$

Where $\frac{9\varepsilon_0\varepsilon_r\mu_{eff}V^n}{8d^3} \times \frac{2}{N_t}\left(\frac{2\pi m_p^* k}{h^2}\right)^{\frac{3}{2}}$ and $\frac{E_v - E_t}{k}$ are independent of the temperature

$$\ln\left(\frac{J_{SCL}}{T^{\frac{3}{2}}}\right) \propto \frac{1}{T} \qquad (2\text{-}17)$$

- Deep traps

Following similar calculations, the temperature dependence of the current in the presence of deep traps is:

$$\ln(J_{SCL}) \propto \frac{1}{T} \qquad (2\text{-}18)$$

Figure 2-23 shows the $\ln(J_{SCL})$ *versus* $\ln(V)$ plots of the data points from the I-V characteristics for 1 and 4 mm electrode separations.

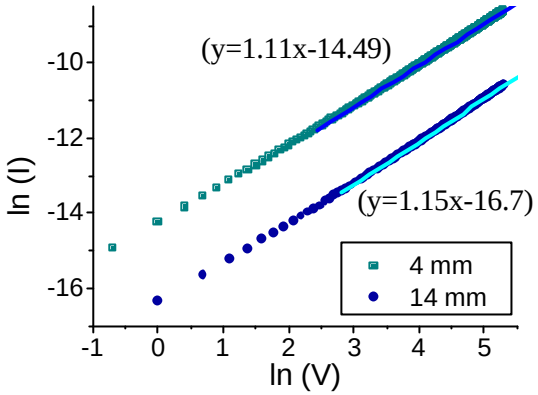

Figure 2-26 $\ln(J_{SCL})$ *versus* $\ln(V)$ *plots of the data points from the I-V characteristics for 1 and 4 mm as electrode separations*

Figure 2-26 shows that *y=1.11x-14.49* and *y=1.15x-16.7* are the equations of the linear fits for the $\ln(I)$ *versus* $\ln(V)$ plots for 4 and 14 mm electrode separations, respectively. In the quadratic regime both slopes are less than 2. According to the theory, higher slope values are expected in the case of a dominant SCLC mechanism. *Figure 2-27* displays the I-T characteristics according to the SCLC model for shallow (a) and deep (b) traps.

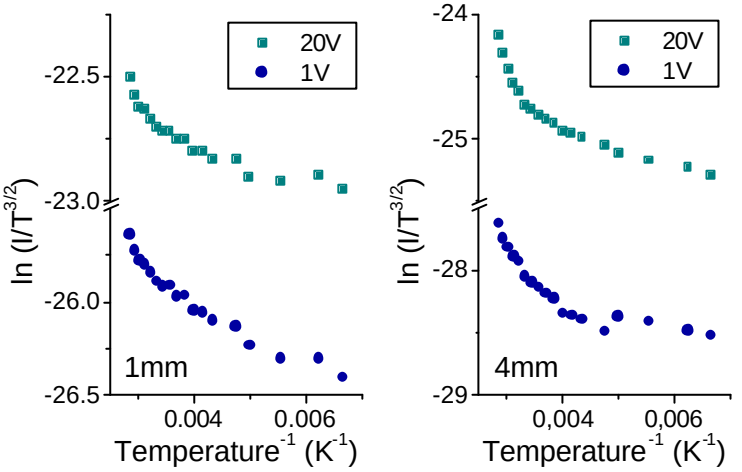

(a)

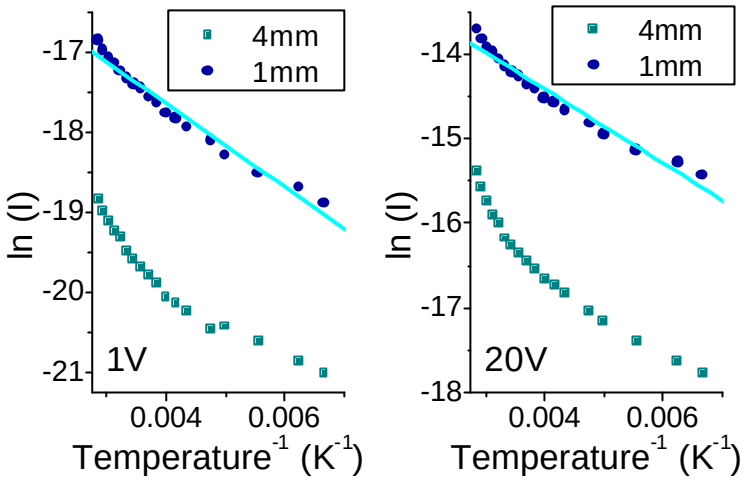

Figure 2-27 (a) $\ln\left(I/T^{3/2}\right)$ *versus* $1/T$ *plots and (b)* $\ln(I)$ *versus* $1/T$ *plots of the data from the I-T characteristics at 1 and 20 V for electrode separations of 1 and 4 mm*

Figure 2-27 displays $\ln\left(I/T^{3/2}\right)$ *versus* $1/T$ and $\ln(I)$ *versus* $1/T$ plots of the data points from the I-T characteristics according to the SCLC for shallow and deep traps, respectively. Decent linear fits are observed within the deep traps model for 1 mm electrode separation at both 1 and 20 V. Apart from them, none of these plots exhibit a linear behaviour. The electrode separation dependence of the current $I \propto d^{-3}$ is directly given by *equation 2-10*. Thus, *I versus* d^{-3} at 10 and 100 V characteristics were plotted in *Figure 2-28*.

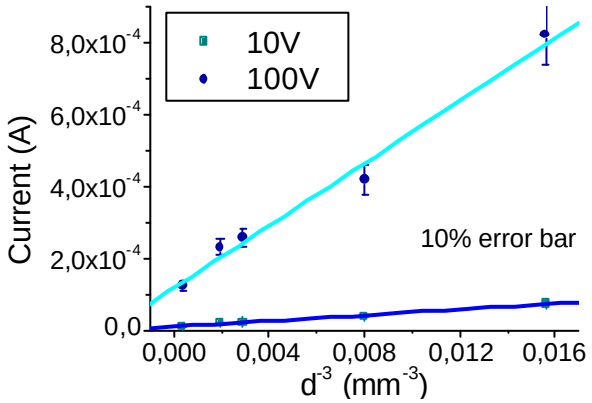

Figure 2-28 I versus d^{-3} *plots at 10 and 100 V of a 5-bi-layers TS-SWCNT LbL film*

Figure 2-28 shows that good linear fit are obtained for *I versus* d^{-3} plots with a 10% margin of error. However, *Figures 2-26* and *2-27* clearly showed that the SCLC is

not the dominant conduction in the SWCNT LbL films as the voltage and the temperature dependence of the current do not follow the SCLC model.

2.6.2.5 Poole-Frenkel conduction model

Impurities present in insulating materials introduce potential wells (traps) in the forbidden band of the structure of their host material. Traps are known to have coulombic-type barriers[169]. Similarly to the Schottky effect, the coulombic potential barriers of the traps attenuate when they are subjected to an electric field. This process takes place in the bulk of the material where the impurities are located and is called the Poole-Frenkel effect. Then, the lowering of the potential barriers decreases the amount of energy necessary to ionise the impurities. Consequently, the probability that the electrons from the traps pass into the conduction band of the insulator by thermionic emission, augments[170]. This process is analogous to the Richardson-Schottky conduction but refers to a bulk phenomenon. The Poole-Frenkel effect is illustrated in *Figure 2-29*.

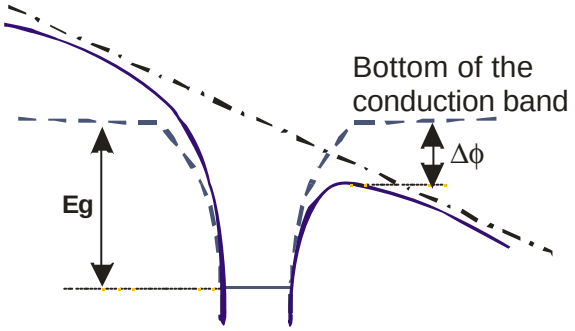

Figure 2-29 Mechanism of Poole-Frenkel effect adapted from Simmons[171]. The dashed line represents the Coulombic barrier without a field. The solid line shows the effect of an electric field on the barrier. The slope of the dash-dot line is proportional to the applied field. [Df is the barrier attenuation]

The potential energy of an electron in the trap is $-e^2/4\pi\varepsilon_0\varepsilon_r$, where e, ε_0 and ε_r are the electron charge, the permittivity of the free space and the dielectric constant of the insulator, respectively. Thus, the potential of an electron from the trap subjected to an electric field F is:

$$E(x) = \frac{-e^2}{4\pi\varepsilon_0\varepsilon_r}\frac{1}{x} - eFx \qquad (2\text{-}19)$$

The expression of the current density in presence of the Poole-Frenkel effect is found[169].

The potential of the electron in the trap will be maximal for $x=x_{max}$, when $dE/dx = 0$.

Applying the derivative to E(x) leads to:

$$\frac{dE}{dx} = \frac{e^2}{4p e_0 e_r} \frac{1}{x^2} - eF \qquad (2\text{-}20)$$

And from $\frac{dE}{dx} = \frac{e^2}{4p e_0 e_r} \frac{1}{x^2} - eF = 0$, x_{max} is found to be:

$$x_{\max} = \left(\frac{e}{4p e_0 e_r F} \right)^{1/2} \qquad (2\text{-}21)$$

E_{max} (=E(x_{max})) is found by substituting x by the expression of x_{max} in E(x):

$$E_{\max} = 2\left(\frac{e^3}{4p e_0 e_r} \right)^{1/2} F^{1/2} = \left(\frac{e^3}{p e_0 e_r} \times \frac{V}{d} \right)^{1/2} = b_{PF} V^{1/2} \qquad (2\text{-}22)$$

Where:

$$b_{PF} = \left(\frac{e^3}{p e_0 e_r d} \right)^{1/2} \qquad (2\text{-}23)$$

is the Poole-Frenkel coefficient

As described in *Figure 2-29* the potential energy barrier E_g is lowered of E_{max} via the Poole-Frenkel effect with $\Delta f = E_g - E_{\max}$. Therefore, the expression of the current density in the Poole-Frenkel conduction is obtained by substituting E_g by $E_g - \Delta f$ in the expression of J[172]:

$$J = e\ m\ N\ \frac{V}{d} \exp\left(-\frac{E_g}{2kT} \right) \qquad (2\text{-}24)$$

$$J_{PF} = e\ m\ N\ \frac{V}{d} \exp\left(\frac{-E_g + b_{PF} V^{1/2}}{2kT} \right) \qquad (2\text{-}25)$$

Ionised traps can possess singly ($h = 1$) or doubly ($h = 2$) charged levels[173]. This characteristic was integrated in the Poole-Frenkel theory via its coefficient[174]. Thus, b_{PF} can be re-written:

$$b_{PF} = \left(\frac{e^3 h}{p e_0 e_r d} \right)^{1/2} \qquad (2\text{-}26)$$

Voltage dependence

The voltage dependence of the current was found applying the logarithm function to *equation 2-27*:

$$\ln\left(\frac{J_{PF}}{V}\right) = \ln\left(\frac{emN}{d}\right) - \frac{E_g}{2kT} + \frac{b_{PF}V^{1/2}}{2kT} \qquad (2\text{-}27)$$

$\ln(emN/d)$ and $E_g/2kT$ are constant for an electric field variable, therefore:

$$\ln\left(\frac{J_{PF}}{V}\right) \propto V^{1/2} \qquad (2\text{-}28)$$

Temperature dependence

The same method was used to find its temperature dependence and *equation 2-28* gives:

$$\ln\left(\frac{J_{PF}}{V}\right) \propto \frac{E_g + b_{PF}}{2kT} \qquad (2\text{-}29)$$

Where both E_g and b_{PF} are temperature independent and *k* is the Boltzmann constant. Note: $I/V = G$, where G is the conductance.

Electrode separation dependence

Equation 2-26 also allows writing the current dependence as a function of the electrode separation. This leads to the same expression between I and d that for the Richardson-Schottky model:

$$\ln(I) \propto d^{-1/2} \qquad (2\text{-}30)$$

As shown in *Figure 2-25* the $\ln(I)$ *versus* $d^{-1/2}$ plots displayed to good linear fits. Thus, the conductance was plotted according to the *equations 2-28* and *2-29* for its voltage and temperature dependence, respectively. *Figures 2-30 (a)* and *(b)* display the $\ln(G)$ *versus* $V^{1/2}$ plots of 20 bi-layers SWCNT LbL films at 4 and 14 mm electrode separation, respectively.

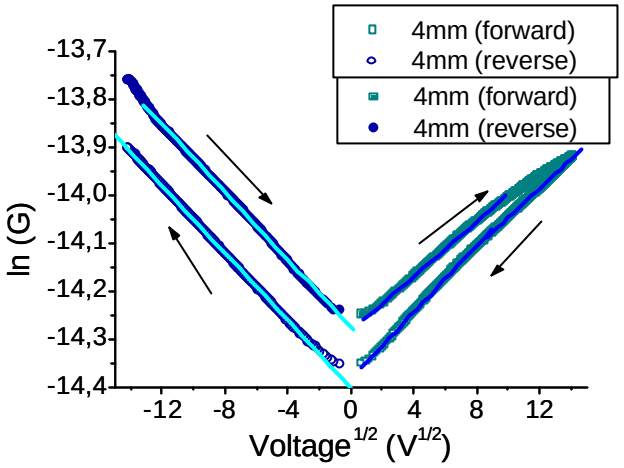

(a)

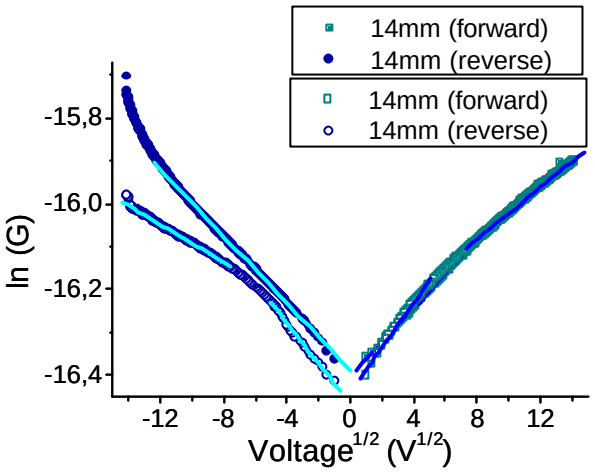

(b)

Figure 2-30 $Ln\,(G)$ versus $V^{1/2}$ for a 20 bi-layers SWCNT LbL film (a) electrode separation of 4 mm (b) electrode separation of 14 mm

Good linear fits of $\ln(G)$ *versus* $V^{1/2}$ plots were obtained for 4 mm electrode separations over the whole range of voltages (*Figure 2-30 (a)*). In comparison, the fittings for the 14 mm electrode separations over the same range of voltages (*Figure 2-30 (b)*) required inflection points. Apart from one inflection point, linear fits were also obtained. Thus, *Figures 2-30 (a)* and *(b)* show good linear fits of the I-V characteristics according to the Poole-Frenkel model. These results contrast with the conduction models previously considered, where no reasonable fits could be obtained. $\ln(G)$ *versus* $1/kT$ (*equation 2-29*) were plotted in *Figure 2-31* at 1, 5, 10 and 20 V.

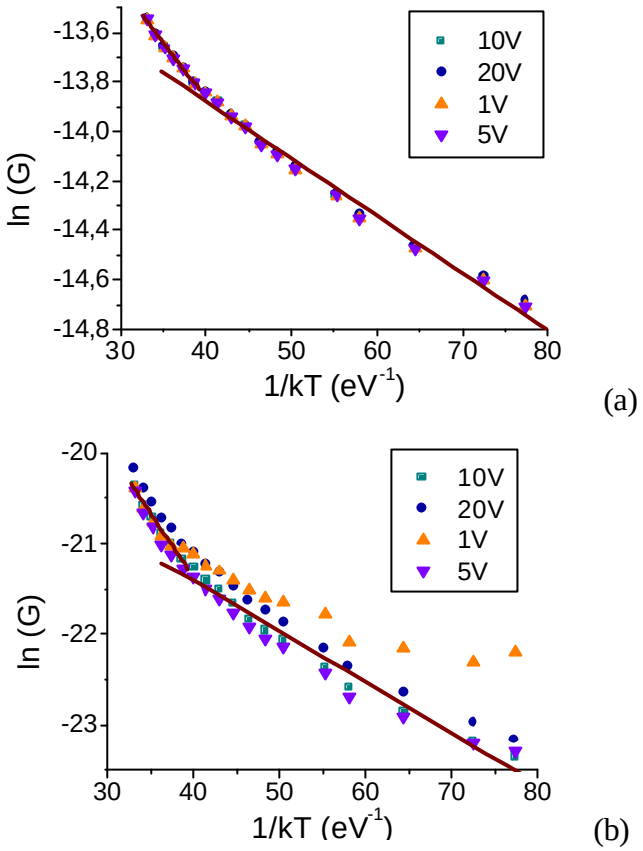

Figure 2-31 $\ln(G)$ *versus* $1/kT$ *of I-T plots of 20 bi-layers SWCNT LbL films for electrode separations of (a) 1 mm and (b) 4 mm*

Though the I-T plots trends shown in *Figures 2-14* and *2-15* appear different, their $\ln(G)$ *versus* $1/kT$ plots give similar behaviours. *Figure 2-31 (a)* shows that for the 1 mm electrode separation the data points are completely overlaid, as expected. Despite the absence of superposition of the measurements for 4 mm of electrode separation, the $\ln(G)$ *versus* $1/kT$ plots appear parallel. The deviations in *Figure 2-31 (b)*, particularly for the 1 V measurement at low temperature, are attributed to the presence of noise in the current signal. Indeed, tens of nanoamps are reached for 20 V at 350 K and the currents for 1 and 5 V are in the order of the nanoamp at 350 K. The currents fall to 2.3×10^{-10} and 3.9×10^{-10} A at 150 K. The deviation at low temperatures of ln (G) at 1 V, seen in *Figure 2-31 (b)* is explained by the instability of the current measured at such low level of magnitude, given that at 250 K (abscise 46.42 in *Figure 2-31 (b)*) the current intensity was already less than 5×10^{-10} A for 1 V. Despite the different profiles found for the I-T characteristics, both plots of *Figures 2-31 (a)* and *(b)* show good linear fits. A transition in the linear slope occurs between 290 and 300 K. According to *equation 2-29*, this indicates that the I-T plots are governed by the Poole-Frenkel

conduction below and above this temperature transition. Activation energies extracted from *Figures 2-37* and *2-38* are shown in *Table 2-3*.

Separation (mm)	Activation energies (meV)	
	T≥300 K	T≤290 K
1	45.11	23.25
4	142.3	55.8

Table 2-3 Activation energies extracted from $\ln(G)$ versus $1/kT$ plots

I-T studies of similar SWCNT LbL films were carried out for a temperature range from 77 K to room temperature. For 10 V bias, temperature transitions at about 155 K were reported. Activation energies below and above this temperature were found to be 11.2 and 19.9 meV, respectively[175]. In this work, within the temperature range 150-350 K, another transition is located between 290 and 300 K. The activation energy found for T ≤ 290 K with electrode separations of 1 mm is close to the figures reported, while the activation energy for 4 mm is of the same order as the ones reported for similar temperature range[175]. The activation energy for electronic conduction corresponds to the energy required for a charge carrier from a trap to reach the conduction band[173]. Thus, it is reduced due to the Poole-Frenkel effect[176], which lowers the potential barriers. In this work, the presence of a transition temperature and two activation energies are explained by trap levels inherent to the Poole-Frenkel model[173] rather than by different conduction models governing the transport in these regions[177]. Indeed, two activation energies can be attributed to the presence of at least two trap levels above and below the transition temperature[174]. This is consistent with the presence of anionic and cationic surfactants, which contribute in the SWCNT LbL films.

The analysis of the in-plane conduction in SWCNT LbL films indicates that the Poole-Frenkel effect governs the conduction mechanisms. This contrasts with the models (VRH and tunnelling) usually reported for SWCNT films (see *Section 1.4*). By definition, the Poole-Frenkel effect requires the de-trapping of the charges following the lowering of the potential barriers by the electric field. The transport of carrier charges occurs from traps to traps. In SWCNT LbL films, this process is understood as ions from the insulator (here ionic surfactant) trap the charge carriers

from the SWCNTs. Thus, the Poole-Frenkel effect occurs as the applied electric field lowers the potential barriers created by the presence of the surfactants.

2.6.3 Conduction model: out-of-plane configuration

The electrical characteristics for the out-of-plane configuration (*Figure 2-10*) were studied similarly to the in-plane measurements. However, none of the conduction models already considered fitted the I-T characteristics of *Figure 2-16*. Given the nanometric electrode separation in the out-of-plane configuration, direct tunnelling phenomenon was also taken into account. *Equation 2-31* expresses the current voltage relationship in tunnel junctions at low electric field is expressed[178]:

$$J = b\left(V + g\,V^3\right) \qquad (2\text{-}31)$$

This gives $J \propto V$ for low voltages and is in agreement with the linear I-V characteristics displayed in *Figure 2-13*. According to Hurd[179], when a tunnelling mechanism dominates the conduction, there is a proportional relationship between the logarithm of the current and the temperature, rather than with the inverse of the temperature. The absence of expression for the temperature dependence of the current in the direct tunnelling model led to plot $\ln(I)$ *versus* T of the I-T characteristics in *Figure 2-32*.

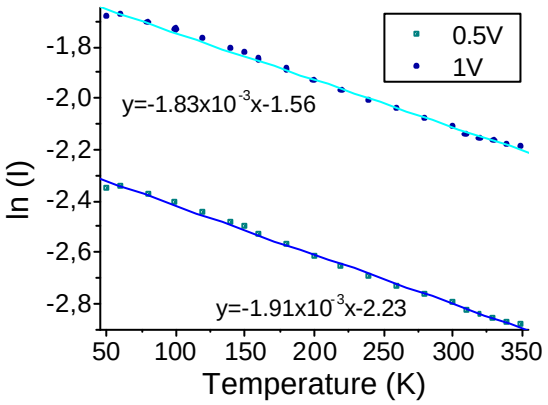

Figure 2-32 ln (I) versus T plots of the out-of-plane I-T characteristics at 0.5 and 1 V

Figure 2-32 displays good linear fits of the ln (I) versus T plots. Therefore the I-T characteristics are in agreement with this model. The $y = ax + b$ fittings of *Figure 2-32* lead to an experimental relationship between the current and the temperature which can be written as *equation 2-32*:

$$I = I_0 \exp(aT) \qquad (2\text{-}32)$$

with I_0=9.3 and 4.76 A at 0.5 and 1 V, respectively, and α=1.87×10^{-3}.

Thus, *Figure 2-32* shows that the conduction in the out-of-plane configuration is governed by tunnelling mechanisms over the whole range of temperatures investigated. Tunnelling mechanisms were already found to be dominant in the out-of-plane configuration of such films[155]. However, the results presented here differ from previous reports since the dominant mechanism is direct tunnelling. The AFM analysis indicated the possibility of having local areas, with thickness of 5 nm or less (see *section 2.4.3*). Thus, the presence of such thickness explains getting direct tunnelling[180]. The voltage range of analysis can also explained the difference, here the bias was limited to 5 V, while 10 V were used in previous reports[155].

2.7 Application: Memory device

In this section, the Poole-Frenkel effect, which governs the conduction, is exploited to provide an example of application for the SWCNT LbL films. *Figure 2-29* shows that the Poole-Frenkel effect allows the ionisation of the traps via the lowering of its energy barrier. This de-trapping mechanism is often reported as dominant in memory devices[181]. Memory devices rely on their charges storage ability, which consists in their charging and discharging. Thus, the Poole-Frenkel effect is comparable to the discharging mechanism occurring in these memory devices. The integration of metallic or semiconducting nanoparticles into an insulator's capacitor was shown to provoke memory effects[182]. Such effects are explained by the nanoparticles, which act as discrete charge trapping centres. This characteristic was exploited to create SWCNT LbL film-based memory devices. SWCNT based memory devices are reported[183-184]. Here, the characteristics of SWCNT LbL film based metal insulator semiconductor (MIS) memory devices are described.

In the LbL films, the formation of SWCNT networks allows releasing these charges, which provokes the electric conduction across the LbL films. SWCNT LbL films without long range SWCNT networks are expected to behave similarly to nanoparticles-loaded insulators. Therefore, the SWCNT were shortened to limit their conduction but enhance their charge storage capability. Thus, the SWCNTs were cut

by heating in a 1:1 mixture of H_2SO_4/HNO_3[185]. DTAB solution and dispersions of cut-SWCNTs in SDS solution were prepared following the methods described in *section 2.3.2*. For their integration in a memory device, cut-SWCNT LbL films were built-up following the process detailed in *section 2.3.3*. The fabrication of SWCNT-based MIS devices, with the architecture (Al electrode/PMMA[x] layer/cut-SWCNT LbL film/SiO2/p-doped Si/Al electrode) described in *Figure 2-33*, were reported[186].

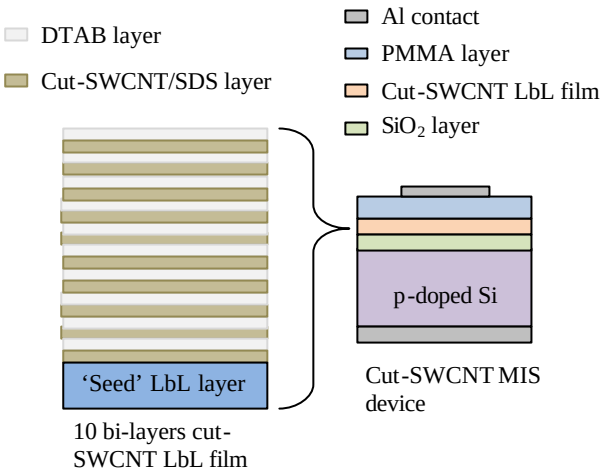

Figure 2-33 Schematic of (a) 10 bi-layers cut-SWCNT LbL film and (b) cut-SWCNT MIS device

Capacitance-voltage (C-V) investigation carried out on LbL film MIS devices are displayed in *Figure 2-34 (a)*. *Figure 2-34 (b)* displays C-V measurements carried out on a gold nanoparticles-based MIS device for comparison.

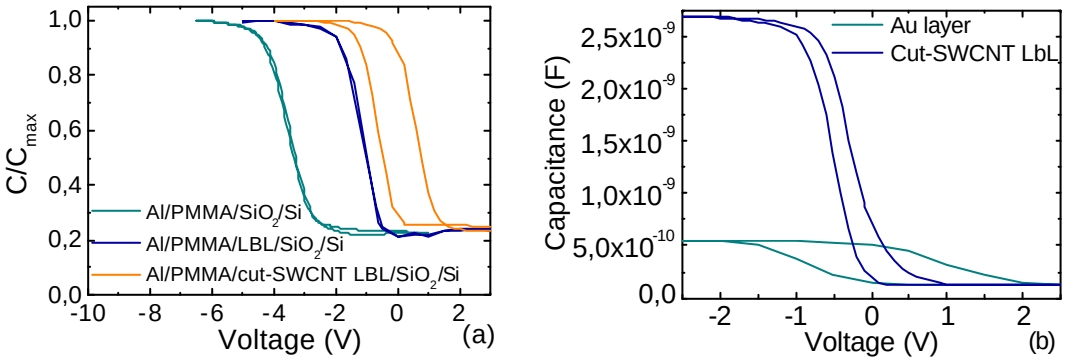

Figure 2-34 (a) Normalised C-V characteristics of cut-SWCNT LbL film, LbL film and PMMA MIS devices at 400 kHz (b) Comparison of C-V characteristics of typical cut SWCNT LbL film and gold MIS devices

Figure 2-34 (a) shows the influence of the cut-SWCNTs on the C-V characteristics of a MIS device. The forward and reverse C-V measurements of the conventional and LbL film MIS devices are almost overlaid. However, the C-V characteristics of cut-

[x] PMMA: Polymethylmethacrylate

SWCNT MIS device display a hysteresis with a window of 1.6 V. The charging effect shown by the hysteresis is indicative of the charge storage capability of the device in presence of the cut-SWCNTs. In *Figure 2-34 (b)*, the hysteresis window is smaller for cut-SWCNT LbL based MIS devices than for Au nanoparticles-based MIS devices. However, cut-SWCNT LbL based MIS devices display a much higher capacitance.

2.8 Discussion/Conclusion

A combined analysis conducted on the in-plane I-V, I-T and I-d characteristics establishes the dominant conduction model in the SWCNT LbL films. The current evolution according to these three parameters (V, T and d) leads to the Poole-Frenkel conduction as the dominant transport mechanism. However, the nature of the film does not discount the occurring of other mechanisms, which would not control the conduction. This finding completes the knowledge of the conduction across SWCNT LbL films given that their in-plane conduction mechanism was not identified[155]. Poole-Frenkel conduction, which involves the ionization of traps in an insulator, is not a conduction model generally displayed by SWCNT materials (see *section 1.6*). According to this transport mechanism, charge carriers (electrons and holes) are successively trapped by potential wells, then released into the conduction band. In SWCNT LbL films, it can be visualised as the carriers from the nanotubes are trapped by the ionic surfactants. Under the influence of the electric field, these carriers are release before being trapped again by another ion and so forth. This process is repeated from one electrode to the other.

Charging effect and self-heating were found to occur during the measurements (see *Appendix A*). These phenomena explain small discrepancies and alterations in the linearity of I-V characteristics. For instance, I-V plots in *Figures 2-12* and *2-13* (*section 2.5.2*) exhibit little charging of the SWCNT LbL films. This charging is explained by the presence of the surfactants, which are insulating as shown in *Figure 2-11.*

In the out-of-plane configuration, the I-V and I-T characteristics of SWCNT LbL films indicate that tunnelling mechanisms govern the conduction. Direct tunnelling conduction was considered dominant because of the linear I-V plots. This hypothesis is supported by the linear I-V characteristics obtained for the C_{60}-mixed SWCNT LbL films and the reference LbL film (see *Appendix A section A.1.2*). These films

also display currents in the same order of magnitude as the SWCNT LbL films. Their I-T characteristics are similar and lead to analogous linear $Ln(I) \propto T$ plots, also in agreement with *Hurd* theory[179]. This contrasts with results on similar films where quantum tunnelling was shown to be dominant[155]. Here, the direct tunnelling model is explained by the thickness of the SWCNT LbL films used.

Current breakdowns in the out-of-plane configuration are reported in *Appendix A.2*, and the resilience of LbL films to a current breakdown was shown to be improved by the presence of SWCNTs. The conduction mechanism after current breakdown of the SWCNT LbL films at 50 K, appears to follow another mechanism which is yet to be identified. LbL film without SWCNTs displayed similar current breakdown. The analysis of breakdowns in SWCNT networks, shows that the Joule heating segments the SWCNTs via a stepwise process[187-188]. Here, the current breakdown does not follow a stepwise process. This suggests that for SWCNT LbL films, the current breakdown is likely to be from the insulating materials (surfactants, polyelectrolytes) rather than from the SWCNTs.

The study of SWCNT LbL film properties is completed by the identification of their equivalent circuit, which is consistent with Nyquist plot results reported[189]. The effects of the integration of cut-SWCNT LbL films in MIS devices are also described. This provides an example of application for SWCNT LbL films in memory devices[186].

2.9 Summary

This chapter reports on the fabrication and characterisation of SWCNT LbL films. A combined analysis of their I-V, I-T and I-d characteristics was required to identify the Poole-Frenkel conduction as the dominant transport mechanism for the in-plane configuration. The conduction in the out-of-plane configuration was found to be governed by direct tunnelling, which is explained by the thickness and non uniformity of the SWCNT LbL films. The charge storage capability of cut-SWCNT LbL films was also demonstrated via their integration into memory devices. This work completes the understanding of transport mechanisms across SWCNT LbL films by finding the mechanisms governing the in-plane conduction. Furthermore, account of current breakdown phenomena and the equivalent circuit of the SWCNT LbL films are provided in *Appendix A*.

Chapter 3
SWCNT precursor networks

3.1 Introduction

Molecular Electronics is often viewed as the ultimate stage of miniaturization for the electronics industry, due to its capacity to create devices made of single molecules or groups of molecules[190]. Thus, a growing number of research activities focus on analysing the electrical properties of organic molecules resulting in ingenious methods designed for their characterisation[191-192]. Studies of molecules positioned between two SWCNT electrodes reported in available literature generally deal with the electrical response of the molecules[193].

The nano-manipulation challenge is particularly critical in molecular electronics. Working with nanotube networks rather than individual SWCNTs allows therefore, a new strategy in the field of molecular junctions. However, SWCNT networks displayed poor performances compared to individual SWCNTs (see *Chapter 1*). These poor performances have generated interest in developing other types of connections through the network to improve its performances. Two approaches are followed in this domain. In the first strategy, carbon nanotubes are connected to each other by their cross-linking due to their irradiation by electrons[194] or ions[195] beams. CNTs networks containing junctions induced by ion irradiations display different conduction type depending on the thickness of the network[196]. The second approach consists of forming molecular bridges between nanotubes and has been adopted since 2003. Electrical measurements on such networks of interconnected SWCNTs via molecular linkers, showed a decrease of conductivity after formation of the linkers[197].

Within this second strategy, molecular junctions are intrinsically integrated in the architecture of the networks which results in the fabrication of a new material. The work presented here was undertaken following this approach. SWCNTs were connected via the construction of conjugated bridges or the coordination of metals. The objective sought in this part of the project is to facilitate the electrical

conduction across the network of SWCNTs by providing electric pathways made of conductive molecules. A theoretical study on the contact transparency of nanotube-molecule-nanotube junctions was recently published[198]. This study as well as previous reports on the quality of covalent contacts between molecules and nanotubes only considers contacts located at the edges of SWCNTs in a configuration of open end. Although molecular bridges are created through different processes, the initial functionalisation of the SWCNTs and the fabrication of the networks remain the same. Therefore, these two aspects are presented in the following chapter, while the formation of the molecular bridges, the analysis, and the study of the resulting networks are dealt with in the subsequent chapters.

The state-of-the-art for the fabrication of carbon nanotubes thin films (or networks) includes advanced technologies such as inkjet printing[199], electrophoretic deposition[200], as well as more basic ones like direct growth[201] and drop drying[202]. Results of the comparison on the electrical resistance and optical transmittance between different techniques are available elsewhere[203]. The deposition technique, based on nanotube filtration, established by *Wu and co-workers*[204] did not display the best performances in this study. However, in this work it was preferred to the other techniques for its simplicity. This method is based on the fabrication of buckypaper and its novelty comes from the fact that the filter membrane is only used as a template. The SWCNT film is detached from it, leaving a free standing SWCNT film. Simple to implement, the filtration method gives an easy way to control the thickness of the thin film and though porous, the film has a good homogeneity[204]. Only limited by the filtration apparatus, the SWCNT films can cover large areas and is not too time consuming.

Such SWCNT films display lower electrical conductivity than indium tin oxide (ITO[xi]). As seen in *Chapter I*, there is no standard for the conductivity of such SWCNT networks instead, their electrical conductivities depend on several parameters such as the length of the nanotubes[205]. Chemical functionalisation of the SWCNTs is also known to affect their electronic structure[76]. Consequently, the electrical properties of SWCNT networks are expected to be altered by different functionalisations. These properties include the electronic transport of SWCNT

[xi] ITO: commercial standard for transparent electrodes with a conductivity of about 10^4 S/cm

networks, whose understanding is required to optimise the performance of SWCNT network devices.

This chapter introduces the diazonium radical additions used to functionalise the SWCNTs alongside their characterisation. It also reports the first record, to our knowledge, of Sonogashira cross-coupling on SWCNTs. The SWCNT networks were fabricated by the filtration method. The dominant conduction mechanism across these functionalised SWCNT networks are identified from the combined study of their electrical characteristics.

3.2 Deposition process

3.2.1 Principle

SWCNT films from filtration are networks of randomly oriented nanotubes deposited onto a filter membrane. As for nanotube bundles, the adhesion between the nanotubes is governed by van der Waals forces[206]. The thickness of the films is controlled by the amount (concentration and volume) of nanotubes deposited and the roughness by the quality of the dispersion. The uniformity of the network's thickness and the fact that the nanotubes are laid straight on the membrane are amongst the three postulates for this process[204].

3.2.1 Network fabrication

Prior to the deposition process, the SWCNT must be dispersed by ultrasonic bath and/or probe in a solvent (surfactant solution or organic solvent). The quality of this dispersion strongly impacts on the quality of the SWCNT networks. Thus the dispersion is left to settle to reduce the presence of micron size particles. The deposition process involves 3 steps: filtration, washing and drying. The SWCNT suspension is filtered through a porous membrane. The SWCNTs are deposited on this membrane to form a porous film. This network is then dried at 120°C in a vacuum oven to remove the solvent. *Figure 3-1* describes the deposition technique and shows a picture of a SWCNT film made by filtration.

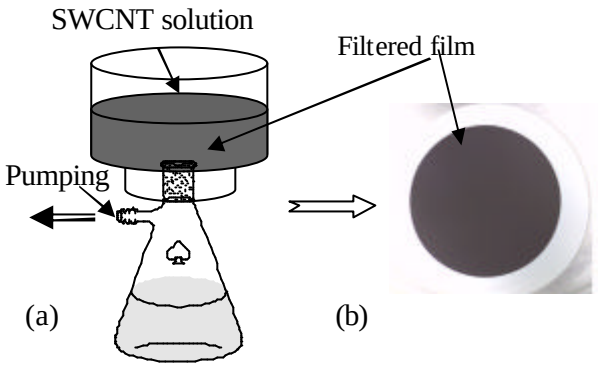

Figure 3-1 (a) Filtration apparatus and process of a SWCNT solution (b) SWCNT-network (bucky paper) on top of a filter membrane

Following this straightforward deposition process, the CNT films can be transferred onto another substrate (e.g. silicon or glass) for subsequent processing when the application requires it (e.g. field effect transistor or study of the transparency). This step is particularly delicate and may explain why variations are available for this phase. Indeed, already in 2004, *Wu and co-workers* presented two transfer methods, though both of them involved the dissolution of the filter membrane. Dry transfer methods were also developed to remediate the difficulties inherent to the membrane dissolution. For instance in 2006, *Rowell and co-workers* transferred nanotube networks made by filtration using a poly(dimethylsiloxane) (PDMS) stamp to make nanotube electrodes. This transfer technique consisted of lifting off the network from the filter membrane with a PDMS stamp and depositing it onto an appropriate substrate[8].

3.3 Network structure

Entangled nanotubes and bundles disposed in a 2-dimension plan form a long range network because they are connected to each other. *Figure 3-2* helps to visualize the organisation of the SWCNTs in such a network.

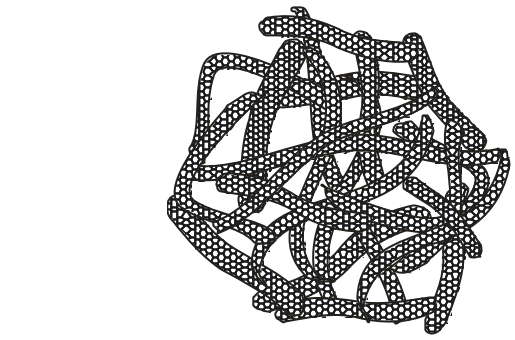

(a)

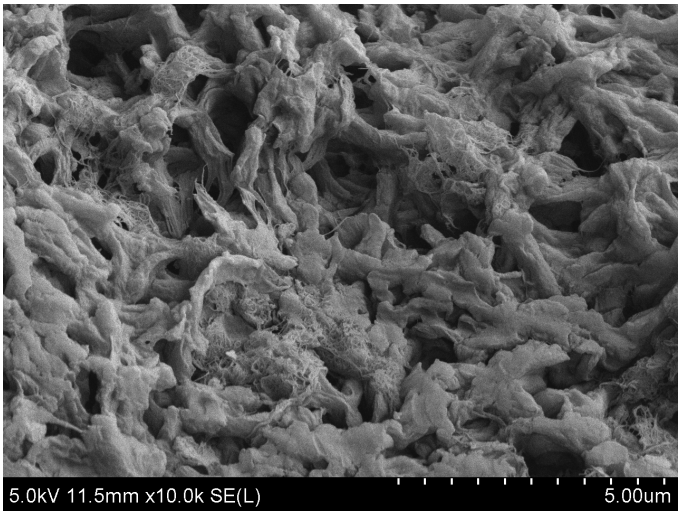

(b)

Figure 3-2 (a) Schematic representation of a SWCNT network made by filtration (b) SEM picture of a Sonogashira-SWCNT network from the filtration of 20 ml of dispersion at 1:10 mg/ml

In such a network, the nanotubes separation is given by the van der Waals radius of carbon which is about 0.17 nm[207], this leads to a distance between two SWCNTs in the contact area of 0.34 nm. Thus, the transport between two metal-metal (MM) or semiconducting-semiconducting (SS) nanotubes involves tunnelling through this distance. In turn, for metal-semiconductor (MS) junctions in addition to this tunnelling barrier, the presence of a Schottky barrier decreases the transmission probability. High conductance levels were found for MM and SS junctions compared to MS junctions as shown elsewhere[208].

The conduction through such SWCNT networks was shown to be dominated by the junction resistance between bundles[209]. It is therefore likely for the conduction of thin networks (metallic threshold not reached) to be dominated by tunnelling phenomena. Surfactants and polymer wrapped SWCNTs in aqueous solution offer a good and stable dispersion and are compatible with a wide range of membranes. On

the other hand, their complete elimination from the network is not assured and their presence can have an impact on the electrical behaviour of these networks. Here, neither surfactant nor membrane dissolution were used when determining the electrical characteristics of the SWCNT networks produced. As a result, contrary to LbL film, the van der Waals diameter between carbon atoms will be considered as the distance between SWCNTs forming a junction.

The filtration deposition technique is versatile and can be applied to any type of SWCNT dispersion as long as the solvent is compatible with the filter membrane. It was therefore used for all type of network[xii]. Few solvents lead to a good dispersion of nanotubes. N-methylpyrrolidone (NMP) and N,N-dimethylformamide (DMF) are amongst the best solvents for this purpose[210]. In this work, DMF was used because it was easily available and nylon membranes were used as substrates because of its compatibility with DMF. The first stage of the process described in this chapter, consists in the functionalisation of the SWCNTs. This first reaction is a radical addition of delocalised groups onto the SWCNTs surface using diazonium salts[211]. The impact of the radical additions on the SWCNTs is presented here. It is followed by the electrical characterisation of the functionalised SWCNT networks.

3.4 Pristine nanotube

Covalent functionalisations are known to introduce defects in the nanotubes' structure which degrade their electrical properties (see *section 1.3.4*). The SWCNTs were annealed at 900°C under dynamic vacuum prior to radical additions. This was done to remove most of the carboxylic groups introduced during their purification[212,213]. Unfortunately the low level of vacuum used allowed the formation of some carboxylic groups during this process. Thus, though efforts were made to remove the carboxylic groups from the nanotubes' surface, some still remained.

[xii] The carbon nanotubes used in our networks were covalently functionalised prior to the filtration.

3.4.1 Spectroscopy

3.4.1.1 Raman

The ratio I_D/I_G between the areas of the sp^3 carbon band I_D and the sp^2 band I_G expresses here the level of perfection of the nanotube structure. Note that I_D and I_G are indicative of the disorder in the structure and the crystalline structure, respectively. The presence of defects (or functional groups) on the nanotubes affects this ratio by increasing the intensity of the disorder band. Thus, the higher a defect's concentration is, the higher I_D. *Figure 3-3* displays the Raman spectra of purified SWCNTs and purified then annealed SWCNTs.

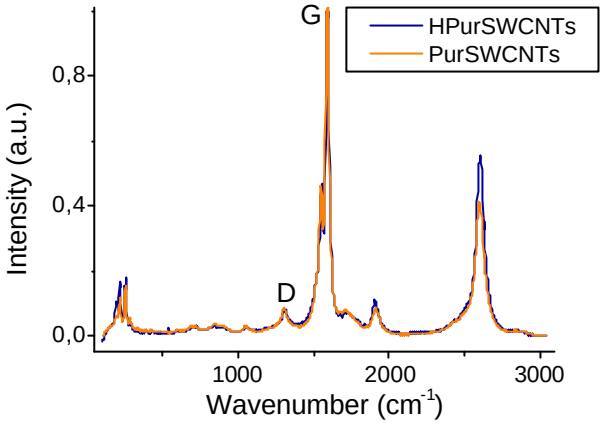

Figure 3-3 Normalised Raman spectra of purified SWCNTs (PurSWCNTs) and heated SWCNTs (HPurSWCNTs) (the spectra include the baseline correction)

The I_D/I_G ratio decreases from 5.8% before to 5% after annealing of the sample. Thus, no notable improvement in the structure was observed from the Raman spectra as a result of the annealing step.

3.4.1.2 UV-visible-near IR

The presence of carboxylic acid groups on nanotubes' surfaces helps their solubility. So, removing these groups with the annealing process leads to a drop in their solubility. Saturated dispersions of purified SWCNTs and purified then annealed SWCNTs, in DMF were analysed by UV-visible-nIR spectroscopy between 300 and 1800 nm. The presence of SWCNTs increases the light absorption of the dispersions. Consequently, a clear drop in the absorption levels after the annealing step will support the assumption of the removal of carboxylic groups.

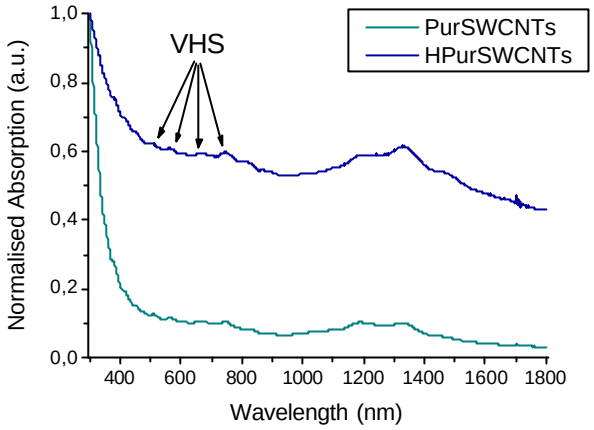

Figure 3-4 Normalised absorption spectra of saturated solutions of purified and purified then annealed SWCNTs in DMF at a nominal concentration of 1:10 mg/ml

Figure 3-4 displays typical SWCNT spectra where the confinement of electronic states in 1-dimension leads to van Hove singularities (VHS)[149]. The VHS shown on these spectra attest to (i) the one dimensional character of the nanotubes and (ii) the presence of both metallic and semiconducting nanotubes. Indeed, the bands centred at ca. 1400 nm and 800 nm are attributed to the first and second singularities in semiconducting nanotubes, respectively. In contrast, the bands centred at ca. 500 nm (much less distinct) are attributed to the first transition in metallic tubes[214]. The empirical Beer-Lambert law (*equation 3-1*) expresses the relationship between the absorbance and the concentration of substances as:

$$A_l = e_l \, l \, C \qquad (3\text{-}1)$$

Where A_l , e_l = 25.5 $(mg/L)^{-1}$ cm^{-1} at 500 nm[153], l and C are the absorbance at the wavelength l , the molar absorptivity, the path length and the concentration of the substance, respectively. Thus, at 500 nm, $C_{PurCNT} = 24$ mg/L and $C_{HPurCNT} = 7$ mg/L. This indicates a strong reduction of the nanotubes' concentration after annealing. Though the annealing has not completely eliminated the carboxylic groups of the nanotubes' surface, an improvement in their structure is anticipated as the concentration of SWCNT in solution drops when the nanotubes become less soluble due to the removal of the groups. This result was expected as the carboxylic groups help the nanotubes solubility[212].

The Raman spectra showed a little improvement (0.8%) of the SWCNT's structure, which is not significant. However, the UV-visible-near IR spectra indicated that the annealing step reduces the concentration of nanotubes in solution drastically, clear evidence for the removal of functional groups. This reduction of solubility was expected as annealing the SWCNT under vacuum is known to remove the functional groups (in this instance, carboxylic acid groups) from the nanotubes' surfaces[212,213].

3.4.2 X-ray photoelectron spectroscopy analysis of SWCNTs

X-ray photoelectron spectroscopy (XPS) analyses were carried out on the purified and annealed SWCNTs. The C1s spectrum of these SWCNTs will be compared to these of pyridine-SWCNTs and iodobenzene-SWCNTs to report any changes in the functionalisation.

The relative concentrations of C and O were found to be 97.8 at% and 2.2 at% respectively. The presence of O in the sample is expected because of the atmosphere contamination (no ion etching was performed). The carboxylic acid from the purification step, which not totally removed after annealing, also contributed to this value (see *section 3.4*). *Figure 3-5* shows the C1s peak in XPS spectra of HiPCO SWCNTs before and after air oxidation and HCl baths reported elsewhere[215].

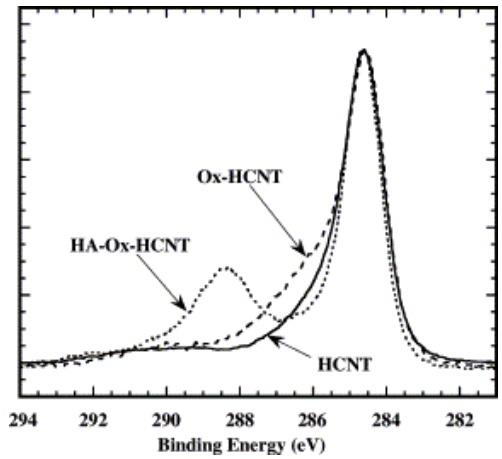

Figure 3-5 C1s XPS spectra of HCNT (HiPCO SWCNT), Ox-HCNT (HiPCO SWCNT after thermal oxidation) and HA-Ox-CNT (HiPCO SWCNT after thermal oxidation followed by washing in HCl) [215]

Table 3-1 gives the binding energies of their different contributions[215].

	C1s peak	Contributions				
		C-OH	C-O-C	C=O	COOH	Not defined
HCNT	284.6	-	-	-	-	-
Ox-HCNT	284.6	286.1	286.1	287.6	288.6	-
HA-Ox-HCNT	284.6	-	-	-	-	287-290

Table 3-1 Binding energies of the contributions in Figure 3-5[215]

Figure 3-6 shows the C1s XPS spectrum obtained in this study for purified then annealed SWCNT. It is comparable to the results reported above[215] given the similarities of the purification techniques employed (thermal oxidation then HCl treatment).

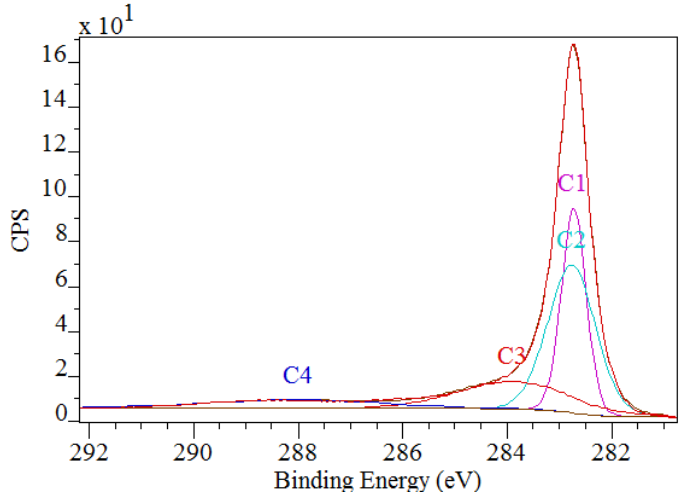

Figure 3-6 C1s XPS spectrum of purified then annealed SWCNTs

Figure 3-6 shows that the C1s peak of purified then annealed SWCNTs displays a similar profile to that of the HCNT C1s peak in *Figure 3-5*. Four contributions were required to produce a good fit. The main fitting parameters of the contributions obtained from the decomposition of the C1s peak are given in *Table 3-2*.

component	C1s in SWCNTS		C3 C-OH or C-O-C	C4 O-C=O
Area	54.4	75.8	33.4	15.9
FWHM	0.6	1.1	2.5	4
Position (eV)	284.6	284.6	285.7	289.7
% concentration	30.3	42.2	18.6	8.8

Table 3-2 Main fitting parameters for the contributions in the C1s in pristine SWCNTs (purified then annealed)

Two contributions (C1 and C2) were needed to fit the main area. It is suspected that C1 and C2 represent the same carbon environment as the difference in their binding energies is smaller than the spectrometer resolution (0.2 eV). According to *Table 3-2*, C3 and C4 are attributed to the C-OH (or C-O-C) and COOH environments, respectively. The annealing step that the SWCNT underwent, explains why the shoulder of the C1s spectrum is less pronounced than in *Figure 3-5*. The absence of a peak between 287 and 290 eV is explained by the washing of the SWCNT after HCl treatment. This indicates that most of the HCl was eliminated after washing. The tail at high binding energies, which contributes to increase the area of the C4 contribution, is the result of the π system in SWCNTs[69]. The C1s XPS spectrum displayed in *Figure 3-6* will later be used as reference.

3.4.3 Thermogravimetric analysis

Thermogravimetric analysis allows estimating the quality of the structure via its thermal stability. The analyses were carried out on SWCNT before and after annealing. *Figure 3-7* displays the TGA in air and in helium for purified SWCNTs (CNTPur) and purified then annealed SWCNTs (HCNTPur).

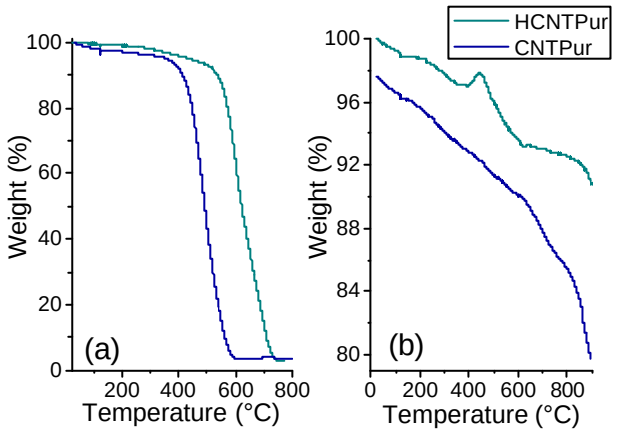

Figure 3-7 TGA from temperature to 900°C of purified SWCNTs and purified then annealed SWCNTs (a) in air and (b) in He

Figure 3-7 (a) shows the degradation via thermal oxidation in air of the samples. SWCNTs thermal degradation starts from ~385°C and from ~500°C for CNTPur and HCNTPur SWCNTs, respectively. This shows an improvement in their thermal stability after annealing. The slight drop before SWCNT degradation is attributed to carboxylic acid groups in the samples[69]. For thermal degradations in He, *Figure 3-7*

(b) shows residual weights of 90.8% and 79.8% for HCNTPur and CNTPur, respectively. The increase of ~10%wt of the residual mass after annealing indicates that the annealing step reduced the amount of groups grafted on the SWCNTs. These results are expected as an annealing step under vacuum is known to improve the purity of SWCNTs[212]. The ignition temperature of HCNTPur SWCNTs is ~500°C, but the true ignition temperature was reported at around 600°C[212]. This reveals the presence of carboxylic groups still grafted on the SWCNTs after annealing.

The TGA analyses confirm the data obtained by Raman and UV-visible-near IR spectroscopies showing an improvement in the SWCNTs' purity after annealing. Indeed, the TGA analysis shows a ~10%wt gain in the mass of the sample. This confirms the overall improvement of the structure as a lesser amount of functional groups is extracted. The annealing step led to an insignificant difference on the Raman spectra. However, both UV-visible-near IR spectra and TGA analysis show an improvement in the nanotubes' structure after annealing.

3.5 SWCNT precursors

This section deals with the functionalisation and characterisation of SWCNT which will be used as precursors in the fabrication of bridges.

3.5.1 Radical addition via diazonium salts

In this work, SWCNTs were covalently functionalised by iodobenzene and pyridine groups via radical additions. Radical additions on SWCNTs by diazonium salts are well reported. At first the aryl diazonium derivation of SWCNT sidewalls was performed via electrochemical reduction in 2001[71] then by a thermal method in which the diazonium salts were created in situ[211]. The formation of ionic bonds due to Coulombic attraction between diazonium salts (positive) and carboxylic acid groups (negative) was also identified[216]. However, ensuring the presence of covalently bonded moieties can be done with an electrochemical method[217]. Reaction mechanisms for such additions have been discussed elsewhere[218-221]. The structure of the SWCNT was shown to influence the reactivity of the radical additions[219-220]. Preferential attacks of diazonium ions were both found on

semiconducting[219] and metallic[75] nanotubes. With sufficient radical additions the metallic nanotubes become non metallic, which impacts on the accepted ratio between metallic and semiconducting nanotubes[75]. In this work, maximum levels of functionalisation were sought so the reactions were performed with a vast excess of diazonium reactants. It is therefore presumed that most of the metallic nanotubes became non-metallic, regardless of whether they reacted before or after the semiconducting nanotubes. SWCNTs were shown to be functionalised with several aryls groups (e.g. Br-, Cl-, F-, CH_3-, SO_3-, COOH-, NO_2-, CO_2CH_3-benzenes, etc.) via radical additions[71,211,222-223]. However, while radical additions of iodobenzene diazoniums were previously reported[224], no functionalisation with pyridine groups, to our knowledge, have been reported. Here, radical additions were carried out on 4-iodoaniline and 4-aminopyridine. The corresponding diazonium salts were generated by an in-situ diazotization.

Radical additions on SWCNTs where the diazonium salts are prepared in-situ were reported[211]. Aniline compounds undergone an in-situ diazotization by the action of an alkyl nitrite on the NH_2 group prior to the radical addition. Diazotization mechanisms are detailed elsewhere[225]. Here, isopentyl nitrite is used as a catalyst for the in-situ diazotization. *Figure 3-8* shows the corresponding scheme.

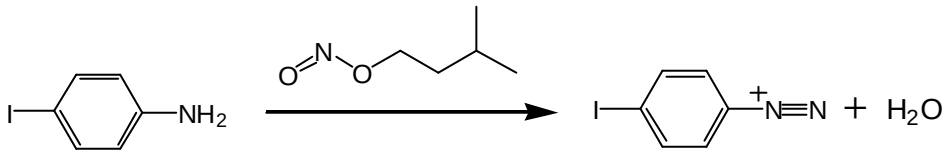

Figure 3-8 Scheme of the diazotization of an iodoaniline group

The same mechanisms are involved in the in-situ diazotization whether the reactants used are 4-iodoaniline (as shown in the scheme) or 4-aminopyridine. This reaction is carried out in organic solvents; dimethylformamide (DMF) for the aminopyridine or dichlorobenzene otherwise. The scheme of the radical addition of 4-iodobenzene and pyridine diazonium salts on SWCNTs is shown in *Figure 3-9*.

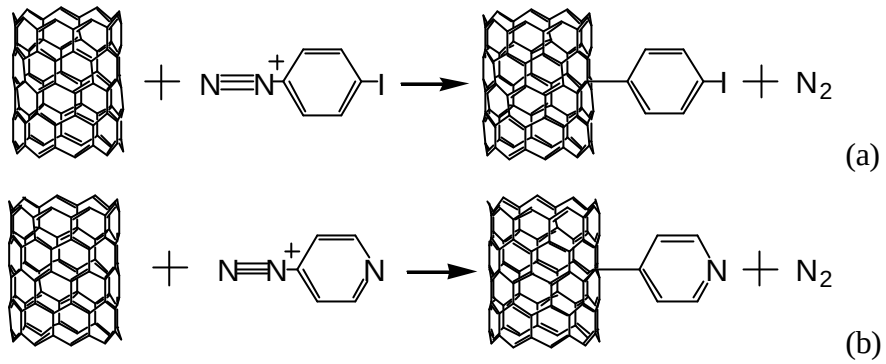

Figure 3-9 Scheme I: radical addition on SWCNTs with (a) 4-iodobenzene diazonium and (b) 4-aminopyridine

According to the radical additions described in *Figures 3-9 (a)* and *(b)*, the functionalisations lead to:

4-iodobenzene-SWCNTs

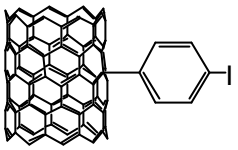

4-pyridine-SWCNTs

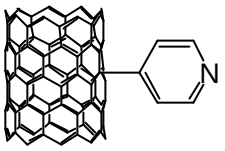

3.5.2 Sonogashira cross-coupling on iodobenzene-SWCNTs

Sonogashira coupling is a method widely used in the formation of conjugated materials[226]. Here, the necessity of bonding the nanotubes with groups where the electrons are delocalised, led to the choice of the Sonogashira coupling as a way to create the carbon-carbon bonds. Therefore, this requirement was achieved by the integration of alkyne groups within the molecular bridges. Thus, the Sonogashira coupling provided an intermediate material and this additional functionalisation step on the SWCNT allowed the creation of two different covalent molecular bridges from the same starting materials (IPhCNT). Indeed, both the homo-coupling and the cross-coupling used the SWCNT having undergone the Sonogashira coupling. Additional reactions can provide complexity, diversity and also change the nature of the molecular bridge however, the versatility of the Sonogashira was not explored here as the length of the bridges could negatively impact on the conduction across it. Thus, short molecular bridges were preferred in this work.

Through the Sonogashira coupling, carbon-carbon bonds are formed between sp and

sp^2 carbon where usually, the sp^2 carbon is part of a phenyl ring. This coupling occurs in the presence of transition metal catalysts (in this instance, $Pd(P(Ph)_3Cl)_2$ and CuI) used to activate the aryl and the acetylene. *Figure 3-10* displays the scheme of the Sonogashira cross-coupling performed here.

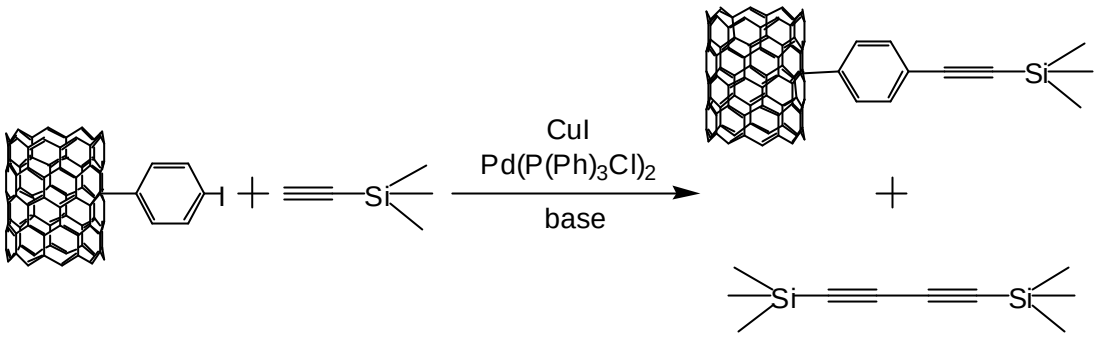

Figure 3-10 Scheme II: Sonogashira coupling performed on iodobenzene-SWCNTs

Figure 3-10 shows the scheme of the Sonogashira coupling where iodobenzene-SWCNTs are coupled to trimethylsilyl acetylene (TMSA). 1-(trimethylsilyl)-2-phenylacetylene is the functional group obtained on the SWCNTs as the result of the Sonogashira coupling. The homo-coupling of the acetylene group obtained as a by-product is eliminated during the washing step following the reaction. 1-(trimethylsilyl)-2-phenylacetylene-SWCNTs will be referred to as Sonogashira-SWCNTs in the following sections.

The SWCNT precursors were characterised by Raman and UV-visible-near IR spectroscopies, thermogravimetry coupled with mass spectrometry and elemental analyses. This set of characterisations allows the verification of the presence of the iodobenzene, pyridine and 1-(trimethylsilyl)-2-phenylacetylene groups covalently bonded on the SWCNT surfaces. The Sonogashira coupling was carried out on the aryl groups previously grafted on the surface of the nanotubes. Vibrational spectroscopy used to confirm a reaction on the SWCNTs through a change in their electronic structure, are not relevant in this case. The Sonogashira coupling is carried out on functional groups and therefore does not affect the electronic structure of the SWCNT. The characterisation methods used here to ascertain the occurring of the Sonogashira coupling are therefore based on the presence of the silicon element added in as part of the trimethylsalyl reactant.

3.5.3 Spectroscopy

Covalent functional groups on SWCNT surfaces induce degradations of their crystalline and electronic structures[56]. Raman and UV-visible-near IR spectroscopies report such changes which indicate that the functionalisation occurred.

3.5.3.1 Raman

The Raman spectra of the iodobenzene-SWCNTs and pyridine-SWCNTs (*Figure 3-11*) were recorded using a 632.8 nm laser excitation. These spectra were compared to the Raman spectrum of purified then annealed SWCNT (*Figure 3-3*).

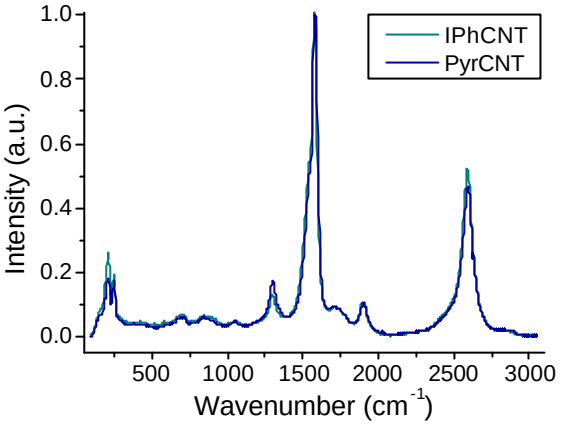

Figure 3-11 Raman spectrum of pyridine-SWCNTs (PyrCNT) and iodobenzene-SWCNTs (IPhCNT), normalised at 1581.31 cm^{-1}. The spectra are averages of spectra taken at 3 different places of the samples and include the baseline correction.

Figure 3-11 shows a modification of the spectrum profile after reaction as the G bands of both spectra become asymmetric. The peak identifying the contribution from the metallic SWCNT to the tangential bands attenuated compared to the Raman spectra in *Figure 3-3*. This reduction is explained by the metallic nanotubes which lose their metallic nature during reaction[75]. In addition, the I_D/I_G ratio increases from 5% (*Figure 3-3*) to 5.6% and 9.1% for iodobenzene-SWCNTs and pyridine-SWCNTs, respectively. The small increase in the I_D/I_G ratios for both reactions used to be considered as a sign of a low functionalisation level[214]. However, Raman spectra evolution of diazonium functionalised SWCNTs showed that after a maximum, the D band intensity decreases when more functional groups are added[75]. Raman spectra of the iodobenzene and pyridine-SWCNTs confirmed that the reaction occurred. Unfortunately, the functionalisation level could not be estimated

from these data. The Raman spectrum of Sonogashira-SWCNTs was not recorded as the coupling was carried out on the iodobenzene functional groups.

3.5.2.2 UV-visible-near IR

The absorption spectra of oversaturated dispersion of functionalised SWCNTs in DMF (1:10 mg/ml) were recorded by UV-visible-near IR spectroscopy from 300 to 1800 nm. These spectra are presented in *Figure 3-12*.

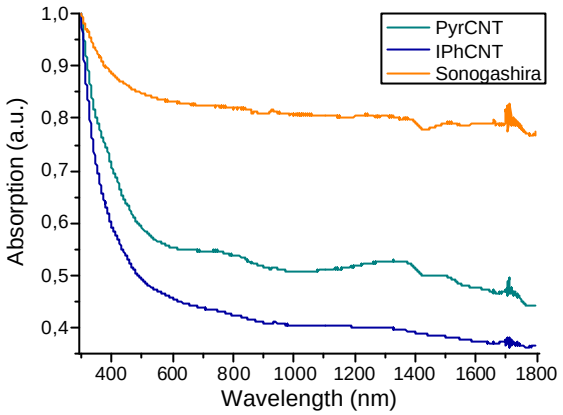

Figure 3-12 Absorption spectra of saturated dispersions of pyridine-SWCNTs (PyrCNT), iodobenzene-SWCNTs (IPhCNT) and Sonogashira-SWCNTs (Sonogashira) in DMF normalised at 300 nm.

Figure 3-12 shows the absorption spectra of pyridine-SWCNT, iodobenzene-SWCNT and Sonogashira-SWCNT dispersions where there is a total absence of VHS. Diazonium reactions are known to lead to the disappearance of the VHS for high functionalisation levels[227]. Indeed, covalent bonding introduces defects in the nanotubes' structure as the functional groups disrupt the conjugated structure. Consequently, the electrons of the π system are more localised. This causes the VHS to diminish[72]. Thus, high degrees of covalent functionalisation lead to the disappearance of those VHS. The absence of VHS signifies that the electronic structure of the nanotubes was disturbed after reaction[72]. Thus, the absorption spectra confirmed the presence of covalent groups on pyridine-SWCNTs and iodobenzene-SWCNTs.

The empirical Beer-Lambert law given by *equation 3-1* was used to calculate the concentration of iodobenzene-SWCNTs and pyridine-SWCNTs in the saturated dispersions. The molar adsorptivities for the pyridine and iodobenzene

functionalised SWCNTs were assumed to be the same: 25.5 $(mg/L)^{-1}$ cm^{-1} at 500 nm[153]. The concentrations of oversaturated dispersions are displayed in *Table 3-3*.

Sample	Pyridine-SWCNT	Iodobenzene-SWCNT	Sonogashira-SWCNT
Concentration (mg/L)	6	6.2	4.7

Table 3-3 Concentrations of oversaturated dispersions of SWCNT precursors at 500 nm

The absorption spectra confirmed the presence of covalent bondings after radical additions on the SWCNTs. The absence of VHS in absorption spectra indicates high degrees of covalent functionalisation. In diazonium reactions, the Raman's D band is known to decrease after reaching a maximum[75]. Then, the absorption spectra suggest that the number of groups added is higher than the number corresponding to the maximum D band value.

Pyridine-SWCNT and iodobenzene-SWCNT precursors showed similar solubility. This was expected as the radical additions were performed in similar conditions. The Sonogashira coupling was performed on iodobenzene-SWCNTs whose electronic structure was already modified after the diazonium reaction. In this case, it is the diminution of the solubility of the material after Sonogashira coupling which indicated a change in the material.

The spectroscopy analyses attest of the covalent bonding of the SWCNTs without identifying the grafted groups or estimating the functionalisation degree. Each functional group contains elements (N, I or Si) which can be detected by elemental analysis (XPS) to ensure that the correct groups are grafted on the SWCNTs.

3.5.4 Elemental analysis of SWCNT precursors

3.5.4.1 CHN analysis of pyridine-SWCNTs

Carbon hydrogen nitrogen (CHN) analyses were carried out on pyridine-SWCNTs to provide quantitative data of their nitrogen concentration. The N amount in the bulk of the material was quantified to about 2.0 at%. 0.3 at% of N was obtained for the purified

then annealed SWCNTs. Thus, 1.7 at% of pyridine groups was estimated to be present in pyridine-SWCNTs. This small functionalisation level contradicts the results of the UV-visible-near IR spectroscopy while corroborating those of Raman spectroscopy.

3.5.4.2 X-ray photoelectron spectroscopy

XPS analyses were carried out on the SWCNT precursors to bring further confirmation of the presence of functional groups. These analyses allow us to ascertain and quantify the presence and relative concentration of elements. The samples were dispersed in isopropanol and drop dried onto an iron substrate. The analysis was performed under vacuum (10^{-8} mbar). Prior to the XPS analysis, the samples were etched by an Ar^{+} ion bombardment for about 30 seconds at 3 kV to remove sample surface contamination. The binding energies and concentrations obtained from the XPS spectra of the precursors will be used as reference in the following *Chapters 4* and *5*.

Figure 3-13 displays the XPS spectra of C, N, I and Si in pyridine-SWCNTs, iodobenzene-SWCNTs and Sonogashira-SWCNTs (when available).

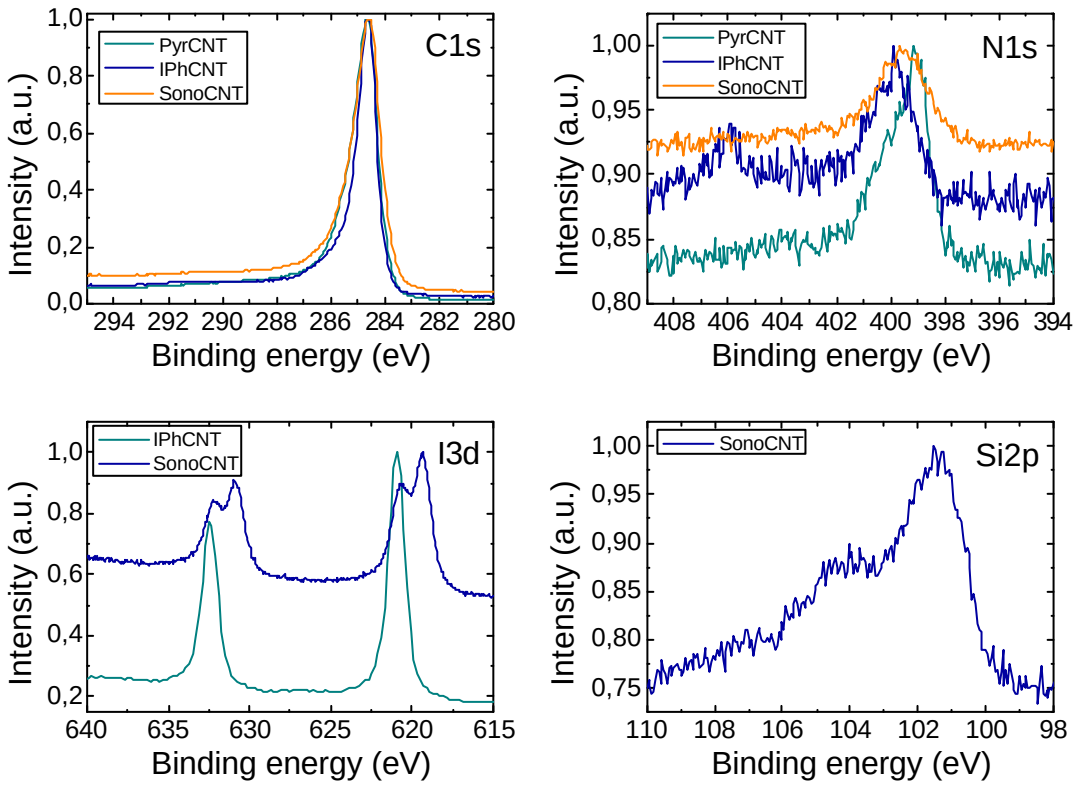

Figure 3-13 C1s, N1s, I3d and Si2p XPS spectra in pyridine-SWCNTs, iodobenzene-SWCNTs and Sonogashira-SWCNTs

Figure 3-13 shows that the C1s spectrum is wider in the pyridine-SWCNTs compared to the iodobenzene-SWCNTs. The Sonogashira coupling appears to broaden the C1s spectrum. The presence of a band at 406 eV in the N1s spectrum of iodobenzene-SWCNTs is attributed to N-O bonds[228] from the isopentyl nitrite catalyst. The N1s spectrum of the pyridine-SWCNTs is further analysed below. After Sonogashira coupling, the I3d spectrum is composed of two components. This indicates the presence of iodine under two forms. The Si2p spectrum displays two 'shoulders' in the high energy range.

The concentrations and the binding energies of the elements in pyridine-SWCNTs, iodobenzene-SWCNTs[xiii] and Sonogashira-SWCNTs are given in *Table 3-4*.

Elements	pyridine-SWCNTs		iodobenzene-SWCNTs		Sonogashira-SWCNTs	
	BE (eV)	Conc (at%)	BE (eV)	Conc (at%)	BE (eV)	Conc (at%)
C1s	284.7	94.7	284.6	89.9	284.6	82.1
O1s	532.3	3.4	533.4	6.1	532.6	9
N1s	399.2	1.9	399.9	1.5[xiv]	399.7	1.2
I3d5/2	-	-	620.2	2.5	619.4	1.2
Si2p	-	-	-	-	101.6	2.8
Cl2p	-	-	-	-	200.7	1.3
Cu2p1/2	-	-	-	-	952.1	0.8
Pd3d5/2	-	-	-	-	335.9	1.7

Table 3-4 Binding energies and concentrations of the elements in pyridine-SWCNTs, iodobenzene-SWCNTs and Sonogashira-SWCNTs

Table 3-4 shows a slightly smaller concentration is obtained from the XPS analysis compared to the CHN analysis on pyridine-SWCNTs. The difference is explained by the Ar^+ etching step which removed nitrogen contamination adsorbed on the nanotubes. It is expected that the CHN analyses results take into account nitrogen contaminant. In iodobenzene-SWCNTs, the iodine concentration is considered as completely from the iodobenzene group. Iodobenzene-SWCNTs were not etched prior to analysis. Higher concentrations of O and N were expected due to contamination from the atmosphere adsorbed on the nanotubes. According to scheme II (*Figure 3-10*), the iodine should have been eliminated after coupling. The

[xiii] This sample had not undergone an Ar ion etching.
[xiv] This sample had not undergone an Ar ion etching.

presence of I and Si in the Sonogashira-SWCNTs suggests that the coupling occurred but was not completed.

The XPS spectra of C, N and I and Si are further analysed to identify their chemical environments in pyridine-SWCNTs and iodobenzene-SWCNTs and Sonogashira-SWCNTs, respectively. The details of this study are now discussed and will later be used as a reference for the analysis in *Chapters 4* and *5*. CasaXPS was used to fit these XPS spectra. *Figure 3-14* displays the C1s XPS spectrum of pyridine-SWCNTs and iodobenzene-SWCNTs.

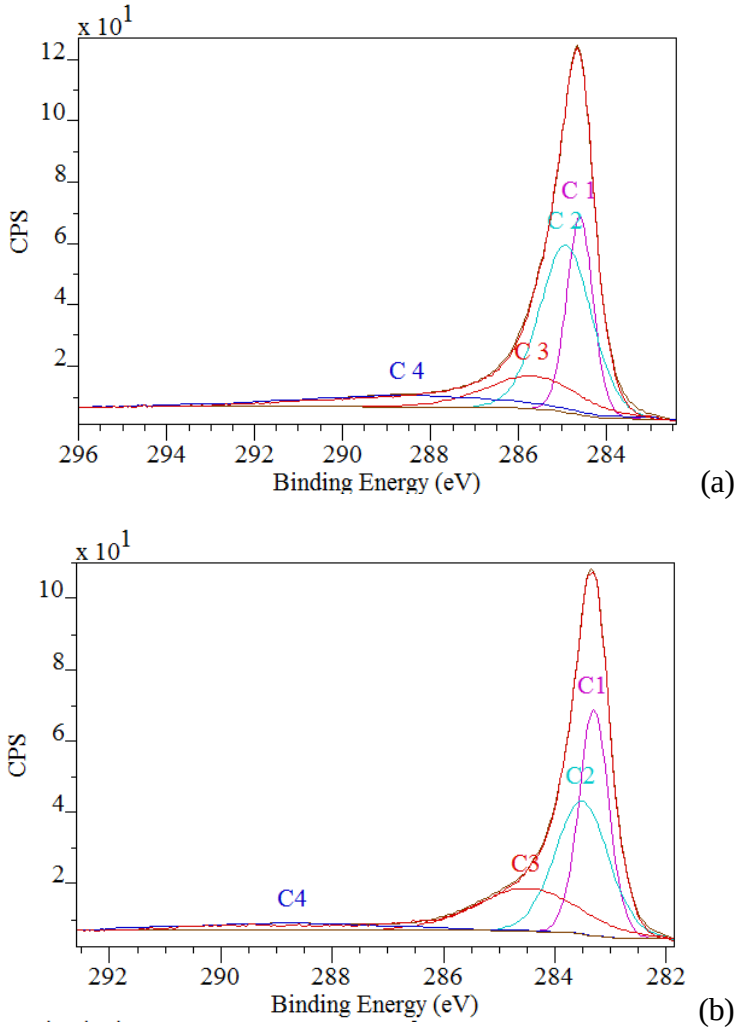

Figure 3-14 XPS spectrum of C1s located at 284.6 eV in (a) pyridine-SWCNT with its contributions from C1 for C=C, C2 for C-C, C3 for C=O or C-OH and C4 for O-C=O positioned at 284.59, 284.92, 285.68 and 288.2 eV, respectively (b) iodobenzene-SWCNTs positioned at 284,6 eV with its 4 contributions C1, C2, C3 and C4 positioned at 284.6, 284.8, 285.6 and 289.6 eV, respectively

Similarly to the study of the purified and annealed SWCNTs in *section 3.4.1.3*, good fits were reached when the C1s spectra in *Figure 3-14* were decomposed with 4 contributions C1, C2, C3 and C4. The fitting parameters of the bands contributing to the C1s peak are given in *Table 3-5*.

Sample	Component	Area	BE (eV)	Conc (at%)	FWHM (eV)	Groups[215]
Pyridine-SWCNTs	C1	49.2	284.6	26.9	0.7	SWCNT
	C2	82.8	284.9	45.2	1.4	
	C3	28.7	285.7	15.7	2.5	C=O or C-OH
	C4	22.5	288.2	12.3	5.8	O-C=O
Iodobenzene-SWCNTs	C1	43.2	284.6	34.4	0.6	SWCNT
	C2	45.5	284.8	36.2	1.1	
	C3	28.2	285.7	22.5	2.2	C=O or C-OH
	C4	8.7	289.6	6.9	4.5	O-C=O

Table 3-5 Main fitting parameters for the contributions in the C1s in pyridine-SWCNTs and iodobenzene-SWCNTs

Figure 3-14 and *Table 3-5* were compared with *Figure 3-6* and *Table 3-3*, respectively. This shows that the profile of the C1s XPS spectrum did not change after functionalisation except for the C4 contribution whose binding energy shifted from 289.7 to 288.2 eV in pyridine-SWCNTs. The possibility for diazonium based radical additions to occur on carboxylic acid groups on SWCNT surface was reported[221]. This reaction pathway further reduces the amount of COOH groups. Thus, shifting of the C4 component is likely to be the result from the diminution of COOH groups. The tail at high binding energy of the C1s spectra is also indicative of the π system in SWCNTs[69].

The N1s XPS spectrum was analysed for the pyridine-SWCNTs as N in both iodobenzene-SWCNTs and Sonogashira-SWCNTs are not related to the functional groups. *Figure 3-15* shows the N1s XPS spectrum in the pyridine-SWCNTs.

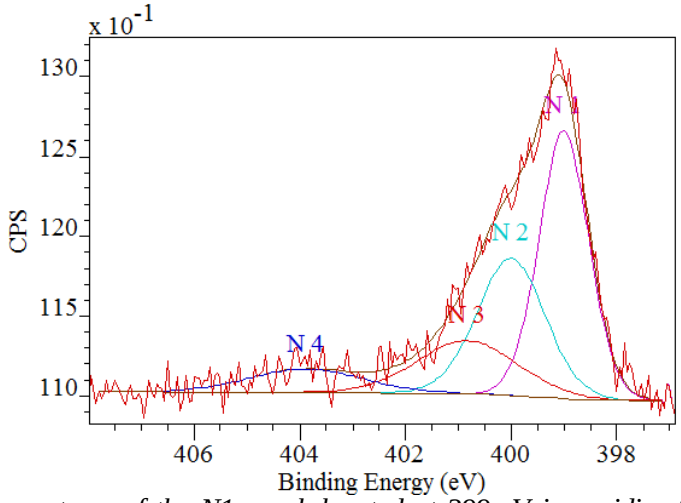

Figure 3-15 XPS spectrum of the N1s peak located at 399 eV in pyridine-SWCNT with its 4 contributions positioned at 399, 400, 400.8 and 403.88 eV for N1, N2, N3 and N4, respectively.

Figure 3-15 shows that a good fit of the N1s XPS peak (at 399 eV) was obtained when decomposed with 4 contributions. The N1s XPS spectrum was not recorded for purified then annealed SWCNTs. So the impact of the radical addition on the N1s peak is not known. However, the fitting of the N1s peak leads to distinct realistic components according to the TGA-MS analysis (see *section 3.5.3*). The main fitting parameters of the contributions obtained from the decomposition of the N1s peak are given in *Table 3-6*.

Component	Area	BE (eV)	FWHM (eV)	Conc. (at%)	Chemical environment
N1	2.0	399	1.1	43.5	Pyridine[229]
N3	0.8	400.8	2.2	17.4	Pyridinium[229]
N2	1.4	400.0	1.5	30.4	Nitrosopyridine [230]
N4	0.4	403.9	2.5	8.7	Adsorbed N_2 [231]

Table 3-6 Main fitting parameters for the contributions in N1s in pyridine-SWCNTs

Table 3-4 showed that the concentration of N was 1.9 at%. According to *Table 3-6*, the relative concentration of N from pyridine groups is 0.8%. XPS analysis of pyridine-SWCNTs indicates that the functionalisation created additional groups (pyridinium and nitrosopyridine) on the SWCNTs which affected the yield of the reaction. The study of the N1s spectrum supports the results obtained with the Raman spectroscopy showing a very small functionalisation level of pyridine-SWCNTs. *Figure 3-16* shows the I3d5/2 spectra of iodobenzene-SWCNTs and Sonogashira-SWCNTs.

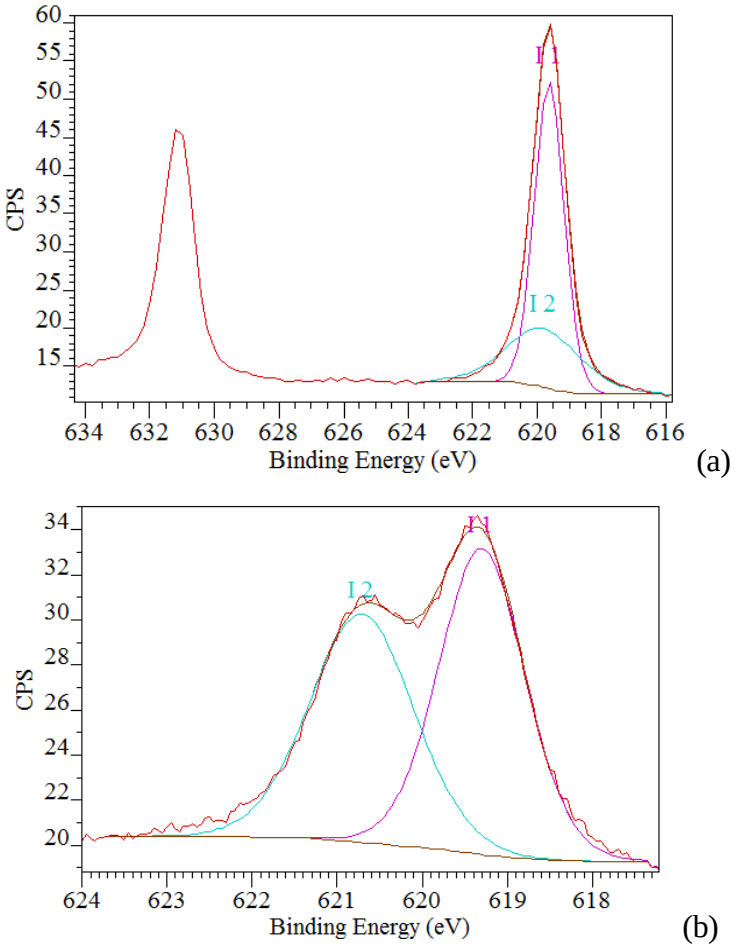

Figure 3-16 XPS spectra of I3d5/2 with 2 contributions I1 and I2 for (a) iodobenzene-SWCNTs and (b) Sonogashira-SWCNTs

Figure 3-16 (a) shows that good fits of the I3d5/2 spectra of iodobenzene-SWCNTs and Sonogashira-SWCNTs were obtained using 2 contributions I1 and I2. Although two components were required in both cases, *Figure 3-16 (b)* shows that the I3d5/2 spectrum in Sonogashira-SWCNTs differs by showing two peaks where only one peak is observed in iodobenzene-SWCNTs (*Figure 3-16 (a)*). The main parameters of the contributions are given in *Table 3-7*.

Contributions		Area	BE (eV)	FWHM (eV)	Conc. (at%)	Groups
Iodobenzene-SWCNTs	I1	46.6	620.2	1.1	67.6	I-C[232]
	I2	22.4	620.4	2.7	32.4	
Sonogashira-SWCNTs	I1	18.4	619.3	1.2	54.3	I[-233]
	I2	15.5	620.7	1.4	45.7	I-C [232]

Table 3-7 Main parameters for the contributions in I3d5/2 of iodobenzene-SWCNTs and Sonogashira-SWCNTs

In *Figure 3-16 (a)*, the difference in the binding energies of I1 and I2 corresponds to the spectrometer resolution. As for the C1 and C2 contributions of the C1s spectrum, so it is the same iodine environment which is probed. The need of another contribution appears as the result of the broadening of I3d5/2 base probably due to the background noise.

In *Figure 3-16 (b)*, the analysis revealed another iodine compound. This second contribution (I1) was attributed to iodide from $[Et_2NH_2]^+ I^-$[233]. I2 was attributed to the contribution of the iodine from the non reacted iodobenzene group according to *Figure 3-16 (a)* [232]. The iodine salt results from the reaction of I from iodobenzene groups and the base solvent during the Sonogashira coupling. The I⁻ salt formed with the base solvent supports the occurring of the Sonogashira coupling according to the catalytic cycle of this reaction[226]. From *Tables 3-4* and *3-7*, 0.6 at% of I from iodobenzene moieties was found in Sonogashira-SWCNTs.

Figure 3-17 displays the Si2p XPS spectrum of Sonogashira-SWCNTs. The ratio $\frac{Area_{Si2p\ 1/2}}{Area_{Si2p\ 3/2}}$ for each contribution was restricted to 0.5 for both contributions according to Si2p fitting method[234].

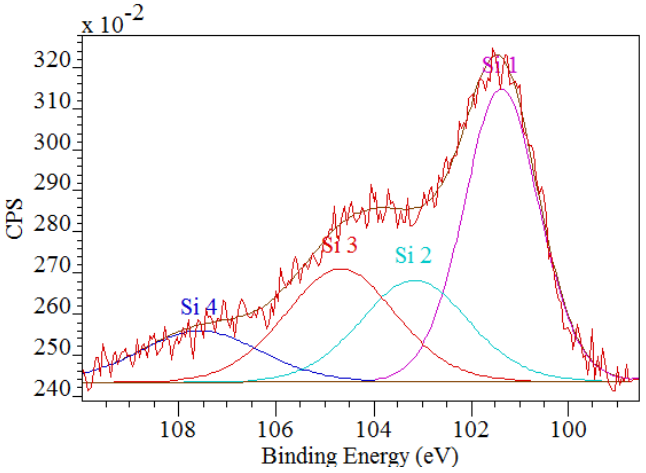

Figure 3-17 XPS spectrum of Si2p with its four components Si1, Si2, Si3 and Si4

Figure 3-17 shows a good fit of the Si2p spectrum using 4 components. The Si2p spectrum is composed of two contributions: Si1 whose Si2p3/2 peak is located at 101.4 eV and Si2 whose Si2p3/2 peak is located at 104.7 eV. Using their binding energies, the Si1 component is identified as the silicon from 1-(trimethylsilyl)-2-phenylacetylene[235]. The Si2 component corresponds to Si-O bonds[235] identified as Si from Si grease contamination used to seal glass vessels used during the reaction. The

presence of Si contaminant explains why in *Table 3-4* the relative concentration of Si is higher than the relative concentration of I. The main parameters of the contributions obtained from the decomposition of Si2p are given in *Table 3-8*.

Contributions	Area	BE (eV)	FWHM (eV)	Conc (at%)	Bonds
Si1 *(Si1 3/2)*	1.4	101.4	1.8	32.2	Si-C [235]
Si2 *(Si1 1/2)*	0.7	103.1	2.6	32	
Si3 *(Si2 3/2)*	0.8	104.7	2.7	18.7	SiO_2 [235]
Si4 *(Si2 1/2)*	0.4	107.6	2.9	17.2	

Table 3-8 Main parameters for the two contributions in Si2p of Sonogashira-SWCNTs

Based on the XPS analysis (*Table 3-4* and *3-8*), the concentration of silicon from 1-(trimethylsilyl)-2-phenylacetylene was estimated to be 1.8at%. XPS analyses report the change in the I3d spectrum profile and the presence of Si from 1-(trimethylsilyl)-2-phenylacetylene. Both absorption spectra and XPS analysis display changes in the SWCNTs after Sonogashira coupling. The decrease in I concentration suggests that the coupling was incomplete (*Table 3-4*). The presence of I^- salts indicates that the Sonogashira coupling occurred.

The XPS analyses indicate low functionalisation levels for all SWCNTs precursors. This confirms the results of Raman spectroscopy and TGA-MS analyses. The small differences observed between C1s spectra before (*section 3.4.1.3*) and after (*section 3.5.4.1*) functionalisation show that the C1s spectrum was not affected by the radical additions. This reflects the small amount of groups grafted on the nanotubes. The N1s, I3d and Si2p spectra will be used as reference for the XPS analysis after further reactions in *Chapters 4* and *5*.

3.5.5 Thermogravimetric analysis

TGA-MS analyses rely on the detection of the mass and/or a meaningful fraction of the mass of the functional groups. As the functionalized SWCNTs are heated in a helium atmosphere, molecular bonds break to release molecules or fragments of molecules. Their masses are detected by a mass spectrometer concurrently. The TGA-MS graphs of the iodobenzene-SWCNTs, pyridine-SWCNTs and Sonogashira-SWCNTs are displayed in *Figure 3-18*. The masses indicating that the reactions

occurred would be the total or a meaningful fraction of masses containing the benzene ring and the trimethylsalyl acetylene.

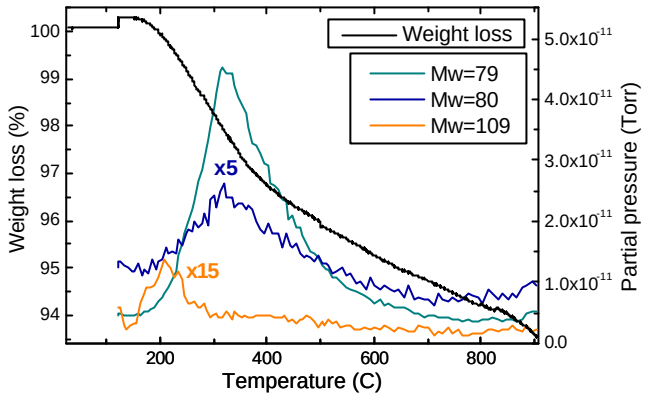

(a)

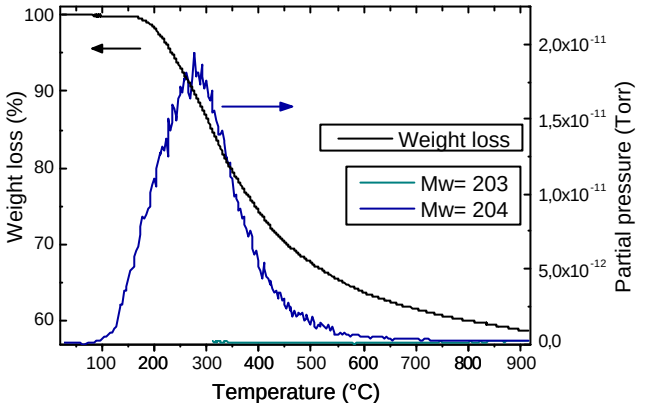

(b)

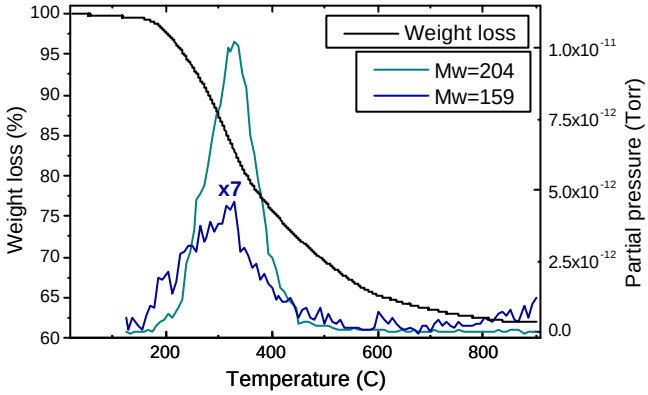

(c)

Figure 3-18 TGA-MS spectra for (a) pyridine-SWCNTs via a radical addition using HCl and NaNO2 with masses of 79, 80 and 109 (b) iodobenzene-SWCNTs with masses of 203 and 204 (c) Sonogashira-SWCNTs with masses of 159 and 204

Figure 3-18 shows that the mass of pyridine, iodobenzene and 1-(dimethylsilyl)-2-phenylacetylene attached were detected during the analysis. The mass of 1-(dimethylsilyl)-2-phenylacetylene results from the coupling of a benzene ring with a trimethylsalyl acetylene. The TGA-MS analyses carried out on pyridine-SWCNTs also revealed the presence of pyridinium and nitrosopyridine groups grafted on the SWCNTs. The presence of such groups is inherent to the diazotization procedure used here (see

Chapter 6). At 600°C, the remaining weights were 95%, 64% and 65% for pyridine-SWCNTs, iodobenzene-SWCNTs and Sonogashira-SWCNTs, respectively. The functional groups in pyridine-SWCNTs have a smaller molecular weight than the iodobenzene group so it is expected that the weight loss will be smaller in pyridine-SWCNTs. This is particularly true as the XPS analysis showed that the functionalisation level was higher for iodobenzene-SWCNTs (2.5at% of I) than for pyridine-SWCNTs (1.9at% of N). The higher weight percentage left for Sonogashira-SWCNTs compared to iodobenzene-SWCNTs was also expected. Indeed, the total weight of functional groups decreased as the iodobenzene groups are transformed into much the lighter 1-(dimethylsilyl)-2-phenylacetylene groups during the Sonogashira coupling.

Table 3-9 shows that the functional groups released by the SWCNT precursors are released in a temperature range of 208-331°C.

Precursor	Masses[xv] (g/mol)	Molecular groups	Weight loss at 600°C (%wt)	Released temperature (°C)
Pyridine-SWCNT	79		-	318
	80	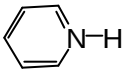	-	318
	109	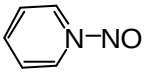	-	208
Iodobenzene-SWCNTs	204	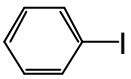	30	277
Sonogashira-SWCNT			7	
Sonogashira-SWCNT	159	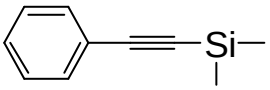	21	331

Table 3-9 Molecular groups detected during the heating of SWCNT precursors

The TGA-MS analyses confirmed the presence of pyridine, iodobenzene and 1-(trimethylsilyl)-2-phenylacetylene grafted on the SWCNTs. Using the concentrations from the XPS analyses, the TGA-MS also provides an estimation of the degree of functionalisation for the SWCNT precursors (*Table 3-9*). For instance,

[xv] Those masses are 1 g/mol higher for all the molecules compared to the usual molecular masses. It is suspected that during the course of the TGA-MS analysis on pyridine-SWCNTs and iodobenzene-SWCNTs, a hydrogen atom is added on the groups.

proportions of I (0.6 at%) and Si (1.8 at%) determined from the XPS analysis were used here to estimate the weight percent corresponding to the functional groups in Sonogashira-SWCNTs. The weight loss in pyridine-SWCNTs (4.7 %wt in *Figure 3-18 (a)*) was not considered as it is abnormally lower than the weight loss in purified then annealed SWCNTs (6.4 %wt in *Figure 3-7 (b)*). This anomaly can be explained by the non homogeneity of the extracts of SWCNTs used in the analysis.

An atomic percentage of 2.5 at% of iodobenzene groups grafted on iodobenzene-SWCNTs was calculated from the TGA-MS data. This agrees with the 2.5 at% relative atomic concentration of iodine obtained from the XPS analysis. In Sonogashira-SWCNTs, atomic percentages of 2.1 at% and 0.4 at% were found for 1-(trimethylsilyl)-2-phenylacetylene and iodobenzene moieties, respectively. These results differ from the relative atomic concentrations obtained from the XPS analyses: 0.3 at% and 0.1 at% for 1-(trimethylsilyl)-2-phenylacetylene and iodobenzene moieties, respectively. Considering that the $[Et_2NH_2]^+ I^-$ adsorbed on the Sonogashira-SWCNTs also contributed to the weight loss, these results are pretty close to the atomic concentrations of I (0.6 at% of I from iodobenzene) and Si (1.8 at% of Si from 1-(trimethylsilyl)-2-phenylacetylene) found from the XPS analysis.

Both XPS and absorption analysis reported changes after Sonogashira cross-coupling on the iodobenzene-SWCNTs. The XPS analysis also confirmed the presence of silicon from TMSA in the sample and the occurring of the coupling via the presence of I^- salt. More conclusive, the TGA-MS analysis showed that the 1-(trimethylsilyl)-2-phenylacetylene groups were grafted on the SWCNTs. This set of data indicates that the Sonogashira coupling was successful. The XPS measurements carried out on purified then annealed SWCNTs revealed 2.2 at% of O without Ar^+ ion etching and 3.4 at% in pyridine-SWCNTs. This shows the presence of additional O in the pyridine-SWCNTs. TGA-MS analysis indicates the presence of nitrosopyridinium grafted on the SWCNTs after the radical addition. Then, the presence of O in the pyridine-SWCNT is attributed to both the carboxylic acid and nitrosopyridinium groups. The chemical environments from the contributions in N1s and I3d5/2 are also concordant with the molecular groups identified by TGA-MS analyses.

3.6 Electrical characterisation of SWCNT precursor networks

In this section, electrical properties of the SWCNT precursor networks were studied to determine their dominant transport mechanism. To this end, networks of SWCNT precursors were prepared by vacuum filtration. Networks with different thicknesses were filtered onto nylon membranes as the volumes of SWCNT precursor dispersions increased from 2 to 20 ml. The roughness and softness of the nylon membrane substrate did not allow finding of the network's thickness by AFM and profilometry, respectively. Ellipsometry could also not be used as the membranes are not reflective. Therefore, SWCNT networks were distinguished by the volume of SWCNT dispersion filtered rather than their thickness. Thereby, the volume of SWCNTs filtered provides a confident parameter used here and in the subsequent chapters. Networks' thicknesses determined by scanning electron microscopy are available in *Appendix E.* However, given the difficulty to distinguish the SWCNT networks from the nylon membranes, these data are displayed for information.

In-plane I-V and I-T measurements of the SWCNT precursor networks were carried out to identify the dominant electrical conduction across these networks. The conduction mechanism found will be used as the reference conduction for molecular bridged and Pt bridged SWCNT networks.

Iodobenzene-SWCNTs and pyridine-SWCNTs were functionalised by diazonium radical additions. Reports showing a preferential attack of diazonium ions on semiconducting[219] or metallic[75] nanotubes are both available. The radical additions of iodobenzene groups were carried out with vast excess of diazonium salts and long reaction time. Thus, it is assumed that both SWCNT types will have reacted regardless of any preferential attack. The Sonogashira cross-coupling being carried out on the iodobenzene groups will therefore not interfere with the type of SWCNTs.

3.6.1 Current-voltage characteristics of SWCNT precursors

The resistivity of SWCNT networks was shown to be dependent on the electrode separation. It decreases as the device width increases and saturates from 20 μm[236]. Thus, Ti/Au top electrodes were deposited by electron beam evaporation using a

shadow mask with 50 µm electrode separation. Networks of SWCNT precursors were fabricated using 2, 5, 10 and 20 ml of SWCNT dispersions in DMF (1:10 mg/ml). These dispersions were filtered on a nylon membrane with a pore size of 0.2 µm using a filtration device of 25 mm diameter. *Figure 3-19* displays the I-V characteristics of the SWCNT precursor networks from -10 to 10 V at room temperature with electrode separation of 50 µm.

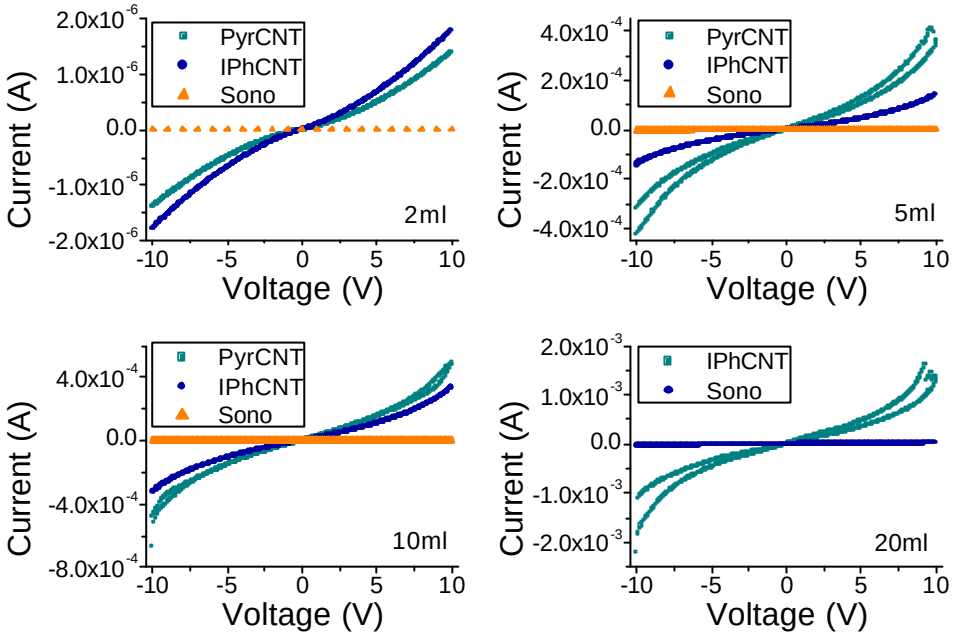

Figure 3-19 I-V measurements of 2, 5, 10 and 20 ml SWCNT precursor networks pyridine-SWCNTs (PyrCNT), iodobenzene-SWCNTs (IPhCNT) and Sonogashira-SWCNTs (Sono)

Metallic SWCNTs were shown to become non-metallic following radical additions[75]. Thus, it is expected that metallic SWCNT percolation cannot be formed. Therefore, SWCNT precursor networks retain semiconducting properties even for networks with high loading of SWCNTs. This is supported by the non linear current-voltage characteristics displayed in *Figure 3-19*. All the networks exhibit non linear I-V characteristics, and the 20 ml iodobenzene-SWCNT network shows some charging effect between 2 and 10 V, while charging effect is observed for both 5 and 10 ml networks of the pyridine-SWCNTs. The apparent insulating behaviour of the I-V characteristics for Sonogashira-SWCNT networks is the result of the scale used. I-V plots for all Sonogashira-SWCNT networks are available in *Figure 3-22*.

3.6.2 Current-filtered volume plots of SWCNT precursors

Figure 3-19 shows that in general, the current is higher for larger volume of SWCNTs dispersions filtered. This is understood as the bigger the volume, the thicker the network. The current-filtered volume evolutions at 1, 5 and 10 V were fitted in *Figure 3-20* according to *equation 3-2*.

$$y = A \exp(x/x_0) + y_0 \qquad (3\text{-}2)$$

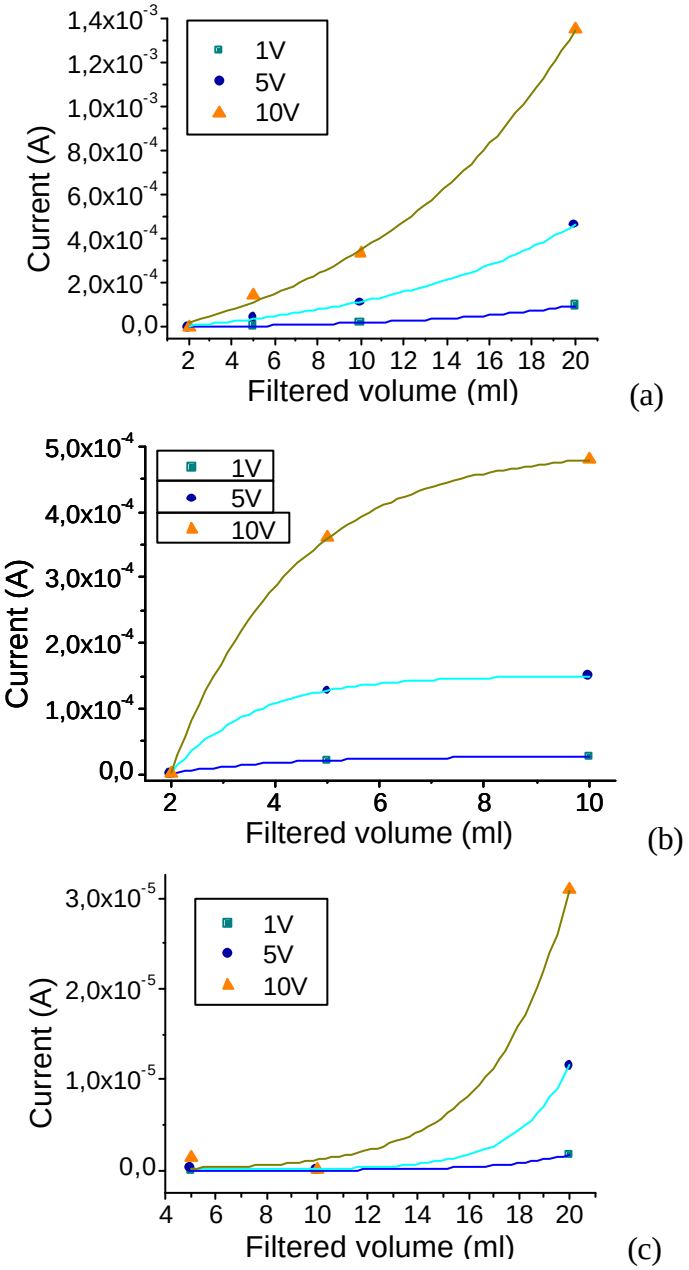

Figure 3-20 Current versus filtered volume plots at 1, 5 and 10 V for (a) iodobenzene-SWCNT networks (b) pyridine-SWCNT networks and (c) Sonogashira-SWCNT networks

Interestingly, the current versus filtered volume plots in *Figures 3-20 (a)* and *3-20 (c)* are drastically different than in *Figure 3-20 (b)*. While the current versus filtered volume characteristics of iodobenzene-SWCNT and Sonogashira-SWCNT networks showed exponential behaviours, pyridine-SWCNT networks display an asymptotic behaviour. The absorption spectra reported the higher solubility of pyridine-SWCNTs than iodobenzene-SWCNTs in DMF. Therefore, for the same dispersion volume, more pyridine-SWCNTs are deposited. A current saturation regime is almost reached for these networks deposited with such volumes of pyridine-SWCNTs. It is assumed that bigger dispersion volumes are required to reach this regime for iodobenzene-SWCNTs. Measurements performed on other regions of the 5 ml network resulted in insulating behaviour. This showed that Sonogashira-SWCNT network was not uniform for 5 ml of Sonogashira-SWCNT dispersion (1:10 mg/ml) filtered. Though it has a lesser current level, the Sonogashira-SWCNT network for 10 ml of filtered dispersion appeared more uniformed as no insulating areas were found. According to the postulate for the filtration process, the self modulation of the permeation rate assures the uniformity of the network[204]. It is suggested that for the 5 ml network, the low SWCNT concentration does not allow the thinner regions of the network compensating their delay during the filtration. For the 10 ml network, this compensation took place as the film is more uniform. But the amount of SWCNTs appears too small to increase the thickness.

3.6.3 Current-temperature characteristics of SWCNT precursors

Current-voltage characteristics of the networks were measured at different temperatures to examine the temperature dependence of the current. The voltage applied was limited to ±10 V over a range of temperature from 100 to 300 K to avoid any current breakdown of the network due to a high electric field. I-T characteristics of SWCNT precursor networks at 0.5, 1, 5 and 10 V are presented for 10 ml networks. Indeed, I-V plots for this thickness showed a minimal range for charging effect and data for all precursors are available. *Figure 3-21* displays the I-T characteristics from 100 to 350 K at 0.5, 1, 5 and 10 V of the SWCNT precursor networks for 10 ml of filtered dispersions for 50 µm of electrode separation.

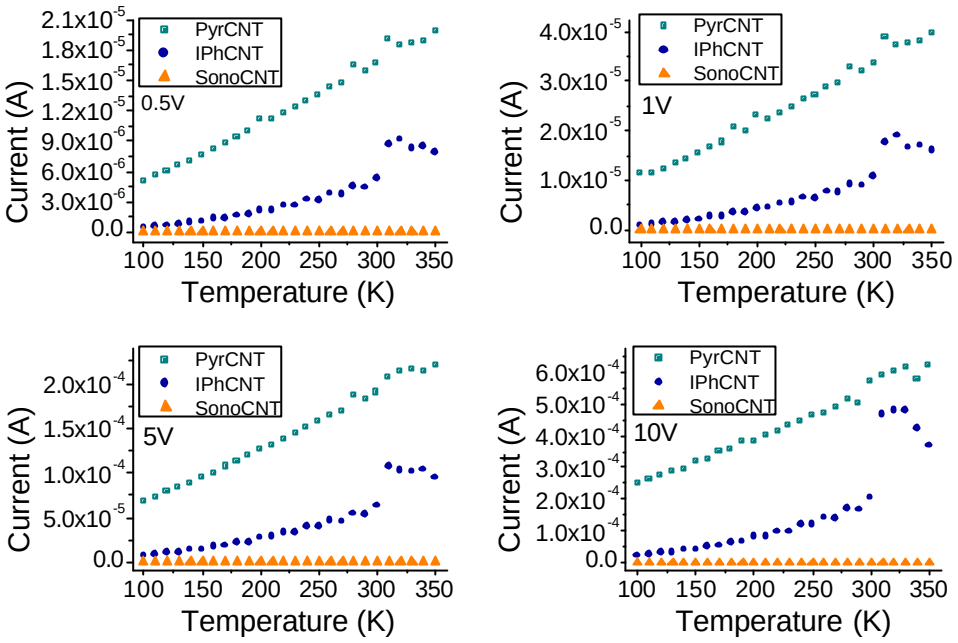

Figure 3-21 I-T characteristics at 0.5, 1, 5 and 10 V of SWCNT precursor networks filtrating 10 ml of SWCNT dispersions

The I-T plots displayed in *Figure 3-21* are from measurements carried out as the temperature is decreased from 300 to 100 K with a step of 20 K and is then increased from 100 K to 300 K with a step of 20 K. This explains the small gaps in the data points below 300 K but also shows that I-T plots follow the same trend after measurements at low temperatures. The electrical behaviour of Sonogashira-SWCNT networks is the result of the scale used in *Figure 3-21*. *Figure 3-23* displays the I-T characteristics for all Sonogashira-SWCNT networks. Note: The measurements in the temperature range 300-350 K were done before the sub 300 K measurements.

Figure 3-21 shows that the current increases with the temperature. Between 310 and 350 K, the I-T characteristics of iodobenzene-SWCNT network do not follow the same behaviour. This difference is still unexplained. However, in the 100-300 K range, the current intensities of the iodobenzene-SWCNT network decrease consistently as the temperature is reduced. Such behaviour confirms the I-V characteristics (*section 3.6.1*) showing that no metallic SWCNTs percolation was reached. This behaviour was also expected as temperature dependence studies in SWCNT networks showed an increase of resistance as the temperature decreases[119]. This increase in resistance was shown to be influence by the network thickness[109]. Here, though the I-T characteristics are comparable, the current increase between 100 and 300 K is equivalent (about one order of magnitude for 10 V) for all network

thicknesses. Thermally assisted tunnelling is expected to have a smaller impact on the intertube junctions[109]. The presence of a majority of SS junctions as the metallic nanotubes became non metallic (see *section 3.5.5*) can be the reason of this improved intertube junction, given that MM and SS junctions are known to have higher conductance levels than MS junctions[208].

3.7 Electrical investigations on Sonogashira-SWCNT networks

This section presents a detailed investigation of the electrical properties of Sonogashira-SWCNT networks to identify their dominant transport mechanism. The method presented here was also applied to the iodobenzene-SWCNT and pyridine-SWCNT networks. The detailed electrical characteristics and studies of conduction mechanisms across pyridine-SWCNT and iodobenzene-SWCNT networks are available in *Appendix B*. Sonogashira-SWCNT networks were selected for this case study as they undergone further reaction and their I-V and I-T characteristics shown in *Figures 3-19* and *3-21* displayed a much lesser current intensity.

3.7.1 Current-voltage characteristics

Networks of Sonogashira-SWCNTs were fabricated using dispersions of 2, 5, 10 and 20 ml of Sonogashira-SWCNTs in DMF (1:10 mg/ml). *Figure 3-22* displays the I-V characteristics of the 2, 5, 10 and 20 ml Sonogashira-SWCNT networks from -10 to 10 V at room temperature with electrode separation of 50 µm.

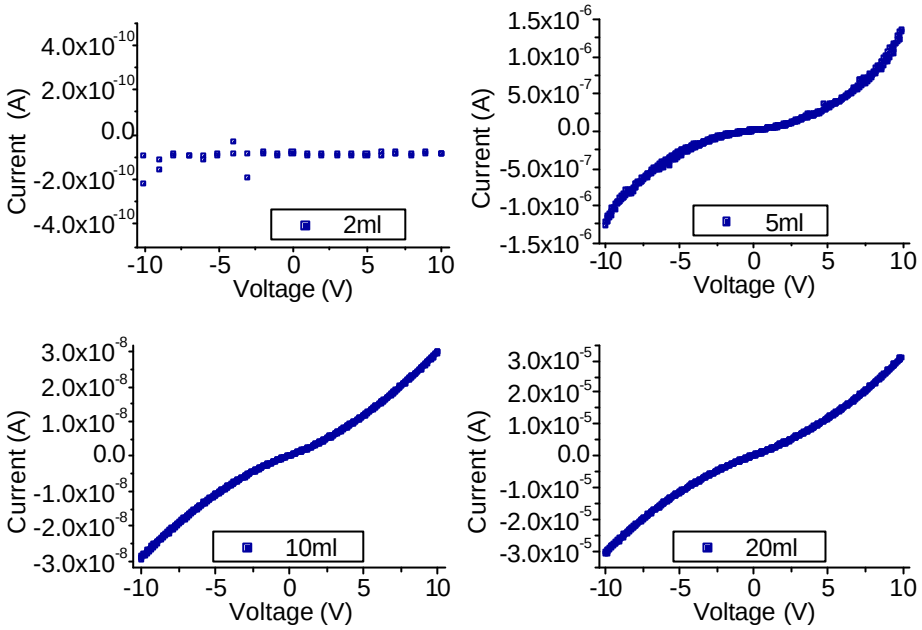

Figure 3-22 I-V characteristics at room temperature for Sonogashira-SWCNT networks with 2, 5, 10 and 20 ml of Sonogashira-SWCNT dispersion filtered

Metallic SWCNTs were shown to become non-metallic following radical additions[75]. Thus, it is expected that metallic SWCNT percolations cannot be formed even for networks with high loading of SWCNTs. This is supported by the non linear current-voltage characteristics displayed in *Figure 3-22*, particularly in the case of thicker networks. The insulating behaviour of the network made of 2 ml of Sonogashira-SWCNT dispersion (2 ml network) is attributed to the absence of percolation path resulting from the low SWCNT loading in the network. The 10 ml network displayed lower current intensity than the 10 ml network. This is unexpected as the larger the volume the more SWCNTs are deposited.

3.7.2 Current-temperature characteristics

Given the insulating nature of the 2 ml Sonogashira-SWCNT network, the I-T measurements were performed on 5, 10 and 20 ml networks. *Figure 3-23* displays the I-T characteristics of the 5, 10 and 20 ml Sonogashira-SWCNT networks from 100 to 350 K at 0.5, 1, 5 and 10 V.

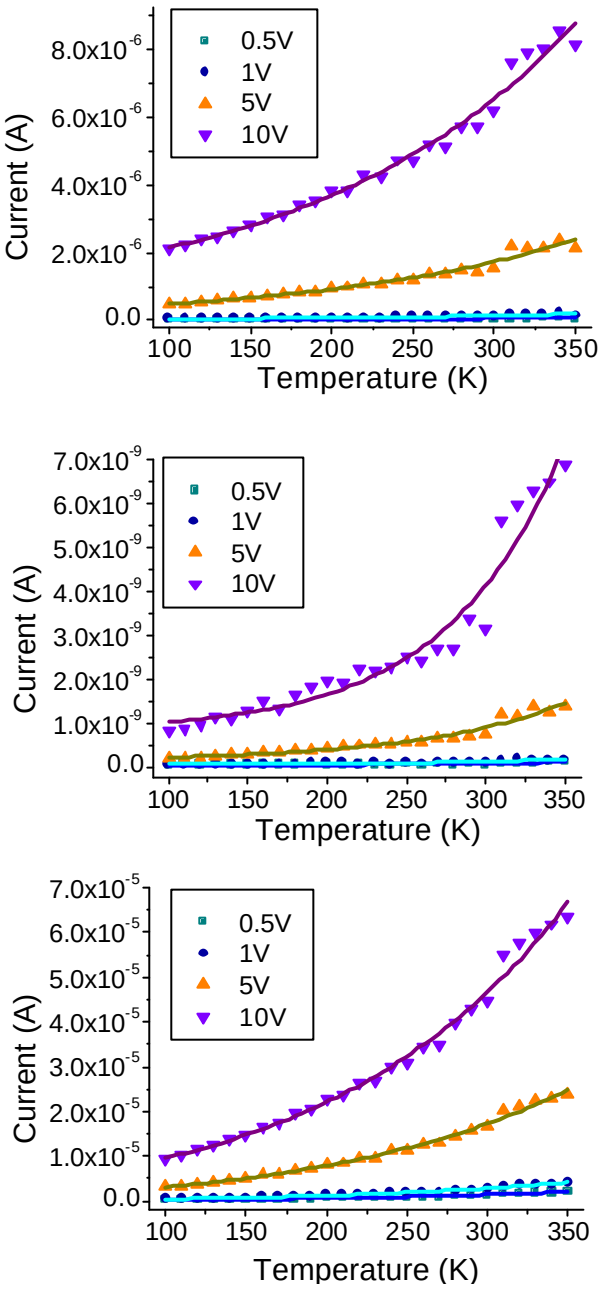

Figure 3-23 I-T characteristics from 100 to 350 K at 0.5, 1, 5 and 10 V for Sonogashira-SWCNT networks of (a) 5 ml, (b) 10 ml and (c) 20 ml of filtered dispersions

The fitting parameter x_0 for the I-T plots of 5, 10 and 20 ml Sonogashira-SWCNT networks is given in *Table 3-10*.

Voltage (V)	x_0 fitting parameter		
	5 ml	10 ml	20 ml
0.5	175	48±21	136±12
1	166	78±26	139±12
5	160	92±14	150±14
10	161	73±10	148±15

Table 3-10 Fitting parameter x_0 of the I-T characteristics for the Sonogashira-SWCNT networks

Figure 3-23 shows that current of the 5, 10 and 20 ml Sonogashira-SWCNT networks decreases as the temperature is reduced. The I-T characteristics displayed in *Figure 3-23 (a)* are the result of the measurement over one area given that other regions were insulating. To reach a uniform network with the filtration method, the amount of SWCNTs in the dispersion has to be sufficient so that it compensates regions of low SWCNT density[204]. The current level observed is explained by the fact that more material was deposited over this area while most of the regions were insulating. A sharp increase in the I-T characteristics is observed at high temperatures (300-350 K) for 0.5 and 1 V. *Figure 3-23 (b)* shows I-T plots which are inconsistent as the current intensity is less than for the 5 ml network. The current intensity in the network fabricated with 10 ml of dispersion was expected to be higher than in the 5 ml network. At 5 and 10 V, nano-amps current levels are obtained. This lower current order compared to the 5 ml Sonogashira-SWCNT network confirmed the non homogenous nature of the 5 ml network. The repartition of SWCNTs in this network is expected to be improved as the filtration technique self modulates its permeation rate[204]. Thus, in the 10 ml network, the coverage is improved but the conductivity does not increase as the additional SWCNTs are located in previously unfilled areas. *Figure 3-23* shows that distinct temperature profiles of the current are obtained depending on the sample thickness and in the case of the 5 and 10 ml network a difference is also observed between the high and low applied voltages. The high values of the x_0 fitting parameter (*Table 3-10*) show the small temperature dependence of the current.

3.7.3 Conduction models

Variable range hopping and tunnelling based conductions were found to be the transport mechanisms in various SWCNT networks as well as ropes and mats (see *Chapter 1 section 1.6*). The structure of the 2-dimensional Sonogashira-SWCNT networks corresponds to those of randomly oriented SWCNTs held together by van der Walls forces (see *section 3.3*). In this section, the analysis of the electrical characteristics is carried out to determine the dominant conduction mechanism across

Sonogashira-SWCNT networks. The method presented here will also be used for the electrical analyses of characteristics of other SWCNT networks.

3.7.3.1 Variable range hopping conduction

The VRH model introduced in *Chapter 2 section 2.6.2.2* is further described here. Hopping conduction takes place in insulating and semiconducting materials whose energy gap contains localized states. In disordered solids, the localised states occupy a large band of the energy gap. For conduction to occur, charges have to be transferred from one state to another. Such charge transfers require the assistance of phonons. For a final state with a higher (lower) energy than the initial state, a phonon has to be absorbed (emitted) by the charge in respect with the energy conservation law. In VRH, the need to minimise the distance and energy requires that the charges are transferred to states whose balance of both parameters is favourable[237]. The impact of the temperature on the mechanism (via the phonons) is expressed by:

$$G(T) = G_0 \exp\left[-(T_0/T)^p\right] \qquad (2\text{-}6)$$

Where G_0 and T_0 are constants with the temperature and p is related to the number of dimensions in which the hopping occurs[237]. Several current density expressions according to the electric field were reported. The conductivity of the VRH is described by *equation 3-3*.

$$s \propto \exp\left[-\left(\frac{\Delta E}{kT} + 2aR\right)\right] \qquad (3\text{-}3)$$

Where ΔE, a, and R are the energy supplied by the phonon, the decay constant of the localised wave function of the supply trap and the radial separation between localised states, respectively. The application of an electric field F reduces the energy of the localised states by eFR. Thus, for moderate fields the forward current is given by *equation 3-4* while *equation 3-5* describes it at high fields[238].

$$J \propto \exp\left[-\left(\frac{\Delta E - eFR}{kT}\right) + 2aR\right] \qquad (3\text{-}4)$$

$$J \propto \exp\left[-\left(2.31\left(\frac{2a^3}{pN_i\,kT}\right)^{1/4}\left(1-\frac{eF}{2akT}\right)^{3/4}\right)\right] \qquad (3\text{-}5)$$

For non uniform trap distribution, the current density is given by *equation 3-6*.

$$J \propto \exp\left[-\left(\frac{1.76a^{3/4}}{(N_i kT)^{1/4}}\right)\left(1-\frac{1}{2}\left(\frac{eF}{4U}\right)^2 (3aN_i kT)^{-1/2}\right)\right] \qquad (3\text{-}6)$$

Others predicted field dependence currents given by *equations 3-7* and *3-8* for flat density of states[239-240].

$$\ln(J) \propto F^2 \qquad (3\text{-}7)$$

$$\ln(J) \propto F^{-1/4} \qquad (3\text{-}8)$$

Equation 3-7 is applicable for low fields when $\ln(J) \propto T^{-1/4}$ while *equation 3-8* is valid for very high fields and temperature independent conductivities. Calculations within a percolation theory model lead to *equation 3-9* for moderated fields[241].

$$G \propto \exp(-A + eFl/kT) \qquad (3\text{-}9)$$

With *G*, *F*, *l*, $\exp(-A)$ and T are the conductance, the electric field, a fraction of the characteristic low-field hopping distance, the low field conductance and the temperature, respectively. The absence of standard field dependence of the current density emphasizes the need to know the field region in which the I-V measurements were carried out. This will later be considered.

3.7.3.2 Donor-trap hopping

For a donor-trap hopping conduction, the charges are transferred from a donor state to a trap state via hopping process. This phenomenon is valid for low electric fields at low temperatures, when the energy difference between donor and trap is small. In this case, the current is described by *equation 3-10*[238].

$$J \propto \exp\left(-1.96\left(\frac{Ae^2}{e_0 e}\right)^{6/7}\left(\frac{1}{pN_t kT}\right)^{1/7}\right) \qquad (3\text{-}10)$$

3.7.3.3 Tunnelling based conduction

Tunnelling is a quantum mechanical phenomenon. In the presence of an energy barrier *E*, there is a non nil probability for a charge of energy E_1 ($E_1 < E$) to be transferred between states S_1 and S_2 due to its wave nature. The tunnelling

corresponds to the transfer of a charge from one state to another through an energy barrier.

Multiple tunnelling mechanisms were reported, amongst them the Fowler-Nordheim tunnelling (see *section 2.6.2.1*) and the direct tunnelling (see *section 2.6.3*). Here, quantum tunnelling described by *equation 3-11* is considered[242].

$$I = 2I_0 \frac{pCkT}{\sin(pCkT)} \exp(-BV^2) \sinh\left(\frac{CV}{2}\right) \qquad (3\text{-}11)$$

With I_0, B and C the low field current and constants, respectively.

3.7.3.4 Conduction in Sonogashira-SWCNT networks

In this section, the dominant electrical conduction across the Sonogashira-SWCNT networks is determined by a combined analysis of their I-V and I-T characteristics. Analysis of the electrical characteristics of Sonogashira-SWCNT networks was conducted considering the models cited in *sections 3.7.3.1* to *3.7.3.3*. I-V and I-T data points at 0.5, 1, 5 and 10 V given in *section 3.6.3.1* and *3.6.3.2* were subsequently plotted according to these models. Note: the I-T characteristics for the 10 ml network are not shown due to their inconsistency.

3.7.3.4.1 3-D VRH

The thicknesses of the networks are likely to be higher than the hopping distance, so 3-dimension VRH is considered here. *Figure 3-24* displays the $\ln(I)$ *versus* $T^{-1/4}$ plots of the I-T characteristics according to 3D-VRH model for the 5 and 20 ml Sonogashira-SWCNT networks, respectively.

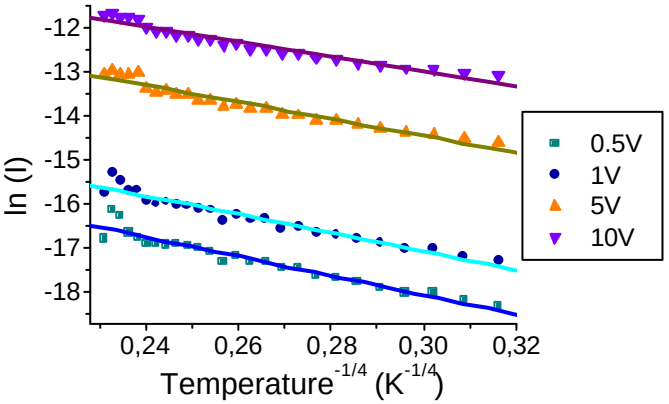

(a)

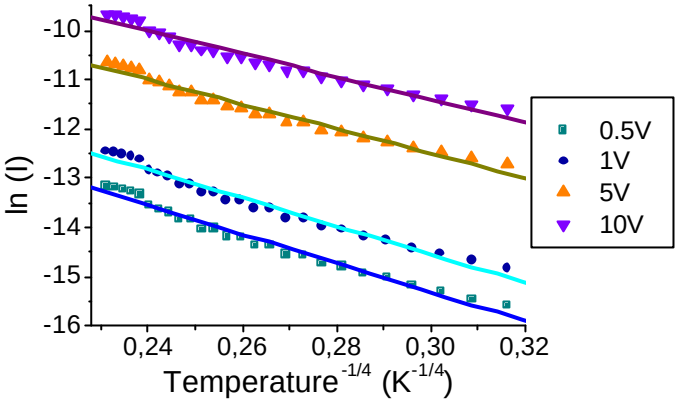

(b)

Figure 3-24 $\ln(I)$ *versus* $T^{-1/4}$ *plots of I-T characteristics at 0.5, 1, 5 and 10 V for Sonogashira-SWCNT networks with filtered volumes of (a) 5 ml and (b) 20 ml*

Figure 3-24 shows that good linear fits of $\ln(I)$ *versus* $T^{-1/4}$ plots were obtained for all I-T plots from 100 to 350 K. This implies that the conduction across the Sonogashira-SWCNT networks could be dominated by VRH. This result was expected given that the conduction within SWCNT networks was shown to follow VRH[119].

I-V measurements were performed with 50 µm electrode separations and a voltage range of ±10 V equating to an electrical field up to 2×10^3 V/cm. 10^4 V/cm is considered here as the limit from low to moderate electric fields[237]. The presence of a temperature dependence of the current, which would not exist at high fields also indicates that the data are within the moderate electric field region[240]. Given that the I-V measurements were carried out in the low electric field region, only *equation 3-7* for low electric fields is considered for the fittings. *Figure 3-25* shows the $\ln(I)$ *versus* V^2 plots from 0 to 10 V for the 5 and 10 and 20 ml Sonogashira-SWCNT networks.

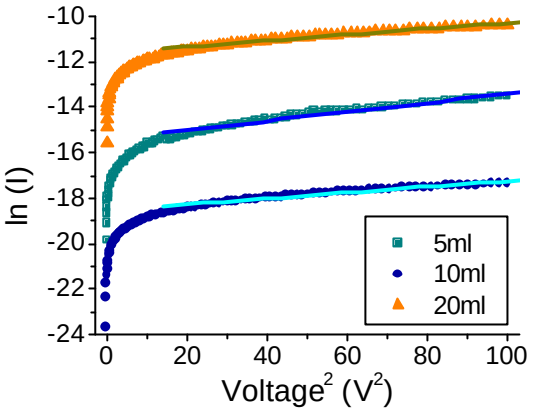

Figure 3-25 $\ln(I)$ *versus* V^2 *plots of I-V characteristics at room temperature for 5, 10 and 20 ml Sonogashira-SWCNT networks*

Figure 3-25 shows the absence of linear behaviour for the $\ln(I)$ *versus* V^2 plots from 0.1 to ~4.7 V for the 5, 10 and 20 ml Sonogashira-SWCNT networks. Beyond ~4.7 V a linear trend is obtained for all networks. Consequently the 3D-VRH model would dominate the conduction from 4.7 to 10 V.

None of the plots fit the VRH equations over the full voltage range as it was expected due to the field range of validity of *equation 3-7*. According to the VRH theory, *Figure 3-25* should have displayed linear trends even at lower voltages. But, the characteristics are not linear in the region where they were most expected to be (below 4.7 V).

Generally, VRH conduction in SWCNT networks is reported only using I-T measurements. To our knowledge, no other analysis of I-V plots according to VRH was available for SWCNT networks to compare these results. Here, a combined analysis of I-V and I-T characteristics was carried out according to the VRH model. It shows that although the I-T plots showed good fittings, the I-V plots did not display the expected results according to the model. This causes to discount the VRH as a dominant transport mechanism as the I-V plots do not validate the model.

3.7.3.4.2 Donor-acceptor hopping

Figure 3-26 displays the $\ln(I)$ *versus* $T^{-1/7}$ plots of the I-T characteristics for the 5 and 20 ml Sonogashira-SWCNT networks.

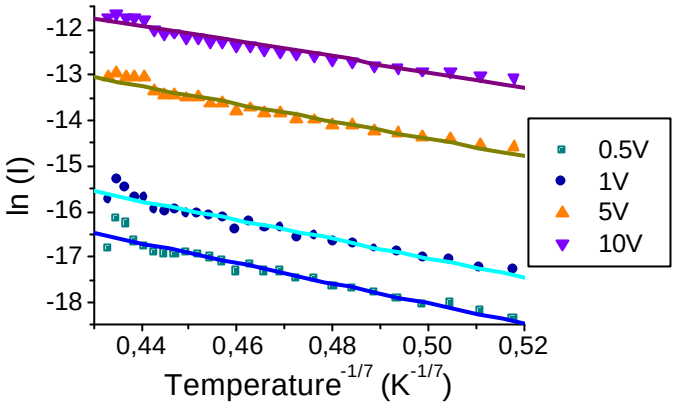

(a)

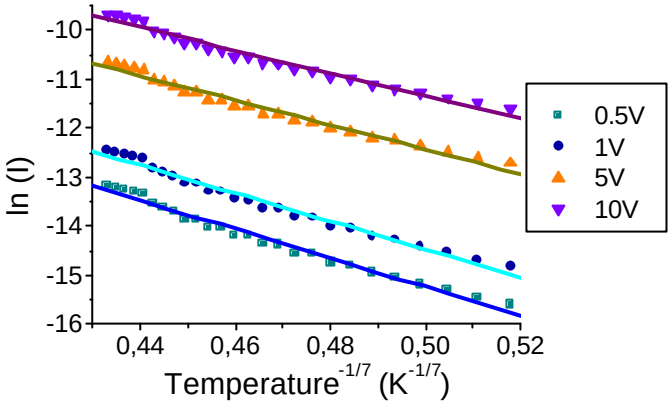

(b)

Figure 3-26 $\ln(I)$ *versus* $T^{-1/7}$ *of I-T characteristics at 0.5, 1, 5 and 10 V for (a) 5 ml and (b) 20 ml Sonogashira-SWCNT networks*

$\ln(I)$ *versus* $T^{-1/7}$ plots of the I-T characteristics were plotted with their linear fits from 100 to 300 K. *Figure 3-26* shows that good linear fits were obtained for all the networks.

This linear behaviour of $\ln(I)$ *versus* $T^{-1/7}$ plots indicates donor-trap hopping across the network. This model is applicable for low electric fields so is here plausible for all the characteristics[238]. *Figure 3-26* suggests that the conduction in the Sonogashira-SWCNT networks is governed by donor-trap hopping. However, this model is valid at low temperatures which contrasts with the linear plots obtained above 300 K. This suggests that the conduction is dominated by another conduction whose $\ln(I) \propto T^{-1/7}$ plots of the I-T characteristics look linear.

$\ln(I) \propto T^{-1/7}$, $\ln(I) \propto T^{-1/3}$ and $\ln(I) \propto T^{-1/4}$ plots were reported to follow the same linear trend over a temperature range a decade below 300 K[238]. Then, though good fits were obtained according to the donor-acceptor hopping model, it is unlikely that

this model governs the conduction across the Sonogashira-SWCNT networks. Unfortunately, the donor-trap hopping model does not provide a field dependence of the current. So the I-V characteristics cannot be exploited according to this model.

Section 3.7.3.4.1 showed that despite the linear behaviour of the I-T plots according to *equation 2-6* the I-V characteristics do not agree with the VRH theory. In *section 3.7.3.4.2*, the I-T plots also fitted *equation 3-10,* however, the donor-acceptor hopping was discounted as the model is not valid in the temperature range analysed.

3.7.3.4.3 Tunnelling conduction

I-V and I-T characteristics were fitted using *equation 3-11*. Good fittings of the I-V characteristics (not shown) were achieved. However, no fitting of the I-T characteristics could be obtained using Origin 7 software[xvi].

In tunnelling mechanisms, the current is known to have an exponential dependence with the temperature[179]. Thus, *equation 3-11* was modified by substituting its temperature related term $pCkT/\sin(pCkT)$ with an exponential dependence $\exp(AT)$ where A is a constant. The intuitive modification of *equation 3-11* simplified it into *equation 3-12*.

$$I = 2I_0 \exp(AT)\ \exp\left(-BV^2\right) \sinh\left(\frac{CV}{2}\right) \qquad (3\text{-}12)$$

Where I_0 is the current at low field and *A*, *B* and *C* are constants.

Equation 3-12 preserves the voltage dependence of the current observed with *equation 3-11*. The general exponential dependency of the current with the temperature for tunnelling conduction is also respected[179]. According to *equation 3-12*, the constant *A* is determined by $\ln(I)$ *versus T* plots of the I-T characteristics.

Thus, $\ln(I)$ *versus T* plots of the I-T characteristics (not shown here) were used to find the constant *A* of *equation 3-12*. The values of *A* for each network, shown in *Table 3-11,* are integrated into *equation 3-12* for the fittings of both I-V and I-T plots.

Filtered volume for networks (ml)	Constant A values
5	0.0065
20	0.0088

Table 3-11 Values of constant A for Sonogashira-SWCNT networks

[xvi] All plots and fittings were performed in Origin 7

Figure 3-27 displays the I-V characteristics fitted according to *equation 3-12*.

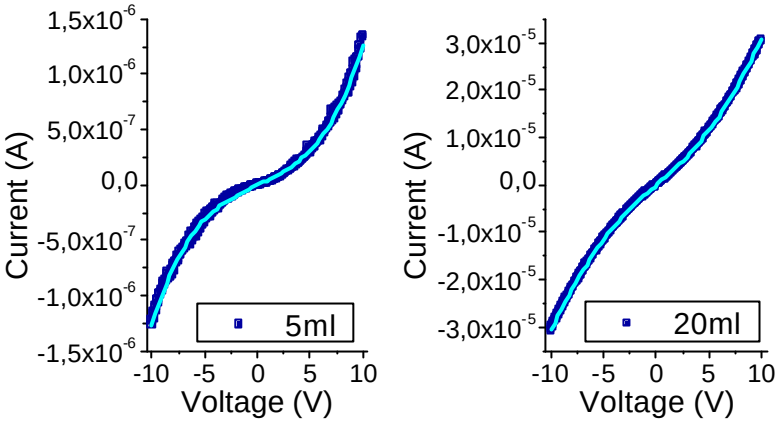

Figure 3-27 I-V characteristics of 5 and 20 ml Sonogashira-SWCNT networks with their fits according to equation 3-12

Figure 3-27 shows that good fits of the characteristics using *equation 3-12* were obtained on the whole voltage range for all networks. *Figure 3-28* displays the I-T characteristics for 5 and 20 ml Sonogashira-SWCNT networks fitted according to *equation 3-12*.

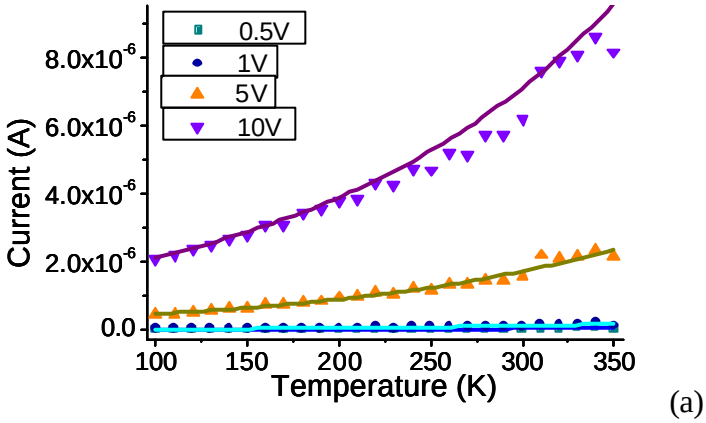

Figure 3-28 I-T characteristics according to equation 3-12 for (a) 5 ml and (b) 20 ml Sonogashira-SWCNT networks

Figure 3-28 shows good fits of the I-T characteristics from 100 to 350 K. Though the fittings do not appear better than in *Figure 3-26*, the tunnelling model is valid in this temperature range contrary to the donor-acceptor hopping model. Thus, both I-V and I-T characteristics display good fittings of *equation 3-12* which suggests a quantum tunnelling based conduction within the Sonogashira-SWCNT networks.

This result is supported by the low temperature dependence of the current, which is highlighted by the high values of x_0, the fitting parameter, which provides the proportionality of temperature dependence with the current, for the I-T plots. Quantum tunnelling also appeared as the dominant conduction mechanism in iodobenzene-SWCNT networks (see *Appendix B.1*). This result was expected given that the Sonogashira cross-coupling modifies the functional groups rather than creating bridges between SWCNTs.

3.7.4 Discussion

The study of the electrical characteristics of the Sonogashira-SWCNT networks led to good fitting of the I-T characteristics according to the hopping and tunnelling models. But, any linear fitting in the I-V plots according to the VRH model, is limited to the high voltage region which is inconsistent with the theory. However, the I-V characteristics for all networks also show good fits of the quantum tunnelling conduction model. The intuitively modified quantum tunnelling model (*equation 3-12*) proposed in this work, showed good fits of both the I-V and I-T characteristics for all networks. Consequently, the conduction across all Sonogashira-SWCNT networks appears to be governed by the modified quantum tunnelling model. This result was partly expected as the conduction across SWCNT networks was shown to be dominated by tunnelling and hopping mechanisms depending on the network thickness[119]. Here, the tunnelling conduction is dominant even for the thick networks. The I-T characteristics displayed good fits according to both hopping and tunnelling models however the donor-acceptor hopping model was invalid and any fitting of the I-V characteristics in the VRH models was limited to the high voltage region which is inconsistent with the theory. Using the same analytical method, quantum tunnelling was also found to be dominant in iodobenzene-SWCNT and

pyridine-SWCNT networks (see *Appendix B*). This supports the results obtained for the Sonogashira-SWCNT networks as the Sonogashira coupling did not bridge SWCNTs, but the reaction coupled iodobenzene-SWCNTs to TMSA to give 1-(trimethylsilyl)-2-phenylacetylene-SWCNTs (Sonogashira-SWCNTs). It was therefore expected that the same mechanism will dominate the conduction across iodobenzene-SWCNT and Sonogashira-SWCNT networks.

3.8 Discussion/Conclusion

This chapter reports on the fabrication and characterisation of SWCNT precursors for bridged-SWCNTs. Numerous diazonium reactions on SWCNTs are reported. Heck and Suzuki couplings on SWCNTs were also reported[243-244]. Here, Sonogashira cross-coupling was performed on SWCNTs. This is, to our knowledge, the first time that this coupling is reported for the functionalisation of SWCNTs.

Spectroscopy analyses attested of the modification of the structure of the SWCNTs after radical addition of aryl groups. Sonogashira cross-coupling was also carried out on iodobenzene-SWCNTs. The absorption spectra showed the lesser solubility for the Sonogashira-SWCNTs than for the iodobenzene-SWCNTs. TGA-MS analyses confirmed the presence of pyridine, iodobenzene and 1-(trimethylsilyl)-2-phenylacetylene groups grafted onto the respective SWCNT samples. Elemental analyses completed the study by giving a qualitative estimation of the level of functionalisation; 2.5 at% and 1.9 at% for iodobenzene and pyridine groups, respectively. The XPS analysis was essential to differentiate the silicon from the trimethylsalyl acetylene from the silicon contaminant (silicon from the grease used to seal glass vessels). The contributing bands centred around 101.4 eV and 104.7 eV binding energies were attributed to the silicon from 1-(trimethylsilyl)-2-phenylacetylene and silicon grease, respectively. A silicon concentration of 1.8 at% was estimated for 1-(trimethylsilyl)-2-phenylacetylene groups. In parallel, the iodine amount decreased from 2.5 at% in iodobezene-SWCNTs to 1.2 at% in Sonogashira-SWCNTs indicating that the Sonogashira cross-coupling has occurred. TGA-MS analysis confirmed the functionalisation level in iodobenzene-SWCNTs and Sonogashira-SWCNTs but

not in pyridine-SWCNTs, where an incongruity was observed in the TGA spectra. The abnormality was attributed to variations in the repartition of the moieties.

SWCNT precursor networks were fabricated by vacuum filtration and details of the structure for such networks were provided. Electrical characteristics of iodobenzene-SWCNT, pyridine-SWCNT and Sonogashira-SWCNT networks were studied. A modified quantum tunnelling model was found to best fit the current-voltage and current-temperature characteristics. Thus, quantum tunnelling was identified as the conduction mechanism governing the charge transport across Sonogashira-SWCNT networks. Using the same analytical method, quantum tunnelling was also identified as the dominant conduction mechanism in iodobenzene-SWCNT and pyridine-SWCNT networks (see *Appendix B*). This tunnelling conduction was found to govern the conduction in all SWCNT networks whatever their thickness.

VRH and tunnelling mechanisms are repeatedly reported for the conduction in SWCNT networks. This result contrasts with previous studies showing that VRH was dominant for thick SWCNT networks. VRH conduction was expected for the non transparent networks as reported elsewhere[119]. This would correspond to the networks made with 10 and 20 ml of SWCNT dispersions as their thicknesses are estimated to ca. 40-50 microns (see *Appendix E*). Recently, *Kaiser and co-workers* proposed a metallic conduction model, where the transport is interrupted by thin tunnelling barriers, backscattering by zone boundary phonons and VRH, to explain the electronic conduction in SWCNT networks[245]. Though this model incorporated conduction within $SOCl_2$ and aniline functionalised SWCNT networks, the analysis is again largely based on the temperature dependence of the current. In the conduction studies reported, the networks were composed of semiconducting and metallic SWCNTs. This model is valid when metallic SWCNTs are present into the networks. This is not the case in our SWCNT precursor networks as the metallic SWCNTs became non metallic after diazonium additions[75].

In this work, the SWCNTs had undergone radical additions. It is known that damages caused by the radical addition degrade the electrical properties of SWCNTs[246]. The vast excess of diazonium reactants and the long reaction time used suggest that metallic nanotubes became non metallic as the SWCNTs were

extensively damaged[75]. Thereby, it is suggested that the SWCNT precursor networks are virtually free of metallic SWCNTs. VRH dominated conduction are typically reported for pristine SWCNT networks[119]. Thus, the changes in the electronic structures of the SWCNT precursors can explain this of difference conduction mechanisms. In addition, the identification of the conduction in SWCNT networks usually results uniquely from the analysis of their I-T plots. Here, a combined analysis of the I-V and I-T characteristics was required as both hopping mechanisms and the modified tunnelling model fitted the I-T plots. The major factor indicating a dominant quantum tunnelling mechanism was extracted from good I-V and I-T fits. This suggests that a combined electrical analysis of other SWCNT networks could also lead to a tunnelling dominated conduction.

The findings for the SWCNT precursor networks will be used as reference, when analysing the conduction mechanisms in bridged SWCNT and Pt-SWCNT networks, in *Chapter 4* and *Chapter 5*, respectively.

3.9 Summary

This chapter reports the formation of functionalised SWCNTs precursors via diazonium radical additions and for the first time to our knowledge, via Sonogashira cross-coupling. The results from the characterisation of Sonogashira-SWCNTs are presented along with the other functionalised SWCNTs. Functionalisation levels of 2.5 at% in iodobenzene-SWCNTs, 2.1 at% in Sonogashira-SWCNTs and 1.9 at% in pyridine-SWCNTs were estimated from both XPS and TGA-MS analyses.

Quantum tunnelling was found to govern the conduction across all SWCNT precursor networks. This result was achieved from a combined analysis of the I-V and I-T characteristics. This contrasts with the VRH conduction typically obtained for such networks. This is particularly true for the thick networks (made with 10 and 20 ml of SWCNT dispersions). This difference in materials and the fact that analyses of conduction mechanisms across SWCNT networks reported in the literature relied only on I-T characteristics are possible explanations for this divergence.

Chapter 4
Organic molecular bridged SWCNT networks

4.1 Introduction

The presence of covalent bondings between molecules and electrodes are expected to provide better junctions and enhance the electronic transmission[247]. So, it is thought that conductive organic molecular bridges covalently built between SWCNTs could facilitate the current flow across SWCNT networks. For instance, the cross-linking of carbon nanotubes was shown to improve the mechanical and electrical performance of pellets made out of them[248]. The electrical behaviour of molecules-SWCNTs junctions reported, mainly involved individual molecules covalently bonded to SWCNT electrodes[193,249-251]. A previous effort in cross-linking nanotubes in bucky papers via diamine linkers was reported elsewhere[197]. However, no evidence was shown that both extremities of the diamine linkers had been bonded[197]. Formation of molecular junctions between nanotubes and charge transfer across the junction were demonstrated by microscopy[252-253]. Both works involved bridging the $SOCl_2$ functionalised SWCNTs with diamine linkers to study the electrical properties of interconnected SWCNT networks. Electrical conductivities of bucky papers whose networks presented 30% of bridged SWCNTs (AFM analysis) were reported to drop to 20 S/cm[253]. However, an increase in electrical conductivity was reported for bridged SWCNT pellets[248]. *Table 4-1* displays electrical conductivities reported for bridged SWCNT networks.

	Pristine purified SWCNTs	Cut SWCNTs	$SOCl_2$ SWCNTs	organic linked SWCNTs	Reference
Conductivity (S/cm)	700	400	120	20	Dettlaff-Weglikowska et al. [253]
	2	-	-	24	Cha et al. [248]
	605	-	1420	590	Dettlaff-Weglikowska et al. [197]
	605	-	1420	720	

Table 4-1 Reported electrical conductivities of bridged SWCNT networks

Previous efforts in characterising the electrical properties of bridged SWCNT networks were limited to their conductivity. In such networks, the transport across direct nanotube-nanotube junctions (see *section 3.3*) competes with the nanotube-molecule-nanotube junctions. However, the transport mechanism was not investigated in these networks.

In this work, networks of bridged-SWCNTs were fabricated and their dominant conduction mechanism was identified. A bridging approach different to those previously reported was followed. Instead of using diamine[253] or cycloaddition[254] bridgings, carbon-carbon bonds are formed using organometallic coupling reactions. The advantage of this method lies in the coupling of the grafted moieties of the SWCNT precursors, whose intermediate elements disappear after reaction. In fact, when a molecule is used to covalently bridge two SWCNTs by forming the same bond with each SWCNT, evidence of the cross-linking cannot be provided with spectroscopic methods[254]. Here, it is the study of elements from SWCNT precursors (Si and I) which indicates whether organic bridges were fabricated. Such organometallic processes were already used in SWCNT chemistry. For instance, photoluminescence studies of anthracenyl derivative SWCNTs and chromophore-functionalized SWCNTs prepared via Heck[244] and Suzuki[243] couplings, respectively, were reported. So far, these couplings have been used to functionalise the nanotubes but not to create molecular bridges. Here, molecular bridges between SWCNTs are formed via homo-coupling and cross-coupling. The creation of molecular bridges involved, at first, the formation of iodobenzene-SWCNTs and Sonogashira-SWCNTs as precursors (see *Chapter 3*). In this chapter, these SWCNT precursors are used to build-up bridges between their moieties, and indirect evidence of the molecular bridging of these SWCNT precursors are provided. In addition, the mechanisms governing the conduction across these covalently bridged SWCNT networks were identified based on a combined analysis of their electrical characteristics.

4.2 Fabrication of organic molecular bridged SWCNTs

4.2.1 Homo-coupling of Sonogashira-SWCNTs

A modified version of the Sonogashira coupling, with a coupling mediated by CuCl, was reported[255]. The scheme of this homo-coupling applied to the Sonogashira-SWCNTs is shown in *Figure 4-1*.

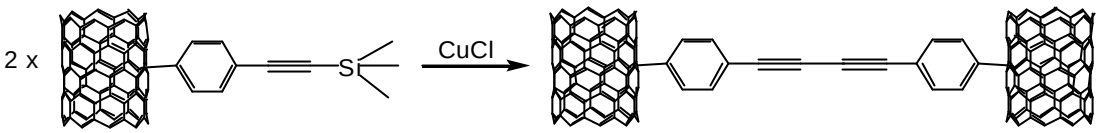

Figure 4-1 Scheme of the homo-coupling reaction on Sonogashira-SWCNTs

The fabrication of covalent molecular bridges using the homo-coupling process not only benefit from the absence of Pd catalyst and nucleophilic activator[255] but also from the fact that the reaction is performed in DMF. DMF is known as a good solvent for the dispersion of carbon nanotubes[210]. The homo- coupling performed in this scheme results in SWCNTs bridged by 1,2 diphenyldiacetylene molecules.

4.2.2 Cross-coupling of iodobenzene-SWCNTs and Sonogashira-SWCNTs

A cross-coupling reaction performed between alkynylsilanes and aryls in DMF was reported[255]. The scheme for the cross-coupling reaction applied to iodobenzene-SWCNTs and Sonogashira-SWCNTs is given in *Figure 4-2.* Following the cross-coupling process, covalent molecular bridges of 1,2-diphenylacetylene molecules are built between SWCNTs.

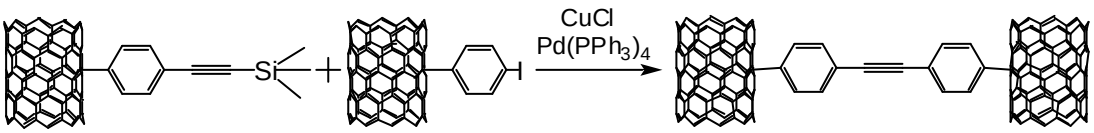

Figure 4-2 Scheme of cross-coupling reaction of iodobenzene-SWCNT and Sonogashira-SWCNT

4.2.3 Ullmann coupling of iodobenzene-SWCNTs

Figure 4-3 displays the scheme of the Ullmann coupling in DMF, using N,N-diisopropylethylamine as base and di-μ-chlorobis[5-chloro-2-[(4-chlorophenyl)(hydroxyimino-κN)methyl]phenyl-κC]palladium dimer as catalyst, leading to the formation of biaryls molecular bridges between SWCNTs[256].

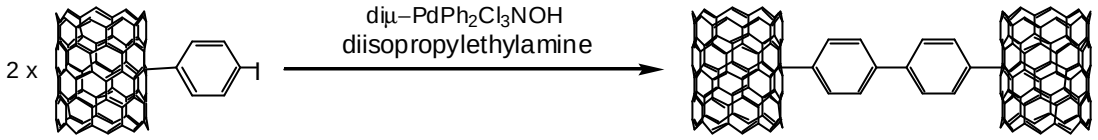

Figure 4-3 Scheme of the Ullmann coupling of two iodobenzene-SWCNTs

Figure 4-3 shows that covalent biaryl bridges are created as a result of the Ullmann coupling.

4.3 Characterisation of molecular bridged SWCNTs

4.3.1 UV-visible-near IR spectroscopy

Absorption spectra of oversaturated dispersions of covalently bridged SWCNTs in DMF (1:10 mg/ml) were recorded before and after couplings. *Figure 4-4* shows the absorption spectra before and after the respective couplings.

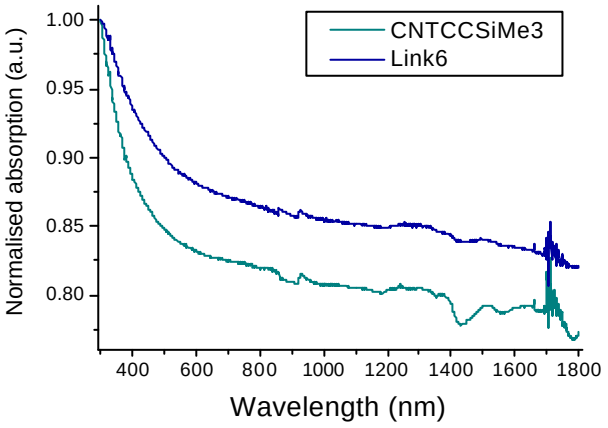

(a)

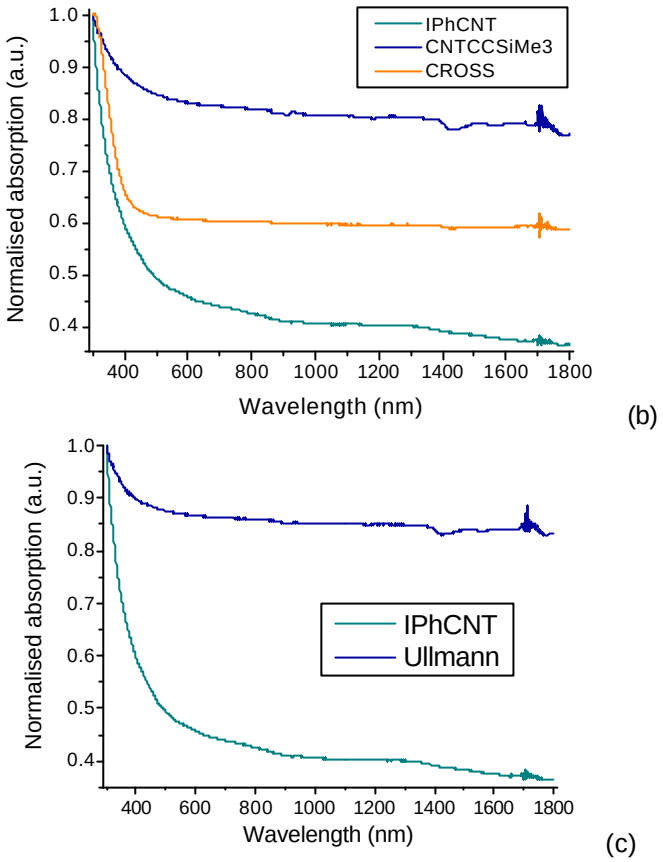

Figure 4-4 Absorption spectra normalised at 300 nm of saturated dispersions in DMF of (a) Sonogashira-SWCNTs and homocoupled-SWCNTs (b) iodobenzene-SWCNTs, Sonogashira-SWCNTs and homocoupled-SWCNTs and (c) iodobenzene-SWCNTs and Ullmann-SWCNTs

Figure 4-4 (a) shows that Sonogashira-SWCNTs and homocoupled-SWCNTs have the same absorption profile. *Figure 4-4 (b)* shows that the absorption profile of the SWCNTs after cross-coupling is different from both precursors (iodobenzene-SWCNTs and Sonogashira-SWCNTs). The absorption profile (*Figure 4-4 (c)*) after the Ullmann coupling is also different to that of its precursor; the iodobenzene-SWCNTs. The concentrations of the oversaturated dispersions at 500 nm were found using *equation 3-1* and $e_l = 25.5\ (\text{mg/L})^{-1}\ \text{cm}^{-1}$ at 500 nm [153]. *Table 4-2* displays these values alongside the concentration of the SWCNT precursors.

Concentration at 500 nm (mg/L)		
SWCNT precursors	Iodobenzene-SWCNTs	6.2
	Sonogashira-SWCNTs	4.7
Molecular bridged SWCNTs	Homocoupled-SWCNTs	4.7
	Crosscoupled-SWCNTs	4.3
	Ullmann-SWCNTs	4.2

Table 4-2 Concentrations of oversaturated dispersions of SWCNT precursors and molecular bridged SWCNTs

Table 4-2 indicates that the solubility decreased as a result of the coupling reactions except for the homo-coupling, which did not affect the solubility. This result was expected, as covalent molecular bridges between nanotubes are expected to create larger SWCNT aggregates. These aggregates are expected to have a smaller solubility. A smaller concentration of 1,2-diphenyldiacetylene bridged SWCNTs (homocoupled-SWCNTs) was expected as two 1-(trimethylsilyl)-2-acetylene moieties coupled to create 1,2-diphenyldiacetylene. The fact that the solubility of the homocoupled-SWCNTs has not changed from it precursor can be explained by a low number of bridges created. In this case, a small enough amount of 1,2-diphenyldiacetylene bridges could not to impact on the solubility of the SWCNTs.

4.3.2 XPS analysis

XPS analyses were carried out on the covalently bridged SWCNTs. Prior to XPS analyses, the bridged-SWCNTs were etched by an Ar^+ bombardment for about 30 seconds at 3 kV to reduce the contamination from the atmosphere. *Figure 4-5* displays the C1s, I3d5/2, Cu2p and O1s XPS spectra in bridged SWCNTs.

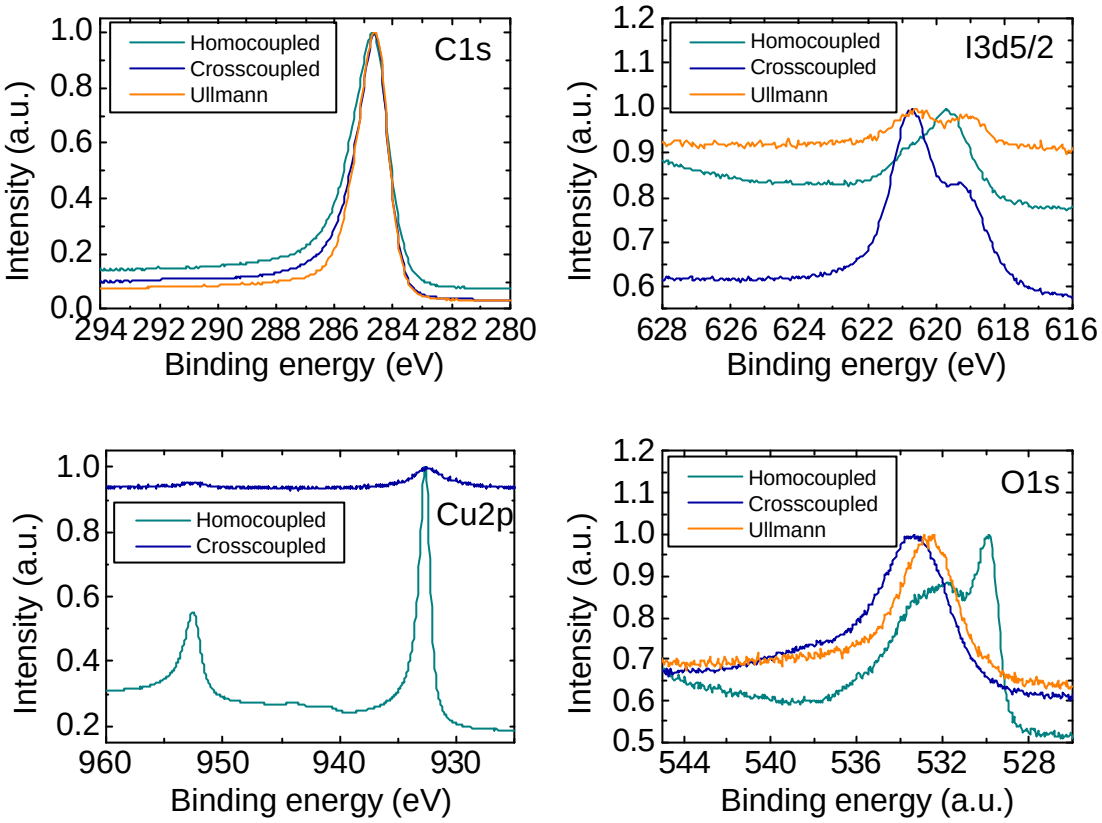

Figure 4-5 C1s, I3d5/2, Cu2p and O1s XPS spectra of molecular bridged SWCNTs

Table 4-3 summarises the atomic concentrations, binding energies and FWHM of elements in molecular bridged SWCNTs.

Elements	Homocoupled-SWCNTs			Crosscoupled-SWCNTs			Ullmann-SWCNTs		
	Conc (at%)	BE (eV)	FWHM	Conc (at%)	BE (eV)	FWHM	Conc (at%)	BE (eV)	FWHM
C1s	72.4	284.7	1.5	85.7	284.7	1.3	90.7	284.6	1.2
O1s	8.8	529.9	4.3	7.9	533.4	3.7	5.8	532.4	2.8
N1s	1.8	400.0	2.3	1.3	399.8	2.3	-	-	-
I3d5/2	0.4	619.7	1.8	0.9	620.7	2.5	0.2	620.6	2.8
Si2p	2.2	104	3.3	1.9	104.2	3.1	-	-	-
Cu2p3/2	12.9	932.7	1.1	0.3	932.6	2.7	-	-	-
Pd3d5/2	0.3	335.9	2.4	1.3	335.6	1.2	1.7	335.5	1.2
Cl2p	1.3	200.5	3.3	0.9	200.7	1.3	-	-	-
F1s	-	-	-	-	-	-	1.5	689	2.1

Table 4-3 Atomic concentrations, binding energies and FWHM of elements identified in molecular bridged SWCNTs

Table 4-3 shows that the relative concentration of Cu is very high in homocoupled-SWCNTs. Cu was used as catalyst in the homo-coupling and should have been removed from the SWCNTs after the washing step. This high Cu concentration suggests that Cu was not eliminated by the washing process, rather, a new a compound containing Cu could have been formed.

Note: the presence of F is explained by the PTFE filtration membrane used during the SWCNTs washing.

Figure 4-5 shows that little variations in the width of the C1s spectra base are observed in the C1s spectra. The I3d5/2 spectra indicate the presence of two iodine compounds whose relative proportions changed according to the molecular bridged SWCNTs. *Figure 4-1* indicates that the homo-coupling reaction does not involve iodine. Thus, in homocoupled-SWCNTs, the intensity of the contribution from I-C bonds is lower than the contribution from I bonds created as a by-product of the coupling. It therefore appears as a shoulder of the I3d5/2 spectrum envelope. Thereby, the envelope of the I3d5/2 spectrum of homocoupled-SWCNTs is, as expected, similar to that of I3d5/2 of Sonogashira-SWCNTs (*Figure 3-16*). The iodobenzene-SWCNTs, used as precursors, intervene into the the cross-coupling and Ullmann reactions. Therefore, the analysis of I3d5/2 XPS spectra in crosscoupled-SWCNTs and Ullmann-SWCNTs is detailed in the following.

The relative atomic concentration of iodine appears to drop from 2.5 at%. in iodobenzene-SWCNTs (*Table 3-4*) and 1.2 at%. in Sonogashira-SWCNTs (*Table 3-4*) to 0.9 at%. in crosscoupled-SWCNTs (*Table 4-3*). The iodine concentration also dropped after Ullmann coupling to reach 1.2 at%. This indicates a release of iodine following these couplings. *Figure 4-6* shows the XPS spectrum of the I3d5/2 after cross-coupling and Ullmann coupling.

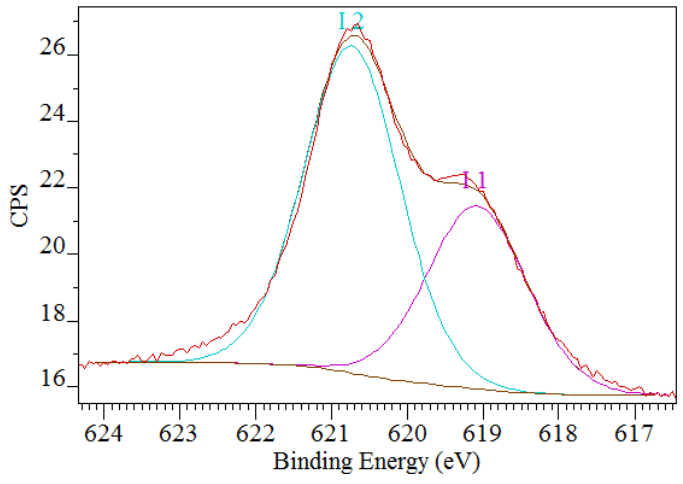

(a)

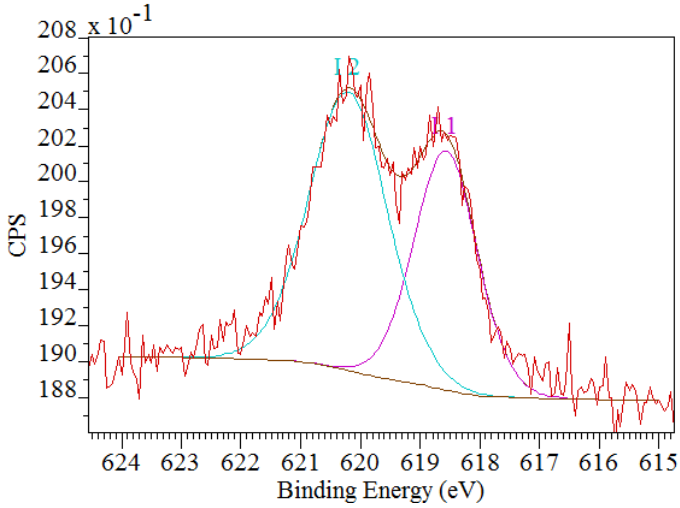

Figure 4-6 I3d5/2 XPS spectrum of (a) crosscoupled-SWCNTs (b) Ullmann-SWCNTs

Figure 4-6 shows two distinct components of the I3d5/2 XPS peak for both crosscoupled-SWCNTs and Ullmann-SWCNTs. The reactants of the cross-coupling reaction provided two sources of iodine in the sample (iodobenzene-SWCNTs and Sonogashira-SWCNTs). The profile of the I3d5/2 peak in iodobenzene-SWCNTs (*Figure 3-16 (a)*) presents only one component but the I3d5/2 peak in Sonogashira-SWCNTs (*Figure 3-16 (b)*) showed two contributions. The comparison between the I3d5/2 spectra before and after cross-coupling was done using the I3d5/2 spectrum of Sonogashira-SWCNTs. The main parameters of the contributions obtained from the decomposition of the I3d5/2 bands are given in *Table 4-4*.

Contributions		Area	BE (eV)	FWHM (eV)	Conc (at%)	Bonds
Iodobenzene-SWCNTs	I 1	46.6	620.2	1.1	67.6	I-C [232]
	I 2	22.4	620.4	2.7	32.4	
Crosscoupled -SWCNTs	I 1	9.2	619.1	1.5	36.6	I^- [233]
	I 2	15.9	620.7	1.5	63.4	I-C [232]
Ullmann-SWCNTs	I 1	1.8	619	1.3	41.2	I^- [233]
	I 2	2.6	620.6	1.6	58.8	I-C [232]

Table 4-4 Main parameters for the contributions of I3d5/2 XPS spectra in iodobenzene-SWCNTs, crosscoupled-SWCNTs and Ullmann-SWCNTs

The comparison between the parameters of the I3d5/2 components in *Table 4-4* shows that their binding energies are the same for the crosscoupled-SWCNTs and Ullmann-SWCNTs. Thus, the chemical environment of the iodine is the same after covalent bridging. The area of I2 stayed almost constant but the area of I1 decreased by a factor

of 2. The proportion of I1 decreased from 54.3 at%. to 36.6 at% after cross-coupling reaction. The fact that iodobenzene-SWCNTs were also reactants in the cross-coupling explains the higher proportion of I2 than I1 compared to *Figure 4-3*. Overall, I from iodobenzene dropped from 2.5 at% and 0.6 at% in iodobenzene-SWCNTs and Sonogashira-SWCNTs to 0.5 at% in crosscoupled-SWCNTs, respectively.

For Ullmann-SWCNTs, the comparative analysis was based on their iodobenzene-SWCNT precursors. After a 93.5% drop, the overall iodine concentration reaches 0.2 at%. The relative concentration of iodine from iodobenzene was found to be 0.1 at%. This corresponds to a maximum of 1.2 at% of biaryl bridges in Ullmann-SWCNTs. The drops of the relative iodine concentrations, after cross-coupling and Ullmann coupling, are indications that these reactions were successful.

The C1s XPS spectrum of homocoupled-SWCNTs shown in *Figure 4-5* is analysed in *Figure 4-7*. The eventuality to create the SWCNT-Ph-C≡C-Cu coupling intermediate during the homo-coupling led to analyse the C1s spectrum of the homocoupled-SWCNTs. The high concentration of Cu in the homocoupled-SWCNTs (*Table 4-3*) could be explained by the presence of the SWCNT-Ph-C≡C-Cu intermediate. If this intermediate was present it would be detected by a band for the C-Cu bond at about 283.6 eV[257].

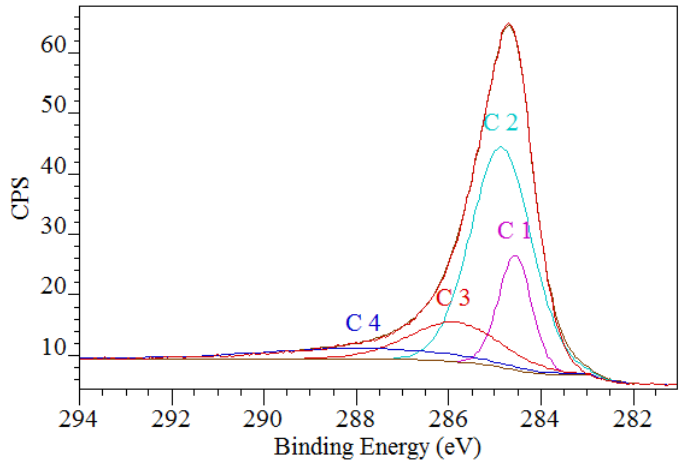

Figure 4-7 C1s XPS spectrum for homocoupled-SWCNTs with its 4 contributions

The C1s XPS spectrum of homocoupled-SWCNTs shown in *Figure 4-7* exhibits the same profile as the spectrum in *Figure 3-14*. Similar to the XPS studies in *sections 3.4.2* and *3.5.4.2*, the deconvolution, using 4 contributions C1, C2, C3 and C4, of the C1s spectrum achieved good fits. The main parameters of the contributions obtained from the decomposition of the C1s spectrum are given in *Table 4-5*.

Component	C1s in SWCNTs (C1+C2)		C3	C4
Area	17.5	61.4	16.7	9.6
FWHM (eV)	0.9	1.6	2.4	4.9
Binding energy, BE (eV)	284.6	284.9	286	288
% concentration	16.3	59.4	15.5	8.9

Table 4-5 Main parameters for the contributions in C1s of homocoupled-SWCNTs

Table 4-5 shows that the three contributions are at least 1 eV above the binding energy of the C-Cu bond (283.6 eV[257]). Thus, C-Cu bonds are absent of the material, which indicates that the SWCNT-Ph-C≡C-Cu coupling intermediate was not created. The absence of this intermediate suggested that the homo-coupling was completed. *Figure 4-8* displays the O1s XPS spectrum of homocoupled-SWCNTs for which a good fit was achieved using 5 contributions.

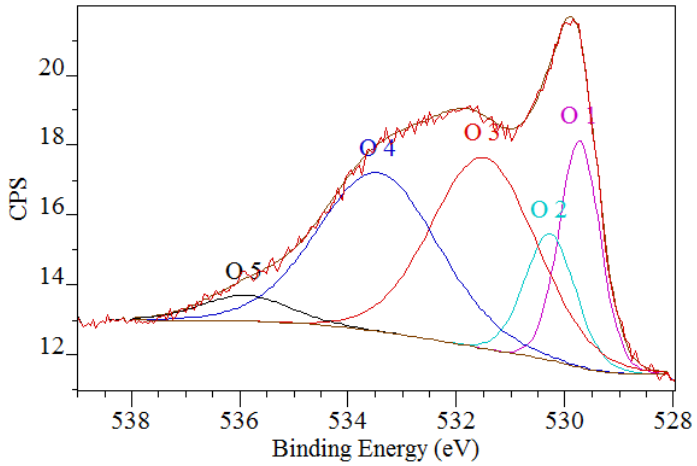

Figure 4-8 O1s XPS spectrum in homocoupled-SWCNTs

Table 4-6 displays the main parameters of the five contributions.

Contributions	Area	BE (eV)	FWHM (eV)	Con. (at%)	Groups
O1	6.2	529.7	0.9	16.1	CuO [258]
O2	4.3	530.3	1.1	11.2	Cu_2O [258]
O3	13.5	531.5	2.3	34.9	COOH [259]
O4	12.9	533.4	2.6	33.4	SiO_2 [260]
O5	1.7	535.9	1.9	4.5	CO_2 [261]

Table 4-6 Main parameters of the contributions of O1s XPS spectrum in homocoupled-SWCNTs

The O1s XPS spectrum indicates that CuO and Cu_2O are created during the homo-coupling. This was expected because this coupling was carried out in air. Contributions from SiO_2 (silicon grease), COOH (carboxylic acid grafted on the SWCNT) and adsorbed CO_2 are also identified. The CO_2 was probably located in the SWCNTs cavity, given that the Ar^+ bombardment had eliminated most of the surface contamination. The presence of CuO and Cu_2O in the homocoupled-SWCNTs explains why high concentrations of Cu and O remain (*Table 4-3*). Note: here, CuO and Cu_2O are part of the homocoupled-SWCNTs but not grafted on the SWCNTs. To further confirm the presence of CuO and Cu_2O in homocoupled-SWCNTs, the Cu2p3/2 spectrum was analysed. *Figure 4-9* displays the Cu2p3/2 XPS spectrum for homocoupled-SWCNTs.

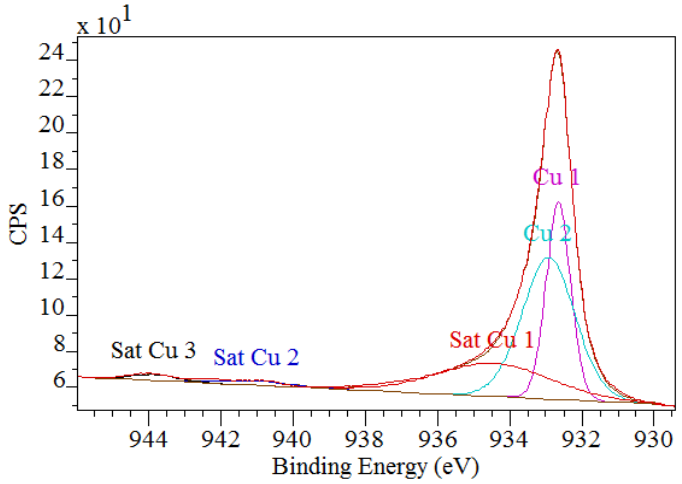

Figure 4-9 Cu2p and Cu2p3/2 XPS spectra for homocoupled-SWCNTs with 5 contributions for the Cu2p3/2 band

Figure 4-9 shows the good fitting of the Cu2p3/2 XPS spectrum with 5 contributions. The contributions consist of two components and 3 satellites[262]. The parameters of the contributions obtained from the Cu2p3/2 spectrum are grouped in *Table 4-7*.

Contributions	Area	BE (eV)	FWHM (eV)	Conc. (at%)	Groups
Cu1	93.2	932.7	0.8	28.9	Cu[263] or CuO[264]
Cu2	145.6	932.9	1.7	45.3	Cu_2O [258,262]
Sat Cu1	72.8	934.5	3.7	22.6	Cu_2O [262]
Sat Cu2	5.2	940.8	2.1	1.6	Cu_2O [262]
Sat Cu3	5.1	943.9	1.4	1.6	Cu_2O [262]

Table 4-7 Main parameters of the contributions of Cu2p3/2 XPS spectrum in homocoupled-SWCNTs

The analysis of the Cu2p3/2 XPS spectrum summarised in *Table 4-7* confirms the presence of CuO and Cu_2O. The absence of a peak at about 933.4 eV for Cu-C bond from copper carbide[265] shows that this species is not present. This supports the observations in C1s XPS spectrum showing the absence of intermediate SWCNT-Ph-C≡C-Cu.

Figures 4-10 (a) and *(b)* compare the Si2p XPS spectra of Sonogashira-SWCNTs with those of homocoupled-SWCNTs and crosscoupled-SWCNTs, respectively.

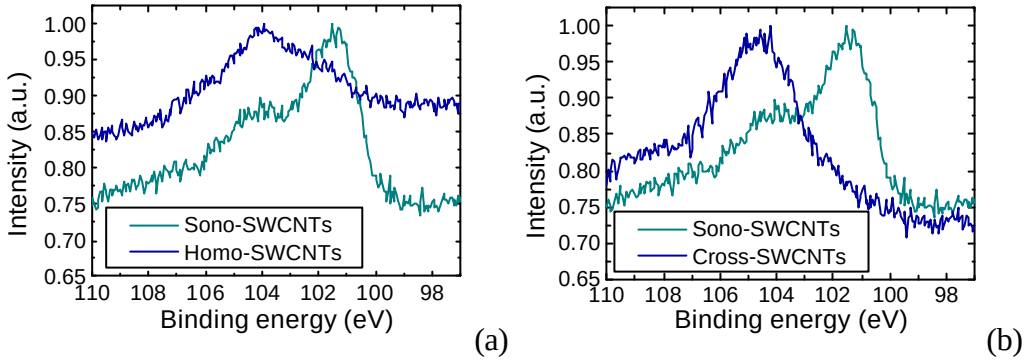

Figure 4-10 Comparison of the Si2p XPS spectra of Sonogashira-SWCNTs and (a) homocoupled-SWCNTs and (b) crosscoupled-SWCNTs

Figure 4-10 shows that the profile of the Si2p XPS spectra changed from a band with two broad 'shoulders' at the high energies in Sonogashira-SWCNTs to a band with two narrow shoulders at high and low energies in homocoupled-SWCNTs and one broad band in crosscoupled-SWCNTs. These profile changes resulted in the upshifting towards higher binding energies of the Si2p bands following both couplings. This indicates a relative decrease the amount of the Si from the functional groups compared to that of SiO_2. Detailed analyses of the Si2p XPS spectra were conducted for homocoupled-SWCNTs and crosscoupled-SWCNTs in *Figure 4-11*.

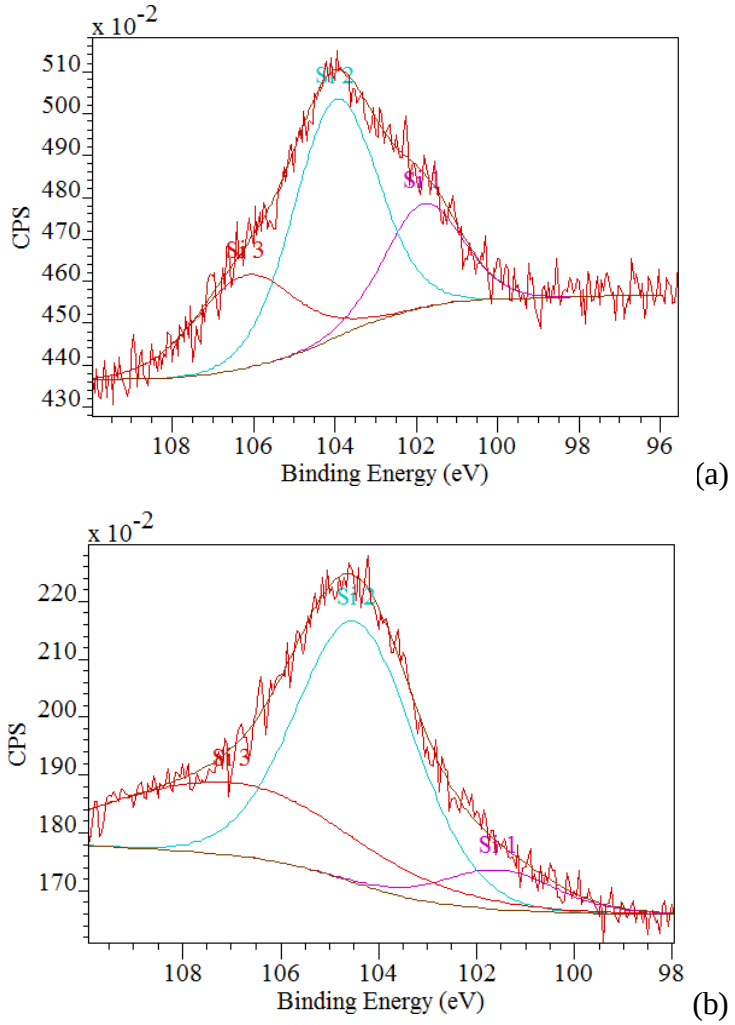

Figure 4-11 Si2p XPS spectrum of (a) homocoupled-SWCNTs and (b) crosscoupled-SWCNTs with their 3 contributions

Figure 4-11 shows that good fits were obtained using 3 components for both spectra. The ratio $\frac{Area_{Si2p\ 1/2}}{Area_{Si2p\ 3/2}}$ of 0.5 for the contribution Si2 was kept for the fitting[234]. Given their small areas, the components Si1 were represented by one peak and their FWHM was not restricted compared to that of Sonogashira-SWCNTs.

The Si2p envelopes of the homocoupled-SWCNTs and crosscoupled-SWCNT in *Figure 4-11* display different profiles to that of Sonogashira-SWCNTs (*Figure 3-17*). Indeed, Sonogashira-SWCNTs display a peak at around 101 eV with two broad "shoulders" at 103 and 107 eV. However, *Figure 4-11 (a)* shows one peak at 104 eV with two narrow "shoulders" at 101.9 and 106.3 eV. At lower binding energies, this peak was followed by a plateau-like behaviour. As a result, the position of the total Si2p spectrum shifted from 101.6 eV to 104 eV. This shifting

and the change of profile indicate the reduction of the component Si1 component at 101.6 eV, which was attributed to the contribution of Si from 1-(trimethylsilyl)-2-phenylacetylene to the Si2p peak[235]. *Figure 4-11 (b)* displays a broad Si2p peak with no visible 'shoulders'.

The main parameters of the contributions obtained from the decomposition of Si2p in homocoupled-SWCNTs and crosscoupled-SWCNTs are given in *Table 4-8.*

Contributions		Area	BE (eV)	FWHM (eV)	Conc. (at%)	Groups
Homocoupled-SWCNTs	Si1	0.6	101.9	2.2	12	Si-C[235]
	Si2	1.5	104	2.4	44.9	SiO_2[266]
	Si3	0.7	106.3	2.9	43.1	SiO_2[235,266]
Crosscoupled-SWCNTs	Si1	0.2	101.5	2.7	7.8	Si-C [235]
	Si2	1.4	104.5	2.9	59.1	SiO_2 [266]
	Si3	0.8	106.6	5.9	33.1	SiO_2 [235,266]

Table 4-8 Main parameters of the contributions for Si2p spectra in homocoupled-SWCNTs and crosscoupled-SWCNTs where Si2 and Si3 components represent the Si2p3/2 and Si2p1/2 contributions

After homo-coupling, the overall Si concentration decreases from 2.8 at% in Sonogashira-SWCNTs to 2.2 at% in crosscoupled-SWCNTs (*Figure 4-11 (a)*). The concentration of Si from 1-(trimethylsilyl)-2-phenylacetylene is calculated using a Si concentration of 2.8% to ignore CuO and Cu_2O species. These species were ignored as they are part of the contamination of the sample. Note: the 2.8 at% of Si corresponds to the Si concentration assuming no Cu and O, as these elements are part of CuO and Cu_2O not eliminated after washing.

For crosscoupled-SWCNTs (*Figure 4-11 (b)*), the comparison of the Si2p peaks, before and after cross-coupling, showed that the proportion of Si from the 1-(trimethylsilyl)-2-phenylacetylene decreased by 92.1% to reach 0.1 at% in crosscoupled-SWCNTs.

The concentration of Si, from the 1-(trimethylsilyl)-2-phenylacetylene grafted molecules, dropped from 1.8 at% in Sonogashira-SWCNTs, to 0.3 at% in homocoupled-SWCNTs. This corresponds to a diminution of 81.3% of Si concentration resulting from the homo-coupling. The reduction of Si from 1-(trimethylsilyl)-2-phenylacetylene was expected, as two trimethylsilyl groups were removed to create carbon-carbon bonds needed for the homo-coupling. The

reduction of the Si concentration added to the absence of SWCNT-Ph-C≡C-Cu intermediate, suggests that the homo-coupling had effectively occurred, and 1,2-diphenyldiacetylenes bridges were created between SWCNTs. The homocoupled-SWCNTs were contaminated by CuO and Cu_2O, which had not been removed by successive washings in organic solvents.

The concentration of the Si attributed to the 1-(trimethylsilyl)-2-phenylacetylene moieties decreased by 92.6% after cross-coupling, to reach 0.1 at% in crosscoupled-SWCNTs. The decrease of the iodine concentration, reported after the cross-coupling and homo-coupling reactions, brought further evidence supporting the covalent bridging of the SWCNTs. After the cross-coupling performed under nitrogen atmosphere, the Cu catalyst was eliminated by the washing process. This was not the case after the homo-coupling, which was carried out under air. The high level of Cu in homocoupled-SWCNTs was explained by the presence of CuO and Cu_2O, which were created due to the air atmosphere required for the homo-coupling. The Si concentrations decreased by 92.6% and 81.3% after the cross-coupling and the homo-coupling, respectively. This indicates a higher yield obtained for cross-coupling reaction. This difference is explained by the iodobenzene moieties which were in excess, compared to the 1-(trimethylsilyl)-2-phenylacetylene moieties, as a result of the use of iodobenzene-SWCNTs as precursors for the cross-coupling. Therefore, more of the 1-(trimethylsilyl)-2-phenylacetylene moieties reacted with the iodobemzene groups (cross-coupling) than with itself (in homo-coupling).

4.4 Electrical characterisation of covalent organic molecular bridged SWCNT networks

4.4.1 Current-voltage characteristics of molecular bridged SWCNT networks

Networks of molecular bridged SWCNTs were fabricated using dispersions of 2, 5, 10 and 20 ml of SWCNTs in DMF (1:10 mg/ml). These dispersions were filtered on a nylon membrane 0.2 µm pore size using a filtration device, 25 mm in diameter. *Figure 4-12* displays the I-V characteristics of the molecular bridged SWCNT networks from -10 to 10 V at room temperature, with electrode separation of 50 µm.

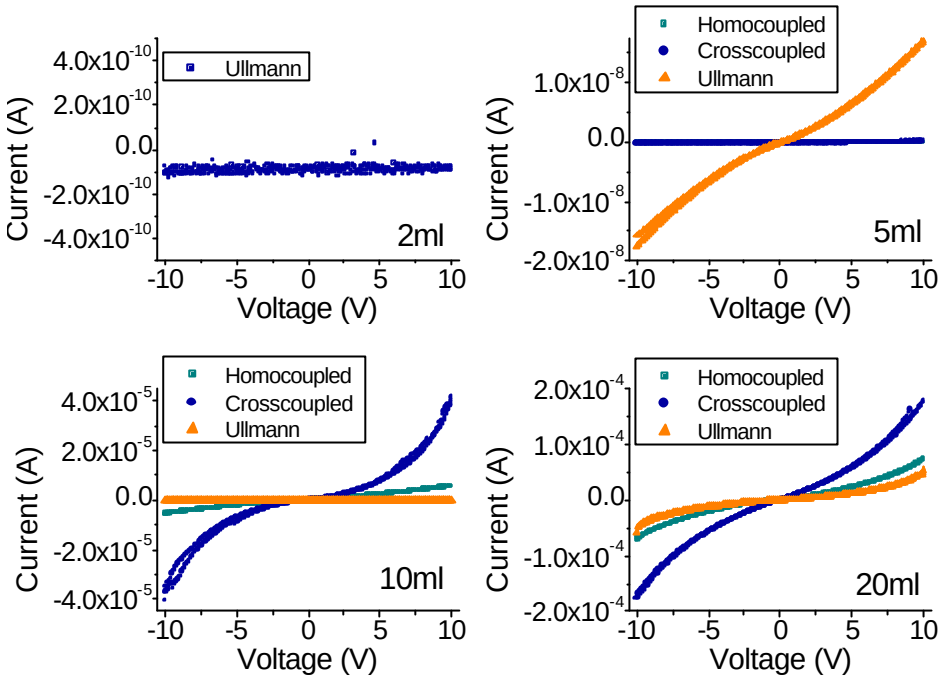

Figure 4-12 I-V characteristics of molecular bridged SWCNT networks at room temperature

Figure 4-12 shows that the Ullmann-SWCNT network fabricated with 2 ml of dispersion is insulating. While the Ullmann-SWCNT network produced with 5 ml of SWCNT dispersion displays an electrical behaviour, networks fabricated with 5 ml of homocoupled-SWCNT and crosscoupled-SWCNT are insulating. However, for 10 and 20 ml networks, the Ullmann-SWCNT networks display a lower current intensity than the homocoupled-SWCNT and crosscoupled-SWCNT networks. The concentrations obtained from the adsorption spectra suggest that higher current intensities should have been found for homocoupled-SWCNT networks as a result of their higher solubility. Homocoupled-SWCNTs displayed similar solubility to Sonogashira-SWCNTs but their 5 ml networks are insulating. This suggests that the behaviour of the 5 ml Sonogashira-SWCNT network in *Figure 3-22* is explained by the non homogeneity of the network, which led to an absence of percolation path, as it was the case for the Sonogashira-SWCNT network fabricated with 2 ml of SWCNT dispersion (see *section 3.7.1*). The I-V characteristics of the molecular bridged SWCNT networks have symmetrical trends, as expected from the junctions between the SWCNT networks and the electrodes. The evolution of the current with the filtered volume is shown in *Figure 4-13*.

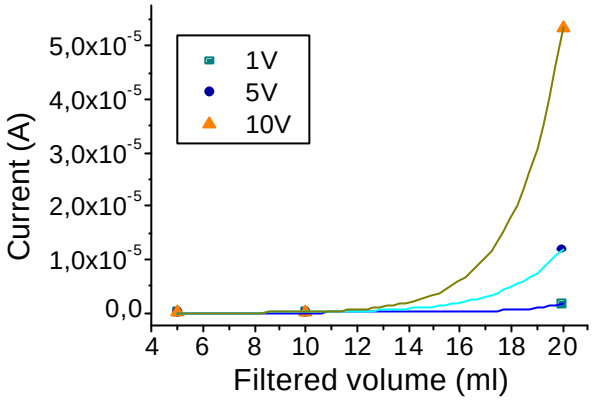

Figure 4-13 Current versus filtered volume plots for Ullmann-SWCNT networks at 1, 5 and 10 V

Figure 4-13 shows that the variation of the current with the filtered volume is analogous to that of Sonogashira-SWCNT networks. The concentration of Ullmann-SWCNTs and Sonogashira-SWCNTs in DMF are 4.2 mg/L and 4.7 mg/L, respectively. This indicates that the solubility of Ullmann-SWCNTs and Sonogashira-SWCNTs are about the same. Thus, the explanation given for the current levels in Sonogashira-SWCNT networks (*section 3.6.2*) is also valid here. The 5 ml networks are also expected to be non homogenous and as a result, these networks should exhibit an insulating behaviour due to the absence of conductive percolation path for 50 µm of electrode separation. Consequently, the I-T characteristics measurements were only carried out for the 10 and 20 ml Ullmann-SWCNT networks.

4.4.2 Current-temperature characteristics of molecular bridged SWCNT networks

Figure 4-14 shows the I-T characteristics from 100 to 350 K at 0.5, 1, 5 and 10 V for molecular bridged SWCNT networks made by filtrating 10 ml of SWCNT dispersions.

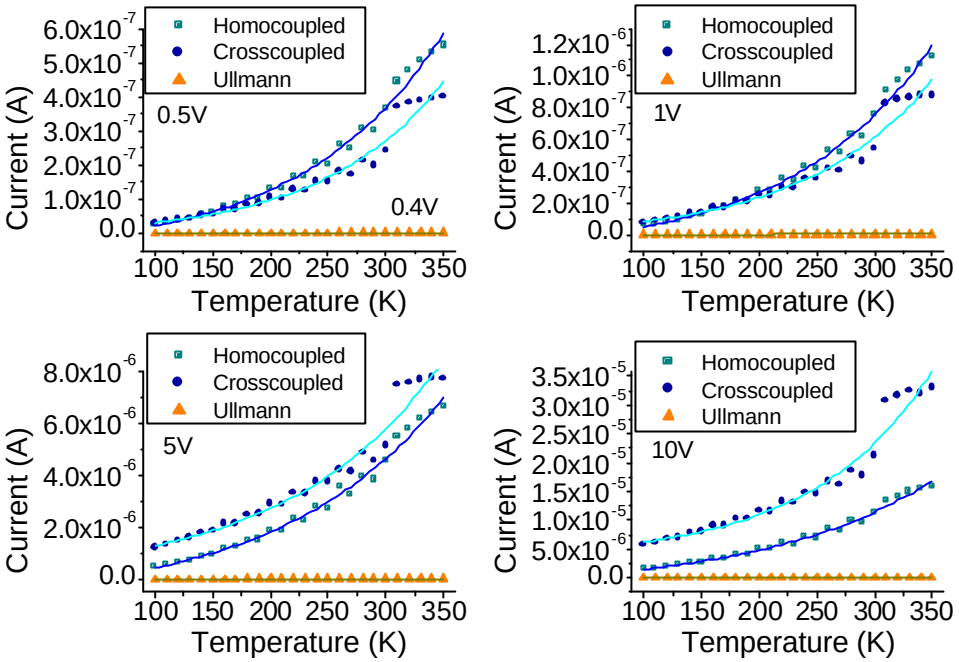

Figure 4-14 I-T characteristics in 10 ml networks of molecular bridged SWCNTs

Figure 4-14 shows that current of the 10 ml molecular bridged SWCNT networks decreases as the temperature is reduced. The I-T characteristics were fitted according to *equation 3-3* and the values of the x_0 fitting parameters are given in *Table 4-9*.

Voltage (V)	Bridged SWCNT networks		
	Homocoupled	Crosscoupled	Ullmann
0.5[xvii]	122±10	105±15	98±8
1	124±11	111±17	109±11
5	139±13	132±23	121±12
10	144±14	103±16	138±13

Table 4-9 Values of x_0 fitting parameters in 10 ml networks of molecular bridged SWCNTs

The high values of the x_0 parameters suggest a weak temperature dependence of the current measured in the molecular bridged SWCNT networks. In the following, I-V and I-T characteristics are detailed for each molecular bridged SWCNT network in order to identify the dominant conduction mechanism across these networks. The same analysis method used to identify the conduction in Sonogashira-SWCNT networks is employed here.

[xvii] 0.4V for Ullmann-SWCNT networks

4.4.3 Conduction mechanisms in bridged SWCNT networks

This section investigates the dominant conduction model governing the electronic transport across networks of SWCNTs covalently bridged by conjugated molecules. The analysis was conducted according to the method used to identify the conduction model across SWCNT precursor networks. The current-temperature characteristics of covalently bridged SWCNT networks were measured within the same temperature range as in SWCNT precursor networks. The donor-acceptor hopping model is invalid within this temperature range (100-350 K) as stated in *section 3.7.4.2*. Thus, this model was discounted in this analysis. The electrical characteristics of the covalently bridged SWCNT were also analysed according to the VRH model. These studies led to the same results as for the SWCNT precursor networks (see *Appendix C*).

$ln(I)$ *versus T* plots of the I-T characteristics (not shown here) were used to find the constant *A* of *equation 3-12*. Then, the values of *A* for each bridged SWCNT network shown in *Table 4-10* were integrated into *equation 3-12* for the fittings of both I-V and I-T plots.

Network	Filtered volume (ml)	Constant A values
Homocoupled-SWCNTs	10	0.011
	20	0.006
Crosscoupled-SWCNTs	10	0.009
	20	0.009
Ullmann-SWCNTs	10	0.01
	20	0.008

Table 4-10 Values of constant A for 10 and 20 ml networks of bridged SWCNTs

Table 4-10 shows the values of the constant *A* for 10 and 20 ml bridged SWCNT networks, which will be used for the fittings of both I-V and I-T plots. *Figure 4-15* displays the I-V plots at room temperature with their fittings according to the modified quantum tunnelling model for networks of homocoupled-SWCNTs, crosscoupled-SWCNTs and Ullmann-SWCNTs.

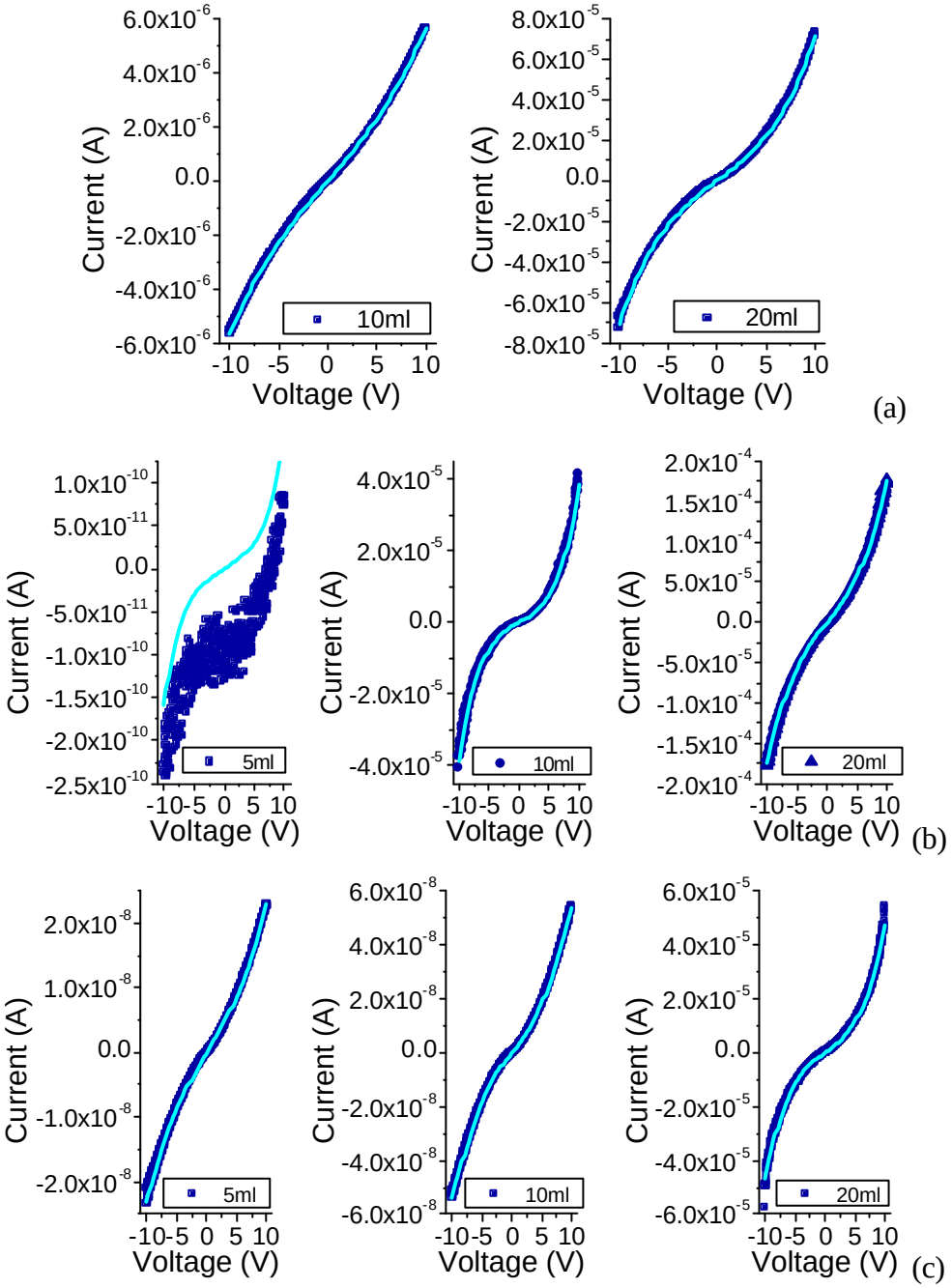

Figure 4-15 I-V characteristics with their fittings according to equation 3-12 for 10 and 20 ml networks of (a) homocoupled-SWCNTs, (b) crosscoupled-SWCNTs and (c) Ullmann-SWCNTs

Figure 4-15 shows that good fits of the I-V characteristics were reached using *equation 3-12* for all bridged SWCNT networks on the whole voltage range.

Figure 4-16 displays the I-T plots at 0.5, 1, 5 and 10 V with their fittings according to *equation 3-12* for the 10 and 20 ml networks of homocoupled-SWCNTs, crosscoupled-SWCNTs and Ullmann-SWCNTs.

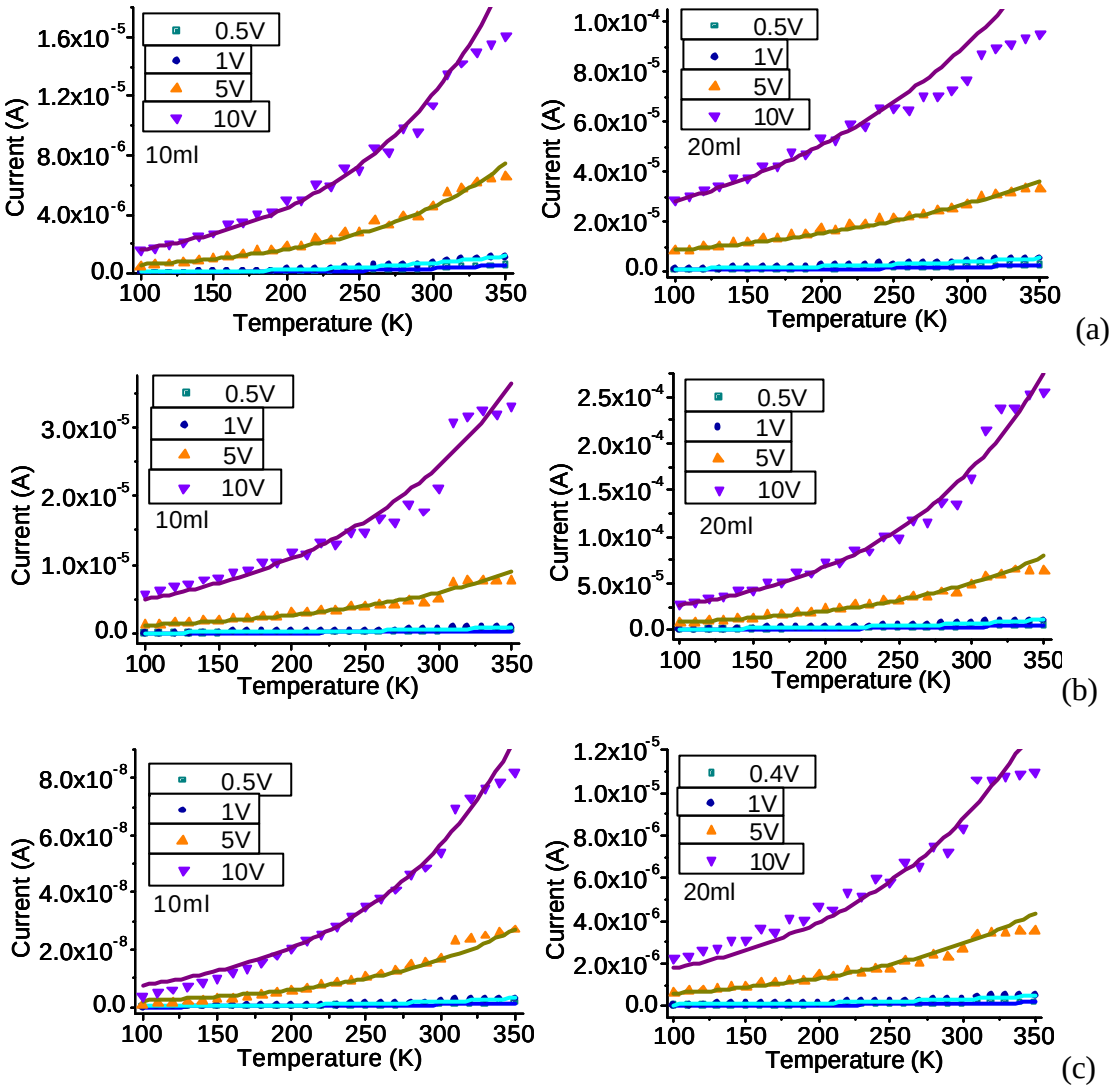

Figure 4-16 I-T characteristics at 0.5, 1, 5 and 10 V with their fittings according to eq. 3-12 for 10 and 20 ml of (a) homocoupled-SWCNTs, (b) crosscoupled-SWCNTs and (c) Ullmann-SWCNTs

Figure 4-16 shows that good fits of *equation 3-12* were reached for the I-T characteristics of all bridged SWCNT networks. This indicates that the conduction is dominated by quantum tunnelling. *Figure 4-16* (a) shows that, between 330 and 350 K, the I-T plots for the 10 ml network at 10 V slightly deviate from the fitting plot. Similar deviation occurs from 260 K on the 10 V plot of the 20 ml homocoupled-SWCNT network. *Equation 3-12* leads to good fits for both I-V and I-T characteristics. Following the analysis in *section 3.5.6.4*, these results indicate that quantum tunnelling govern the conduction mechanisms across all covalently bridged SWCNT networks. This was expected, given that the I-V and I-T plots of bridged SWCNT networks follow similar trends than those of SWCNT precursor networks.

4.4.4 Discussion on bridged SWCNTs

A modified version of the Sonogashira reaction was used to create carbon-carbon bonds from the homo-coupling of two silyl groups (see *Figure 4-1*). This homo-coupling reaction presents two advantages: the bridging of SWCNTs occurs in DMF and no activator of the reaction is required[255]. The UV-visible-near IR analysis was inconclusive on determining whether or not the bridging occurred. However, XPS analysis suggested that the homo-coupling was successful. In fact, the XPS analysis established that the relative concentration of silicon from the 1-(trimethylsilyl)-2-phenylacetylene moieties decreased by 82.1% to reach 0.3 at%. in homocoupled-SWCNTs. The high atomic concentrations of Cu and O after homo-coupling were attributed to CuO and Cu_2O. Overall, the data provided by the analyses of the homocoupled-SWCNTs suggests that the bridging of the SWCNTs with 1,2-diphenyladicetylene molecules occurred.

The cross-coupling of silyl and aryl groups from the SWCNT precursors created 1,2 diphenylacetylene bridges, according to the reaction scheme shown in *Figure 4-2*. These crosscoupled-SWCNTs displayed an absorption spectrum clearly different than the spectra of Sonogashira-SWCNTs and iodobenzene-SWCNT. XPS analysis carried out on crosscoupled-SWCNTs established that after the cross-coupling reaction, the silicon concentration from the 1-(trimethylsilyl)-2-phenylacetylene moieties fell by 92.6% to reach 0.1 at% in crosscoupled-SWCNTs. The relative iodine concentration obtained in the crosscoupled-SWCNTs was shown to be lower than in Sonogashira-SWCNTs and iodobenzene-SWCNTs. This indirect evidence suggests that 1,2 diphenylacetylene molecules bridge the SWCNTs.

SWCNTs were also bridged by biaryls molecules via Ullmann reaction according to the scheme presented in *Figure 4-3*. Absorption spectra showed that the solubility of the SWCNTs decreased after Ullmann reaction. XPS analysis performed on the Ullmann-SWCNTs established that the reaction causes the amount of iodine to drop from 2.5 at%. to 0.2 at%.

The electrical characterisations of the homocoupled-SWCNT, crosscoupled-SWCNT and Ullmann-SWCNT networks were carried out under conditions identical to those used for the SWCNT precursor networks. Good fittings of both I-V and I-T characteristics were obtained using the modified quantum tunnelling model proposed

in *section 3.7*. Consequently, quantum tunnelling was found as the dominant conduction mechanism across the bridged SWCNT networks. The result of a conduction dominated by tunnelling mechanisms is further supported by *Figure 4-14* and *Table 4-9*, where small current variations with the temperature are observed, as tunnelling currents are known to display little temperature dependence[173]. For thin SWCNT networks, a conduction dominated by tunnelling mechanisms would be expected, as stated in *section 3.7.4*[119]. The study of electrical characteristics of bridged SWCNTs networks led to the same conclusion as for the SWCNT precursor networks. Thus, the presence of these molecules, covalently bridging the SWCNTs in the networks, does not alter the conduction mechanisms.

4.5 Conclusion

Interconnecting carbon nanotubes with molecules was shown to improve their interaction so that better mechanical and electrical properties are expected[248,267]. In this chapter, iodobenzene-SWCNTs and Sonogashira-SWCNTs precursors were coupled to create organic molecular bridges between SWCNTs. Modified Sonogashira couplings were used to perform homo-couplings and cross-couplings with the Sonogashira-SWCNTs, and Ullmann coupling was used for the homo-coupling of iodobenzene-SWCNTs. 1,2-phenyl diacetylene, 1,2-phenyl acetylene and biaryls were created, as molecular linkers between SWCNTs, following the homo-coupling of Sonogashira-SWCNTs, the cross-coupling of iodobenzene-SWCNTs with Sonogashira-SWCNTs and the Ullmann-coupling of iodobenzene-SWCNTs, respectively. Given that the coupling occurred on the functional groups, the use of Raman and UV-visible-near IR spectroscopies to monitor changes on the SWCNTs was irrelevant. These spectroscopies are used to detect changes in the SWCNT structure so their structures are not affected by the subsequent coupling on the functional groups. The fact that these spectroscopies were inadequate made difficult the characterisation of the bridged-SWCNTs, as the bridges are organic molecules. Thus, indirect evidence (XPS and absorption spectra) suggested that SWCNT bridging occurred for all couplings. This conclusion was essentially based on the study of Si and I concentrations. XPS analysis showed a maximum of 1.6 at% of carbon in crosscoupled-SWCNTs contributes to the bridging. This proportion

decreases to 1.2 at% and 0.7 at% in Ullmann-SWCNTs and homocoupled-SWCNTs, respectively. Small amounts of these covalent bridges are presented in the SWCNTs, as expected from the low functionalisation level following the radical addition. Different approaches, where both extremities of molecules were simultaneously bonded to SWCNTs, were reported to covalently bridge SWCNTs[248,253-254]. Contrary to the methods reported, the work presented in this chapter relies on organometallic couplings with an intermediate step, which helps to attest by spectroscopy the success of the bridging. In this case, the bridging of SWCNTs occurs when carbon-carbon bonds are created between two functionalised groups.

The conjugated molecular bridges add another type of junction between SWCNTs. These junctions are represented in small amounts; equivalent to around 1 at% of C atoms. Networks of homocoupled-SWCNTs, crosscoupled-SWCNTs and Ullmann-SWCNTs were prepared by filtration where SWCNT dispersions are filtered on nylon membranes (see *section 3.2*).

Electrical characteristics from measurements carried out with 50 µm electrode separation were studied, to determine the dominant conduction mechanism in these networks. The characteristics were analysed according to the method used in *section 3.7* where both current-voltage and current-temperature measurements were exploited. The quantum tunnelling model[242] provided pretty good fits of the I-V characteristics. Nonetheless, it is an intuitively modified expression of this model which described best both the I-V and I-T characteristics. Thus, quantum tunnelling was identified as the mechanism governing the electronic conduction across these four types of bridged SWCNT networks. The possibility of VRH mechanisms occurring in parallel could not be totally discounted, particularly within the high temperature range, where deviations for the I-T plot fitting were observed. It is expected that the probability for hopping mechanisms to occur increases at higher temperature as hopping is known to be a thermally activated transfer[179]. In addition, the temperature dependence of the electrical conductivity in MWCNT bulk materials showed that the conduction followed a heterogeneous model of both fluctuation-assisted tunnelling and VRH in the 328-958°K temperature range[268]. Thus, it is suggested that the small deviations of plots from the fitting lines in the 310-350 K temperature range are explained by a higher occurrence of VRH in this temperature range.

The results of the electrical characteristics analysis of the organic molecular bridged SWCNT networks are consistent with those obtained for SWCNT precursor networks in *Chapter 3*. This indicates that the presence of conductive molecular bridges between some SWCNTs, does not affect the conduction mechanism across SWCNT networks.

This can be explained by three reasons:

1) the bonds created between the SWCNTs and the conductive bridges block charges, therefore they do not facilitate the charge transport
2) compared to the nanotube-nanotube junctions, the molecular bridges junctions have less charge transfer capability
3) there is no continuous bridged SWCNT network which extends across the 50 µm electrode separation, as a result of a low level of SWCNT functionalisation.

4.6 Summary

This chapter dealt with the fabrication and electrical study of organic molecular bridged SWCNTs. SWCNT precursors were bridged via carbon-carbon bonds created by modified Sonogashira couplings and Ullmann couplings. This contrasts with the diamide approach usually employed to bridge the SWCNTs. In previously reported work, the SWCNT bridging was assessed by microscopic analyses, as demonstrating the simultaneous bonding of both extremities of diamide molecules with nanotubes is not possible. Here, indirect evidence provided by spectroscopic analyses support the presence of 1,2-phenylacetylene, 1,2-phenyldiacetylene and biaryls as molecular bridged.

A modified quantum tunnelling model was found to best describe the electrical characteristics of all molecularly bridged SWCNT networks. However, the occurrence of VRH mechanisms cannot be discounted, particularly for high temperatures. These results are the same as those found for the SWCNT precursor networks. Thus, the presence of such molecular bridges between SWCNTs does not affect the conduction mechanism across the SWCNT networks.

Chapter 5
Platinum-enriched SWCNT networks

5.1 Introduction

Metallic functionalisation of nanotubes was achieved by employing both non covalent[269] and covalent[270-271] methods for applications such as hydrogen storage[272], nanowire actuators[273], glucose sensors[274] and proton exchange membrane fuel cells[275]. The fabrication of nanocomposite networks of SWCNT/Pt nanoparticles were also demonstrated but their charge transport was not analysed[276].

In this chapter, efforts were focused on coordinating Pt with pyridine-SWCNTs. An attempt to bridge two SWCNTs with Pt via pyridine ligands is also discussed. The electronic conduction across Pt-SWCNTs networks was subsequently identified from the combined study of their I-V and I-T characteristics.

5.2 Principle

Lewis adducts are created between pyridine (Lewis base) and metal (Lewis acid) by the formation of coordinate covalent bonds, using the nitrogen's lone pairs. Pyridine-SWCNTs constituted the system ligand-SWCNTs and were coordinated to the Pt. The scheme of the reaction is shown in *Figure 5-1*.

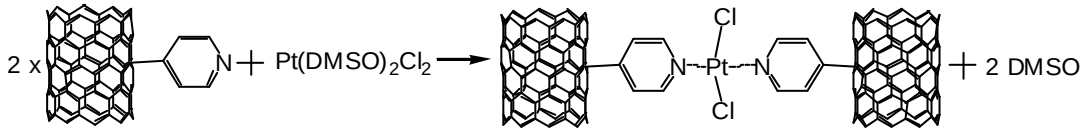

Figure 5-1 Scheme of the coordination of Pt with pyridine-SWCNTs to form Pt-SWCNTs

During the coordination, the amount of Pt was limited to about half of the quantity of N from pyridine to avoid saturating pyridine groups with Pt and achieve the Pt-bridging of pyridine-SWCNTs.

5.3 Characterization of Pt-SWCNTs

5.3.1 UV-visible-near IR spectroscopy

Absorption spectra recorded before and after Pt coordination are displayed in *Figure 5-2.*

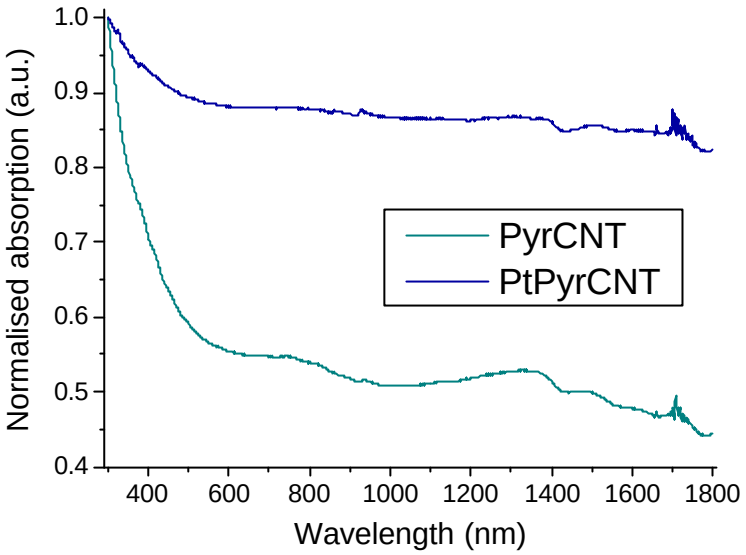

Figure 5-2 Absorption spectra normalised at 300 nm of saturated dispersions in DMF of pyridine-SWCNTs and Pt-SWCNTs

The absorption profile found after the coupling reaction is different than that found before reaction. *Table 5-1* displays the concentrations at 500 nm (using *equation 3-1*) of dispersions of Pt-SWCNTs and its pyridine-SWCNT precursors in DMF.

	Pyridine-SWCNTs	Pt-SWCNTs
Concentration at 500 nm (mg/L)	6	5

Table 5-1 Concentrations of oversaturated dispersions of pyridine-SWCNTs and Pt-SWCNTs

Table 5-1 shows a reduction of solubility of the SWCNTs as a result of the Pt coordination.

5.3.2 ICP spectroscopy

Inductively coupled plasma (ICP) spectroscopy attests to the presence of Pt in the Pt-SWCNTs. The Pt level in Pt-SWCNTs was typically 3.1%wt. As a control reaction,

methyl-1-pyridine-SWCNTs were mixed with Pt. The presence of the methyl group bonded to the nitrogen of the pyridine moieties is known to neutralise the lone pair of the nitrogen atom. Thus, traces of Pt were expected for the control sample. However, the Pt weight concentration in methyl-1-pyridine-SWCNTs yielded 3.4%wt. Similar quantities of Pt were obtained for the control reaction. This indicates that the presence of Pt in the SWCNTs does not only result from the coordination of Pt with the pyridine groups. Thus, the ICP spectroscopy data suggests that Pt is either adsorbed on the SWCNTs or coordinated with other groups grafted on the SWCNTs surface. In *Chapter 3, Table 3-9* indicated the presence of pyridinium and nitrosopyridine groups on the pyridine-SWCNTs. For the pyridinium, the H bonded to the N does not allow the coordination. However, for the nitroso groups, the two lone pairs of O suggest that nitrosopyridine groups can also coordinate with the Pt.

5.3.3 XPS analysis

XPS spectra of the Pt-SWCNTs were recorded after Ar^+ etching of the surface at 3 kV for 30 s. The C1s, O1s, N1s and Pt4f XPS spectra in pyridine-SWCNTs and Pt-SWCNTs are displayed in *Figure 5-3*.

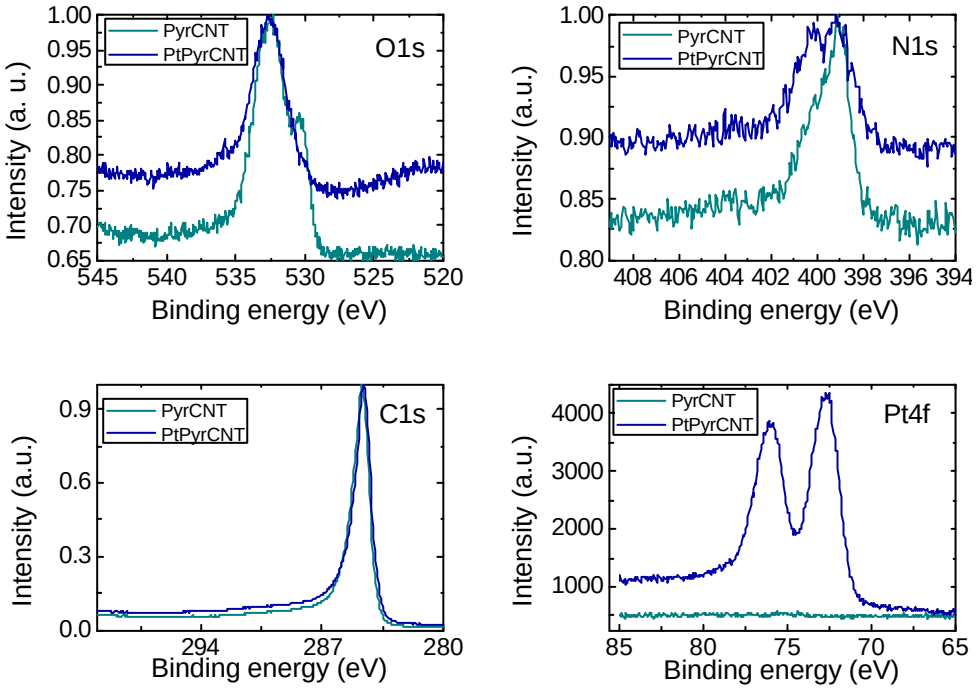

Figure 5-3 C1s, O1s, N1s and Pt4f XPS spectra in pyridine-SWCNTs and Pt-SWCNTs

Figure 5-3 shows that the C1s spectrum did not change and the Pt4f spectrum appeared in the Pt-SWCNTs as expected. Changes in the O1s and N1s spectra are both visible. After coordination, the low energy contribution disappeared in the O1s spectrum. In the N1s spectrum of Pt-SWCNTs, the 'shoulder', already present in the N1s spectrum in pyridine-SWCNTs, became a separate band, moreover, a new component appeared at low energy. Atomic concentrations, binding energies and FWHM of the elements identified in Pt-SWCNTs are grouped in *Table 5-2*.

Elements	Concentration (at%)	BE (eV)	FWHM (eV)
C1s	94.4	284.6	1.1
O1s	2.6	532.6	2.7
N1s	1.5	399.2	2.7
Cl2p	0.8	200	3.1
Pt4f	0.7	72.5	1.9

Table 5-2 Relative atomic concentration of the elements present in Pt-SWCNTs

The proportion of N from the pyridine groups in Pt-SWCNTs is considered the same as its proportion in pyridine-SWCNTs: 43.5% (see *Table 3-6*). Thus, the concentration of N from pyridine groups in Pt-SWCNTs is estimated at 0.7 at%. *Table 5-2* shows that in Pt-SWCNTs, the concentrations of Pt and N from pyridine are the same. Detailed analysis of the XPS spectra of Pt4f, N1s and O1s are available below.

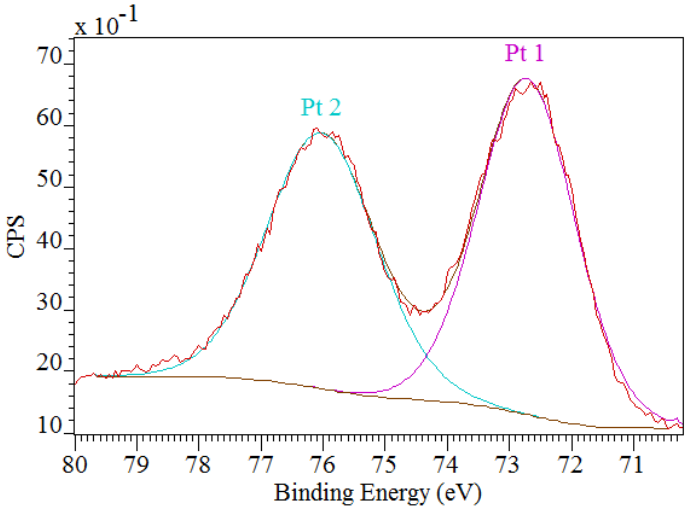

Figure 5-4 Pt4f XPS spectrum in Pt-SWCNTs

The main parameters of Pt1 and Pt2 components are grouped in *Table 5-3*.

Component	Area	Binding energy (eV)	FWHM (eV)	Concentration (at%)	Groups
Pt1 (Pt4f7/2)	10.8	72.7	1.8	53.1	Pt→O[277] Pt→N[278]
Pt2 (Pt4f5/2)	9.5	76.0	2.1	46.9	-

Table 5-3 M ain parameters of Pt1 and Pt2 components

Figure 5-4 displays the Pt4f XPS spectrum in Pt-SWCNTs and shows a well defined doublet of the Pt4f spectrum. Given the wide range of binding energies reported for Pt4f in presence of Cl, O and N ligands[278], it was not possible to assign confidently, the binding energy of Pt4f to coordination with O or N from the Pt4f spectrum. *Figure 5-5* displays the N1s XPS spectrum in Pt-SWCNTs.

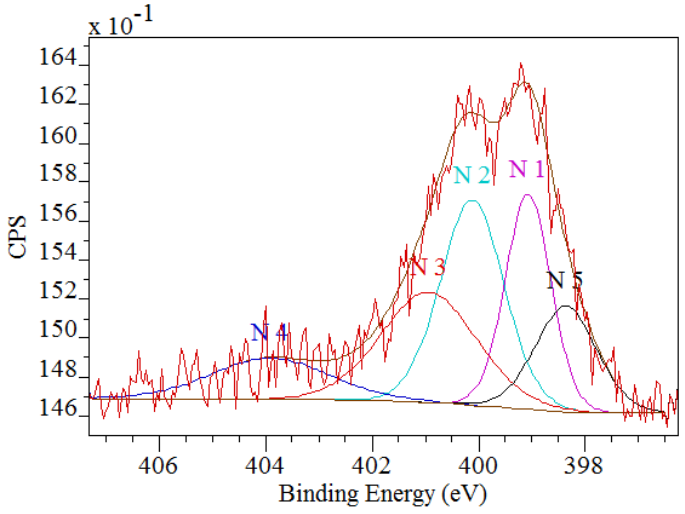

c)

Figure 5-5 N1s XPS spectrum in Pt-SWCNTs

Figure 5-5 shows good fits of the N1s spectrum using 5 components. Note that the binding energies of components N1 to N4 were constrained to ± 0.1 eV of their binding energies in pyridine-SWCNTs (see *Table 3-6*). *Table 5-4* displays the main parameters of the components of the N1s spectrum.

Component	Area	BE (eV)	FWHM (eV)	Conc. (at%)	Groups
N1	1.2	399.1	1	21.2	Pyridine[229]
N2	1.6	400.1	1.4	28.9	Pyridinium[229]
N3	1.3	400.9	2.1	23.4	Nitrosopyridine[230]
N4	0.6	403.8	2.6	11.3	Adsorbed N_2 [231]
N5	0.8	398.4	1.4	15.3	N-Pt bond[279]

Table 5-4 Main parameters of the components of N1s spectrum

Table 5-4 shows that only 0.6 at% of N from the pyridine moieties were available in the Pt-SWCNTs compared to the 0.8 at% expected from the XPS analysis in *section 3.5.4.2*. This difference is attributed to local variations in the surface samples. According to *Table 5-4*, 42% of N from pyridine moieties coordinated with the Pt. This corresponds to 0.2 at% of N-Pt bonds. Less than half of the pyridine moieties coordinated with the Pt, indicating that the coordination was not completed. *Table 5-2* showed that Pt-SWCNTs contained 0.7 at% of Pt. However, only 34.9% of the Pt coordinated with the pyridine moieties. This confirms the results obtained from the ICP spectroscopy, which showed that the presence of Pt in the Pt-SWCNTs was not only due to the coordination with pyridine moieties. The low level of coordination also suggests that Pt bridges were not formed. *Figure 5-6* displays the O1s XPS spectra for pyridine-SWCNTs and Pt-SWCNTs.

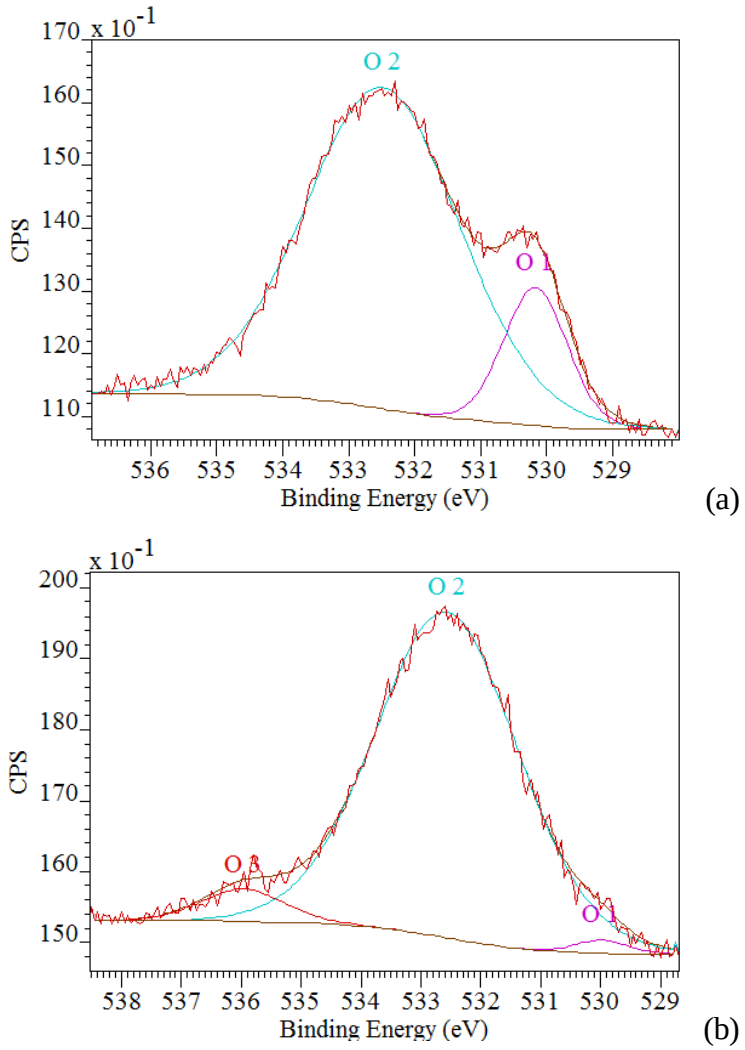

Figure 5-6 O1s XPS spectrum in (a) pyridine-SWCNTs and (b) Pt-SWCNTs

Figure 5-6 (b) shows that the O1s spectrum was fitted using three components where O1 and O2 were constrained to ±0.2 eV[xviii] of the binding energy and FWHM in pyridine-SWCNTs. The profile of the O1s band noticeably changed after Pt exposure and a good fit required the addition of a new component O3 indicating a change after exposure to Pt. *Table 5-5* displays the parameters of the O1s spectra's components.

Components		Area	BE (eV)	FWHM (eV)	Conc (at%)	Groups
Pyridine-SWCNTs	O1	2.7	530.2	1.1	15.0	O-Fe[280-281]
	O2	15.2	532.5	2.7	85	N_2O[282]
Pt-SWCNTs	O1	0.2	530	1[xix]	1.0	O-Fe[280-281]
	O2	14	532.6	2.8	93.8	N_2O[282]
	O3	0.8	536	1.6	5.2	Adsorbed H_2O[283] Carbonate complexes[284]

Table 5-5 O1s components in pyridine-SWCNTs and Pt-SWCNTs

The O1 component found in pyridine-SWCNTs is believed to be residues of iron catalyst oxidised during the purification process. The O2 component was attributed to nitroso groups. This was expected as nitrosopyridine groups were detected by TGA-MS (see *section 3.5.5*). The binding energy of the O3 component does not correspond to the binding energies reported for O-Pt bonds at about 528.8[285] or 531.9 eV[277]. Adsorbed H_2O was identified as a possible chemical environment for the O3 component. Thus, O1s spectra showed that O-Pt bonds were not created after Pt exposure. This eliminates any possibility of coordination of the Pt with nitrosopyridine, as suggested in *section 5.3.2*. Thus, most of the Pt (0.4 at%) in Pt-SWCNTs is adsorbed on the SWCNTs.

Pt-N bonds detected in Pt-SWCNTs showed that the coordination of the Pt to the pyridine-SWCNT is possible despite a low yield. The low concentration of Pt-N bonds in Pt-SWCNTs suggests that it is unlikely that Pt bridges were built between SWCNTs. The N1s and O1s XPS spectra analyses indicated that most of the Pt (0.4 at%) is adsorbed on the SWCNTs rather than coordinated to the pyridine moieties. These results confirm the ICP spectroscopy analysis, which showed that the same

[xviii] Resolution of the X-ray photoelectron spectrometer
[xix] Minimum FWHM restricted to 1 eV

amount of Pt was detected for the control reaction. Thus, rather than bridging pyridine-SWCNTs, one Pt coordinated with one pyridine as described by the scheme in *Figure 5*-7.

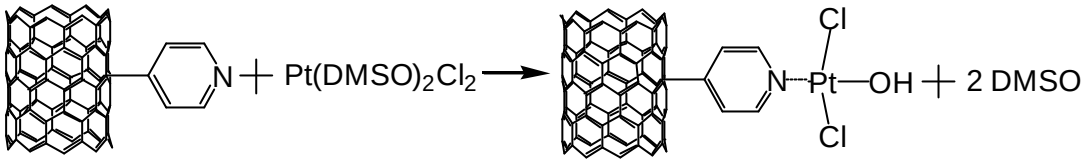

Figure 5-7 Scheme of actual Pt coordination with pyridine-SWCNT

Although the Pt-SWCNTs do not contain bridged SWCNTs, the presence of Pt enriches the SWCNTs. It is possible for the Pt enriching the SWCNT networks to create localised states whose presence can influence the conduction mechanisms. For instance, the electrical study of SWCNT LbL networks (see *Chapter 2*) revealed that the ionic surfactants introduced traps, which induced a Poole-Frenkel conduction mechanism. Thus, the electrical characteristics of Pt-SWCNTs networks were studied to identify their conduction mechanism.

5.4 Electrical characterization of Pt-SWCNT networks

Networks of Pt-SWCNTs were fabricated by filtering 2, 5 and 10 ml of the supernatant of Pt-SWCNT dispersion (1:10 mg/ml) in DMF on a nylon membrane. Electrical characteristics of the Pt-SWCNT networks were measured, in a ±10 V voltage range and 100-350 K temperature range, using Ti/Au electrodes with 50 μm of electrode separation deposited on top of the network using a shadow mask.

5.4.1 Current-voltage characteristics

I-V characteristics of Pt-SWCNT networks at room temperature are presented in *Figure 5-8* using the electrode configuration mentioned above.

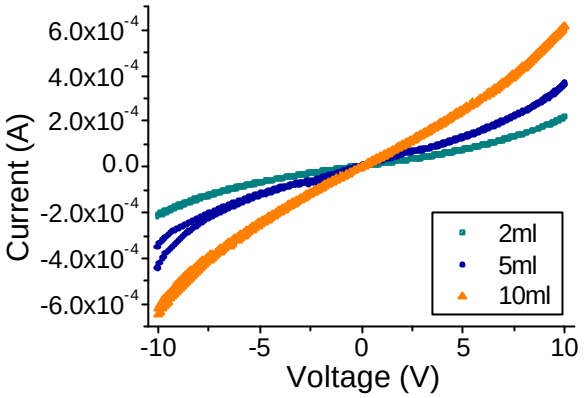

Figure 5-8 I-V characteristics at room temperature for 2, 5 and 10 ml Pt-SWCNT networks

Figure 5-8 shows that the reverse and forward I-V characteristics are symmetrical in the range of ± 10 V as expected. The current network thickness characteristics at 1, 5 and 10 V are extracted from these plots and displayed in *Figure 5-9*.

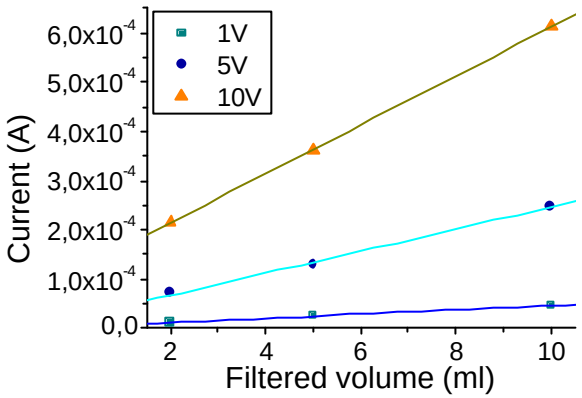

Figure 5-9 Current versus filtered volume plots at 1, 5 and 10 V for Pt-SWCNT networks

Figure 5-9 shows that the current versus filtered volume characteristics of the Pt-SWCNT networks were well fitted by linear *equation 5-1*.

$$y = Ax + B \qquad (5\text{-}1)$$

The linear behaviour of the current versus network thickness characteristics, observed for Pt-SWCNT networks, contrast with those of pyridine-SWCNT networks, which displayed an asymptotic behaviour (see *Figure 3-20 (b)*).

5.4.2 Current-temperature characteristics

The temperature dependence of the current was extracted from the I-V measurements. *Figure 5-10* displays I-T characteristics at 0.5, 1, 5 and 10 V.

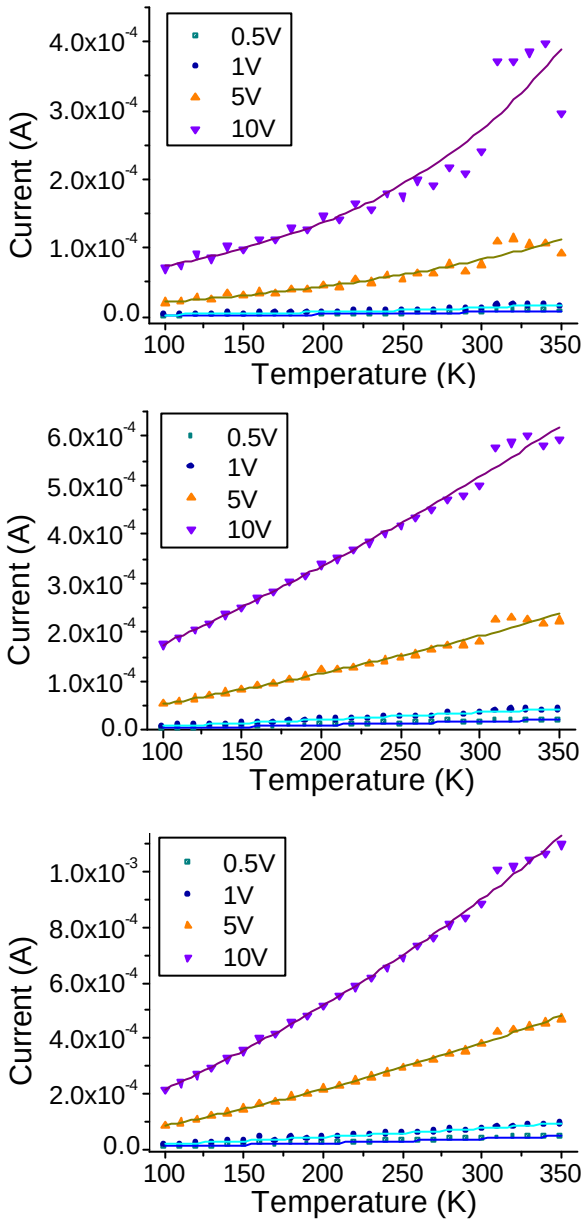

Figure 5-10 I-T characteristics at 0.5, 1, 5 and 10 V for Pt-SWCNT network fabricated with dispersions of (a) 2 ml (b) 5 ml and (c) 10 ml

Figure 5-10 shows that the current decreases with the temperature for all voltages. The fitting parameter x_0 for the I-T plots of 2, 5 and 10 ml Pt-SWCNT networks are grouped in *Table 5-6*.

Voltage	x_0 fitting parameter		
(V)	2 ml	5 ml	10 ml
0.5	187	1042	504
1	187	1116	532
5	189	509	433
10	132	695	433

Table 5-6 x_0 fitting parameters for I-T plots of 2, 5 and 10 ml Pt-SWCNT networks

The high values of x_0 fitting parameters shown in *Table 5-6* indicate a small current dependence on the temperature. This is similar to the I-T plots fitted in *Chapters 3* and *4*. This therefore suggests that tunnelling mechanisms govern the conduction.

5.4.3 Conduction mechanism in Pt-SWCNT networks

The current dependence on the temperature and voltage were used to identify the dominant conduction in the Pt-SWCNT networks. The electrical characteristics of Pt-SWCNT networks were measured within the same temperature and voltage range as in SWCNT precursor and bridged SWCNT networks. These characteristics were both plotted, according to the analytical expressions of the donor-acceptor hopping and VRH models in *Appendix D*. The analyses conducted for these models resulted in the conclusions stated in *section 3.7.4.2*, so both models were discounted. This section presents the analysis conducted according to the modified quantum tunnelling mechanism proposed in *Chapter 3*.

Values of *A* for each network shown in *Table 5-7* are integrated into *equation 3-12* for the fittings of I-V and I-T plots.

Filtered volume (ml)	Constant A values
2	0.007
5	0.006
10	0.007

Table 5-7 Values of constant A for Pt-SWCNT networks

Figure 5-11 displays the I-V characteristics of Pt-SWCNT networks fitted according to *equation 3-12*.

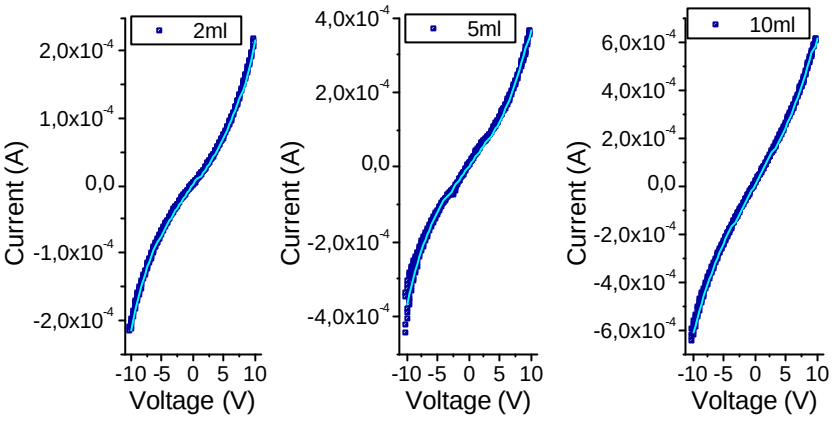

Figure 5-11 Room temperature I-V characteristics of 2, 5 and 10 ml Pt-SWCNT networks fitted according to equation 3-12

Figure 5-11 shows that good fits of the characteristics using *equation 3-12* were obtained on the entire voltage range for all Pt-SWCNT networks. *Figure 5-12* displays the I-T characteristics for 2, 5 and 10 ml Pt-SWCNT networks fitted according to *equation 3-12*.

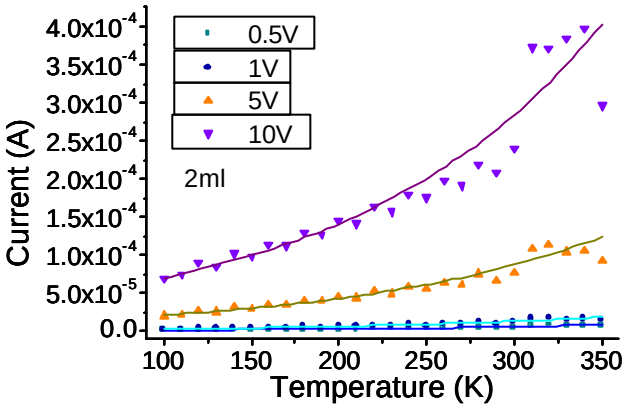

(a)

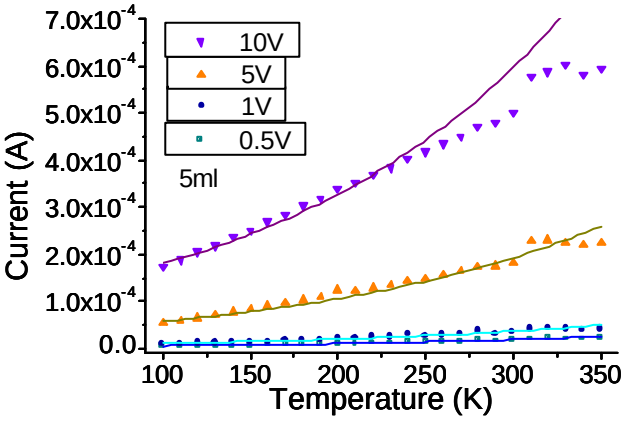

(b)

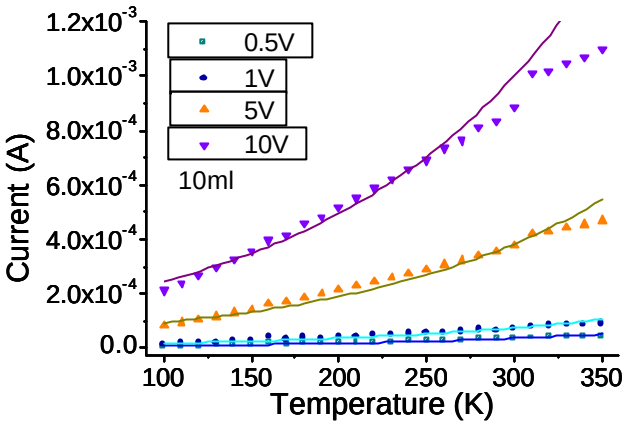

(c)

Figure 5-12 I-T characteristics fitted with equation 3-12 for (a) 2 ml, (b) 5 ml and (c) 10 ml Pt-SWCNT networks

Figure 5-12 shows acceptable fits of the I-T characteristics from 100 to 350 K. Deviations from the fitting plots are observed in the high temperature range. These deviations are explained by the VRH, which has a higher probability to occur as more carriers are thermally activated[179].

Both I-V and I-T characteristics displayed good fittings of *equation 3-12*, which suggests that the conduction across the Pt-SWCNT networks is governed by quantum tunnelling. This result was expected, as the XPS analysis showed that Pt bridges were not created between the pyridine-SWCNT precursors whose conduction is also dominated by quantum tunnelling.

The occurrence of VRH in parallel to this dominant conduction cannot however be dismissed. Deviations from the quantum tunnelling mechanism fits are observed in the high temperature range similarly to homocoupled-SWCNT networks. A heterogeneous model based on tunnelling and VRH was shown to govern the conduction in MWCNT bulk materials in the 328-958 K temperature range[268]. It is suggested that the deviations from the fitting curves are explained by a higher occurrence of VRH in this temperature range. However, the good fits obtained for the I-V characteristics indicate that the quantum tunnelling mechanism remains dominant.

5.5 Discussion/Conclusion

Platinum was coordinated with the pyridine groups of pyridine-SWCNTs. The presence of Pt in the SWCNT sample was attested by ICP analysis. The ICP analysis

also revealed that the control reaction, where the pyridine ligands were neutralised, yielded similar concentration levels of Pt. The XPS analysis indicated that only 34.9% of Pt in Pt-SWCNTs was coordinated with the pyridine moieties, and adsorbed Pt was present in larger quantities than coordinated Pt. This explained the large amount of Pt found in the control reaction product as Pt adsorbed on the SWCNTs. The small quantity of Pt-N bonds present in Pt-SWCNTs, according to the XPS analysis, suggests that it is unlikely that any Pt bridges were built between nanotubes. Instead, the coordination enriched the SWCNTs with Pt, and as a result the Pt added metallic impurities to the SWCNT networks.

The small number of Pt coordinated with the pyridine moieties is partially explained by the coordination procedure used. In order to create Pt-bridged SWCNTs, an amount of Pt corresponding to about half of the estimated pyridine group concentration was added for the coordination. However, the low yield of Pt coordination suggests that Pt bridges were not formed between the SWCNTs. Therefore, it is expected that increasing the amount of $Pt(DMSO)_2Cl_2$ reactant will augment the Pt coordination yield.

The linear current versus network thickness characteristics of Pt-SWCNT networks, differs from those of pyridine-SWCNT networks which displayed an asymptotic behaviour. The reason for this difference is yet not understood. I-V and I-T measurements of the Pt-SWCNT networks displayed similar results than the previous networks. A combined analysis of the I-V and I-T characteristics indicated that the conduction was governed by quantum tunnelling. The Pt introduced metallic impurities in the SWCNT networks but it is suggested that these impurities did not impact on the electrical behaviour of the Pt-SWCNT networks. This result was expected given the low Pt concentration and the absence of Pt bridges between the SWCNTs. Thus, Pt-SWCNT networks displayed the same conduction mechanism as their precursors; the pyridine-SWCNT (see *Appendix B.2*). The sheet resistance of SWCNT/Pt nanoparticles nanocomposite networks was shown to decrease with the increase of Pt[276]. Thus, it is expected that the increase of Pt in the Pt-SWCNT networks will also lead to a diminution of their sheet resistivity. The electrical conductivities of the 10 ml networks (ca. 40 µm thick) of Pt-SWCNTs and pyridine-SWCNTs were found to be 7.3×10^{-4} and 5.5×10^{-4} S/cm (see *Appendix E*), respectively. This was expected, as low levels of metallic nanoparticles were found to decrease the resistance of MWCNT networks[286].

5.6 Summary

This chapter dealt with the Pt coordination with pyridine-SWCNTs. The presence of Pt in the Pt-SWCNTs was attested by ICP spectroscopy. XPS analysis indicated that only 34.9% of the Pt present was coordinated to the pyridine moieties but it is expected that this figure should rise by increasing the amount of $Pt(DMSO)_2Cl_2$ reactant.

Chapter 6
Experimental details

6.1 SWCNTs' preparation

6.1.1 SWCNTs' purification and annealing

There are impurities present after the SWCNT growth, whatever the production process chosen. These impurities include amorphous carbon, fullerenes, metal catalysts or graphitic nanostructures. The purification technique is generally dictated by the nature of the impurities present within the SWCNTs materials. For the experiments described here, commercial purified SWCNTs were bought from Thomas Swan (TS-SWCNTs) and from Carbon Nanotechnologies Inc now Unidym. The TS-SWCNTs were used only for LbL film fabrication while the SWCNTs from Unidym produced by the HiPCO process were used in both LbL films and vacuum filtered networks. Residual ion catalysts embedded in amorphous carbon were the impurities found in these purified SWCNTs. Therefore, a purification step prior to all experiments was conducted to improve the quality of the as-received SWCNTs. In our case, purifying the nanotubes successively involved:

- heating in atmosphere to fissure and remove amorphous carbon shells
- exposure to 6 M of hydrochloric acid to dissolve the metal catalysts
- washing with high purity water to eliminate the dissolved metal and the acid.

Note: the TS-SWCNTs were used as received.

6.1.2 Process

6.1.2.1 Heating

The SWCNTs were placed in a furnace at 350°C for 3 hours (or 250°C overnight) under air. Amorphous carbon was removed by the thermal oxidation and unfortunately, carboxylic acid groups are also created on the nanotubes' surface[69]. After heating, the SWCNTs are withdrawn from the furnace and left to cool down to ambient temperature.

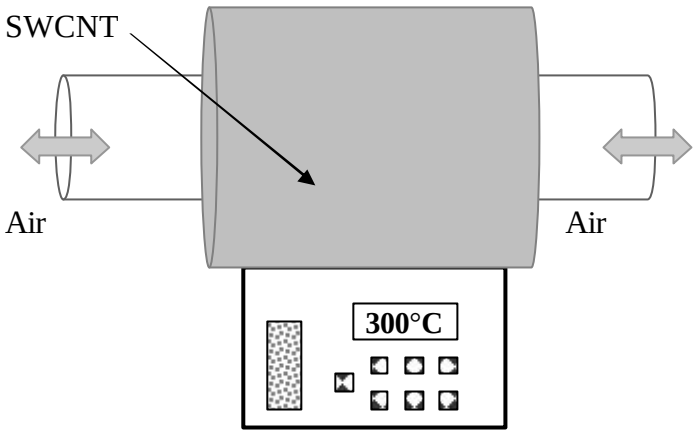

Figure 6-1 Schematic of a furnace in which SWCNTs are thermally oxidised

6.1.2.2 Acid exposure

The exposure to acid was done following two methods. Hydrochloric acid (a non oxidizing acid) was always used to avoid further oxidation of the SWCNTs. Thus, SWCNTs were either dispersed in a concentrated solution of hydrochloric acid (6 M HCl) or directly put in a glassfibre thimble.

The SWCNTs were dispersed by ultrasonication in 6 M of HCl and left soaked overnight at room temperature to allow dissolving the ion catalysts.

The second method consisted of a Soxhlet reflux of 6 M of HCl for 3 to 4 days. A thimble of SWCNTs was placed in a Soxhlet extractor and the ion catalyst was extracted from the thimble back to the acid bath during the acid reflux. The advantages and drawbacks of both acid exposure methods are provided in *Table 6-1*.

Method	Advantages	Drawbacks
Bath	No further contamination Risk of shortening the SWCNTs during the ultrasonication	SWCNTs in contact with catalysts Quality of process strongly dependent on washing Longer washing time
Reflux	Catalyst extracted from SWCNTs as reflux is carried on Many acid cycles on SWCNTs Washing step only for excess acid Shorter washing time	Big loss of SWCNTs as they stay trapped in the thimble Risk of fibreglass remaining Time consuming method

Table 6-1 Benefits and downsides of the acidic exposure methods

Following the hydrochloric acid exposure, a washing step was undergone to remove the acid from the SWCNTs. It consisted of rinsing the SWCNTs with deionised water until the pH level of the water released after rinsing reached the pH of the deionised water (about pH 5.5). Polycarbonate filter membranes with pores size of 0.22 µm were used for the filtration process. The SWCNTs were then dried at 120°C in a vacuum oven.

6.1.2.3 SWCNTs annealing

Following their purification, the SWCNTs used for the filtered networks were annealed overnight at 900°C under dynamic vacuum to consume their defect sites[287]. This process allows the elimination of carboxylic groups created on the surface of the SWCNTs during the heating under air. The vacuum level (mbar) of this annealing still allowed the formation of these carboxylic groups. However, the rate at which the carboxylic groups are removed is faster than the rate at which they are created. This leads to a reduction of the amount of these groups and the structure of the SWCNT is consequently improved. *Figure 3-7* showed that as a result of the annealing, the weight loss at 900°C decreases by about 10%wt.

6.1.2.4 Characterisation

SWCNTs, which were purified and purified then annealed were characterised by Raman, UV-visible-near IR spectroscopy along with XPS and TGA-MS. The results from these characterisations are detailed in *section 3.4*.

6.2 Non covalently functionalised SWCNTs and LbL deposition

6.2.1 Preparation of polyelectrolyte solutions

Tris buffer solution at 0.01 M was prepared by dissolving Tris buffer in deionised water. HCl solution at 6 M was added drop by drop to reach a pH level of 6.5.

2×10^{-2} M of PEI solution was prepared by diluting the PEI into Tris buffer solution.

2%wt of PSS solution was prepared by dilution of the PSS into Tris buffer solution.

6.2.2 Preparation of surfactant solutions

SDS solutions at 1%wt and DTAB solutions at 0.65%wt were prepared by dissolving SDS and DTAB in high purity deionised water, respectively.

6.2.3 Preparation of SWCNT dispersions in surfactants

Dispersions of SWCNTs at 1:4 mg/ml in the respective SDS and DTAB solutions were prepared using an ultrasonic probe at 35% power for 5 min with a pulse of 5 sec ON and 1 sec OFF. SWCNT solutions were left to stand for one day before being used.

6.2.4 Preparation of C60 solutions

1:4 mg/ml solutions of C_{60} in SDS and in DTAB were prepared following the same procedure as the SWCNT dispersions. The C_{60} solutions were also left to settle for one day before being used.

6.3 Covalently functionalised SWCNTs

6.3.1 Preparation of SWCNT precursors

6.3.1.1 Iodobenzene-SWCNTs

The aniline groups are transformed in diazonium group after oxidation by isopentyl nitrite. The reaction happens under N_2 atmosphere at 60°C and large excess of reactants were used to maximize the yield.

25 ml of purified then annealed SWCNTs in dichlorobenzene at 3.5 mg/ml were mixed with 5 ml of 4-iodoaniline in acetonitrile at 0.2 g/ml. 2 g of isopentyl nitrite was added and the mixture was stirred at 60°C under static N_2 atmosphere for 3 days.

6.3.1.2 Pyridine-SWCNTs

1.5 ml of $NaNO_3$ in water at 1 g/ml was added to 6 ml of aminopyridine in 4 M HCL at 0.17 g/ml. The temperature was kept below 5°C while the mixture was stirred for 30 min. 10 ml of purified and annealed SWCNTs in DMF at 2 mg/ml was added drop by drop and the mixture was stirred for 4h.

6.3.1.3 Sonogashira-SWCNTs

10 ml of iodobenzene-SWCNTs in triethylamine at 5 mg/ml was mixed with 750 mg of trimethylsalyl acetylene. 0.05 mM of CuI and 0.04 mM of $Pd(P(Ph)_3Cl)_2$ catalysts were added and the mixture was stirred at 60°C under static N_2 atmosphere for 4 days.

6.3.2 Preparation of bridged-SWCNTs

6.3.2.1 Homocoupled-SWCNTs

5 ml of dispersion of Sonogashira-SWCNTs in DMF at 6 mg/ml were stirred with 0.1 mM of CuCl at 60°C under air atmosphere for 5 days.

6.3.2.2 Crosscoupled-SWCNTs

10 ml of Sonogashira-SWCNTs in DMF at 2 mg/ml were mixed with 10 ml of iodobenzene-SWCNTs at 1.5 mg/ml. 0.06 mM of CuCl and 0.05 mM of $Pd(P(Ph)_3Cl)_2$ were added and the mixture was stirred at 80°C for 5 days.

6.3.2.3 Ullmann-SWCNTs

16.9 mM of N,N-diethylisopropylamine were added to 20 ml of iodobenzene-SWCNTs in DMF at 0.5 mg/ml. 17.2 mM of di-μ-chlorobis[5-chloro-2-[(4-chlorophenyl) (hydroxyimino-κN)methyl] phenyl-κC]palladium were added and the mixture was stirred at 110°C under static N_2 atmosphere for 5 days.

6.3.3 Preparation of Pt-SWCNTs

3 ml of $Pt(DMSO)_2Cl_2$ in methanol at 1.6 mg/ml was added to a reflux of 4 ml of pyridine-SWCNTs in methanol at 3.5 mg/ml over 10 days. Note: $Pt(DMSO)_2Cl_2$

solution was added by portions of 100 µl (4 times), follower by portions of 200 µl (6 times) then portions of 400 µl (2 times) and 600 µl (1 time).

After their respective reactions, SWCNT precursors and bridged-SWCNTs were rinsed by successive filtrations in DMF, dichloromethane, acetone and methanol while Pt-SWCNTs were rinsed by methanol filtration.

6.3.4 SWCNTs' washing

After reactions, the SWCNT precursors and molecularly bridged SWCNTs were washed to remove the catalysts and by-products of the reactions. Thus, successive filtrations and bath ultrasonications in dichloromethane, DMF, acetone and ethanol (or methanol) were carried out. PTFE filtration membranes with 0.2 µm pore size were used for the filtration.

Pt-SWCNTs were washed in 200 ml of methanol using polycarbonate filtration membranes with 0.2 µm pore size.

6.4 SWCNT network fabrication

6.4.1 Layer-by-layer deposition

Glass substrates were cleaned for 20 min in a bomb solution (H_2SO_4: H_2O_2 at 1:1 conc) and rinsed in water. This was followed by bath ultrasonication in water then propan-2-ol. Thin films of Ti (50 nm)/Au (nm) metal contact were deposited by thermal or e-beam evaporation using brass shadow masks to deposit the electrodes[xx]. The glass substrates were dipped in PEI-Tris buffer solution (pH 6.5) for 45 min then in PAA (or PSS) solution (30 min) to deposit "seed" LbL layers (PEI/PAA)3. The deposition time for the following dip was 30 min. The glass substrates were rinsed in 3 successive deionised water baths then dried with nitrogen after each dipping.

The charged glass substrates were then dipped successively in SWCNT dispersion in DTAB and in SWCNT dispersion in SDS for 30 min per dip. Between each dipping, the glass substrates were rinsed in a deionised water bath then dried using a nitrogen

[xx] Cr was also used instead of Ti

gun. The process was repeated 5, 10 or 20 times depending on the thickness desired for the SWCNT LbL films.

6.4.2 Filtered networks

Dispersions of SWCNT precursors, bridged-SWCNTs at 1 mg/ml in DMF and Pt-SWCNTs at 1 mg/ml in methanol were prepared by bath ultrasonication. The dispersions were allowed to settle for one day. 2, 5, 10 and 20 ml of the SWCNT supernatants were vacuum filtered on nylon membranes (diameter: 2.5 mm, pore size: 0.2 μm). The SWCNT precursor networks, molecular bridged SWCNT networks and Pt-SWCNT networks were then dried overnight at 120°C in a vacuum oven.

6.5 SWCNTs characterisation

6.5.1 Raman spectroscopy

Raman spectroscopy was performed using a Jobin Yvon Horiba LabRAM spectrometer equipped with a confocal microscope (50x magnification objective) and a He-Ne laser (632.8 nm) on SWCNT powder.

6.5.2 UV-visible-near IR spectroscopy

Absorption spectra of dispersions of SWCNTs in DMF (or aqueous surfactant solutions for LbL depositions) were recorded with a Perkin-Elmer Lambda 900 spectrometer. All SWCNT dispersions had settled for one day before measurement.

6.5.3 TGA-MS analysis

SWCNTs were heated up in a He atmosphere from room temperature to 900°C at a rate of 10°C/min. The heating was held at 120°C for 20 min to allow the evacuation of potential solvent. The Perkin-Elmer Pyris I TGA recorded the mass loss of the sample from room temperature while the Hiden HPR20 mass spectrometer detected the groups released from 120°C.

6.5.4 XPS analysis

Steel stubs were coated by thick layers of SWCNTs. The samples were analysed in a chamber under vacuum (~10^{-9} Torr) with an Al KR X-ray source (1486.6 eV) in a Scienta ESCA hemispherical analyzer. The C1s XPS spectrum at 284.5 eV was used as reference for the recording.

6.5.5 ICP spectroscopy

SWCNTs were dissolved in nitric acid to extract the metal and the solution was diluted in deionised water and then centrifuged at 4500 rpm for 4 min. The supernatant obtained after centrifugation was used for the analysis. The measurements were recorded using the inductively coupled plasma optical emission spectrometer (ICP-OES) Ultima 2 from Horiba Jobin Yvon.

6.5.6 CHN analysis

SWCNT samples were combusted in a pure oxygen atmosphere under static conditions. At the end of the combustion, a dynamic burst of oxygen was added to ensure total combustion. The temperature of combustion reached over 1800 °C. The CHN elemental analyses were carried out with the CE440 Exeter Analytical Elemental Analyser.

6.6 SWCNT networks characterisation

6.6.1 Scanning electron microscope

Cr/Pt layer (8 nm) was coated on the SWCNT networks prior to SEM analysis. High resolution Hitachi SU-70 FEG-SEM was then used to image the networks.

6.6.2 Electrical measurement kit

6.6.2.1 Room temperature I-V characteristics

The measurements were carried out at room temperature in a dark rig at ~10^{-1} mbar using a 2400 Keithley source meter. The rig consisted of a 3 probes driven by a Labview-based software and a high-performance PCI-GPIB interface card.

6.6.2.2 I-T characteristics

The measurements were carried out using a Janis Research/CTI cryogenics' cryostat rig at about 2×10^{-4} mbar with a 331 temperature controller from LakeShore. The voltage was applied using a Keithley 2400 source meter. All measurements were carried out in the dark.

Conclusion

In this thesis, SWCNTs were functionalised following non covalent and covalent approaches. The non covalently functionalised SWCNTs consisted of surfactants wrapped SWCNTs; electrostatic LbL depositions were used to build up networks from anionic and cationic surfactants wrapped up SWCNTs. The combined analysis of I-V, I-T and I-d characteristics showed that the in-plane conduction was dominated by Poole-Frenkel mechanisms. This characteristic was exploited to integrate cut-SWCNT LbL network into organic MIS devices. The charge storage capacity, displayed by cut-SWCNT LbL networks based MIS devices, illustrates their relevance for applications such as non volatile memory devices.

With the covalent approach, SWCNTs had undergone radical additions which were followed by coupling reactions or coordination. In relation to the coupling reactions, this thesis examines a novel strategy to create organic molecules to covalently bridge SWCNTs. For this purpose, iodobenzene-SWCNT and Sonogashira-SWCNT precursors were prepared by diazonium radical addition and Sonogashira cross-coupling. This represents the first time that Sonogashira cross-coupling on SWCNTs was reported, to our knowledge. Subsequently, the SWCNT precursors were covalently bridged via modified Sonogashira and Ullmann couplings and spectroscopic evidence was used to ascertain that the couplings were successful. Concerning the coordination, Pt-enriched SWCNT were prepared by Pt coordination with the pyridine group from pyridine-SWCNT precursors.

Networks of SWCNT precursors, molecularly bridged SWCNTs and Pt-SWCNTs were subsequently deposited by vacuum filtration. Following electrical analysis, a modified quantum tunnelling model was proposed as it best described the current-voltage characteristics and the temperature dependence of the current. This implies that, neither the covalent bridging of the SWCNTs nor the addition of platinum at a low concentration altered the dominant conduction mechanism.

Summary of contributions

The achievements presented in this thesis are for both the chemistry and electrical properties of SWCNTs. Thus, this work contributes to progress in the SWCNT field by reporting novel SWCNT couplings (Sonogashira cross-coupling and Ullmann coupling) and functional groups (pyridine and Pt coordinated pyridine). In addition, homo-coupling and cross-coupling reactions introduced a new strategy to bridge the SWCNTs.

A modified quantum tunnelling model is proposed, and found to govern the conduction mechanisms across all networks of covalently modified SWCNTs (bridged SWCNTs, Pt-SWCNTs and SWCNT precursors). Furthermore, the Poole-Frenkel effect was found to dominate the conduction in SWCNT LbL films. The charge storage capacity displayed by cut-SWCNT LbL films was also emphasised.

Future research directions

This research opens a new route to covalently bridge SWCNTs via organometallic couplings. The bridging was demonstrated using stoichiometric quantities of catalysts, which are yet to be optimised. Within the scope of this thesis, small conjugated molecules were used as organic linker. In further work, conjugated molecules with electroluminescent properties could be used to produce materials for organic light emitting devices. Furthermore, a study of the alternating current behaviour of the bridged SWCNT networks will extend our understanding of their electrical properties. The transfer of the SWCNT networks onto rigid substrates should provide better estimations of their thickness and complete our knowledge of reliable electrical conductivities.

Pt coordination with pyridine-SWCNTs was also demonstrated but not the Pt-bridging of the SWCNTs. Therefore, further work should contribute to achieving Pt-bridged SWCNTs via the pyridine groups and study the potential impact of the Pt bridging on the electrical conduction. Pyridine-SWCNT networks could be used for the fabrication of SWCNT based metal sensors.

Appendix A

Additional information for Chapter 2

A.1 C60-mixed SWCNT LbL films

Carbon nanotubes and fullerenes are similar isomers of carbon as seen in *section 1.3.1* of *Chapter I.* From a structural point of view, the differences between them lay in their shapes and their lattices. Nevertheless, while SWCNTs can be either semiconducting or metallic, fullerenes are semiconducting materials. Integrating C_{60} into LbL film would therefore increase the ratio of semiconducting versus metallic nanoparticles within the LbL films. In this regard, LbL films integrating both SWCNT and C_{60} were prepared.

UV-visible-near IR spectra of C_{60} in DTAB and SDS solutions were recorded between 300 nm and 1300 nm to avoid the noise resulting from the presence of water in the solution. Normalised transmittance spectra of these spectra are presented *Figure A-1*.

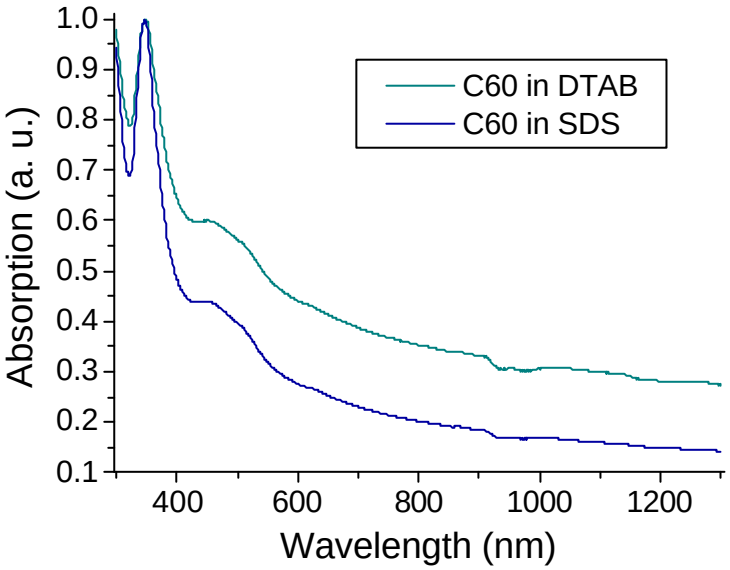

Figure A-1 Absorption spectra normalised at 348 and 347 nm for C_{60} in DTAB and SDS solutions, respectively. Nominal concentrations of 1:4 mg/ml of SWCNT in solutions were prepared and their well-dispersed part was analysed.

UV-visible-near IR spectra from 300 to 1300 nm displayed in *Figure A-1* show transmittance spectra for C_{60}. The transmittance peak is located at 348 and 347 nm

in DTAB and SDS, respectively. The absence of van Hove singularities is explained by the 0-dimension of the C_{60}. The absorption of C_{60} in DTAB and SDS solutions remained of the same order of magnitude though it almost doubled. These spectra concord with data already published[288].

A.1.1 In-plane characteristics

A.1.1.1 C60 LbL films

C_{60} LbL films were built-up as reference. *Figure A-2 (a)* and *(b)* shows the in-plane I-V characteristics of C_{60} LbL films with 10 and 30 bi-layers, respectively.

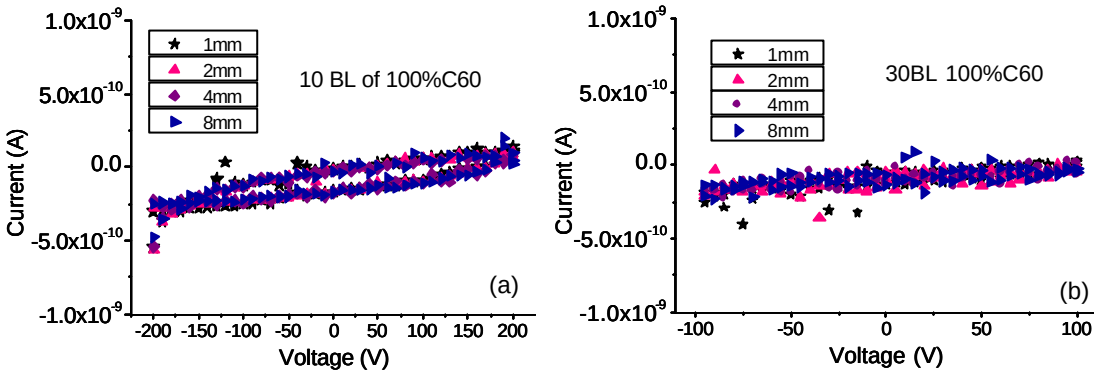

Figure A-2 Current-voltage characteristics of 100% C_{60} LbL thin films with electrode separations of 1, 2, 4 and 8 mm. (a) 10 bi-layers LbL film and (b) 30 bi-layers LbL film.

Figure A-2 indicates that C_{60} LbL films are insulating in the in-plane configuration with a current level in the order of 10^{-10} A. However, these low currents increase very slowly with the voltage.

A.1.1.2 C60–mixed SWCNT LbL films: I-V characteristics

LbL films using dispersions made with mixtures of solutions of 1:4 mg/ml of C_{60} and SWCNT in DTAB and SDS were also built-up. The ratios of SWCNT solutions in C_{60} solutions were taken as 5/95, 10/90, 25/75, 50/50 and 75/25. *Figure A-3* shows the I-V characteristics (in log-log scale) at room temperature for 15, 20, 25 and 30 bi-layers C_{60}–mixed SWCNT LbL films built-up with these solutions.

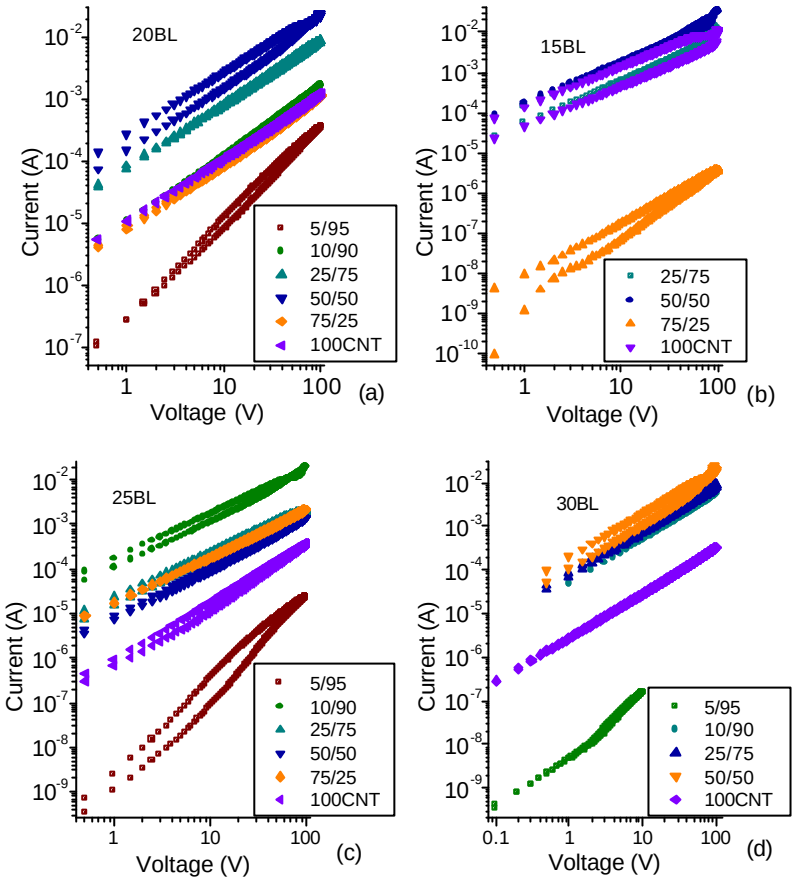

Figure A-3 Room temperature in-plane I-V characteristics in log-log scale of (a) 20, (b) 15, (c) 25 and (d) 30 bi-layers C_{60}-mixed SWCNT LbL films with SWCNT/C_{60} concentration ratios of 5/95, 10/90, 25/75, 50/50 and 75/25 at 1.5 mm electrode separation. SWCNT LbL films are also shown.

Figure A-3 shows that apart from the film with a SWCNT/C_{60} ratio of 5/95 (film with the lowest nanotubes content) all the C_{60}-mixed SWCNT LbL films follow the same trend. Abnormal high current levels are obtained particularly for LbL films with small loading of SWCNTs. For instance, for a 20 bi-layers C_{60}-mixed SWCNT LBL film (*Figure A-3 (a)*), the films made with SWCNT/C_{60} ratios of 50/50 and 25/75 display current levels of about one order of magnitude higher than the SWCNT LbL film. Such inconsistency is repeated in *Figures A-3 (b), (c)* and *(d)*. This contrasts with previous data where the current level was shown to be dependent on the amount of SWCNT loaded in the LbL films[175]. Given the presence of C_{60} should influence the conductivity (*Figure A-2*) by decreasing it when SWCNTs are replaced by C_{60}. It is assumed that such current levels are the result of heating effect of the films.

A.1.1.3 C60–mixed SWCNT LbL films: I-T characteristics

Measurements, with a voltage limited to ±20 V to limit the self-heating, were carried out. I-T characteristics from 50 to 350 K and their associate I-V plot at 300 K were recorded for C_{60}-mixed SWCNT films with SWCNT/C_{60} ratios of 33.33/66.66 and 50/50. *Figure A-4* shows the I-V and I-T characteristics of the 20 bi-layers C_{60}-mixed SWCNT LbL film with a SWCNT/C_{60} ratio of 33.33/66.66 at 4 and 1 mm electrode separations.

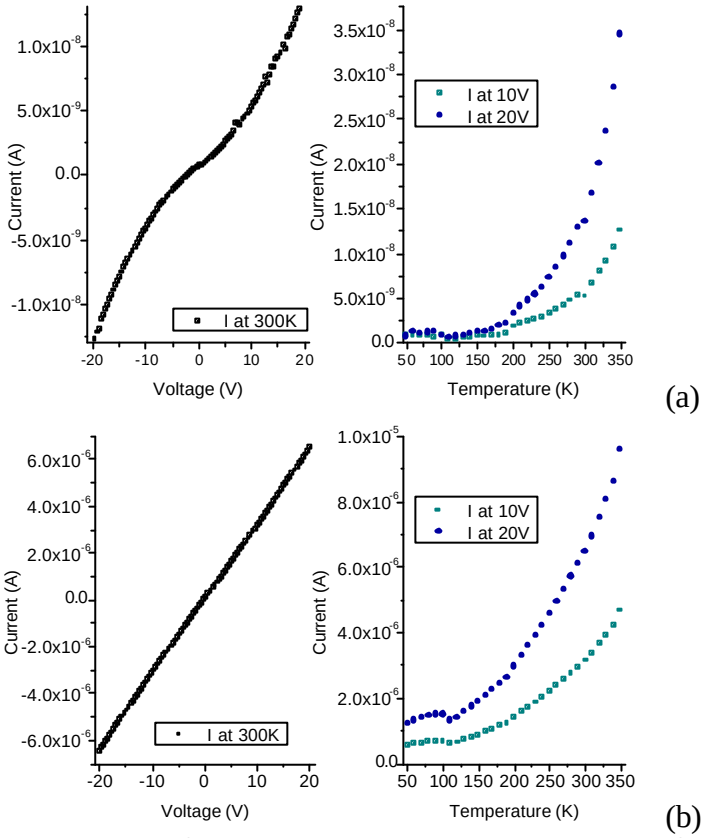

Figure A-4 I-V characteristics of 20 bi-layers 33.3%CNT-66.6%C_{60} LbL film at 300 K and the I-T characteristics of this LbL film at 10 and 20 V – for electrode separations of (a) 4 mm and (b) 1 mm

Both I-V and I-T characteristics in *Figures A-4 (a)* and *(b)* are different. The difference is more noticeable for the I-V characteristics. Indeed while the I-V plot for 1 mm electrode separation at 300 K (*Figure A-4 (b)*) is linear the one for a 4 mm electrode separation is not. Also there are more than 2 orders of magnitude between the current levels. Regarding the I-T plots, the current appears rather stable at low temperature; up to 200 K and up to 150 K for 4 mm and 1 mm electrode separation, respectively. *Figure A-5* shows the I-V and I-T characteristics of the 20 bi-layers C_{60}-mixed SWCNT LbL film at 4 and 1 mm electrode separations.

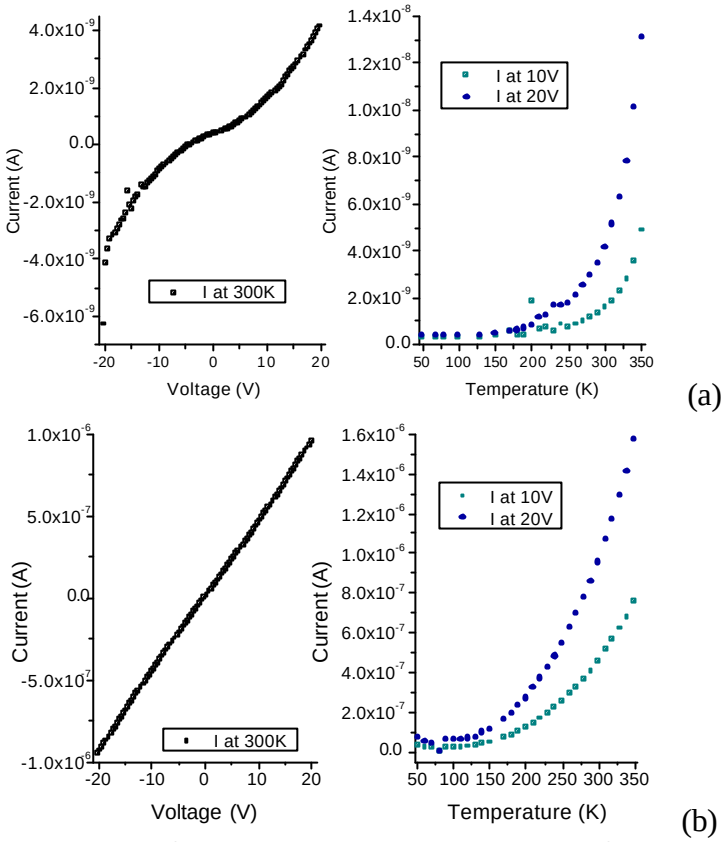

Figure A-5 I-V characteristics of 20 bi-layers 50%CNT-50%C_{60} LbL film at 300 K and the I-T characteristics of this LbL film at 10 and 20 V with electrode separation of (a) 4 mm and (b) 1 mm

The examination of *Figures A-5 (a)* and *(b)* led to the same observations than for *Figures A-4 (a)* and *(b)*. Thus, these two C_{60}-mixed SWCNT LbL films display the same behaviour.

The current levels obtained for the 50/50 C_{60}-mixed SWCNT LbL film (4×10^{-9} A and 1×10^{-6} A) are lower than the ones for the 33.3/66.6 C_{60}-mixed SWCNT LbL film (1×10^{-8} A and 6×10^{-6} A). This result contrasts with the observation of an increase of current with the loading of SWCNTs on the film[155,175]. This inconsistency is attributed to a self-heating of the films during measurements. Indeed, LbL films made with low SWCNTs loading shows higher current intensity than those with higher loading. The in-plane measurements carried out on the C_{60}-mixed SWCNT LbL films show that providing a loading of the SWCNTs high enough in the film the heating is limited and consistent results are obtained. However one cannot disregard the possibility of having some heating even for higher proportions of nanotubes.

A.1.2 Out-of-plane characteristics

Current-voltage characteristics

I-V measurements at room temperature carried out on 20 bi-layers C_{60} LbL film and a C_{60}-mixed SWCNT with a SWCNT ratio of 50/50 from 0 to 5 V are shown in *Figure A-6 (a)*. *Figure A-6 (b)* shows out-of-plane I-V measurements at 300 K carried out on 20 bi-layers C_{60}-mixed SWCNT LbL films made with SWCNT/C_{60} mixtures ratios of: 5/95; 10/90 and 50/50. Measurements done on the C_{60} LbL film and LbL film made just with surfactants are also shown as reference in *Figure A-6 (b)*.

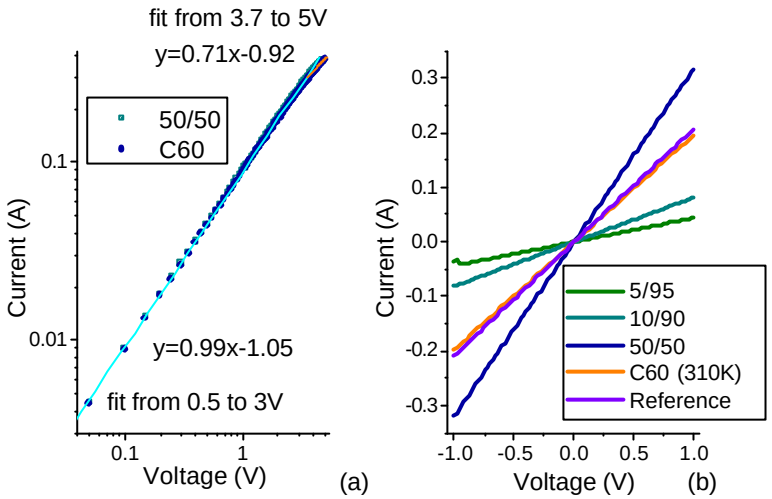

Figure A-6 Out-of-plane I-V characteristics (a) at room temperature for C_{60} and 50/50 C_{60}-mixed SWCNT LbL films in log-log scale (b) at 300 K (310 K for C_{60} LbL film) of C_{60}-mixed SWCNT LbL films and a LbL film as reference.

Figure A-6 (a) shows that the 50/50 C_{60}-mixed SWCNT LbL films and C_{60} LbL film follow the same linear dependence up to 3 V before inclination (from 3.7 to 5 V). The high current obtained has the same order of magnitude and these I-V plots follow the same trend than the out-of-plane I-V plots of SWCNT LbL displayed in *Figure 2-13 (b)*. *Figure A-6 (b)* shows the loading of SWCNT or C_{60} in the LbL film does not impact on the current level.

The out-of-plane I-V characteristic of the reference sample (*Figure A-6 (b)*) displays the same linear trend and same order of magnitude than the C_{60}-mixed SWCNT and C_{60} LbL films. This indicates that the presence of SWCNT and/or C_{60} in LbL films does not influence the conduction. The resemblance of *Figure A-6 (a)* and *Figure 2-13 (b)* suggests that the processes occurring in a SWCNT LbL film (see *section 2.5.2.2*) are also happening in the LbL films presented here. Given the restricted

voltage range shown in *Figure A-6 (a)* (±1 V), I-T plots of the C_{60}-mixed SWCNT LbL films were recorded to complete the comparison between these films.

Current-temperature characteristics

I-T characteristics of these films C_{60}-mixed SWCNT LbL films are shown from 350 to 50 K (before current breakdown at 50 K) in *Figure A-7* for a bias of 1 V.

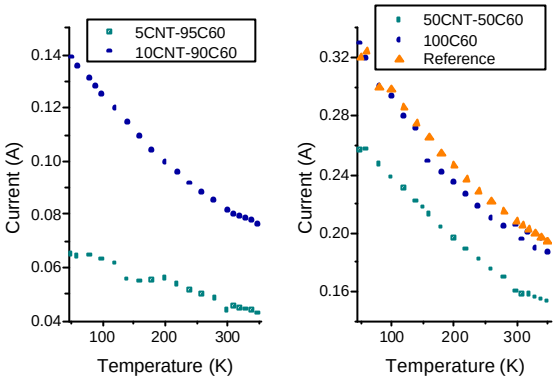

Figure A-7 Out-of-plane I-T plots at 1 V for C_{60} and C_{60}-mixed LbL films with SWCNT/C60 ratios of: 5/95, 10/90, 50/50, and their reference LbL sample

The out-of-plane I-T characteristics shown in *Figure A-7* appear to be similar to those displayed in *Figure 2-16*. Indeed, over the same temperature range the current increases as the temperature is reduced with the analogous trends. $Ln(I) \propto T$ plots of the I-T characteristics displayed in *Figure A-7* are plotted in *Figure A-8*.

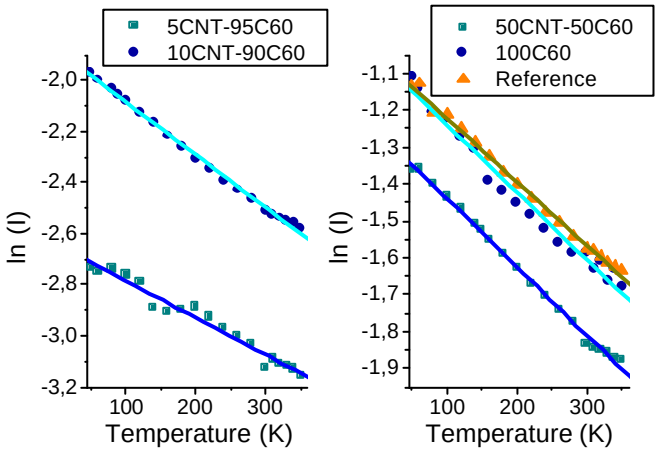

Figure A-8 $\ln(I) \propto T$ plots of the out-of-plane I-T characteristics for C_{60} and C_{60}-mixed LbL films with SWCNT/C60 ratios of: 5/95, 10/90, 50/50, and their reference LbL sample

As found from the out-of-plane I-T measurement for the SWCNT LbL films (*Figure 2-16*), the $\ln(I) \propto T$ plots (*Figure A-8*) of the out-of-plane I-T characteristics also

exhibit a linear behaviour. As stated above, such behaviour is indicative of a conduction dominated by a tunnelling phenomenon according to *Hurd*[179].

A.2 Current breakdown phenomenon

In *sections 2.5.2.2* and *2.7.2*, log-log plots of the out-of-plane I-V characteristics showed that for a sufficient voltage their slope were decreasing from 1 to about 0.7. Subsequent to this non linear region, current breakdowns occurred during I-V measurements with the out-of-plane configuration. This section describes and analyses that phenomenon.

A.2.1 I-V characteristics

Figure A-9 shows I-V measurements carried out at room temperature with the out-of-plane configuration which led to current breakdowns.

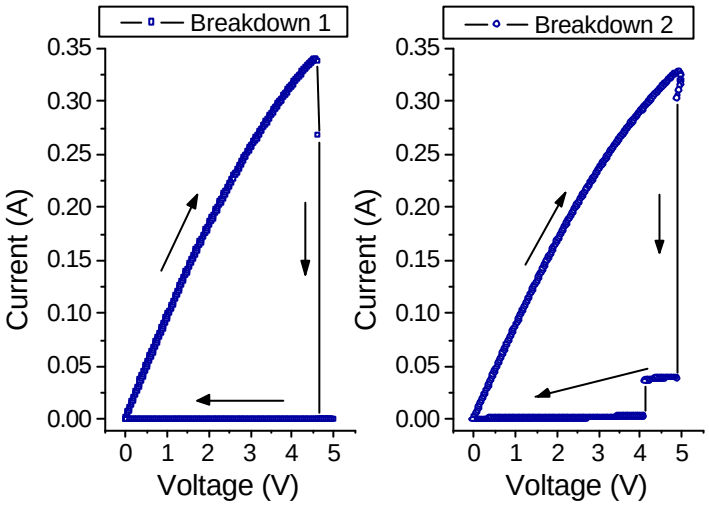

Figure A-9 Typical current breakdowns during I-V measurements at room temperature on 20 bi-layers SWCNT LbL film

Figure A-9 shows that current breakdowns occur around 5 V at room temperature. Before those, the I-V characteristics are similar to those obtained for SWCNT LbL film in *Figure 2-16 (a)*. After breakdown, the current drops of several orders of magnitude. *Figure A-10* shows I-V measurements from -10 to 10 V carried out following the respective current breakdowns shown in *Figure A-9*.

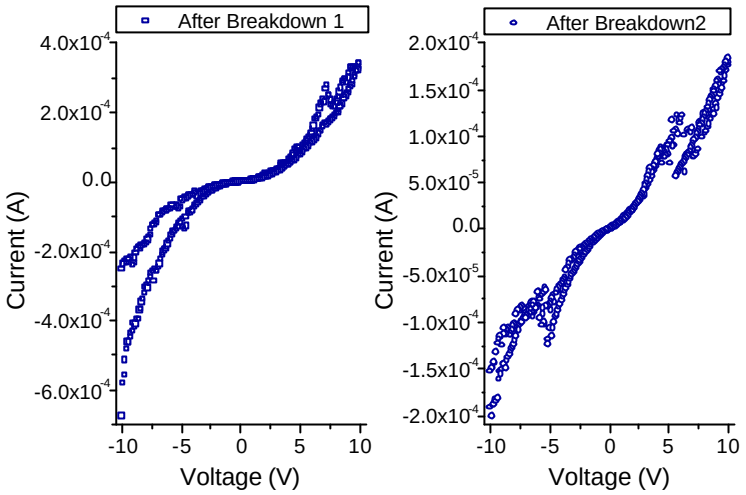

Figure A-10 I-V plots of SWCNT LbL film after current breakdowns shown in Figure A-9[xxi]

Figure A-10 shows that the I-V characteristics of the samples after their respective current breakdowns (*Figure A-9*). A difference of about 3 orders of magnitude between current levels before and after breakdown is observed. A noticeably different I-V behaviour compared to those before breakdown illustrates the irreversible nature of the breakdown. This is indicative of different conduction model followed after current breakdown.

The occurrence and use of current breakdowns of carbon nanotubes are reported[289-290] However, no current breakdown on such SWCNT LbL films was reported to our knowledge. In fact, out-of-plane I-V characteristics on similar films were shown to undergo voltages up to ±10 V at room temperature without the occurrence of a current breakdown[155]. Negative resistance followed by a significantly reduced current was reported on Langmuir-Blodgett SWCNT films. A morphologic study of the SWCNT film revealed that SWCNTs disappeared after the electrical measurements[291]. This structural modification is explained by the Joule heating during the measurement. Thus, oxidation-induced breakdown are the result of SWCNTs being oxidised away[292].

[xxi] These plots were obtained after intermediate measurements due to a lack of stability in the characteristics.

A.2.2 I-T characteristics

I-T characteristics of a 20 bi-layers SWCNT LbL film which undergone a current breakdown were analysed to help determining the transport mechanism which governs the conduction after current breakdown. Thus, a current breakdown was voluntarily provoked at 50 K[xxii]. The semi-log I-V plot of the current breakdown at 50 K accompanied by an I-V plot at 50 K recorded after breakdown are shown in *Figure A-11 (a)* and *(b)*, respectively.

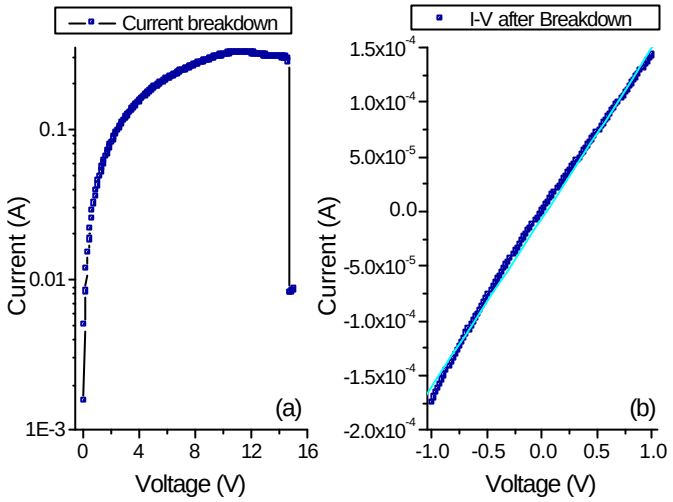

Figure A-11 (a) I-V characteristics of the current breakdown at 50 K in semi-log scale (b) I-V characteristic at 50 K performed on same area the following the current breakdown.

Figure A-11 (a) shows that the breakdown at 50 K causes the current to decrease by more than one order of magnitude. The current at 1 V dropped from 38.86 mA (*Figure A-11 (a)*) to 0.14 mA (*Figure A-11 (b)*). However, only an insignificant difference is perceived in the I-V characteristics as the I-V plot in *Figure A-11 (b)* slightly deviates from a linear behaviour. The fact that at 50 K, the breakdown occurs at higher voltages than at room temperature (*Figure A-9*) is explained by the absence of oxygen during the measurements. Indeed, the oxygen in the environment impacts the dynamic of the breakdown as breakdowns occur at smaller electric fields than in vacuum[293]. *Figure A-12* displays the out-of-plane I-T characteristics at 0.5 and 1 V of the SWCNT LBL film after current breakdown.

[xxii] Breakdown performed at 50 K to reduce the risk of having an insulating film. Indeed, breakdowns happening at room temperature can sometimes result in an insulating film.

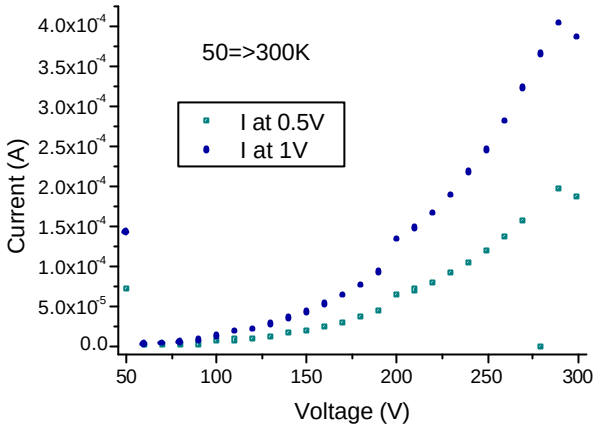

Figure A-12 Out-of-plane I-T characteristics at 0.5 V and 1 V after breakdown of a SWCNT LbL film

The out-of-plane I-T characteristics display in *Figure A-12* follow a completely different behaviour that those shown in *Figure II-16*. Here, not only the current increases as the temperature is raised but it does so with an exponential trend. These dissimilarities support the idea that another type of transport is dominant in the SWCNT LbL films after current breakdown (see *section 2.8.1*).

The reason for the current breakdown is not known yet. However, given that the temperature at which the breakdown takes place impacts on the breakdown voltage, the I-V characteristics trends and current level after breakdown (*Figures A-9* to *A-11*) the possibility for a thermal breakdown is suspected. Indeed, Joule heating during I-V measurements was reported to damage MWCNTs and lead to current breakdowns[294].

A.2.3 Reference sample

The in-plane I-V measurements of DTAB/SDS LbL films displayed insulating characteristics (see *Figure 2-11*). This section focuses on the unexpected results obtained for the out-of-plane I-V plots of the reference 20 bi-layers DTAB/SDS LbL film in Figures *2-38 (b)* and *2-39 (b)*. The surfactants and polyelectrolytes used to build-up the LbL films are insulating. Thus, two conduction types are possible across such films: tunnelling mechanism and ionic conduction. This sample displays the same out-of-plane I-V and I-T characteristics that the rest of the LbL films. Thus, identify the transport mechanisms in these films will shed a new light on the dominant in the out-of-plane direction of the pure SWCNT and C_{60} LbL film as well as the C_{60}-mixed SWCNT LbL films. A current breakdown was provoked during at 50 K to study the electrical properties of a DTAB/SDS LbL film. Out-of-plane I-V

characteristics of the current breakdown at 50 K and after current breakdown at 300 K are shown in *Figure A-13 (a)* and *(b)*, respectively.

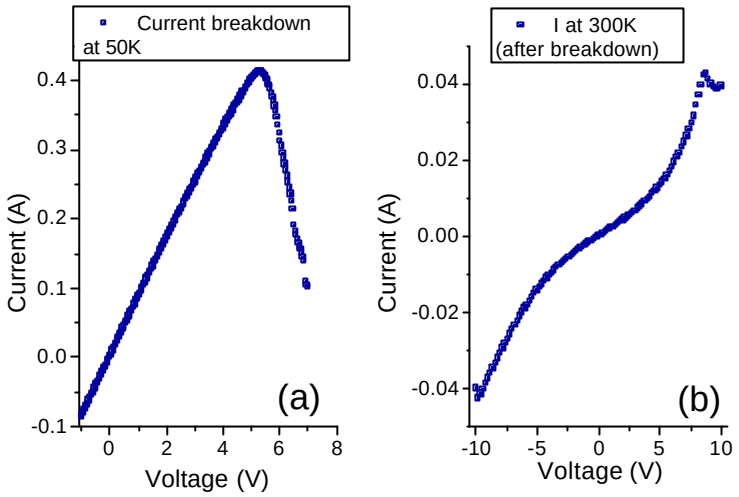

Figure A-13 Typical out-of-plane I-V plots of the reference sample at 50 K during the current breakdown (a) and at 300 K after breakdown (b)

Figure A-13 (a) shows an expected linear I-V characteristic before current breakdown. Compared to the SWCNT LbL breakdown shown in *Figure A-11 (a)*, a smaller breakdown voltage is required here (5.32 V instead of 14.66 V) for the same vacuum level. Also, *Figure A-13 (a)* does not display any current saturation region while such region lasted for at least 6.5 V in *Figure A-11 (a)*. The comparison of *Figure A-13 (a)* with *A-11 (a)* highlights the protective role of the SWCNTs in the electrical resilience of the LbL films. *Figure A-13 (b)* shows a non linear I-V characteristic after breakdown with differential negative resistance at high voltage. The parameters of the linear $y = ax + b$ fittings of the log-log plots (not shown) of *Figures A-13 (b), A-11 (a) and (b)* are given in *Table A-1*.

Figure	Low voltages		High voltages	
	A	B	A	B
A-13 (b)	1.05	-2.69	2.14	-3.40
A-10 (a)	1.18	-5	2.12	-5.36
A-10 (b)	1.4	-5.3	1.99	-5.4

Table A-1 Fitting parameters of the log-log plot of Figures A-13 and A-10

Table A-1 shows that the slopes of the linear fittings at both low and high voltages are similar. This indicates that the I-V behaviours of the SWCNT LbL film and the reference LbL film after current breakdown are comparable. However, the current is

two orders of magnitude higher for the reference film (*Figure A-13 (b)*) than for SWCNT LbL films (*Figure A-10).* This difference can be explained by the temperature at which the current breakdown was performed. The breakdown leading to the plots displayed in *Figure A-10* occurred at room temperature while the one in *Figure A-13* occurred at 50 K. In *section 2.8.2*, the comparison between *Figure A-9* and *A-11 (a)* has highlighted the impact of the temperature on the breakdown. The vacuum conditions were also reported to impact on current breakdown of nanotubes[294]. The breakdowns in *Figure A-9* (leading to *Figure A-10*) were performed at low vacuum level. So, the presence of oxygen could also worsen the damages created by the current breakdown. Thus, the difference of two orders of magnitude between the current level can be explained by both the temperature and the vacuum levels at which the current breakdowns were performed.

Figure A-14 displays the I-T plots after current breakdown at 1 V (*a*) and 10 V (*b*)

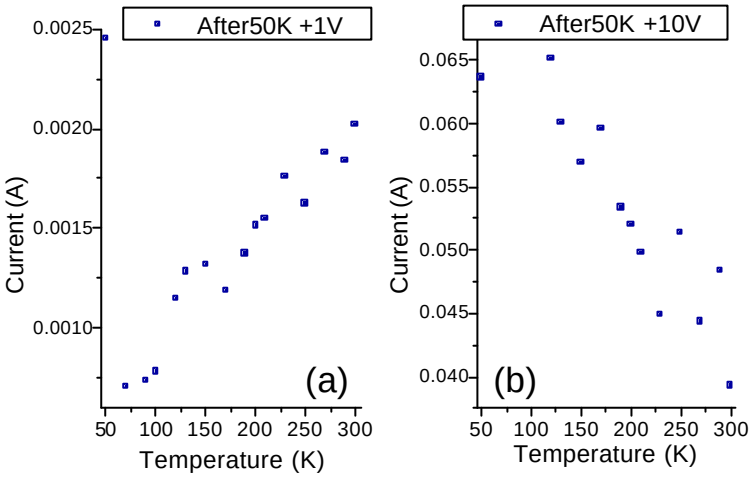

Figure A-14 Out-of-plane I-T characteristics of the reference LbL film after current breakdown for (a) 1 V and (b) 10 V

Figure A-14 indicates that the temperature dependence of the current follows two opposite trends depending on the bias applied. Indeed at V=+1 V (*Figure A-14 (a)*) the current increases with the temperature whereas at V=10 V (*Figure A-14 (b)*) the current decreases as the temperature augments. This implies that different conduction mechanisms dominate the low and high voltage range. Unfortunately, the data points in *Figure A-14* were too scattered to give decent fittings of conduction models. The bad quality of the I-T plots in *Figure A-14* is attributed to

the damages done to film during the current breakdown. As a result only the I-V plots can be exploited to determine the dominant transport mechanism.

The nature of the reference LbL film led to consider conductions based on ionic transport or tunnelling mechanisms. The ionic conduction model given by *equation A-1*[295] was considered:

$$J \sim \frac{E}{T} \exp\left(-\frac{\Delta E_{ai}}{kT}\right) \qquad (A\text{-}1)$$

Where E and ΔE_{ai} are the electric field and the activation energy of ions.

Table A-1 indicates that after current breakdown, the I-V plots of the reference film has a linear behaviour at low voltage (from -2 to +2 V) before shifting to an exponential behaviour at higher voltages. Given that a linear behaviour is only observed at low voltages, any control of the conduction by the ionic transport would occur in this range according to *equation A-1*.

Other conduction models were also considered. The I-V characteristic at 300 K displayed in *Figure A-13 (b)* was plotted according to the Fowler-Nordheim (F-N) and Poole-Frenkel (P-F) models in *Figure A-15 (a)* and *(b)*, respectively. *Figure A-16* shows it plotted according to the Richardson-Schottky (R-S) model.

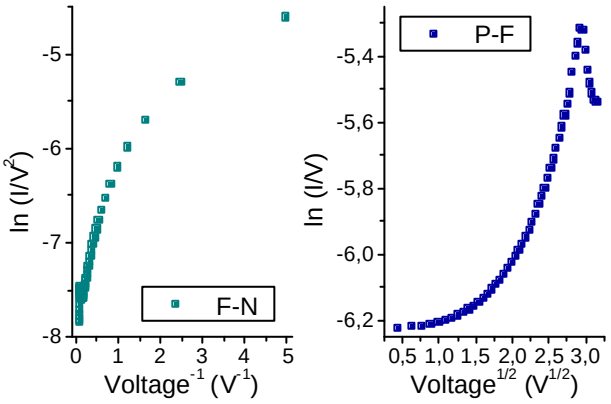

Figure A-15 $\ln(I/V^2)$ *vs* $1/V$ *plot (a) and* $\ln(I/V)$ *vs* $\sqrt{V}$ *plot (b) of I-V characteristics at 300 K of reference sample after current breakdown at 50 K according to the Fowler-Nordheim and Poole-Frenkel model, respectively*

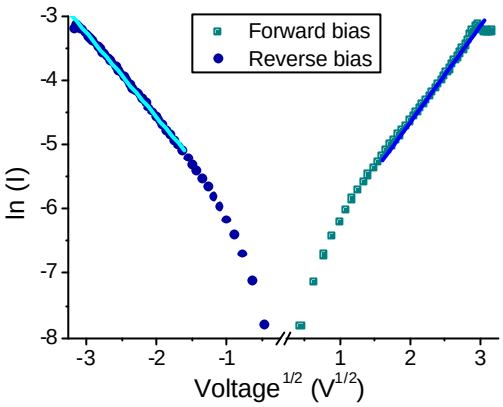

Figure A-16 $\ln(I)$ *vs* $\sqrt{V}$ *plots for reverse and forward bias of I-V characteristics at 300 K of reference sample after current breakdown at 50 K according to the Richardson-Schottky model*

The plots in *Figure A-15* do not display any linear behaviour. That shows that the I-V plot after current breakdown does not respect the Poole-Frenkel and Fowler-Nordheim conduction model. In *Figure A-16*, $\ln(I)$ *vs* $\sqrt{V}$ shows a linear behaviour for V≥ 3 V at both reverse and forward bias. Note: the region of negative differential resistance (from 8.6 to 10 V) of the I-V plot in *Figure A-13 (b)* has not been considered.

The linearity of the I-V plot at low voltages (±2 V) points out to the ionic conduction model. A dominance of direct tunnelling conduction at low voltages was discounted given that this range extends to ±2 V. For a dominant direct tunnelling mechanism, the current voltage dependence should be $I \propto V^3$ beyond the linear region, according to *equation 2-31*. It is not the case here, however, the occurrence of tunnelling phenomena cannot be discounted. Beyond 3 V, the conduction is dominated by the Richardson-Schottky conduction model. The presence of two different conductions governing the low and high voltage region is supported by the opposite evolution of the I-T plots in *Figure A-14*.

A.3 Alternating current measurements

The AC behaviour of SWCNT LbL films was analysed. Impedance measurements were carried out in the in-plane configuration at 300 K on 20 bi-layers SWCNT LbL films. Measurements on 20 bi-layers C_{60}-mixed SWCNT LbL films with SWCNT/C_{60} ratios of 33.3/66.6 and 50/50 were also performed. *Figure A-17* shows the frequency

dependence of the capacitance from 0.3 Hz (0.1Hz for 50/50 C_{60}-mixed SWCNT LbL film) to 5 MHz. *Figure A-18* shows their associated Nyquist plots.

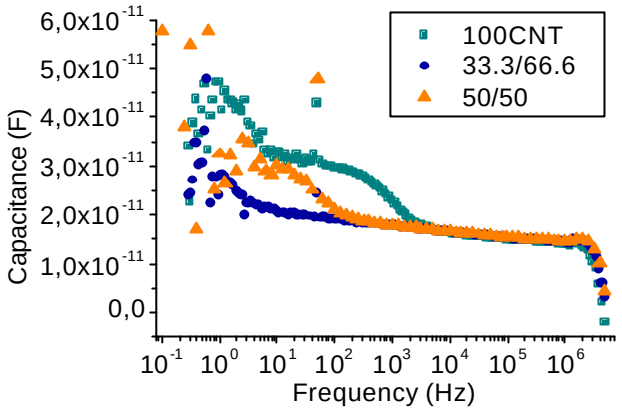

Figure A-17 Semi-log of capacitance-frequency plots of SWCNT (100 CNT) and C_{60}-mixed SWCNT LbL films with ratios of 33.3/66.6 and 50/50

Figure A-17 shows that for all films the capacitance is quasi constant at about 15 pF between 3 kHz and 2 MHz. This steadiness is preserved up to about 10 Hz for the 33.3/66.6 C_{60}-mixed SWCNT LbL film while it ends up at about 200 Hz for the 50/50 C_{60}-mixed SWCNT LbL film. The capacitance of the SWCNT LbL film deviates at about 2.81 kHz. The capacitance is however unstable at low frequencies (f<10 Hz). Note: the out of range points observed at 50 Hz are due to noise from the equipment and not in the film.

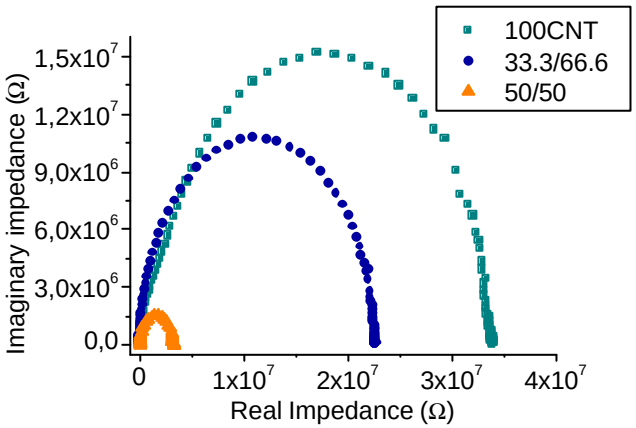

Figure A-18 Nyquist plots for SWCNT and C_{60}-mixed SWCNT LbL films

A negative phase was obtained for the Nyquist plots displayed in *Figure A-18*. That indicates that equivalent circuits for SWCNT and C_{60}-mixed SWCNT LbL films are a resistance RC and a capacitor C1 in series with a resistance R1 as shown by *Figure A-19*.

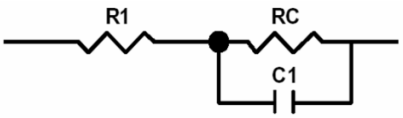

Figure A-19 Equivalent circuit of the SWCNT and C_{60}-mixed SWCNT LbL films

The values of R1 and RC for the 100%CNT, 50%CNT-50%C_{60} and 33.3%CNT-66.6%C_{60} LbL films extracted from *Figure A-19* are reported in *Table A-2*.

Proportion of SWCNTs and C_{60} in LbL films	R1 (Ω)	RC (Ω)
33.3%SWCNT-66.6%C60	1132.65	2.27×10^{7}
50%SWCNT-50%C60	1574.59	3.26×10^{6}
100%SWCNT	2477.8	3.4×10^{7}

Table A-2 Values of R1 and RC in the LbL films

Different Nyquist plots and subsequently their equivalent circuits were reported for SWCNT LbL films[189,296-297]. The result for the Nyquist plots of SWCNT LbL films obtained in this study was reported for another type of SWCNT LbL film.

Appendix B

Additional information for Chapter 3

B.1 Conduction in iodobenzene-SWCNT networks

VRH

Figure B-1 displays the $ln(I)\ versus T^{-1/4}$ plots and $ln(I)\ versus V^2$ plots according to the 3D-VRH model for the 2, 5 10 and 20 ml iodobenzene-SWCNT networks, respectively.

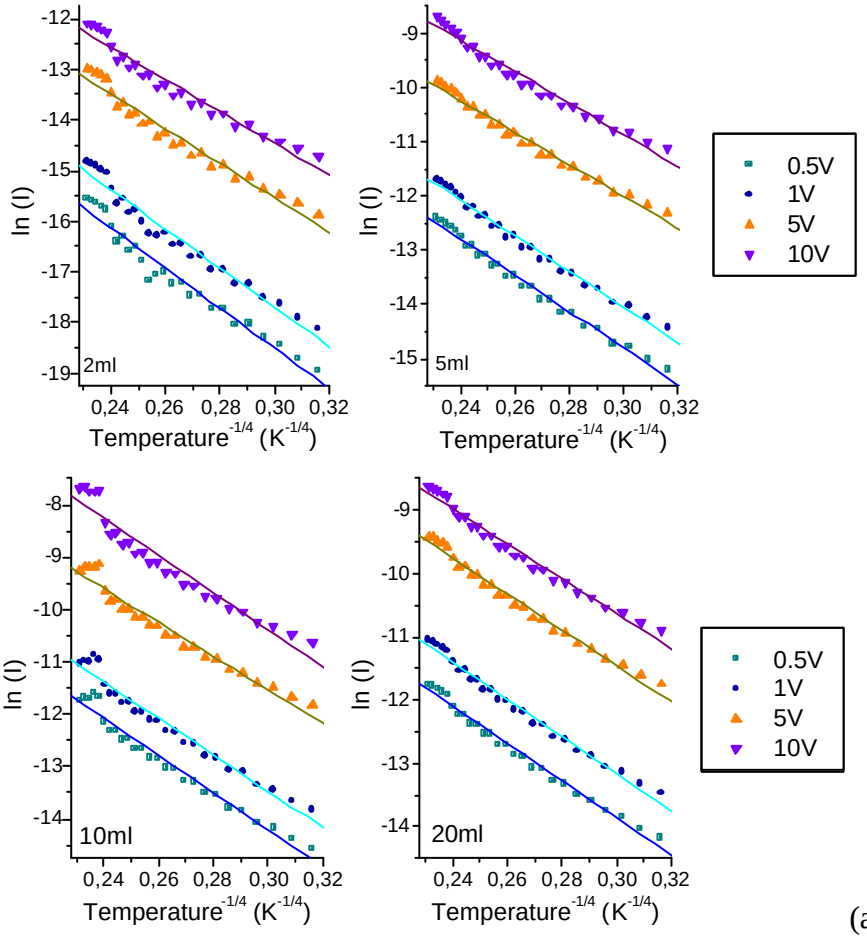

(a)

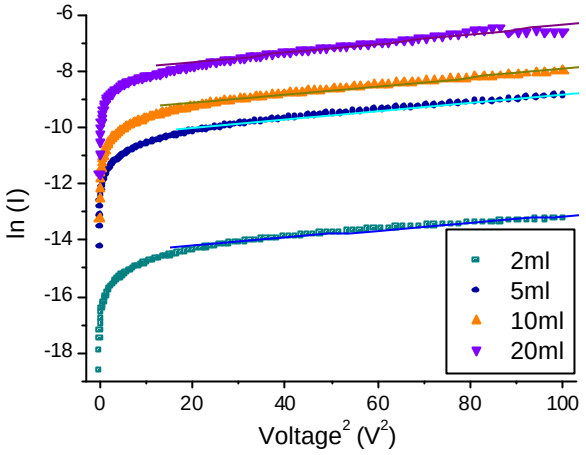

(b)

Figure B-1 (a) $\ln(I)$ *versus* $T^{-1/4}$ *plots of the I-T characteristics at 0.5, 1, 5 and 10 V (b)* $\ln(I)$ *versus* V^2 *plots of I-V plots for 2, 5, 10 and 20 ml iodobenzene-SWCNT networks*

Donor-acceptor hopping

Figure B-2 shows the I-T characteristics of the iodobenzene-SWCNT networks plotted according to the donor-trap hopping conduction.

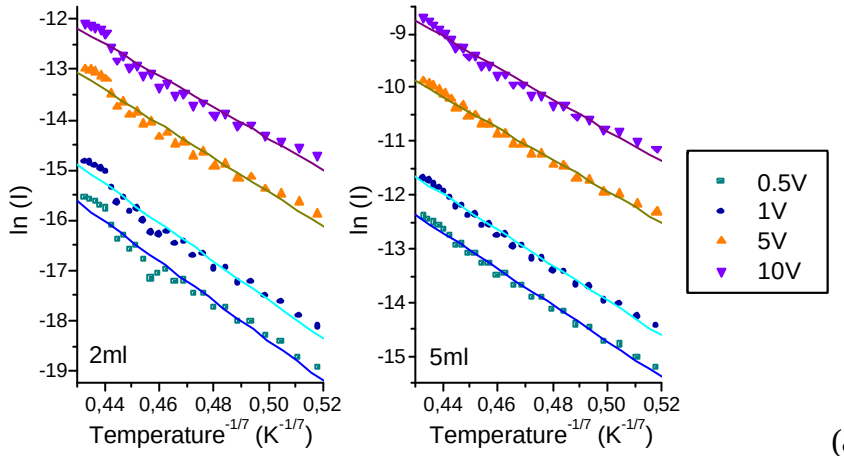

(a)

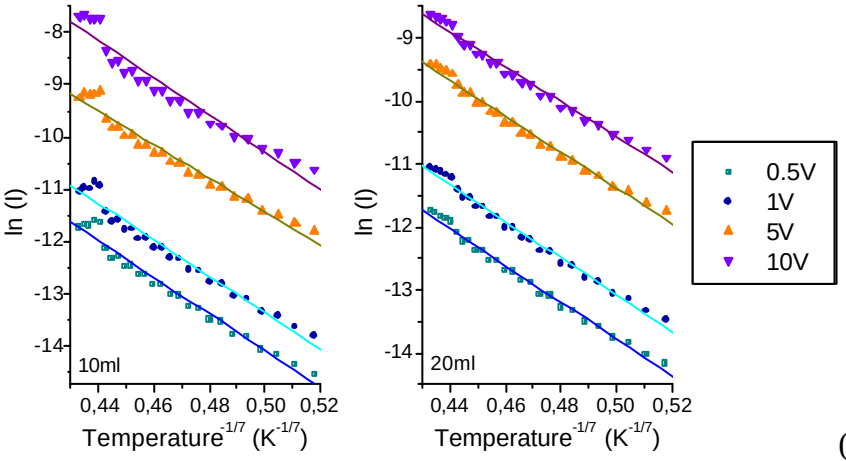

(b)

Figure B-2 $\ln(I)$ *versus* $T^{-\frac{1}{7}}$ *plots of the I-T plots for iodobenzene-SWCNT networks*

Tunnelling conduction

$\ln(I)$ *versus T* plots of the I-T characteristics (not shown here) were used to find the constant *A* of *equation 3-12*. The values of *A* for each network, shown in *Table B-1*, are integrated into *equation 3-12* for the fittings of both I-V and I-T plots.

Filtered volume (ml)	Constant A values
2	0.01
5	0.01
10	0.01
20	0.0095

Table B-1 Average values of constant A for iodobenzene-SWCNT networks

The I-V characteristics of the iodobenzene-SWCNT networks, fitted according to *equation 3-12*, are displayed in *Figure B-3*.

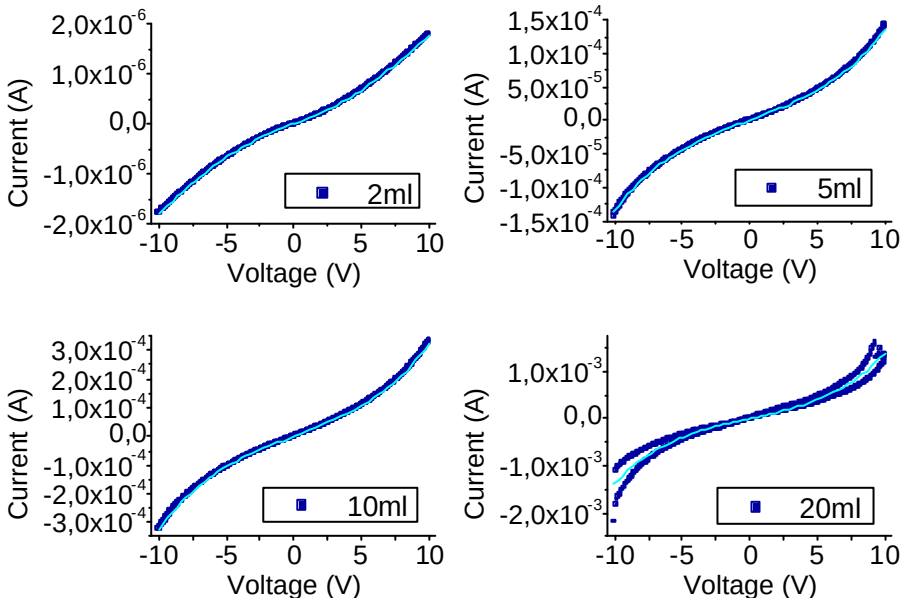

Figure B-3 I-V characteristics of 2, 5, 10 and 20 ml iodobenzene-SWCNT networks with their fits according to equation 3-12

The I-T characteristics at 0.5, 1, 5 and 10 V were fitted according to *equation 3-12* and displayed in *Figure B-3* for 2, 5, 10 and 20 ml iodobenzene-SWCNT networks.

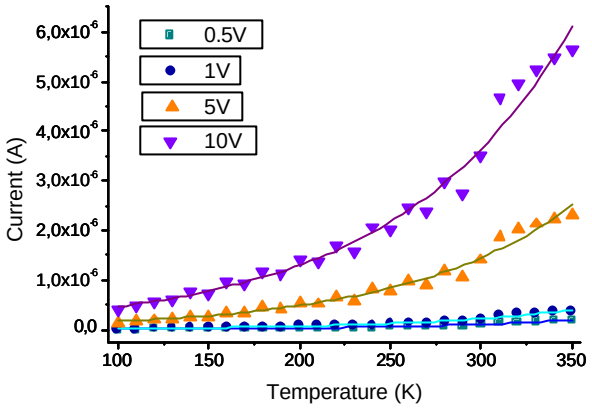

(a)

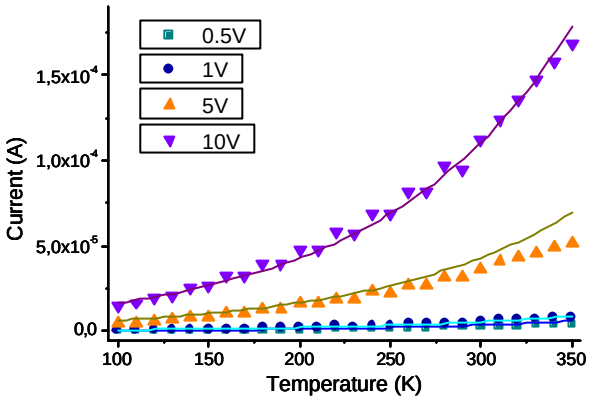

(b)

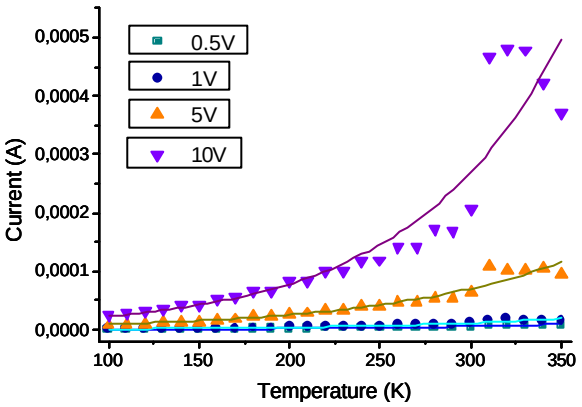

(c)

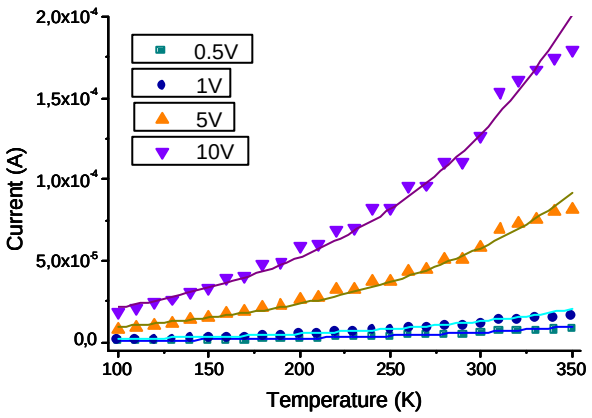

(d)

Figure B-4 Plots of I-T characteristics at 0.5, 1, 5 and 10 V according to eq. 3-12 for iodobenzene-SWCNT networks made with (a) 2 ml, (b) 5 ml, (c) 10 ml and (d) 20 ml SWCNT dispersions

B.2 Conduction mechanism in pyridine-SWCNT networks

VRH

Figure B-5 displays the $ln(I)\ versus T^{-1/4}$ plots and $ln(I)\ versus V^2$ plots of the electrical characteristics and according to 3D-VRH model for the 2, 5 and 10 ml pyridine-SWCNT networks, respectively.

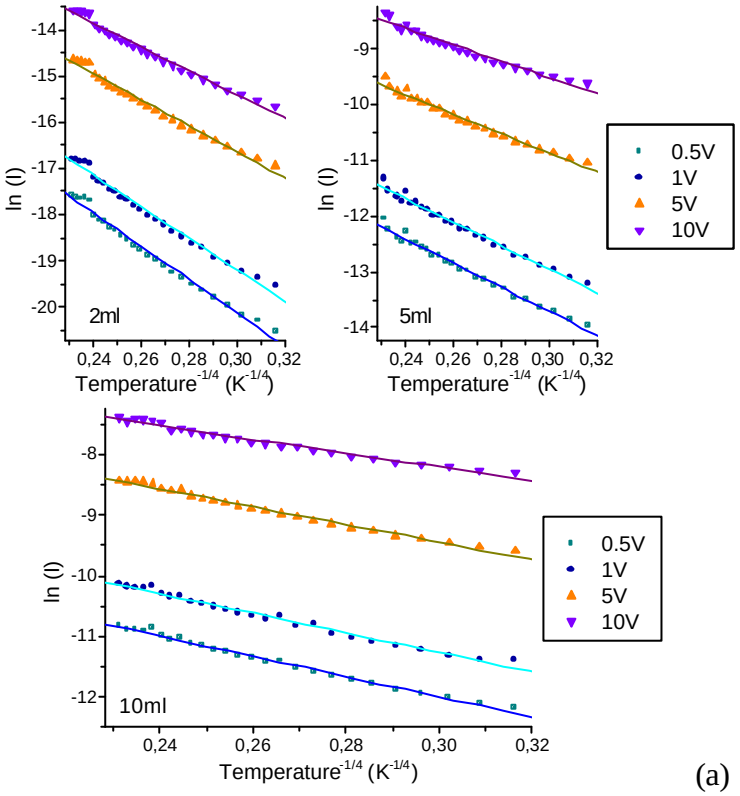

(a)

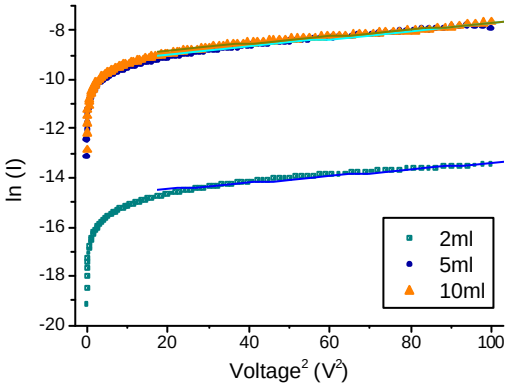

(b)

Figure B-5 (a) $\ln(I)\ versus T^{-\frac{1}{4}}$ *plots of the I-T plots at 0.5, 1, 5 and 10 V and (b)* $\ln(I)$ *versus* V^2 *plots of I-V characteristics for 2, 5 and 10 ml pyridine-SWCNT networks*

Donor-acceptor hopping

The I-T characteristics given in *Figure III-36* were plotted according to the donor-trap hopping conduction.

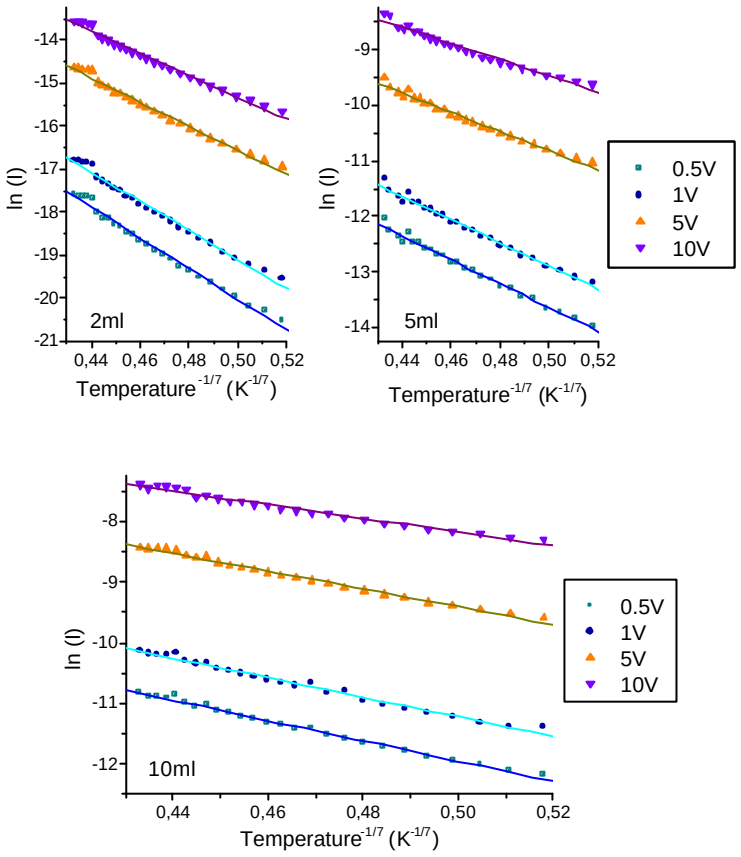

Figure B-6 $\ln(I)$ *versus* $T^{-1/7}$ *plots of the I-T characteristics at 0.5, 1, 5 and 10 V for 2, 5 and 10 ml pyridine-SWCNT networks*

Tunnelling conduction

The averaged values of A from $ln(I)$ *versus* T plots for each pyridine-SWCNT network are shown in *Table B-2*.

Network thickness (ml)	Constant A values
2	0.01
5	0.006
10	0.005

Table B-2 Averaged values of constant A for Pyridine-SWCNT networks

The I-V characteristics of the pyridine-SWCNT networks, fitted with *eq. 3-12*, are displayed in *Figure B-7*.

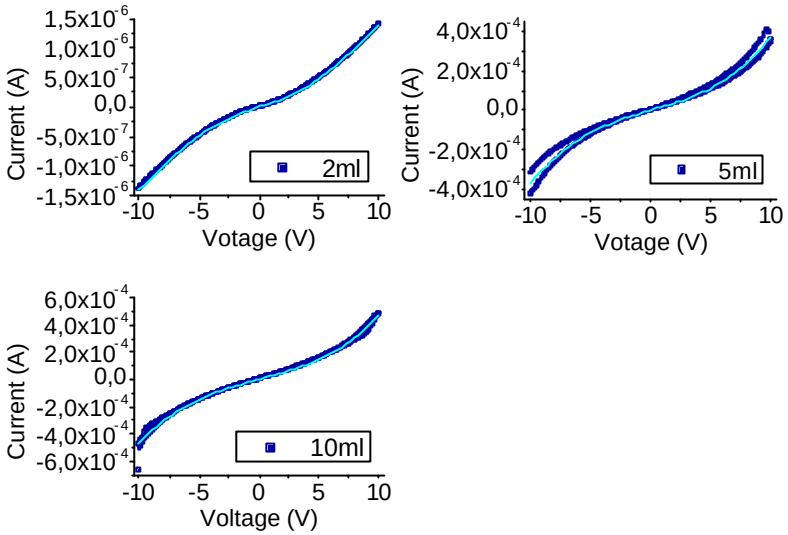

Figure B-7 I-V characteristics of pyridine-SWCNT networks made of 2, 5 and 10 ml of SWCNT dispersions with their fits according to equation 3-12

The I-T characteristics at 0.5, 1, 5 and 10 V were fitted according to *equation 3-12* for 2, 5 and 10 ml pyridine-SWCNT networks and displayed in *Figure B-8*.

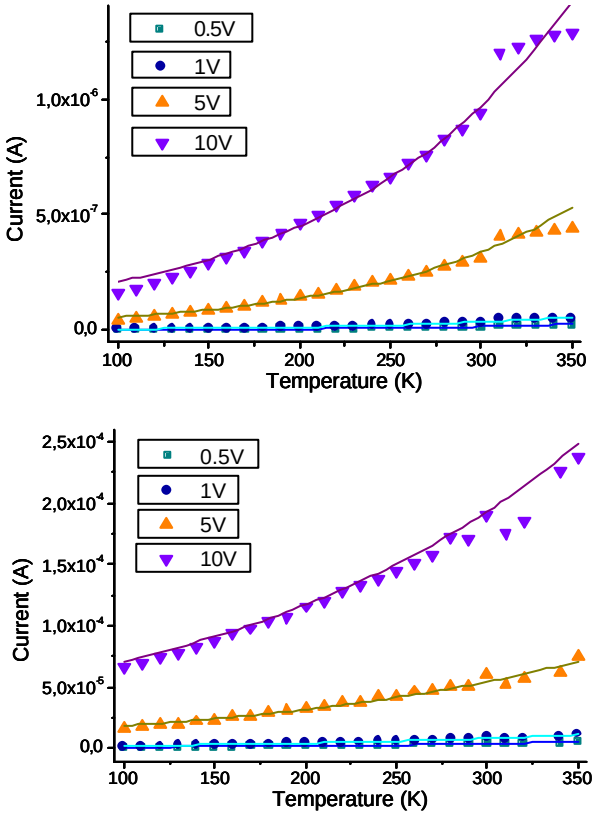

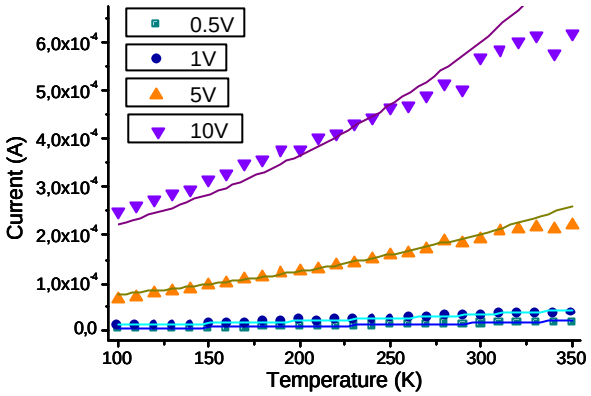

(c)

Figure B-8 Plots of I-T characteristics at 0.5, 1, 5 and 10 V according to equation 3-12 for pyridine-SWCNT networks of (a) 2 ml, (b) 5 ml and (c) 10 ml of SWCNT dispersions

B.3 Fitting parameters

Fitting parameters for I-V characteristics of Sonogashira-SWCNT networks

Filtered volume (ml)	Fitting parameters for Sonogashira-SWCNT networks			
	B (P1)	C (P2)	I_0 (p3)	A (P4)
5	4.87×10^{-3}	0.69	1.01×10^{-8}	6.3×10^{-3}
20	9.45×10^{-3}	0.66	2.13×10^{-7}	8.9×10^{-3}

Table B-3 Fitting parameters of the I-V plots of Sonogashira-SWCNT networks

Appendix C

Additional information for Chapter 4

C.1 VRH in molecularly bridged SWCNT networks

Figure C-1 displays the $ln(I)\ versus T^{-1/4}$ plots of the I-T characteristics according to 3D-VRH model for molecular bridged-SWCNT networks.

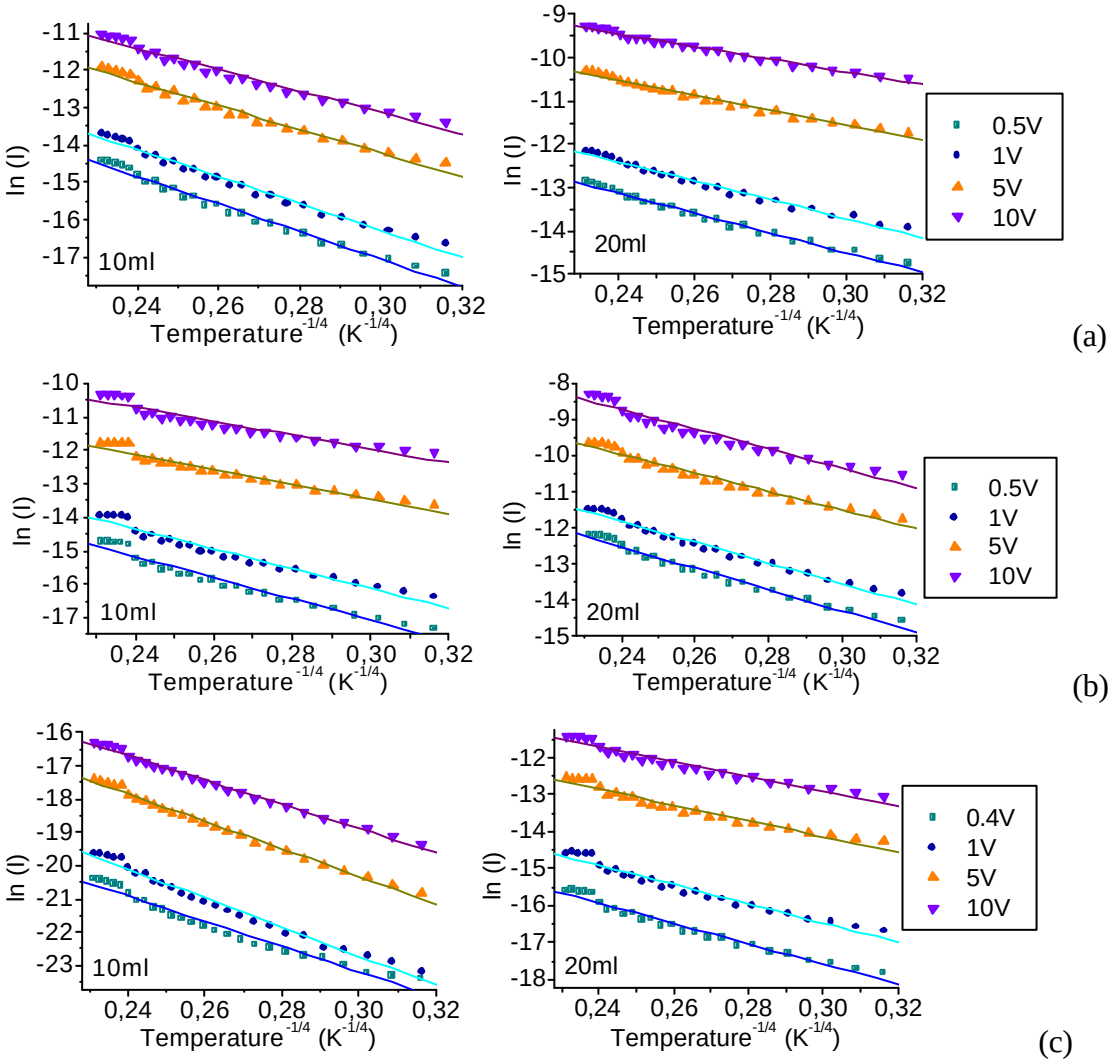

Figure C-1 $ln(I)\ versus T^{-1/4}$ *plots of the I-T characteristics for 10 and 20 ml networks of (a) homocoupled-SWCNTs (b) crosscoupled-SWCNTs and (c) Ullmann-SWCNTs*

Figure C-2 displays the $\ln(I)$ *versus* V^2 plots of the I-V characteristics at room temperature according to the 3D-VRH model for bridged SWCNT networks.

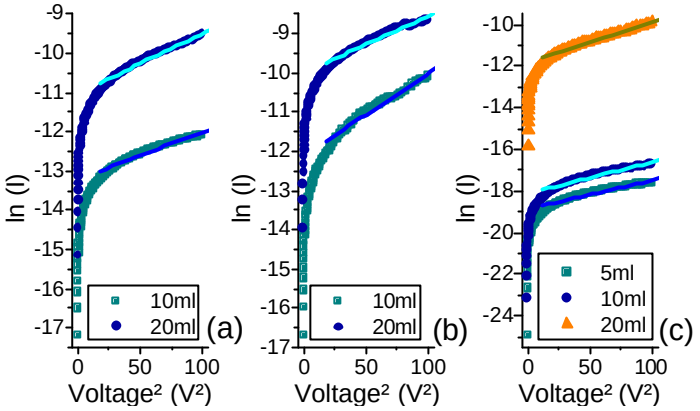

Figure C-2 $\ln(I)$ *versus* V^2 *plots of I-V characteristics at room temperature for 10 and 20 ml networks of (a) homocoupled-SWCNTs (b) crosscoupled-SWCNTs and (c) Ullmann-SWCNTs*

C.2 Donor-acceptor hopping in bridged SWCNT networks

Figure C-3 displays the $ln(I)$ $versus T^{-1/7}$ plots of the I-T characteristics for the 10 and 20 ml networks of homocoupled-SWCNTs, crosscoupled-SWCNTs and Ullmann-SWCNTs.

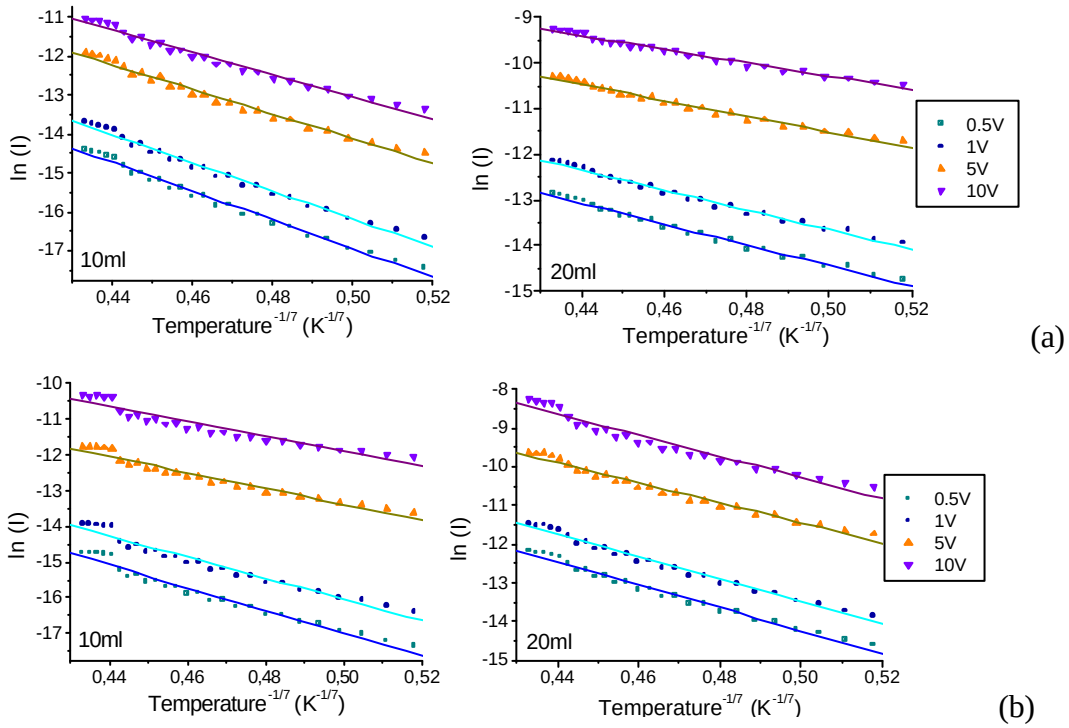

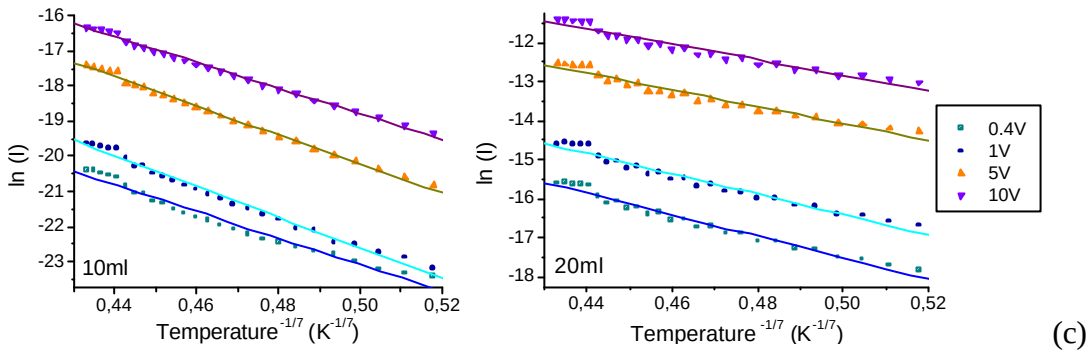

Figure C-3 $ln(I)$ $versus T^{-1/7}$ plots of the I-T characteristics for 10 ml and 20 ml networks of (a) homocoupled-SWCNTs, (b) crosscoupled-SWCNTs and (c) Ullmann-SWCNTs

C.3 Fitting parameters

Fitting parameters for I-V characteristics of homocoupled-SWCNT, crosscoupled-SWCNT and Ullmann-SWCNT networks

Volume Filtered volume (ml)	Fitting parameters for homocoupled-SWCNT networks			
	B (P1)	C (P2)	I_0 (p3)	A (P4)
10	1×10^{-4}	0.28	8×10^{-8}	1×10^{-2}
20	1.53×10^{-3}	0.48	1.29×10^{-6}	6×10^{-3}

Table C-1 Fitting parameters of the I-V plots of homocoupled-SWCNT networks

Filtered volume (ml)	Fitting parameters for crosscoupled-SWCNT networks			
	B (P1)	C (P2)	I_0 (p3)	A (P4)
10	5.25×10^{-3}	0.8	1.06×10^{-7}	8×10^{-3}
20	5×10^{-3}	0.58	1×10^{-6}	9.5×10^{-3}

Table C-2 Fitting parameters of the I-V plots of crosscoupled-SWCNT networks

Filtered volume (ml)	Fitting parameters for Ullmann-SWCNT networks			
	B (P1)	C (P2)	I_0 (p3)	A (P4)
5	1.8×10^{-4}	0.32	3×10^{-10}	0.0095
10	1.4×10^{-2}	0.85	1.68×10^{-10}	1×10^{-2}
20	7.61×10^{-3}	0.79	1.9×10^{-7}	8×10^{-3}

Table C-3 Fitting parameters of the I-V plots of Ullmann-SWCNT networks

Appendix D

Additional information for Chapter 5

D.1 3D-VRH in Pt-SWCNT networks

Figure D-1 displays the $ln(I)\ versus T^{-1/4}$ plots and $\ln(I)$ *versus* V^2 plots of the electrical characteristics and according to 3D-VRH model for the 2, 5 and 10 ml Pt-SWCNT networks.

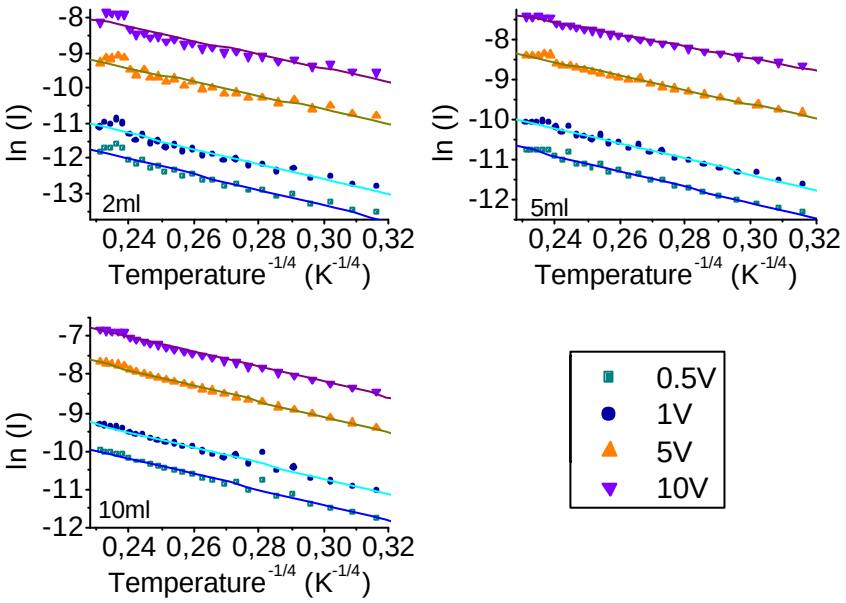

(a)

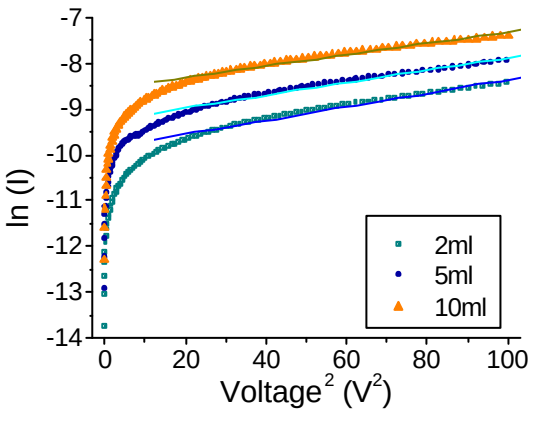

(b)

Figure D-1 (a) $ln(I)\ versus T^{-1/4}$ *plots of the I-T characteristics and (b)* $\ln(I)$ *versus* V^2 *plots of I-V characteristics for Pt-SWCNT networks*

D.2 Donor-acceptor hopping in Pt-SWCNT networks

Figure D-2 displays the $ln(I)\ versus T^{-1/7}$ plots of the I-T characteristics for the Pt-SWCNT networks.

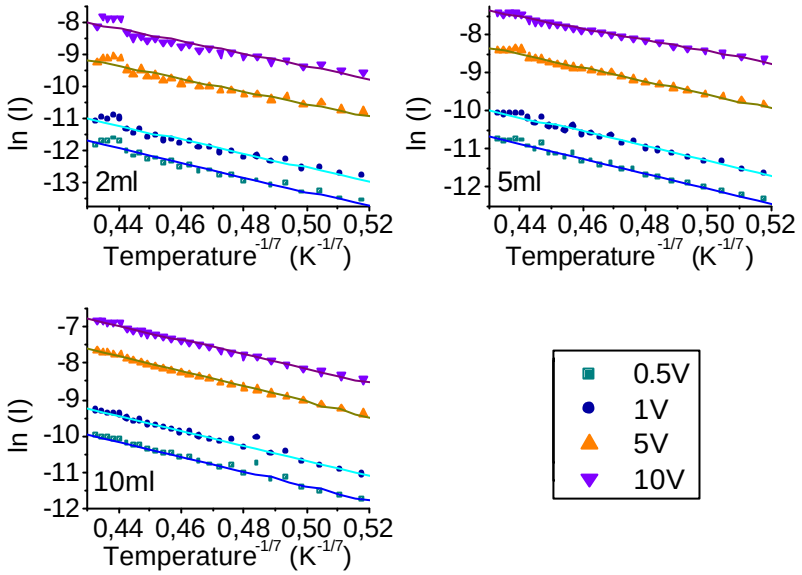

Figure D-2 $ln(I)\ versus T^{-1/7}$ *plots of the I-T characteristics for Pt-SWCNT networks*

D.3 Fitting parameters

Fitting parameters for I-V characteristics of Pt-SWCNT networks

Filtered volume (ml)	Fitting parameters for Pt-SWCNT networks			
	B (P1)	C (P2)	I_0 (p3)	A (P4)
2	-4.97×10^{-3}	0.1	2×10^{-5}	7×10^{-3}
5	-5.14×10^{-3}	0.04	9×10^{-5}	6×10^{-3}
10	-2.61×10^{-3}	0.09	6×10^{-5}	7×10^{-3}

Table D-1 Fitting parameters of the I-V plots of Pt-SWCNT networks

Appendix E

Cross-section pictures and electrical conductivities

The thicknesses of the filtered SWCNT networks were estimated from cross-section pictures using a SEM. Electrical conductivities were subsequently calculated from these measurements and the known geometry of the metal contacts. The SEM cross-section pictures, the networks' thickness and the electrical conductivities are presented in *Table E-1*.

Network	Filtered volume (ml)	SEM picture	Thickness	Conductivity at 10 V ($S.cm^{-1}$)
Pyridine-SWCNTs	5	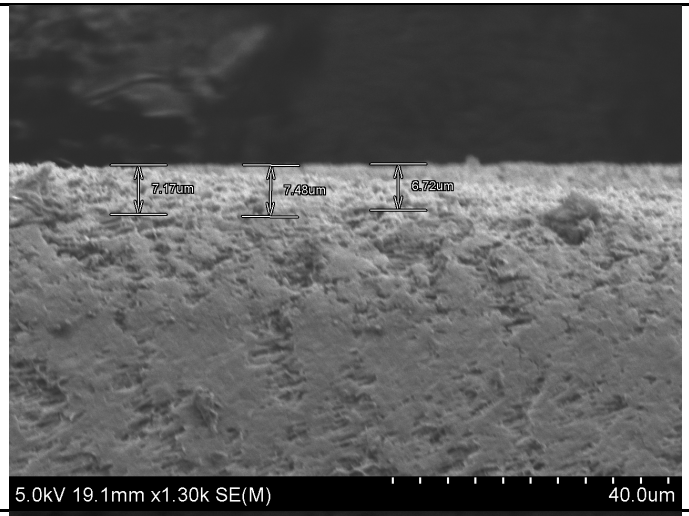	7.1 µm	2.5×10^{-3}
Pyridine-SWCNTs	10	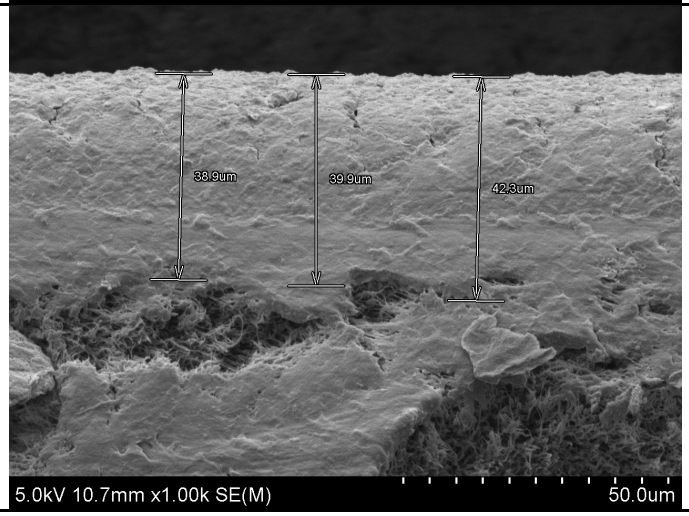	40.4 µm	5.5×10^{-4}

Iodobenzene-SWCNTs	2		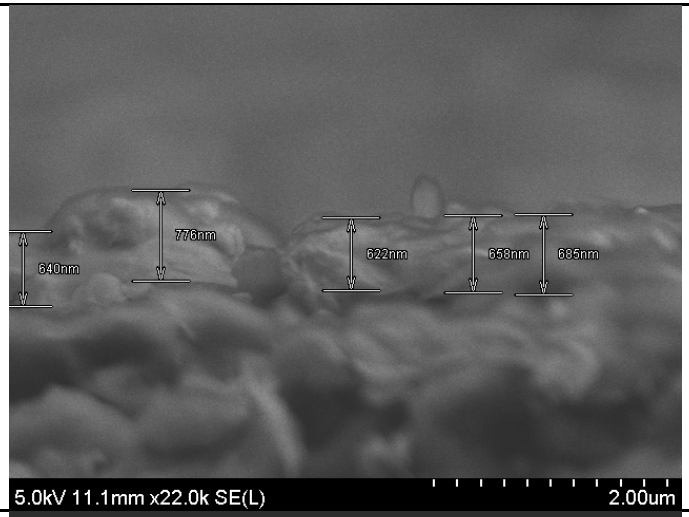	676 nm	1.3×10^{-4}
Iodobenzene-SWCNTs	5		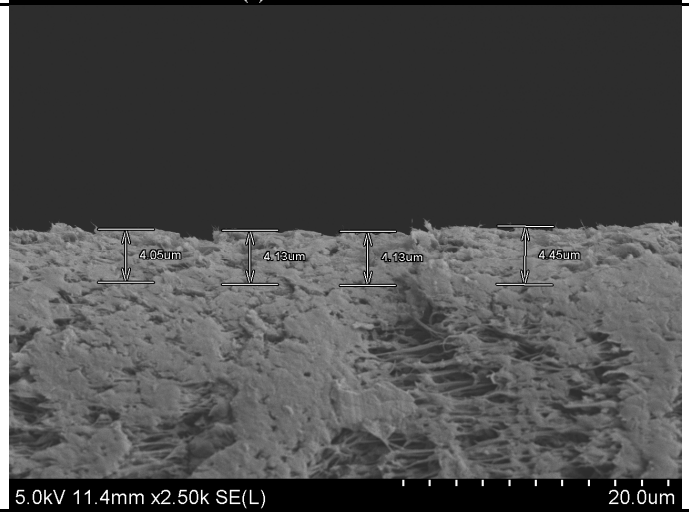	4.2 µm	1.7×10^{-3}

Iodobenzene-SWCNTs	10		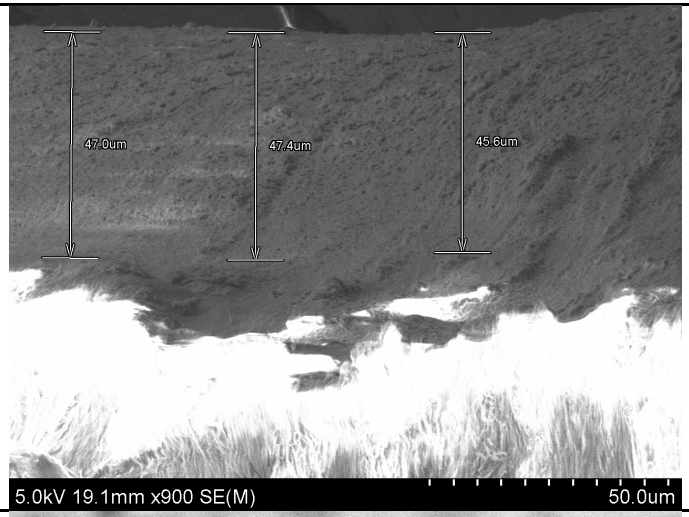	46.7 μm	3.6×10^{-4}
Iodobenzene-SWCNTs	20		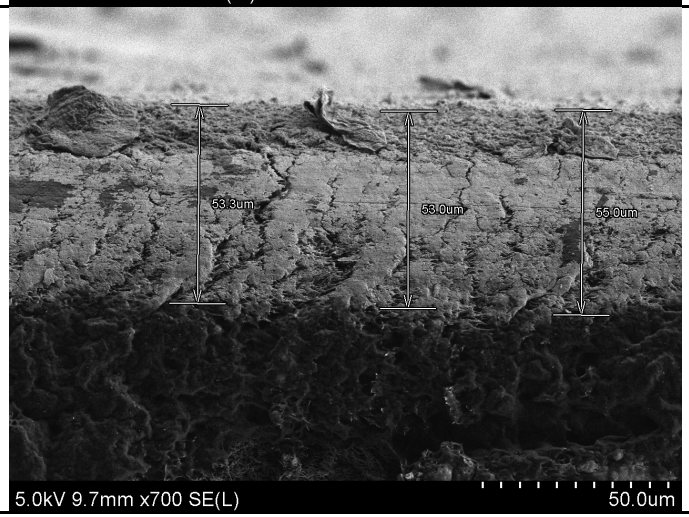	53.8 μm	1.3×10^{-3}

Sonogashira-SWCNTs	5		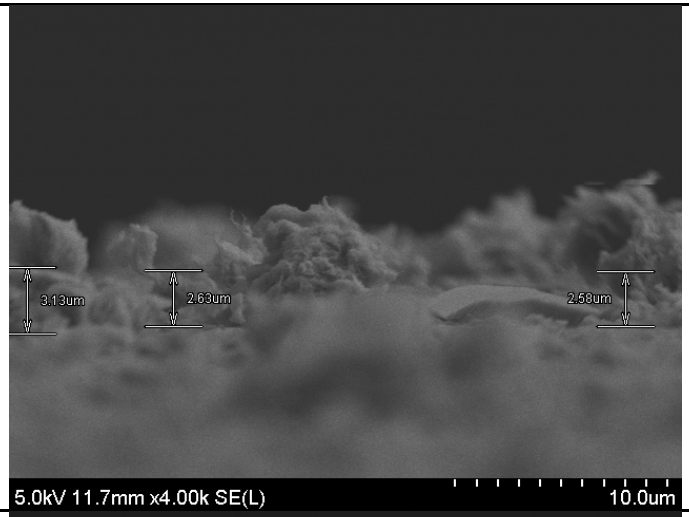	2.8 µm	2.5×10^{-6}
Sonogashira-SWCNTs	10		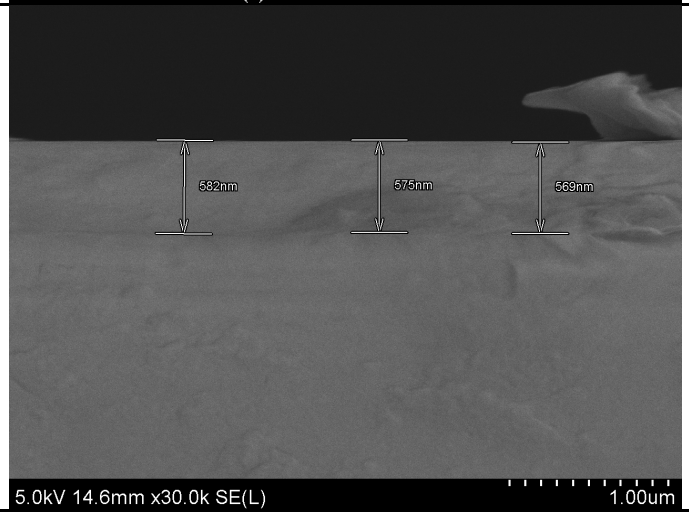	575 nm	2.6×10^{-6}

Sonogashira-SWCNTs	20		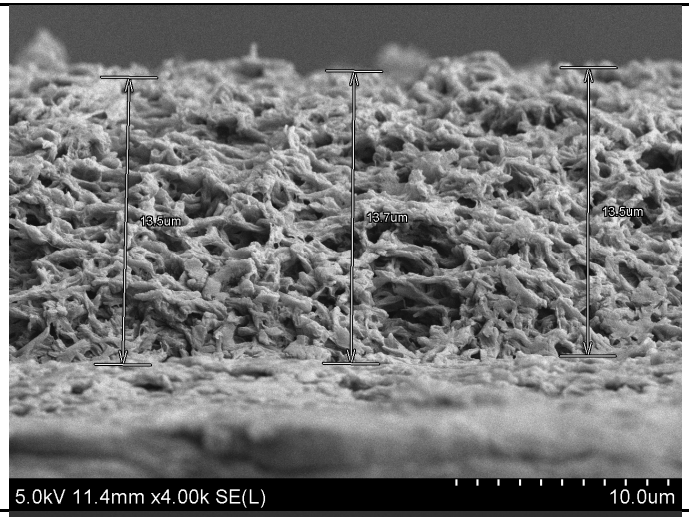	13.6 μm	1.1×10^{-4}
Homocoupled-SWCNTs	10			1.1 μm	6.6×10^{-6}

Homocoupled-SWCNTs	20		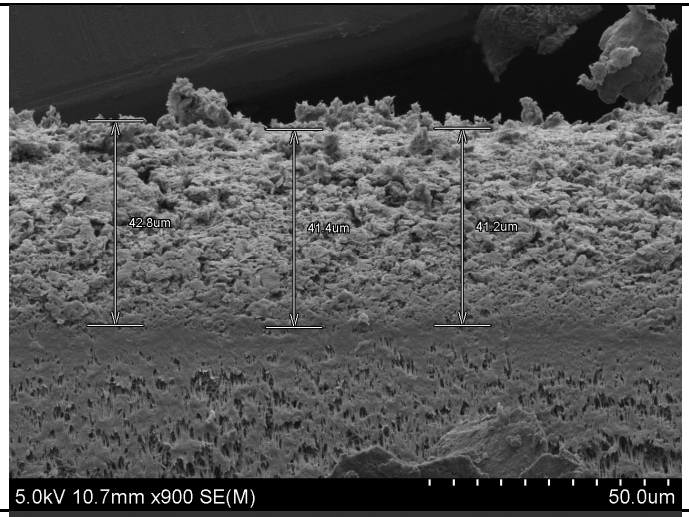		41.8 μm	8.7×10^{-5}
Crosscoupled-SWCNTs	10		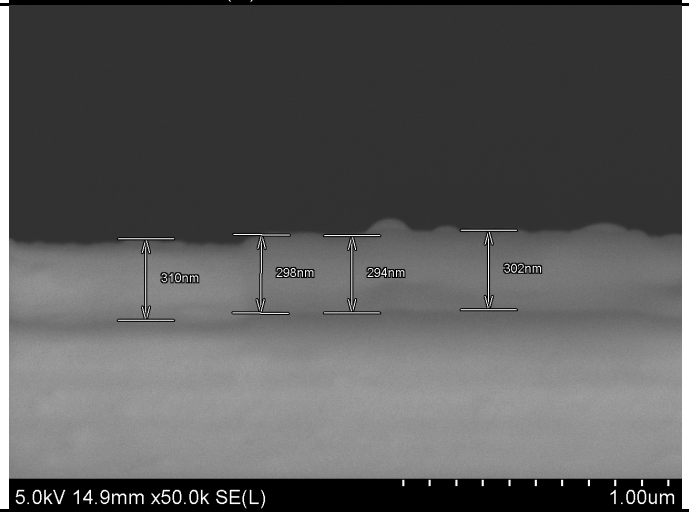		301 nm	6.9×10^{-3}

Crosscoupled-SWCNTs	20		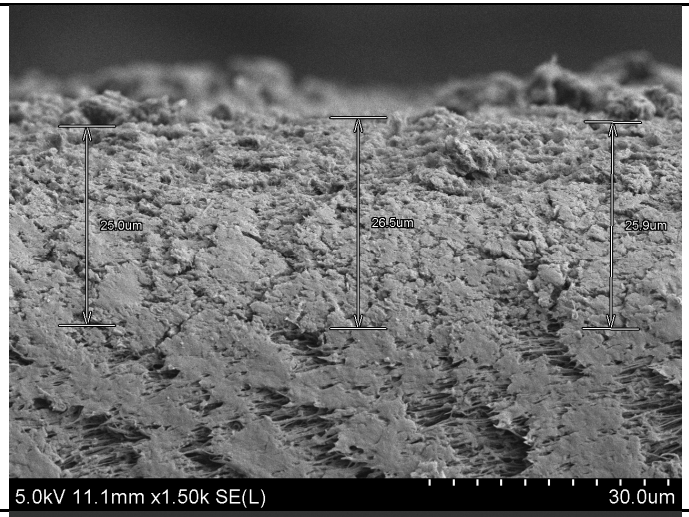		25.8 µm	3.4×10^{-4}
Ullmann-SWCNTs	10		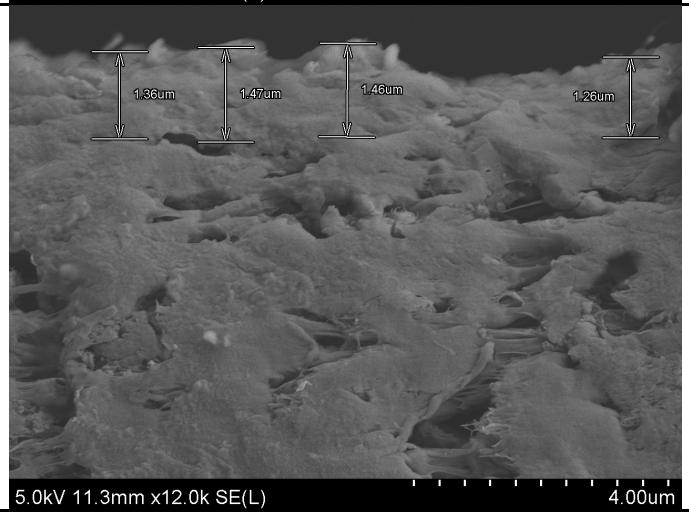		1.4 µm	2×10^{-7}

Ullmann-SWCNTs	20		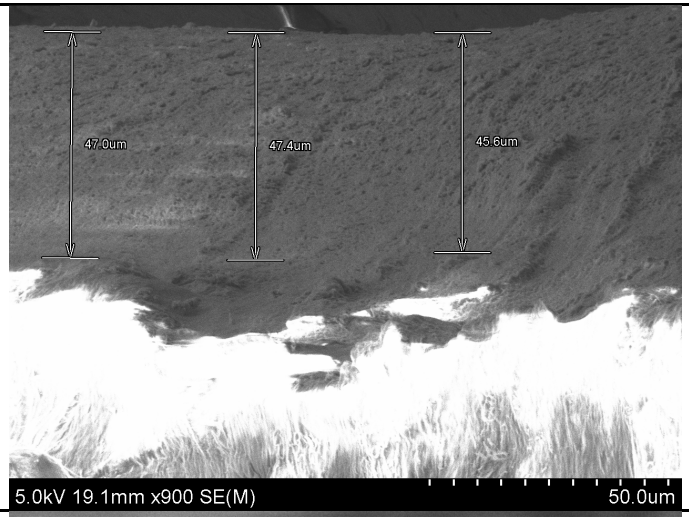	46.7 μm	5.7×10^{-5}
Pt-SWCNTs	10		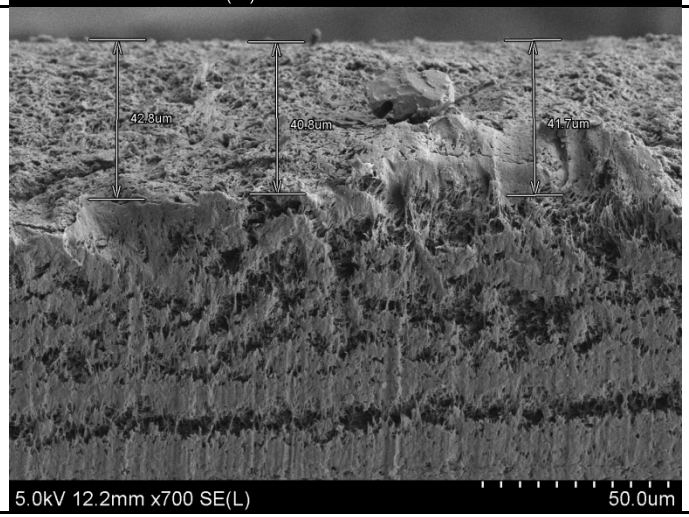	41.8 μm	7.3×10^{-4}

Table E-1 Cross-section SEM pictures, thickness and electrical conductivities of SWCNT networks

References

1 S. Iijima *Helical microtubules of graphitic carbon* Nature ***354***, 6348, p.56 (1991)

2 G. Dresselhaus, M. S. Dresselhaus and R. Saito *Physical properties of carbon nanotubes*; Imperial College Press London (2003)

3 P. Avouris, Z. H. Chen and V. Perebeinos *Carbon-based electronics* Nature Nanotechnology ***2***, 10, p.605 (2007)

4 A. Vijayaraghavan, S. Blatt, D. Weissenberger, M. Oron-Carl, F. Hennrich, D. Gerthsen, H. Hahn and R. Krupke *Ultra-large-scale directed assembly of single-walled carbon nanotube devices* Nano Letters ***7***, 6, p.1556 (2007)

5 Q. Cao and J. A. Rogers *Ultrathin films of single-walled carbon nanotubes for electronics and sensors: a review of fundamental and applied aspects* Advanced Materials ***21***, 1, p.29 (2009)

6 G. Gruner *Carbon nanotube films for transparent and plastic electronics* Journal of Materials Chemistry ***16***, 35, p.3533 (2006)

7 Q. Cao, H. S. Kim, N. Pimparkar, J. P. Kulkarni, C. J. Wang, M. Shim, K. Roy, M. A. Alam and J. A. Rogers *Medium-scale carbon nanotube thin-film integrated circuits on flexible plastic substrates* Nature ***454***, 7203, p.495 (2008)

8 M. W. Rowell, M. A. Topinka, M. D. McGehee, H. J. Prall, G. Dennler, N. S. Sariciftci, L. B. Hu and G. Gruner *Organic solar cells with carbon nanotube network electrodes* Applied Physics Letters ***88***, 23 (2006)

9 Y. Wang, C. A. Di, Y. Q. Liu, H. Kajiura, S. H. Ye, L. C. Cao, D. C. Wei, H. L. Zhang, Y. M. Li and K. Noda *Optimizing single-walled carbon nanotube films for applications in electroluminescent devices* Advanced Materials ***20***, 23, p.4442 (2008)

10 P. Bondavalli, P. Legagneux and D. Pribat *Carbon nanotubes based transistors as gas sensors: State of the art and critical review* Sensors and Actuators B-Chemical ***140***, 1, p.304 (2009)

11 M. Burghard *Electronic and vibrational properties of chemically modified single-wall carbon nanotubes* Surface Science Reports ***58***, 1-4, p.1 (2005)

12 M. Monthioux and V. L. Kuznetsov *Who should be given the credit for the discovery of carbon nanotubes?* Carbon ***44***, 9, p.1621 (2006)

13 P. A. Thrower *Novel carbon materials - What if?* Carbon ***37***, 11, p.1677 (1999)

14 S. Iijima and T. Ichihashi *Single-shell carbon nanotubes of 1-nm diameter* Nature ***363***, 6430, p.603 (1993)

15 S. Iijima, P. M. Ajayan and T. Ichihashi *Growth-model for carbon nanotubes* Physical Review Letters ***69***, 21, p.3100 (1992)

16 D. Ugarte *Morphology and structure of graphitic soot particles generated in arc-discharge c60 production* Chemical Physics Letters ***198***, 6, p.596 (1992)

17 N. Hamada, S. Sawada and A. Oshiyama *New one-dimensional conductors - graphitic microtubules* Physical Review Letters ***68***, 10, p.1579 (1992)

18 L. Langer, L. Stockman, J. P. Heremans, V. Bayot, C. H. Olk, C. Vanhaesendonck, Y. Bruynseraede and J. P. Issi *Electrical-resistance of a carbon nanotube bundle* Journal of Materials Research ***9***, 4, p.927 (1994)

19 J. W. Mintmire, B. I. Dunlap and C. T. White *Are fullerene tubules metallic* Physical Review Letters ***68***, 5, p.631 (1992)

20 J. W. G. Wildoer, L. C. Venema, A. G. Rinzler, R. E. Smalley and C. Dekker *Electronic structure of atomically resolved carbon nanotubes* Nature ***391***, 6662, p.59 (1998)

21 R. Saito, M. Fujita, G. Dresselhaus and M. S. Dresselhaus *Electronic-structure of chiral graphene tubules* Applied Physics Letters ***60***, 18, p.2204 (1992)

22 P. Kim, T. W. Odom, J. L. Huang and C. M. Lieber *Electronic density of states of atomically resolved single-walled carbon nanotubes: Van Hove singularities and end states* Physical Review Letters ***82***, 6, p.1225 (1999)

23 H. Kataura, Y. Kumazawa, Y. Maniwa, I. Umezu, S. Suzuki, Y. Ohtsuka and Y. Achiba *Optical properties of single-wall carbon nanotubes* Synthetic Metals ***103***, 1-3, p.2555 (1999)

24 W. Zhang, Z. Y. Zhu, F. Wang, T. T. Wang, L. T. Sun and Z. X. Wang *Chirality dependence of the thermal conductivity of carbon nanotubes* Nanotechnology ***15***, 8, p.936 (2004)

25 P. L. McEuen, M. S. Fuhrer and H. K. Park *Single-walled carbon nanotube electronics* Ieee Transactions on Nanotechnology ***1***, 1, p.78 (2002)

26 C. T. White and T. N. Todorov *Carbon nanotubes as long ballistic conductors* Nature ***393***, 6682, p.240 (1998)

27 P. J. de Pablo, C. Gomez-Navarro, M. T. Martinez, A. M. Benito, W. K. Maser, J. Colchero, J. Gomez-Herrero and A. M. Baro *Performing current versus voltage measurements of single-walled carbon nanotubes using scanning force microscopy (vol 80, pg 1462, 2002)* Applied Physics Letters ***80***, 13, p.2421 (2002)

28 S. Frank, P. Poncharal, Z. L. Wang and W. A. de Heer *Carbon nanotube quantum resistors* Science ***280***, 5370, p.1744 (1998)

29 H. Kajiura, H. J. Huang and A. Bezryadin *Quasi-ballistic electron transport in double-wall carbon nanotubes* Chemical Physics Letters ***398***, 4-6, p.476 (2004)

30 T. W. Ebbesen, H. J. Lezec, H. Hiura, J. W. Bennett, H. F. Ghaemi and T. Thio *Electrical conductivity of individual carbon nanotubes* Nature ***382***, 6586, p.54 (1996)

31 Y. Ando, X. Zhao, H. Shimoyama, G. Sakai and K. Kaneto *Physical properties of multiwalled carbon nanotubes* International Journal of Inorganic Materials ***1***, 1, p.77 (1999)

32 C. W. Zhou, J. Kong and H. J. Dai *Electrical measurements of individual semiconducting single-walled carbon nanotubes of various diameters* Applied Physics Letters ***76***, 12, p.1597 (2000)

33 Z. Yao, C. L. Kane and C. Dekker *High-field electrical transport in single-wall carbon nanotubes* Physical Review Letters ***84***, 13, p.2941 (2000)

34 B. Q. Wei, R. Vajtai and P. M. Ajayan *Reliability and current carrying capacity of carbon nanotubes* Applied Physics Letters ***79***, 8, p.1172 (2001)

35 F. Li, H. M. Cheng, S. Bai, G. Su and M. S. Dresselhaus *Tensile strength of single-walled carbon nanotubes directly measured from their macroscopic ropes* Applied Physics Letters ***77***, 20, p.3161 (2000)

36 H. R. Lusti and A. A. Gusev *Finite element predictions for the thermoelastic properties of nanotube reinforced polymers* Modelling and Simulation in Materials Science and Engineering ***12***, 3, p.S107 (2004)

37 M. M. J. Treacy, T. W. Ebbesen and J. M. Gibson *Exceptionally high Young's modulus observed for individual carbon nanotubes* Nature ***381***, 6584, p.678 (1996)

38 A. Krishnan, E. Dujardin, T. W. Ebbesen, P. N. Yianilos and M. M. J. Treacy *Young's modulus of single-walled nanotubes* Physical Review B ***58***, 20, p.14013 (1998)

39 O. Lourie and H. D. Wagner *Evaluation of Young's modulus of carbon nanotubes by micro-Raman spectroscopy* Journal of Materials Research ***13***, 9, p.2418 (1998)

40 R. J. McGlen, R. Jachuck and S. Lin *Integrated thermal management techniques for high power electronic devices* Applied Thermal Engineering ***24***, 8-9, p.1143 (2004)

41 M. A. Osman and D. Srivastava *Temperature dependence of the thermal conductivity of single-wall carbon nanotubes* Nanotechnology ***12***, 1, p.21 (2001)

42 S. Berber, Y. K. Kwon and D. Tomanek *Unusually high thermal conductivity of carbon nanotubes* Physical Review Letters ***84***, 20, p.4613 (2000)

43 S. V. Garimella *Advances in mesoscale thermal management technologies for microelectronics* Microelectronics Journal ***37***, 11, p.1165 (2006)

44 N. Mingo and D. A. Broido *Carbon nanotube ballistic thermal conductance and its limits* Physical Review Letters ***95***, 9 (2005)

45 P. Kim, L. Shi, A. Majumdar and P. L. McEuen *Thermal transport measurements of individual multiwalled nanotubes* Physical Review Letters ***87***, 21 (2001)

46 C. H. Yu, L. Shi, Z. Yao, D. Y. Li and A. Majumdar *Thermal conductance and thermopower of an individual single-wall carbon nanotube* Nano Letters ***5***, 9, p.1842 (2005)

47 E. Pop, D. Mann, Q. Wang, K. Goodson and H. J. Dai *Thermal conductance of an individual single-wall carbon nanotube above room temperature* Nano Letters ***6***, 1, p.96 (2006)

48 J. Hone, M. Whitney, C. Piskoti and A. Zettl *Thermal conductivity of single-walled carbon nanotubes* Physical Review B ***59***, 4, p.R2514 (1999)

49 J. Hone, M. C. Llaguno, M. J. Biercuk, A. T. Johnson, B. Batlogg, Z. Benes and J. E. Fischer *Thermal properties of carbon nanotubes and nanotube-based materials* Applied Physics a-Materials Science & Processing ***74***, 3, p.339 (2002)

50 J. Hone In *Carbon Nanotubes* 2001; Vol. 80, p 273.

51 C. A. Dyke and J. M. Tour *Covalent functionalization of single-walled carbon nanotubes for materials applications* Journal of Physical Chemistry A ***108***, 51, p.11151 (2004)

52 P. M. Ajayan and J. M. Tour *Materials science - Nanotube composites* Nature ***447***, 7148, p.1066 (2007)

53 R. C. Haddon and S. Y. Chow *Hybridization as a metric for the reaction coordinate of chemical reactions* Journal of the American Chemical Society ***120***, 40, p.10494 (1998)

54 R. C. Haddon *Pi-electrons in 3 dimensions* Accounts of Chemical Research ***21***, 6, p.243 (1988)

55 R. C. Haddon *Chemistry of the fullerenes - the manifestation of strain in a class of continuous aromatic-molecules* Science ***261***, 5128, p.1545 (1993)

56 S. Niyogi, M. A. Hamon, H. Hu, B. Zhao, P. Bhowmik, R. Sen, M. E. Itkis and R. C. Haddon *Chemistry of single-walled carbon nanotubes* Accounts of Chemical Research ***35***, 12, p.1105 (2002)

57 J. T. Titantah, K. Jorissen and D. Lamoen *Density functional theory calculations of energy-loss carbon near-edge spectra of small diameter armchair and zigzag nanotubes: Core-hole, curvature, and monientum-transfer orientation effects* Physical Review B ***69***, 12 (2004)

58 F. Torrens *Periodic properties of carbon nanotubes based on the chiral vector* Internet Electronic Journal of Molecular Design ***4***, 1 (2005)

59 S. Osswald, M. Havel and Y. Gogotsi *Monitoring oxidation of multiwalled carbon nanotubes by Raman spectroscopy* Journal of Raman Spectroscopy ***38***, 6, p.728 (2007)

60 M. Q. Tran, C. Tridech, A. Alfrey, A. Bismarck and M. S. P. Shaffer *Thermal oxidative cutting of multi-walled carbon nanotubes* Carbon ***45***, 12, p.2341 (2007)

61 O. Byl, J. Liu and J. T. Yates *Etching of carbon nanotubes by ozone - A surface area study* Langmuir ***21***, 9, p.4200 (2005)

62 F. Cataldo *A study on the action of ozone on multiwall carbon nanotubes* Fullerenes Nanotubes and Carbon Nanostructures ***16***, 1, p.1 (2008)

63 J. P. Deng, C. Y. Mou and C. C. Han *Oxidation of fullerenes by ozone* Fullerene Science and Technology ***5***, 7, p.1325 (1997)

64 A. Kukovecz, C. Kramberger, M. Holzinger, H. Kuzmany, J. Schalko, M. Mannsberger and A. Hirsch *On the stacking behavior of functionalized single-wall carbon nanotubes* Journal of Physical Chemistry B ***106***, 25, p.6374 (2002)

65 M. W. Marshall, S. Popa-Nita and J. G. Shapter *Measurement of functionalised carbon nanotube carboxylic acid groups using a simple chemical process* Carbon ***44***, 7, p.1137 (2006)

66 J. Qiu, G. J. Wang, Z. H. Qu and L. Chang *Relationship between oxidation treatment method and carboxylic group content on the surface of MWCNTs* New Carbon Materials ***21***, 3, p.269 (2006)

67 Y. B. Wang, Z. Iqbal and S. Mitra *Rapidly functionalized, water-dispersed carbon nanotubes at high concentration* Journal of the American Chemical Society ***128***, 1, p.95 (2006)

68 J. Zhang, H. L. Zou, Q. Qing, Y. L. Yang, Q. W. Li, Z. F. Liu, X. Y. Guo and Z. L. Du *Effect of chemical oxidation on the structure of single-walled carbon nanotubes* Journal of Physical Chemistry B ***107***, 16, p.3712 (2003)

69 H. Ago, T. Kugler, F. Cacialli, W. R. Salaneck, M. S. P. Shaffer, A. H. Windle and R. H. Friend *Work functions and surface functional groups of multiwall carbon nanotubes* Journal of Physical Chemistry B ***103***, 38, p.8116 (1999)

70 S. H. Jhi, S. G. Louie and M. L. Cohen *Electronic properties of oxidized carbon nanotubes* Physical Review Letters ***85***, 8, p.1710 (2000)

71 J. L. Bahr, J. P. Yang, D. V. Kosynkin, M. J. Bronikowski, R. E. Smalley and J. M. Tour *Functionalization of carbon nanotubes by electrochemical reduction of aryl diazonium salts: A bucky paper electrode* Journal of the American Chemical Society ***123***, 27, p.6536 (2001)

72 C. A. Dyke and J. M. Tour *Overcoming the insolubility of carbon nanotubes through high degrees of sidewall functionalization* Chemistry-a European Journal ***10***, 4, p.813 (2004)

73 J. Liu, M. R. I. Zubiri, M. Dossot, B. Vigolo, R. H. Hauge, Y. Fort, J. J. Ehrhardt and E. McRae *Sidewall functionalization of single-wall carbon nanotubes (SWNTs) through aryl free radical addition* Chemical Physics Letters ***430***, 1-3, p.93 (2006)

74 T. Gunji, M. Akazawa, K. Arimitsu and Y. Abe *Chemical modification of SWCNT and VGCF by radical addition reaction* Chemistry Letters ***35***, 6, p.630 (2006)

75 M. S. Strano, C. A. Dyke, M. L. Usrey, P. W. Barone, M. J. Allen, H. W. Shan, C. Kittrell, R. H. Hauge, J. M. Tour and R. E. Smalley *Electronic structure control of single-walled carbon nanotube functionalization* Science ***301***, 5639, p.1519 (2003)

76 R. Q. Pan, Z. J. Xu, Z. Y. Zhu and Z. X. Wang *Thermal conductivity of functionalized single-wall carbon nanotubes* Nanotechnology ***18***, 28 (2007)

77 C. W. Padgett and D. W. Brenner *Influence of chemisorption on the thermal conductivity of single-wall carbon nanotubes* Nano Letters ***4***, 6, p.1051 (2004)

78 V. Skakalova, A. B. Kaiser, U. Dettlaff-Weglikowska, K. Hrncarikova and S. Roth *Effect of chemical treatment on electrical conductivity, infrared absorption, and Raman spectra of single-walled carbon nanotubes* Journal of Physical Chemistry B ***109***, 15, p.7174 (2005)

79 B. Z. Tang and H. Y. Xu *Preparation, alignment, and optical properties of soluble poly(phenylacetylene)-wrapped carbon nanotubes* Macromolecules ***32***, 8, p.2569 (1999)

80 M. S. Strano, V. C. Moore, M. K. Miller, M. J. Allen, E. H. Haroz, C. Kittrell, R. H. Hauge and R. E. Smalley *The role of surfactant adsorption during ultrasonication in the dispersion of single-walled carbon nanotubes* Journal of Nanoscience and Nanotechnology ***3***, 1-2, p.81 (2003)

81 V. C. Moore, M. S. Strano, E. H. Haroz, R. H. Hauge, R. E. Smalley, J. Schmidt and Y. Talmon *Individually suspended single-walled carbon nanotubes in various surfactants* Nano Letters ***3***, 10, p.1379 (2003)

82 M. F. Islam, E. Rojas, D. M. Bergey, A. T. Johnson and A. G. Yodh *High weight fraction surfactant solubilization of single-wall carbon nanotubes in water* Nano Letters ***3***, 2, p.269 (2003)

83 C. Richard, F. Balavoine, P. Schultz, T. W. Ebbesen and C. Mioskowski *Supramolecular self-assembly of lipid derivatives on carbon nanotubes* Science ***300***, 5620, p.775 (2003)

84 Y. H. Xie and A. K. Soh *Investigation of non-covalent association of single-walled carbon nanotube with amylose by molecular dynamics simulation* Materials Letters ***59***, 8-9, p.971 (2005)

85 A. Star, Y. Liu, K. Grant, L. Ridvan, J. F. Stoddart, D. W. Steuerman, M. R. Diehl, A. Boukai and J. R. Heath *Noncovalent side-wall functionalization of single-walled carbon nanotubes* Macromolecules ***36***, 3, p.553 (2003)

86 K. D. Ausman, M. J. O'Connell, P. Boul, L. M. Ericson, M. J. Casavant, D. A. Walters, C. Huffman, R. Saini, Y. H. Wang, E. Haroz, E. W. Billups and R. E. Smalley In *Electronic properties of molecular nanostructures*; Kuzmany, H., Fink, J., Mehring, M., Roth, S., Eds. 2001; Vol. 591, p 226.

87 D. W. Steuerman, A. Star, R. Narizzano, H. Choi, R. S. Ries, C. Nicolini, J. F. Stoddart and J. R. Heath *Interactions between conjugated polymers and single-walled carbon nanotubes* Journal of Physical Chemistry B ***106***, 12, p.3124 (2002)

88 D. Baskaran, J. W. Mays and M. S. Bratcher *Noncovalent and nonspecific molecular interactions of polymers with multiwalled carbon nanotubes* Chemistry of Materials ***17***, 13, p.3389 (2005)

89 I. Gurevitch and S. Srebnik *Monte Carlo simulation of polymer wrapping of nanotubes* Chemical Physics Letters ***444***, 1-3, p.96 (2007)

90 S. E. Moya, A. Ilie, J. S. Bendall, J. L. Hernandez-Lopez, J. Ruiz-Garcia and W. T. S. Huck *Assembly of polyelectrolytes on CNTs by Van der Waals interactions and fabrication of LBL polyelectrolyte/CNT composites* Macromolecular Chemistry and Physics ***208***, 6, p.603 (2007)

91 C. A. Hunter, K. R. Lawson, J. Perkins and C. J. Urch *Aromatic interactions* Journal of the Chemical Society-Perkin Transactions 2, 5, p.651 (2001)

92 R. J. Chen, Y. G. Zhang, D. W. Wang and H. J. Dai *Noncovalent sidewall functionalization of single-walled carbon nanotubes for protein immobilization* Journal of the American Chemical Society ***123***, 16, p.3838 (2001)

93 A. Maiti, C. J. Brabec and J. Bernholc *Kinetics of metal-catalyzed growth of single-walled carbon nanotubes* Physical Review B ***55***, 10, p.R6097 (1997)

94 G. Dresselhaus, Ph. Avouris and M. S. Dresselhaus *Carbon nanotubes synthesis, structure, properties, and applications*; Springer (2001)

95 M. J. Bronikowski, P. A. Willis, D. T. Colbert, K. A. Smith and R. E. Smalley *Gas-phase production of carbon single-walled nanotubes from carbon monoxide via the HiPco process: A parametric study* Journal of Vacuum Science & Technology a-Vacuum Surfaces and Films ***19***, 4, p.1800 (2001)

96 H. J. Dal, A. G. Rinzler, P. Nikolaev, A. Thess, D. T. Colbert and R. E. Smalley *Single-wall nanotubes produced by metal-catalyzed disproportionation of carbon monoxide* Chemical Physics Letters ***260***, 3-4, p.471 (1996)

97 P. J. F. Harris *Solid state growth mechanisms for carbon nanotubes* Carbon ***45***, 2, p.229 (2007)

98 L. B. Hu, D. S. Hecht and G. Gruner *Infrared transparent carbon nanotube thin films* Applied Physics Letters ***94***, 8 (2009)

99 M. S. Fuhrer, A. K. L. Lim, L. Shih, U. Varadarajan, A. Zettl and P. L. McEuen *Transport through crossed nanotubes* Physica E ***6***, 1-4, p.868 (2000)

100 D. Simien, J. A. Fagan, W. Luo, J. F. Douglas, K. Migler and J. Obrzut *Influence of nanotube length on the optical and conductivity properties of thin single-wall carbon nanotube networks* Acs Nano ***2***, 9, p.1879 (2008)

101 M. Shiraishi and M. Ata *Conduction mechanisms in single-walled carbon nanotubes* Synthetic Metals ***128***, 3, p.235 (2002)

102 L. Hu, D. S. Hecht and G. Gruner *Percolation in transparent and conducting carbon nanotube networks* Nano Letters ***4***, 12, p.2513 (2004)

103 H. E. Unalan, G. Fanchini, A. Kanwal, A. Du Pasquier and M. Chhowalla *Design criteria for transparent single-wall carbon nanotube thin-film transistors* Nano Letters ***6***, 4, p.677 (2006)

104 V. Derycke, R. Martel, J. Appenzeller and P. Avouris *Controlling doping and carrier injection in carbon nanotube transistors* Applied Physics Letters ***80***, 15, p.2773 (2002)

105 E. S. Snow, J. P. Novak, P. M. Campbell and D. Park *Random networks of carbon nanotubes as an electronic material* Applied Physics Letters ***82***, 13, p.2145 (2003)

106 R. Martel, V. Derycke, C. Lavoie, J. Appenzeller, K. K. Chan, J. Tersoff and P. Avouris *Ambipolar electrical transport in semiconducting single-wall carbon nanotubes* Physical Review Letters ***87***, 25 (2001)

107 J. Hone, M. C. Llaguno, N. M. Nemes, A. T. Johnson, J. E. Fischer, D. A. Walters, M. J. Casavant, J. Schmidt and R. E. Smalley *Electrical and thermal transport properties of magnetically aligned single walt carbon nanotube films* Applied Physics Letters ***77***, 5, p.666 (2000)

108 A. Thess, R. Lee, P. Nikolaev, H. J. Dai, P. Petit, J. Robert, C. H. Xu, Y. H. Lee, S. G. Kim, A. G. Rinzler, D. T. Colbert, G. E. Scuseria, D. Tomanek, J. E. Fischer and R. E. Smalley *Crystalline ropes of metallic carbon nanotubes* Science ***273***, 5274, p.483 (1996)

109 E. Bekyarova, M. E. Itkis, N. Cabrera, B. Zhao, A. P. Yu, J. B. Gao and R. C. Haddon *Electronic properties of single-walled carbon nanotube networks* Journal of the American Chemical Society ***127***, 16, p.5990 (2005)

110 N. Saran, K. Parikh, D. S. Suh, E. Munoz, H. Kolla and S. K. Manohar *Fabrication and characterization of thin films of single-walled carbon nanotube bundles on flexible plastic substrates* Journal of the American Chemical Society ***126***, 14, p.4462 (2004)

111 T. V. Sreekumar, T. Liu, S. Kumar, L. M. Ericson, R. H. Hauge and R. E. Smalley *Single-wall carbon nanotube films* Chemistry of Materials ***15***, 1, p.175 (2003)

112 T. Durkop, S. A. Getty, E. Cobas and M. S. Fuhrer *Extraordinary mobility in semiconducting carbon nanotubes* Nano Letters ***4***, 1, p.35 (2004)

113 M. Radosavljevic, J. Lefebvre and A. T. Johnson *High-field electrical transport and breakdown in bundles of single-wall carbon nanotubes* Physical Review B ***64***, 24 (2001)

114 J. E. Fischer, H. Dai, A. Thess, R. Lee, N. M. Hanjani, D. L. Dehaas and R. E. Smalley *Metallic resistivity in crystalline ropes of single-wall carbon nanotubes* Physical Review B ***55***, 8, p.R4921 (1997)

115 G. T. Kim, S. H. Jhang, J. G. Park, Y. W. Park and S. Roth *Non-ohmic current-voltage characteristics in single-wall carbon nanotube network* Synthetic Metals ***117***, 1-3, p.123 (2001)

116 A. B. Kaiser, Y. W. Park, G. T. Kim, E. S. Choi, G. Dusberg and S. Roth *Electronic transport in carbon nanotube ropes and mats* Synthetic Metals ***103***, 1-3, p.2547 (1999)

117 J. Hone, I. Ellwood, M. Muno, A. Mizel, M. L. Cohen, A. Zettl, A. G. Rinzler and R. E. Smalley *Thermoelectric power of single-walled carbon nanotubes* Physical Review Letters ***80***, 5, p.1042 (1998)

118 L. Grigorian, G. U. Sumanasekera, A. L. Loper, S. Fang, J. L. Allen and P. C. Eklund *Transport properties of alkali-metal-doped single-wall carbon nanotubes* Physical Review B ***58***, 8, p.R4195 (1998)

119 V. Skakalova, A. B. Kaiser, Y. S. Woo and S. Roth *Electronic transport in carbon nanotubes: From individual nanotubes to thin and thick networks* Physical Review B ***74***, 8 (2006)

120 M. Baxendale, K. G. Lim and G. A. J. Amaratunga *Thermoelectric power of aligned and randomly oriented carbon nanotubes* Physical Review B ***61***, 19, p.12705 (2000)

121 K. Bradley, S. H. Jhi, P. G. Collins, J. Hone, M. L. Cohen, S. G. Louie and A. Zettl *Is the intrinsic thermoelectric power of carbon nanotubes positive?* Physical Review Letters ***85***, 20, p.4361 (2000)

122 R. E. Smalley, Y. B. Li, V. C. Moore, B. K. Price, R. Colorado, H. K. Schmidt, R. H. Hauge, A. R. Barron and J. M. Tour *Single wall carbon nanotube amplification: En route to a type-specific growth mechanism* Journal of the American Chemical Society ***128***, 49, p.15824 (2006)

123 S. A. Sukhishvili *Responsive polymer films and capsules via layer-by-layer assembly* Current Opinion in Colloid & Interface Science ***10***, 1-2, p.37 (2005)

124 G. Decher *Fuzzy nanoassemblies: Toward layered polymeric multicomposites* Science ***277***, 5330, p.1232 (1997)

125 X. Q. Cui, R. J. Pei, X. Z. Wang, F. Yang, Y. Ma, S. J. Dong and X. R. Yang *Layer-by-layer assembly of multilayer films composed of avidin and biotin-labeled antibody for immunosensing* Biosensors & Bioelectronics ***18***, 1, p.59 (2003)

126 J. S. Lee, J. Cho, C. Lee, I. Kim, J. Park, Y. M. Kim, H. Shin, J. Lee and F. Caruso *Layer-by-layer assembled charge-trap memory devices with adjustable electronic properties* Nature Nanotechnology ***2***, 12, p.790 (2007)

127 A. A. Mamedov, N. A. Kotov, M. Prato, D. M. Guldi, J. P. Wicksted and A. Hirsch *Molecular design of strong single-wall carbon nanotube/polyelectrolyte multilayer composites* Nature Materials ***1***, 3, p.190 (2002)

128 W. Xue and T. H. Cui *Characterization of layer-by-layer self-assembled carbon nanotube multilayer thin films* Nanotechnology ***18***, 14 (2007)

129 R. K. Iler *Multilayers of colloidal particles* Journal of Colloid and Interface Science ***21***, 6, p.569 (1966)

130 G. A. Ozin and A. C. Arsenault *Nanochemistry: A chemical approach to nanomaterials* RSC Publishing (2005)

131 S. Beyer, W. C. Mak and D. Trau *Reverse-phase LbL - Encapsulation of highly water soluble materials by layer-by-layer polyelectrolyte self-assembly* Langmuir ***23***, 17, p.8827 (2007)

132 H. H. Yu, T. Cao, L. D. Zhou, E. D. Gu, D. S. Yu and D. S. Jiang *Layer-by-layer assembly and humidity sensitive behavior of poly(ethyleneimine)/multiwall carbon nanotube composite films* Sensors and Actuators B-Chemical ***119***, 2, p.512 (2006)

133 G. Wang, J. H. Zhou and J. H. Li *Layer-by-layer self-assembly aluminum Keggin ions/Prussian blue nanoparticles ultrathin films towards multifunctional sensing applications* Biosensors & Bioelectronics ***22***, 12, p.2921 (2007)

134 K. V. a. Y. Lvov *Nanomanufacturing by layer-by-layer assembly - from nanoscale coating to device applications* Journal of Nanoengineering and Nanosystems ***220***, 1, p.29 (2006)

135 N. A. Kotov *Layer-by-layer self-assembly: The contribution of hydrophobic interactions* Nanostructured Materials ***12***, 5-8, p.789 (1999)

136 J. H. Rouse, P. T. Lillehei, J. Sanderson and E. J. Siochi *Polymer/single-walled carbon nanotube films assembled via donor-acceptor interactions and their use as scaffolds for silica deposition* Chemistry of Materials ***16***, 20, p.3904 (2004)

137 A. Baptiste, A. Gibaud, J. F. Bardeau, K. Wen, R. Maoz, J. Sagiv and B. M. Ocko *X-ray, micro-Raman, and infrared spectroscopy structural characterization of self-assembled multilayer silane films with variable numbers of stacked layers* Langmuir ***18***, 10, p.3916 (2002)

138 G. Decher and J. B. Schlenoff *Multilayer thin films*; Wiley-VCH (2003)

139 A. Pfau, W. Schrepp and D. Horn *Detection of a single molecule adsorption structure of poly(ethylenimine) macromolecules by AFM* Langmuir ***15***, 9, p.3219 (1999)

140 R. Meszaros, I. Varga and T. Gilanyi *Adsorption of poly(ethyleneimine) on silica surfaces: Effect of pH on the reversibility of adsorption* Langmuir ***20***, 12, p.5026 (2004)

141 E. Poptoshev and P. M. Claesson *Forces between glass surfaces in aqueous polyethylenimine solutions* Langmuir ***18***, 7, p.2590 (2002)

142 T. F. Tadros *Applied surfactants: principles and applications* Wiley-VCH (2005)

143 J. Galsworthy, S. Hammond and D. Hone *Oil-soluble colloidal additives* Current Opinion in Colloid & Interface Science ***5***, 5-6, p.274 (2000)

144 J. M. Bonard, T. Stora, J. P. Salvetat, F. Maier, T. Stockli, C. Duschl, L. Forro, W. A. deHeer and A. Chatelain *Purification and size-selection of carbon nanotubes* Advanced Materials ***9***, 10, p.827 (1997)

145 J. B. Schlenoff, S. T. Dubas and T. Farhat *Sprayed polyelectrolyte multilayers* Langmuir ***16***, 26, p.9968 (2000)

146 J. Cho, K. Char, J. D. Hong and K. B. Lee *Fabrication of highly ordered multilayer films using a spin self-assembly method* Advanced Materials ***13***, 14, p.1076 (2001)

147 M. Palumbo, C. Pearson and M. C. Petty *Atomic force microscope characterization of poly(ethyleneimine)/poly(ethylene-co-maleic acid) and poly(ethyleneimine)/poly(styrene sulfonate) multilayers* Thin Solid Films ***483***, 1-2, p.114 (2005)

148 M. S. Dresselhaus, G. Dresselhaus, A. Jorio, A. G. Souza, M. A. Pimenta and R. Saito *Single nanotube Raman spectroscopy* Accounts of Chemical Research ***35***, 12, p.1070 (2002)

149 M. S. Dresselhaus, G. Dresselhaus, R. Saito and A. Jorio *Raman spectroscopy of carbon nanotubes* Physics Reports-Review Section of Physics Letters ***409***, 2, p.47 (2005)

150 C. A. Cooper, R. J. Young and M. Halsall *Investigation into the deformation of carbon nanotubes and their composites through the use of Raman spectroscopy* Composites Part a-Applied Science and Manufacturing ***32***, 3-4, p.401 (2001)

151 M. Zheng, A. Jagota, M. S. Strano, A. P. Santos, P. Barone, S. G. Chou, B. A. Diner, M. S. Dresselhaus, R. S. McLean, G. B. Onoa, G. G. Samsonidze, E. D. Semke, M. Usrey and D. J. Walls *Structure-based carbon nanotube sorting by sequence-dependent DNA assembly* Science ***302***, 5650, p.1545 (2003)

152 M. J. O'Connell, S. M. Bachilo, C. B. Huffman, V. C. Moore, M. S. Strano, E. H. Haroz, K. L. Rialon, P. J. Boul, W. H. Noon, C. Kittrell, J. P. Ma, R. H. Hauge, R. B. Weisman and R. E.

Smalley *Band gap fluorescence from individual single-walled carbon nanotubes* Science ***297***, 5581, p.593 (2002)

153 G. W. Lee and S. Kumar *Dispersion of nitric acid-treated SWNTs in organic solvents and solvent mixtures* Journal of Physical Chemistry B ***109***, 36, p.17128 (2005)

154 D. F. Acevedo, J. Balach, C. R. Rivarola, M. C. Miras and C. A. Barbero *Functionalised conjugated materials as building blocks of electronic nanostructures* Faraday Discussions ***131***, p.235 (2006)

155 M. Palumbo, K. U. Lee, B. T. Ahn, A. Suri, K. S. Coleman, D. Zeze, D. Wood, C. Pearson and M. C. Petty *Electrical investigations of layer-by-layer films of carbon nanotubes* Journal of Physics D-Applied Physics ***39***, 14, p.3077 (2006)

156 J. H. Fendler *Self-assembled nanostructured materials* Chemistry of Materials ***8***, 8, p.1616 (1996)

157 H. Paloniemi, M. Lukkarinen, T. Aaritalo, S. Areva, J. Leiro, M. Heinonen, K. Haapakka and J. Lukkari *Layer-by-layer electrostatic self-assembly of single-wall carbon nanotube polyelectrolytes* Langmuir ***22***, 1, p.74 (2006)

158 V. V. Tsukruk, V. N. Bliznyuk, D. Visser, A. L. Campbell, T. J. Bunning and W. W. Adams *Electrostatic deposition of polyionic monolayers on charged surfaces* Macromolecules ***30***, 21, p.6615 (1997)

159 H. J. Park, K. A. Oh, M. Park and H. Lee *Electrical properties and conductivity mapping of thin multilayered films containing different types of carbon nanotubes* Journal of Physical Chemistry C ***113***, 30, p.13070 (2009)

160 W. Kim, A. Javey, R. Tu, J. Cao, Q. Wang and H. J. Dai *Electrical contacts to carbon nanotubes down to 1 nm in diameter* Applied Physics Letters ***87***, 17 (2005)

161 N. Nemec, D. Tomanek and G. Cuniberti *Contact dependence of carrier injection in carbon nanotubes: An ab initio study* Physical Review Letters ***96***, 7 (2006)

162 Y. Matsuda, W. Q. Deng and W. A. Goddard *Contact resistance properties between nanotubes and various metals from quantum mechanics* Journal of Physical Chemistry C ***111***, 29, p.11113 (2007)

163 J. D. Huang, Y. Yang, H. B. Shi, Z. Song, Z. X. Zhao, J. Anzai, T. Osa and Q. Chen *Multi-walled carbon nanotubes-based glucose biosensor prepared by a layer-by-layer technique* Materials Science & Engineering C-Biomimetic and Supramolecular Systems ***26***, 1, p.113 (2006)

164 H. Haick, J. Ghabboun and D. Cahen *Pd versus Au as evaporated metal contacts to molecules* Applied Physics Letters ***86***, 4 (2005)

165 J. G. Simmons *Generalized formula for the electric tunnel effect between similar electrodes separated by a thin insulatig film* Journal of Applied Physics ***34***, 6 (1963)

166 M. Lezlinger and E. H. Snow *Fowler-Nordheim tunnelling into thermally grown SiO_2* Journal of Applied Physics ***4***, 1 (1969)

167 S. Kasap and P. Capper *Handbook of electronic and photonic materials*; Springer.2006

168 M. Jaiswal, W. Wang, K. A. S. Fernando, Y. P. Sun and R. Menon *Charge transport in transparent single-wall carbon nanotube networks* Journal of Physics-Condensed Matter ***19***, 44 (2007)

169 J. G. Simmons *Conduction in thin dielectric flims* Journal of Physics D: Applied Physics ***4***, (1971)

170 S. Habermehl and R. T. Apodaca *Dielectric breakdown and Poole-Frenkel field saturation in silicon oxynitride thin films* Applied Physics Letters ***86***, 7 (2005)

171 J. G. Simmons *Poole-Frenkel effect and Schottky effect in metal-insulator-metal systems* Physical Review ***155***, 3, p.657 (1967)

172 S. Senthilarasu, R. Sathyamoorthy, S. Lalitha and A. Subbarayan *Electrical conduction properties of ZnPc/TiO2 thin films* Solar Energy Materials and Solar Cells ***90***, 6, p.783 (2006)

173 G. G. Roberts, N. Apsley and R. W. Munn *Temperature-dependent electronic conduction in semiconductors* Physics Reports-Review Section of Physics Letters ***60***, 2, p.59 (1980)

174 X. Mathew, J. P. Enriquez, P. J. Sebastian, M. Pattabi, A. Sanchez-Juarez, J. Campos, J. C. McClure and V. P. Singh *Charge transport mechanism in a typical Au/CdTe Schottky diode* Solar Energy Materials and Solar Cells ***63***, 4, p.355 (2000)

175 A. S. Jombert, K. S. Coleman, D. Wood, M. C. Petty and D. A. Zeze *Poole-Frenkel conduction in single wall carbon nanotube composite films built up by electrostatic layer-by-layer deposition* Journal of Applied Physics ***104***, 9 (2008)

176 D. Ielmini and Y. G. Zhang *Evidence for trap-limited transport in the subthreshold conduction regime of chalcogenide glasses* Applied Physics Letters ***90***, 19 (2007)

177 B. Y. Lee, K. Heo, J. H. Bak, S. U. Cho, S. Moon, Y. D. Park and S. Hong *Scalable assembly method of vertically-suspended and stretched carbon nanotube network devices for nanoscale electro-mechanical sensing components* Nano Letters ***8***, 12, p.4483 (2008)

178 J. G. Simmons *Low-voltage current-voltage relationship of tunnel junctions* Journal of Applied Physics ***34***, 1, p.238 (1963)

179 C. M. Hurd *Quantum tunnelling and the temperature dependent DC conduction in low-conductivity semiconductors* Journal of Physics C-Solid State Physics ***18***, p.6487 (1985)

180 T. Nguyen, D. A. Carl, S. V. Nguyen, D. M. Dobuzinsky and J. W. Korejwa *New leakage mechanism in sub-5-nm oxynitride dielectrics* Applied Physics Letters ***63***, 14, p.1972 (1993)

181 J. S. Lee, Y. M. Kim, J. H. Kwon, H. Shin, B. H. Sohn and J. Lee *Tunable memory characteristics of nanostructured, nonvolatile charge trap memory devices based on a binary mixture of metal nanoparticles as a charge trapping layer* Advanced Materials ***21***, 2, p.178 (2009)

182 C. L. Heng and T. G. Finstad *Electrical characteristics of a metal-insulator-semiconductor memory structure containing Ge nanocrystals* Physica E-Low-Dimensional Systems & Nanostructures ***26***, 1-4, p.386 (2005)

183 J. B. Cui, R. Sordan, M. Burghard and K. Kern *Carbon nanotube memory devices of high charge storage stability* Applied Physics Letters ***81***, 17, p.3260 (2002)

184 X. B. Lu and J. Y. Dai *Memory effects of carbon nanotubes as charge storage nodes for floating gate memory applications* Applied Physics Letters ***88***, 11 (2006)

185 Y. Kim, D. Lee, Y. Oh, J. Choi and S. Baik *The effects of acid treatment methods on the diameter dependent length separation of single walled carbon nanotubes* Synthetic Metals ***156***, 16-17, p.999 (2006)

186 M. F. Mabrook, A. S. Jombert, S. E. Machin, C. Pearson, D. Kolb, K. S. Coleman, D. A. Zeze and M. C. Petty *Memory effects in MIS structures based on silicon and polymethylmethacrylate with nanoparticle charge-storage elements* Materials Science and Engineering B-Advanced Functional Solid-State Materials ***159-60***, p.14 (2009)

187 D. H. Lien, H. F. Kuo and W. K. Hsu *Segmentation of single-walled carbon nanotubes by camera flash* Applied Physics Letters ***88***, 9 (2006)

188 J. G. Park, S. Li, R. Liang, C. Zhang and B. Wang *Structural changes and Raman analysis of single-walled carbon nanotube buckypaper after high current density induced burning* Carbon ***46***, 9, p.1175 (2008)

189 K. J. Loh, J. P. Lynch and N. A. Kotov In *4th World conference on structural control and monitoring* 2006.

190 C. Joachim, J. K. Gimzewski and A. Aviram *Electronics using hybrid-molecular and mono-molecular devices* Nature ***408***, 6812, p.541 (2000)

191 J. R. Heath *Molecular electronics* Annual Review of Materials Research ***39***, p.1 (2009)

192 R. L. McCreery *Molecular electronic junctions* Chemistry of Materials ***16***, 23, p.4477 (2004)

193 X. F. Guo, J. P. Small, J. E. Klare, Y. L. Wang, M. S. Purewal, I. W. Tam, B. H. Hong, R. Caldwell, L. M. Huang, S. O'Brien, J. M. Yan, R. Breslow, S. J. Wind, J. Hone, P. Kim and C. Nuckolls *Covalently bridging gaps in single-walled carbon nanotubes with conducting molecules* Science ***311***, 5759, p.356 (2006)

194 M. Terrones, F. Banhart, N. Grobert, J. C. Charlier, H. Terrones and P. M. Ajayan *Molecular junctions by joining single-walled carbon nanotubes* Physical Review Letters ***89***, 7 (2002)

195 Z. X. Wang, L. P. Yu, W. Zhang, Y. F. Ding, Y. L. Li, J. G. Han, Z. Y. Zhu, H. J. Xu, G. W. He, Y. Chen and G. Hu *Amorphous molecular junctions produced by ion irradiation on carbon nanotubes* Physics Letters A ***324***, 4, p.321 (2004)

196 V. Skakalova, A. B. Kaiser, Z. Osvath, G. Vertesy, L. P. Biro and S. Roth *Ion irradiation effects on conduction in single-wall carbon nanotube networks* Applied Physics a-Materials Science & Processing ***90***, 4, p.597 (2008)

197 U. Dettlaff-Weglikowska, V. Skakalova, R. Graupner, L. Ley and S. Roth In *Molecular nanostructures*; Kuzmany, H., Fink, J., Mehring, M., Roth, S., Eds. 2003; Vol. 685, p 277.

198 S. H. Ke, H. U. Baranger and W. T. Yang *Contact transparency of nanotube-molecule-nanotube junctions* Physical Review Letters ***99***, 14 (2007)

199 P. Beecher, P. Servati, A. Rozhin, A. Colli, V. Scardaci, S. Pisana, T. Hasan, A. J. Flewitt, J. Robertson, G. W. Hsieh, F. M. Li, A. Nathan, A. C. Ferrari and W. I. Milne *Ink-jet printing of carbon nanotube thin film transistors* Journal of Applied Physics ***102***, 4 (2007)

200 A. R. Boccaccini, J. Cho, J. A. Roether, B. J. C. Thomas, E. J. Minay and M. S. P. Shaffer *Electrophoretic deposition of carbon nanotubes* Carbon ***44***, 15, p.3149 (2006)

201 J. Chen, A. I. Minett, Y. Liu, C. Lynam, P. Sherrell, C. Wang and G. G. Wallace *Direct growth of flexible carbon nanotube electrodes* Advanced Materials ***20***, 3, p.566 (2008)

202 A. S. Adekunle and K. I. Ozoemena *Electron transfer behaviour of single-walled carbon nanotubes electro-decorated with nickel and nickel oxide layers* Electrochimica Acta ***53***, 19, p.5774 (2008)

203 M. J. de Andrade, M. D. Lima, V. Skakalova, C. P. Bergmann and S. Roth *Electrical properties of transparent carbon nanotube networks prepared through different techniques* Physica Status Solidi-Rapid Research Letters ***1***, 5, p.178 (2007)

204 Z. C. Wu, Z. H. Chen, X. Du, J. M. Logan, J. Sippel, M. Nikolou, K. Kamaras, J. R. Reynolds, D. B. Tanner, A. F. Hebard and A. G. Rinzler *Transparent, conductive carbon nanotube films* Science ***305***, 5688, p.1273 (2004)

205 D. Hecht, L. B. Hu and G. Gruner *Conductivity scaling with bundle length and diameter in single walled carbon nanotube networks* Applied Physics Letters ***89***, 13 (2006)

206 S. N. Song, X. K. Wang, R. P. H. Chang and J. B. Ketterson *Electronic-properties of graphite nanotubules from galvanomagnetic effects* Physical Review Letters ***72***, 5, p.697 (1994)

207 A. Bondi *Van der Waals volumes + radii* Journal of Physical Chemistry ***68***, 3, p.441 (1964)

208 M. S. Fuhrer, J. Nygard, L. Shih, M. Forero, Y. G. Yoon, M. S. C. Mazzoni, H. J. Choi, J. Ihm, S. G. Louie, A. Zettl and P. L. McEuen *Crossed nanotube junctions* Science ***288***, 5465, p.494 (2000)

209 M. Stadermann, S. J. Papadakis, M. R. Falvo, J. Novak, E. Snow, Q. Fu, J. Liu, Y. Fridman, J. J. Boland, R. Superfine and S. Washburn *Nanoscale study of conduction through carbon nanotube networks* Physical Review B ***69***, 20 (2004)

210 K. D. Ausman, R. Piner, O. Lourie, R. S. Ruoff and M. Korobov *Organic solvent dispersions of single-walled carbon nanotubes: Toward solutions of pristine nanotubes* Journal of Physical Chemistry B ***104***, 38, p.8911 (2000)

211 J. L. Bahr and J. M. Tour *Highly functionalized carbon nanotubes using in situ generated diazonium compounds* Chemistry of Materials ***13***, 11, p.3823 (2001)

212 A. G. Rinzler, J. Liu, H. Dai, P. Nikolaev, C. B. Huffman, F. J. Rodriguez-Macias, P. J. Boul, A. H. Lu, D. Heymann, D. T. Colbert, R. S. Lee, J. E. Fischer, A. M. Rao, P. C. Eklund and R. E. Smalley *Large-scale purification of single-wall carbon nanotubes: process, product, and characterization* Applied Physics a-Materials Science & Processing ***67***, 1, p.29 (1998)

213 A. F. Holloway, G. G. Wildgoose, R. G. Compton, L. D. Shao and M. L. H. Green *The influence of edge-plane defects and oxygen-containing surface groups on the voltammetry of acid-treated, annealed and "super-annealed" multiwalled carbon nanotubes* Journal of Solid State Electrochemistry ***12***, 10, p.1337 (2008)

214 J. L. Bahr and J. M. Tour *Covalent chemistry of single-wall carbon nanotubes* Journal of Materials Chemistry ***12***, 7, p.1952 (2002)

215 C. M. Yang, K. Kaneko, M. Yudasaka and S. Iijima *Surface chemistry and pore structure of purified HiPco single-walled carbon nanotube aggregates* Physica B-Condensed Matter ***323***, 1-4, p.140 (2002)

216 B. Li, T. B. Cao, W. X. Cao, Z. J. Shi and Z. N. Gu *Self-assembly of single-walled carbon nanotube based on diazoresin* Synthetic Metals ***132***, 1, p.5 (2002)

217 G. G. Wildgoose, S. J. Wilkins, G. R. Williams, R. R. France, D. L. Carnahan, L. Jiang, T. G. J. Jones and R. G. Compton *Graphite powder and multiwalled carbon nanotubes chemically modified with 4-nitrobenzylamine* Chemphyschem ***6***, 2, p.352 (2005)

218 P. Abiman, G. G. Wildgoose and R. G. Compton *Investigating the mechanism for the covalent chemical modification of multiwalled carbon nanotubes using aryl diazonium salts* International Journal of Electrochemical Science ***3***, 2, p.104 (2008)

219 C. D. Doyle, J. D. R. Rocha, R. B. Weisman and J. M. Tour *Structure-dependent reactivity of semiconducting single-walled carbon nanotubes with benzenediazonium salts* Journal of the American Chemical Society ***130***, 21, p.6795 (2008)

220 N. Nair, W. J. Kim, M. L. Usrey and M. S. Strano *A structure-reactivity relationship for single walled carbon nanotubes reacting with 4-hydroxybenzene diazonium salt* Journal of the American Chemical Society ***129***, 13, p.3946 (2007)

221 M. Toupin and D. Belanger *Spontaneous functionalization of carbon black by reaction with 4-nitrophenyldiazonium cations* Langmuir ***24***, 5, p.1910 (2008)

222 C. G. R. Heald, G. G. Wildgoose, L. Jiang, T. G. J. Jones and R. G. Compton *Chemical derivatisation of multiwalled carbon nanotubes using diazonium salts* Chemphyschem ***5***, 11, p.1794 (2004)

223 P. R. Marcoux, P. Hapiot, P. Batail and J. Pinson *Electrochemical functionalization of nanotube films: growth of aryl chains on single-walled carbon nanotubes* New Journal of Chemistry ***28***, 2, p.302 (2004)

224 B. K. Price and J. M. Tour *Functionalization of single-walled carbon nanotubes "on water"* Journal of the American Chemical Society ***128***, 39, p.12899 (2006)

225 S. Patai *The chemistry of diazonium and diazo groups Part 2*; John Wiley & Sons New-York.(1978)

226 K. Sonogashira, Y. Tohda and N. Hagihara *Convenient synthesis of acetylenes - catalytic substitutions of acetylenic hydrogen with bromoalkenes, iodoarenes, and bromopyridines* Tetrahedron Letters, 50, p.4467 (1975)

227 C. A. Dyke and J. M. Tour *Unbundled and highly functionalized carbon nanotubes from aqueous reactions* Nano Letters ***3***, 9, p.1215 (2003)

228 S. Q. Lud, M. Steenackers, R. Jordan, P. Bruno, D. M. Gruen, P. Feulner, J. A. Garrido and M. Stutzmann *Chemical grafting of biphenyl self-assembled monolayers on ultrananocrystalline diamond* Journal of the American Chemical Society ***128***, 51, p.16884 (2006)

229 J. R. Pels, F. Kapteijn, J. A. Moulijn, Q. Zhu and K. M. Thomas *Evolution of nitrogen functionalities in carbonaceous materials during pyrolysis* Carbon ***33***, 11, p.1641 (1995)

230 G. Cunningham, A. M. Panich, A. I. Shames, I. Petrov and O. Shenderova *Ozone-modified detonation nanodiamonds* Diamond and Related Materials ***17***, 4-5, p.650 (2008)

231 G. L. Chen, Y. Li, J. Lin, C. H. A. Huan and Y. P. Guo *The effect of thermal annealing on reactive radio-frequency magnetron-sputtered carbon nitride films* Journal of Physics D-Applied Physics ***32***, 3, p.195 (1999)

232 M. T. Buelow and A. J. Gellman *The transition state for metal-catalyzed dehalogenation: C-I bond cleavage on Ag(111)* Journal of the American Chemical Society ***123***, 7, p.1440 (2001)

233 P. Reiller, F. Mercier-Bion, N. Gimenez, N. Barre and F. Miserque *Iodination of humic acid samples from different origins* Radiochimica Acta ***94***, 9-11, p.739 (2006)

234 L. A. O'Hare, B. Parbhoo and S. R. Leadley *Development of a methodology for XPS curve-fitting of the Si 2p core level of siloxane materials* Surface and Interface Analysis ***36***, 10, p.1427 (2004)

235 P. W. Wang, S. Bater, L. P. Zhang, M. Ascherl and J. H. Craig *XPS investigation of electron-beam effects on a trimethylsilane dosed Si(100) surface* Applied Surface Science ***90***, 4, p.413 (1995)

236 A. Behnam and A. Ural *Computational study of geometry-dependent resistivity scaling in single-walled carbon nanotube films* Physical Review B ***75***, 12 (2007)

237 H. Overhof In *Festkoerperprobleme 16* ***16*** Springer Berlin (1976)

238 R. M. Hill *Hopping conduction in amorphous solids* Philosophical Magazine ***24***, 192, p.1307 (1971)

239 N. Apsley, E. A. Davis, A. P. Troup and A. D. Yoffe *Electronic properties of ion-bombarded evaporated germanium and silicon* Journal of Physics C-Solid State Physics ***11***, 24, p.4983 (1978)

240 N. Apsley and H. P. Hughes *Temperature-dependence and field-dependence of hopping conduction in disordered systems .2* Philosophical Magazine ***31***, 6, p.1327 (1975)

241 M. Pollak and I. Riess *Percolation treatment of high-field hopping transport* Journal of Physics C-Solid State Physics ***9***, 12, p.2339 (1976)

242 R. Stratton *Volt-current characteristics for tunnelling through insulating films* Journal of Physics and Chemistry of Solids ***23***, 9, p.1177 (1962)

243 F. Y. Cheng and A. Adronov *Suzuki coupling reactions for the surface functionalization of single-walled carbon nanotubes* Chemistry of Materials ***18***, 23, p.5389 (2006)

244 M. J. Gomez-Escalonilla, P. Atienzar, J. L. G. Fierro, H. Garcia and F. Langa *Heck reaction on single-walled carbon nanotubes. Synthesis and photochemical properties of a wall functionalized SWNT-anthracene derivative* Journal of Materials Chemistry ***18***, 13, p.1592 (2008)

245 A. B. Kaiser, V. Skakalova and S. Roth *Modelling conduction in carbon nanotube networks with different thickness, chemical treatment and irradiation* Physica E-Low-Dimensional Systems & Nanostructures ***40***, 7, p.2311 (2008)

246 C. J. Wang, Q. Cao, T. Ozel, A. Gaur, J. A. Rogers and M. Shim *Electronically selective chemical functionalization of carbon nanotubes: Correlation between Raman spectral and electrical responses* Journal of the American Chemical Society ***127***, 32, p.11460 (2005)

247 W. Ren, J. R. Reimers, N. S. Hush, Y. Zhu, J. Wang and H. Guo *Models for the structure and electronic transmission of carbon nanotubes covalently linked by a molecular bridge via amide couplings* Journal of Physical Chemistry C ***111***, 9, p.3700 (2007)

248 S. I. Cha, K. T. Kim, K. H. Lee, C. B. Mo, Y. J. Jeong and S. H. Hong *Mechanical and electrical properties of cross-linked carbon nanotubes* Carbon ***46***, 3, p.482 (2008)

249 X. F. Guo, A. A. Gorodetsky, J. Hone, J. K. Barton and C. Nuckolls *Conductivity of a single DNA duplex bridging a carbon nanotube gap* Nature Nanotechnology ***3***, 3, p.163 (2008)

250 N. Wang, K. Yano, C. Durkan, N. Plank, M. E. Welland, Y. Zhang, H. E. Unalan, M. Mann, G. A. J. Amaratunga and W. I. Milne *Direct measurement of charge transport through helical poly(ethyl propiolate) nanorods wired into gaps in single walled carbon nanotubes* Nanotechnology ***20***, 10 (2009)

251 Y. Xu, G. Zhang and B. W. Li *Large negative differential resistance in a molecular junction of carbon nanotube and anthracene* Journal of Physical Chemistry B ***112***, 51, p.16891 (2008)

252 P. W. Chiu, G. S. Duesberg, U. Dettlaff-Weglikowska and S. Roth *Interconnection of carbon nanotubes by chemical functionalization* Applied Physics Letters ***80***, 20, p.3811 (2002)

253 U. Dettlaff-Weglikowska, J. M. Benoit, P. W. Chiu, R. Graupner, S. Lebedkin and S. Roth *Chemical functionalization of single walled carbon nanotubes* Current Applied Physics ***2***, 6, p.497 (2002)

254 M. Holzinger, J. Steinmetz, D. Samaille, M. Glerup, M. Paillet, P. Bernier, L. Ley and R. Graupner *2+1 cycloaddition for cross-linking SWCNTs* Carbon ***42***, 5-6, p.941 (2004)

255 Y. Nishihara, K. Ikegashira, K. Hiraba yashi, J. Ando, A. Mori and T. Hiyama *Coupling reactions of alkynylsilanes mediated by a Cu(I) salt: Novel syntheses of conjugate diynes and disubstituted ethynes* Journal of Organic Chemistry ***65***, 6, p.1780 (2000)

256 D. A. Alonso, C. Najera and M. C. Pacheco *Highly active oxime-derived palladacycle complexes for Suzuki-Miyaura and Ullmann-type coupling reactions* Journal of Organic Chemistry ***67***, 16, p.5588 (2002)

257 D. Popovici, G. Czeremuzkin, M. Meunier and E. Sacher *Laser-induced metal-organic chemical vapor deposition (MOCVD) of Cu(hfac)(TMVS) on amorphous Teflon AF1600: an XPS study of the interface* Applied Surface Science ***126***, 3-4, p.198 (1998)

258 S. B. Jung, H. H. Park and H. Kim *Investigation of the bonding states of the SiO2 aerogel film/metal interface* Thin Solid Films ***447***, p.575 (2004)

259 B. Kakade, S. Patil, B. Sathe, S. Gokhale and V. Pillai *Near-complete phase transfer of single-wall carbon nanotubes by covalent functionalization* Journal of Chemical Sciences ***120***, 6, p.599 (2008)

260 L. Jaber-Ansari, M. G. Hahm, S. Somu, Y. E. Sanz, A. Busnaina and Y. J. Jung *Mechanism of very large scale assembly of SWNTs in template guided fluidic assembly process* Journal of the American Chemical Society ***131***, 2, p.804 (2009)

261 A. F. Carley, M. W. Roberts and A. J. Strutt *Chemical-reactivity of CO and CO_2 at a Cu(110)-Cs surface* Catalysis Letters ***29***, 1-2, p.169 (1994)

262 M. Yin, C. K. Wu, Y. B. Lou, C. Burda, J. T. Koberstein, Y. M. Zhu and S. O'Brien *Copper oxide nanocrystals* Journal of the American Chemical Society ***127***, 26, p.9506 (2005)

263 S. J. Ding, Q. Q. Zhang, D. W. Zhang, J. T. Wang and W. W. Lee *Copper metallization of low-dielectric-constant a-SiCOF films for ULSI interconnects* Journal of Physics-Condensed Matter ***13***, 31, p.6595 (2001)

264 C. M. Whelan, J. Ghijsen, J. J. Pireaux and K. Maex *Cu adsorption on carboxylic acid-terminated self-assembled monolayers: a high-resolution X-ray photoelectron spectroscopy study* Thin Solid Films ***464***, p.388 (2004)

265 R. Holze and Y. P. Wu *Novel composite anode materials for lithium ion batteries with low sensitivity towards humidity* Journal of Solid State Electrochemistry ***8***, 1, p.66 (2003)

266 T. A. Desai, D. J. Hansford, L. Kulinsky, A. H. Nashat, G. Rasi, J. Tu, Y. Wang, Z. M. and F. M. *Nanopore technology for biomedical applications* Biomedical Microdevices ***2***, 1, p.11 (1999)

267 A. A. Koos, Z. E. Horvath, Z. Osvath, L. Tapaszto, K. Niesz, Z. Konya, I. Kiricsi, N. Grobert, M. Ruhle and L. P. Biro *STM investigation of carbon nanotubes connected by functional groups* Materials Science & Engineering CBiomimetic and Supramolecular Systems ***23***, 6-8, p.1007 (2003)

268 H. L. Zhang, J. F. Li, B. P. Zhang, K. F. Yao, W. S. Liu and H. Wang *Electrical and thermal properties of carbon nanotube bulk materials: Experimental studies for the 328-958 K temperature range* Physical Review B ***75***, 20 (2007)

269 L. Liu, T. X. Wang, J. X. Li, Z. X. Guo, L. M. Dai, D. Q. Zhang and D. B. Zhu *Self-assembly of gold nanoparticles to carbon nanotubes using a thiol-terminated pyrene as interlinker* Chemical Physics Letters ***367***, 5-6, p.747 (2003)

270 K. R. Reddy, B. C. Sin, K. S. Ryu, J. C. Kim, H. Chung and Y. Lee *Conducting polymer functionalized multi-walled carbon nanotubes with noble metal nanoparticles: Synthesis, morphological characteristics and electrical properties* Synthetic Metals ***159***, 7-8, p.595 (2009)

271 R. Q. Yu, L. W. Chen, Q. P. Liu, J. Y. Lin, K. L. Tan, S. C. Ng, H. S. O. Chan, G. Q. Xu and T. S. A. Hor *Platinum deposition on carbon nanotubes via chemical modification* Chemistry of Materials ***10***, 3, p.718 (1998)

272 S. C. Mu, H. L. Tang, M. Pan and R. Z. Yuan *Synthesis and evaluation on performance of hydrogen storage of multi-walled carbon nanotubes decorated with platinum* Journal of Wuhan University of Technology-Materials Science Edition ***18***, 3, p.33 (2003)

273 S. X. Lu and B. Panchapakesan *Hybrid platinum/single-wall carbon nanotube nanowire actuators: metallic artificial muscles* Nanotechnology ***17***, 3, p.888 (2006)

274 J. N. Xie, S. Wang, L. Aryasomayajula and V. K. Varadan *Platinum decorated carbon nanotubes for highly sensitive amperometric glucose sensing* Nanotechnology ***18***, 6 (2007)

275 S. P. Somani, P. R. Somani, A. Sato and M. Umeno *Platinum and Ruthenium nanoparticles decorated multi walled carbon nanotubes as electrodes for polymer electrolyte membrane fuel cells* Diamond and Related Materials ***18***, 2-3, p.497 (2009)

276 G. N. Ostojic, Y. T. Liang and M. C. Hersam *Catalytically active nanocomposites of electronically coupled carbon nanotubes and platinum nanoparticles formed via vacuum filtration* Nanotechnology ***20***, 43 (2009)

277 L. A. da Silva, V. A. Alves, S. C. de Castro and J. F. C. Boodts *XPS study of the state of iridium, platinum, titanium and oxygen in thermally formed IrO2+TiO2+PtOx films* Colloids and Surfaces a-Physicochemical and Engineering Aspects ***170***, 2-3, p.119 (2000)

278 A. Drelinkiewicz, J. W. Sobczak, E. Sobczak, M. Krawczyk, A. Zieba and A. Waksmundzka-Gora *Physicochemical and catalytic properties of Pt-poly(4-vinylpyridine) composites* Materials Chemistry and Physics ***114***, 2-3, p.763 (2009)

279 J. P. Macquet, M. M. Millard and T. Theophanides *X-ray photoelectron-spectroscopy of porphyrins* Journal of the American Chemical Society ***100***, 15, p.4741 (1978)

280 K. Chiba, R. Ohmori, H. Tanigawa, T. Yoneoka and S. Tanaka *H2O trapping on various materials studied by AFM and XPS* Fusion Engineering and Design ***49***, p.791 (2000)

281 R. De Palma, S. Peeters, M. J. Van Bael, H. Van den Rul, K. Bonroy, W. Laureyn, J. Mullens, G. Borghs and G. Maes *Silane ligand exchange to make hydrophobic superparamagnetic nanoparticles water-dispersible* Chemistry of Materials ***19***, 7, p.1821 (2007)

282 C. P. Vinod, J. W. N. Hans and B. E. Nieuwenhuys *Interaction of small molecules with Au(310): Decomposition of NO* Applied Catalysis a-General ***291***, 1-2, p.93 (2005)

283 M. Schindler, F. C. Hawthorne, M. S. Freund and P. C. Burns *XPS spectra of uranyl minerals and synthetic uranyl compounds. II: The O 1s spectrum* Geochimica Et Cosmochimica Acta ***73***, 9, p.2488 (2009)

284 D. Ochs, B. Braun, W. Maus-Friedrichs and V. Kempter *CO2 chemisorption at Ca and CaO surfaces: a study with MIES, UPS(HeI) and XPS* Surface Science ***417***, 2-3, p.406 (1998)

285 R. Luque, J. H. Clark, K. Yoshida and P. L. Gai *Efficient aqueous hydrogenation of biomass platform molecules using supported metal nanoparticles on Starbons (R)* Chemical Communications, 35, p.5305 (2009)

286 D. H. Marsh, G. A. Rance, R. J. Whitby, F. Giustiniano and A. N. Khlobystov *Assembly, structure and electrical conductance of carbon nanotube-gold nanoparticle 2D heterostructures* Journal of Materials Chemistry ***18***, 19, p.2249 (2008)

287 T. J. Park, S. Banerjee, T. Hemraj-Benny and S. S. Wong *Purification strategies and purity visualization techniques for single-walled carbon nanotubes* Journal of Materials Chemistry ***16***, 2, p.141 (2006)

288 G. V. Andrievsky, V. K. Klochkov, A. B. Bordyuh and G. I. Dovbeshko *Comparative analysis of two aqueous-colloidal solutions of C60 fullerene with help of FTIR reflectance and UV-Vis spectroscopy* Chemical Physics Letters ***364***, 1-2, p.8 (2002)

289 P. Avouris *Carbon nanotube electronics* Chemical Physics ***281***, 2-3, p.429 (2002)

290 K. Kaneto, M. Tsuruta, G. Sakai, W. Y. Cho and Y. Ando *Electrical conductivities of multi-wall carbon nano tubes* Synthetic Metals ***103***, 1-3, p.2543 (1999)

291 C. C. Venet, C. Pearson, A. S. Jombert, M. F. Mabrook, D. A. Zeze and M. C. Petty *The morphology and electrical conductivity of single wall carbon nanotube thin films prepared by the Langmuir Blodgett technique* Colloids and Surfaces A: Physicochemical and Engineering Aspects ***354*** p.113 (2010)

292 E. Pop *The role of electrical and thermal contact resistance for Joule breakdown of single-wall carbon nanotubes* Nanotechnology ***19***, 29 (2008)

293 P. G. Collins, M. Hersam, M. Arnold, R. Martel and P. Avouris *Current saturation and electrical breakdown in multiwalled carbon nanotubes* Physical Review Letters ***86***, 14, p.3128 (2001)

294 K. Molhave, S. B. Gudnason, A. T. Pedersen, C. H. Clausen, A. Horsewell and P. Boggild *Transmission electron microscopy study of individual carbon nanotube breakdown caused by Joule heating in air* Nano Letters ***6***, 8, p.1663 (2006)

295 S. M. Sze *Physics of semiconductor devices* J Wiley & Sons (1981)

296 K. U. Lee, Y. H. Cho, M. C. Petty and B. T. Ahn *Electrical conductivity of single-wall carbon nanotube film deposited by electrostatic layer-by-layer assembly with the aid of polyelectrolytes* Carbon ***47***, 2, p.475 (2009)

297 Y. Z. Zhang, Y. J. Cai and S. Su *Determination of dopamine in the presence of ascorbic acid by poly(styrene. sulfonic acid) sodium salt/single-wall carbon nanotube film modified glassy carbon electrode* Analytical Biochemistry ***350***, 2, p.285 (2006)

Publications

The morphology and electrical conductivity of single-wall carbon nanotube thin films prepared by the Langmuir-Blodgett technique
C. Venet, C. Pearson, A. S. Jombert, M. F. Mabrook, D. A. Zeze and M. C. Petty
Colloids and Surfaces A: Physicochemical and Engineering Aspects 354 pp. 113 (2010)

The morphology, electrical conductivity and vapour sensing ability of inkjet-printed thin films of single-wall carbon nanotubes
M. F. Mabrook, C. Pearson, A. S. Jombert, D. A. Zeze and M. C. Petty
Carbon Vol. 47 Is. 3, pp. 752 (2009)

Memory effects in MIS structures based on silicon and polymethylmethacrylate with nanoparticle charge-storage elements
M. F. Mabrook, A. S. Jombert, S. E. Machin, C. Pearson, D. Kolb, K. S. Coleman, D. A. Zeze and M. C. Petty
Materials Science and Engineering B-Advanced Functional Solid-State Materials Vol. 159-60 Is. Sp. Iss. SI, pp. 14 (2009)

Poole-Frenkel conduction in single wall carbon nanotube composite films built up by electrostatic layer-by-layer deposition
A. S. Jombert, K. S. Coleman, D. Wood, M. C. Petty and D. A. Zeze
Journal of Applied Physics Vol. 104 Is. 9, 094503 (2008)